Sheffield Hallam University

A Sheffield Hallam University thesis

High Power Impulse Magnetron Sputtering (HIPIMS) - Fundamental Plasma Studies and Material Synthesis

Ante Hecimovic

A thesis submitted in partial fulfilment of the requirements of
Sheffield Hallam University
for the degree of Doctor of Philosophy

October 2009

Abstract

Physical vapour deposition (PVD) technology is widely used for deposition of coatings with applications in various industries; coatings in semiconductor industry, optical coatings or hard coatings mostly used in car and aerospace industries. In 1999 novel physical vapour deposition technology entitled high power impulse magnetron sputtering (HIPIMS) was suggested. The principle of HIPIMS is to utilize impulses (short pulses) of high power delivered to the target in order to generate high amount of metal ions with degree of metal ionization up to 90% and ions with energies up to 100 eV.

Given that HIPIMS technology has been developed only 10 years ago, extensive amount of fundamental properties of the discharge has not yet been investigated. This thesis describes fundamental research of the plasma properties, mainly temporal and spatial evolution of ions and electrons in dependence on the external parameters such as applied power and working gas pressure. The initial period of the PhD project consisted of learning to use and interpret a data from plasma diagnostic techniques. These diagnostic techniques are Optical emission spectroscopy, Optical absorption spectroscopy, Plasma sampling mass spectrometry and Langmuir probe.

The dependence of ion energy distribution function (IEDF) of metal and gas ions on applied power and working gas pressure was investigated. The results show increase in the amount and both average and maximum energy of metal and gas ions with increase in the power. Increase in the pressure, on the other hand, resulted in reduction of the amount of detected ions and lower average energies. The IEDF of both the target and gas ions was found to comprise of two Maxwellian distributions. First cold Maxwellian distribution was fitted to the main peak of the IEDF that had the lower average energy which is attributed to collisions with thermalised gas atoms and ions. The higher energy distribution is assumed to originate from a Thompson distribution of sputtered metal atoms which due to collisions are thermalised and appear as a Maxwell distribution. The time resolved measurements of the IEDF during HIPIMS of Cr target show that hot Maxwellian distribution originates from the pulse-on phase of the pulse while first cold Maxwellian distribution originates from period after the end of the pulse when metal ions are thermalised in collisions with gas particles. Additional measurements using Optical absorption spectroscopy showed increase in the ion to neutral ratio with increasing power.

Time resolved measurements of the IEDF at different distances from the target showed that at low pressure the metal ions promptly diffuse through the chamber and at 1.2 ms metal ion density was equally distributed in the chamber. At high pressure metal ions diffuse slower due to short mean free path, nevertheless after 1.2 ms significant density of metal ions could be found at distance of 10 cm reducing equally in space closer to the target and further away from the target.

The HIPIMS plasma discharge of most frequently used elements; C, Al, Ti, Cr, Cu and Nb was measured to investigate the temporal evolution and life-span of each element. The life-span of elements measured at low pressure showed dependence on the mass of the element with only Nb ions being detected at the start of the consequent pulse. At high pressure metal ions of all elements except C were detected at the beginning of the consequent pulse. Calculated metal to gas ion ratio showed increase with sputter yield equally at high and low pressure.

In the final stage of the PhD project CrAlSiN nanocomposite coatings were deposited. One coating with DC power applied on both Cr and AlSi target and three coatings with DC power applied on AlSi target and HIPIMS power applied on Cr target were deposited. Increase in metal to gas ratio was observed, using Mass spectrometer, with increase of the discharge power, particularly increase of Cr ions. Surface of the deposited coatings, recorded with SEM, was considerably smoother when deposited with HIPIMS compared to DC magnetron sputtering. Column size, calculated from micrographs recorded with AFM, was compared to metal to gas ion ratio and it showed decrease in columnar size with increase in metal to gas ion ratio.

Acknowledgments

Advanced studies

The following conferences were attended during the course of this study:

1. Fourth Sheffield HIPIMS days Conference, July 2007, Sheffield, UK

2. Fifth Sheffield HIPIMS days Conference, July 2008, Venlo, Netherlands

3. The Eleventh International Conference on Plasma Surface Engineering, September 2008 Garmisch-Partenkirchen, Germany

4. Society of Vacuum Coaters 52nd Annual Technical Conference, May 2009,Santa Clara, CA, USA

5. Sixth Sheffield HIPIMS days Conference, July 2009, Sheffield, UK,

Publications

1) Hecimovic, A. Burcalova, K.; Ehiasarian, A.P., " Origins of ion energy distribution function (IEDF) in high power impulse magnetron sputtering (HIPIMS) plasma discharge ", *Journal of Physics D: Applied Physics*, v 41, n 9, May 7, 2008, p 095203

2) Burcalova, K.; Hecimovic, A.; Ehiasarian, A.P., "Ion energy distributions and efficiency of sputtering process in HIPIMS system", *Journal of Physics D: Applied Physics*, v 41, n 11, Jun 7, 2008, p 115306

3) Ehiasarian, A.P.; Vetushka A.; Hecimovic, A.; Konstantinids, S., " Ion composition produced by high power impulse magnetron sputtering discharges near the substrate", *Journal of Applied Physics*, v 104, n 8, 2008, p 083305

4) Hecimovic, A.; Ehiasarian, A.P., "Time evolution of ion energies in HIPIMS of Chromium plasma discharge", *Journal of Physics D: Applied Physics*. 42 (2009) 135209

5) Hecimovic, A.; Ehiasarian, A.P., "Spatial and temporal evolution of ion energies in HIPIMS plasma discharge", *Journal of Applied Physics*. submitted for peer review, 2009

6) Ch. Wüstefeld, D. Rafaja, A.P. Ehiasarian, A. Hecimovic, V. Klemm, J. Kutzner, J. Kortus, D. Heger, *Thin Solid Films* submitted for peer review, 2010

7) Hecimovic, A.; Ehiasarian, A.P., "Temporal evolution of the ion fluxes for various elements in HIPIMS plasma discharge", *IEEE Transactions on Plasma Science*, submitted for peer review, 2010

Table of Contents

List of Figures and Tables

List of Figures

Figure 4.1.3 Ion energy distribution function for Cr^+ ions fitted with sum of Maxwell and Thompson measured in HIPIMS plasma discharge of Cr in Ar at pressure of p = 0.29 Pa, peak current 26 A and pulse duration 70 μs

Figure 4.1.4 Ion energy distribution functions for Cr^+ ions at the lower pressure of p = 0.29 Pa for different peak target currents a) 14 A, b) 26 A and c) 40 A. The thick dash-dot line represents experimental data. The thick solid line represents the sum of two Maxwell distributions; the thin short dashed for the first Maxwellian and the thin dash dot line for the second Maxwellian.

Figure 4.1.5 Ion energy distribution functions for Cr^+ ions at the higher pressure of p = 2.67 Pa for different peak target currents a) 14 A, b) 26 A and c) 40 A. Legend is as for Figure 4.1.3.

Figure 4.1.6 Time resolved measurements of the HIPIMS Ion energy distribution functions for Cr^+ ions at 0.29 Pa and 40 A peak current, compared with time-averaged measurement. Hollow circles represent Cr IEDF between 100 and 120 μs after the start of the pulse, hollow squares represent Cr IEDF between 230 and 1200 μs and hollow triangles represent time-averaged Cr IEDF.

Figure 4.1.7 Plasma potential as a function of time, of Ti HIPIMS at low pressure of 0.29 Pa for two peak currents 14A and 40A

Figure 4.1.8 Ion energy distribution functions for Ar^+ ions at the lower pressure of p = 0.29 Pa for different peak target currents a) 14 A, b) 26 A and c) 40 A. Legend is as for Figure 4.1.3.

Figure 4.1.9 Ion energy distribution functions for Ar^+ ions at the higher pressure of p = 2.67 Pa for different peak target currents a) 14 A, b) 26 A and c) 40 A. Legend is as for Figure 4.1.3.

Figure 4.1.10 Time resolved measurements of the HIPIMS Ion energy distribution functions for Ar^+ ions at 0.29 Pa and 40 A peak current, compared with time-averaged measurement. Hollow triangles represent Ar IEDF between 100 and 120 μs after the start of the pulse, hollow squares represent Ar IEDF between 220 and 240 μs and solid squares represent time-averaged Ar IEDF. Time resolved measurements are connected with the smoothing line to ease the data recognition on the figure.

Figure 4.1.11 Ratio of second Maxwell distribution integral to experimental data integral (solid line) and average energy of experimental data (dashed line) as a function of the peak target current for three different targets a) Chromium, b) Titanium and c) Carbon

Figure 4.1.12 Metal ion-to-gas ion ratio as a function of peak current at low pressure for three elements (Cr, Ti and C)

Figure 4.1.13 Ion saturation current measured with flat probe at a) pressure of 0.29 Pa and b) pressure of 2.9 Pa as a function of peak current, in HIPIMS plasma discharge with Cr target

in HIPIMS plasma discharge of Cr at pressure of 0.3 Pa. The energy scale measured by mass spectrometry is represented in volts, to obtain it in eV it was multiplied by two for doubly charged ions.

Figure 4.2.6 Temporal evolution of Ar^{2+} IEDF from the start of the pulse until 5ms from the start of the pulse in a) ascending scale and b) descending scale in HIPIMS plasma discharge of Cr at pressure of 0.3 Pa. The energy scale measured by mass spectrometer is represented in volts, to obtain it in eV it was multiplied by two for doubly charged ions.

Figure 4.2.7 Ion saturation current of HIPIMS plasma discharge with Cr target at pressure of 0.3 Pa and peak current of 40 A

Figure 4.2.8 Average energy of species measured in HIPIMS plasma discharge with Cr target at pressure of 0.3 Pa and peak current of 40 A

Figure 4.2.9 Integral values of the ion energy distribution function in HIPIMS plasma discharge with Cr target at pressure of 0.29 Pa and peak current of 40A

Figure 4.2.10 Ion density of the HIPIMS plasma discharge with Cr target at pressure of 0.29 Pa and peak current of 40 A at the position of the mass spectrometer

Figure 4.3.1 The electron density as a function of time and distance from the target at a) pressure of 1 Pa and b) pressure of 3 Pa, in HIPIMS plasma discharge with Ti target

Figure 4.3.2 Time averaged ion energy distribution (IEDF) of a) Ti^{1+} ions and b) Ar^{1+} ions as function of distance at pressure of 1Pa

Figure 4.3.3 Time averaged ion energy distribution (IEDF) of a) Ti^{1+} ions and b) Ar^{1+} ions as function of distance at pressure of 3Pa

Figure 4.3.4 The ion flux of Ar^{1+}, Ti^{1+}, Ar^{2+}, Ti^{2+} ions as a function of distance for a) pressure of 1 Pa and b) pressure of 3 Pa in HIPIMS plasma discharge

Figure 4.3.5 The ion flux of a) Ti^{1+} and b) Ar^{1+} as a function of time and distance at pressure of 1 Pa in HIPIMS plasma discharge with Ti target

Figure 4.3.6 The average energy of a) Ti^{1+} IEDF and b) Ar^{1+} IEDF as a function of time at different distances from the target at pressure of 1 Pa

Figure 4.3.7 The ion flux of a) Ti^{1+} and b) Ar^{1+} as a function of time and distance at pressure of 3 Pa in HIPIMS plasma discharge with Ti target

Figure 4.3.8 The average energy of a) Ti^{1+} IEDF and b) Ar^{1+} IEDF as a function of time at different distances from the target at pressure of 3 Pa

Figure 4.3.9 Comparison of the spatial distribution between electron density and ion fluxes at pressure of 3 Pa and at 80 μs

List of Tables

CHAPTER 1
Introduction

Physical vapour deposition (PVD) is a coating technique, based on vacuum deposition to deposit thin films by the condensation of a vaporized material onto various surfaces. PVD is a process by which a thin film of material is deposited on a substrate in three steps [1]:

- o the material from a source, target, is converted into vapour; by evaporation, sputtering or chemical vapours
- o the vapour is transported from source to the substrate either by line-of-sight or, in case of sufficient pressure the metal vapour is ionised creating a plasma
- o the vapour undergoes condensation on the substrate through nucleation and growth processes to form the thin film.

Sputter deposition of metallic films is used for a wide range of applications. From 1852, when sputtering was discovered [2] inside a discharge tube, sputtering was developed into numerous methods for thin film deposition. Sputtering is a mechanism by which atoms are ejected from the surface of a material as a result of collision with high energetic particles. To improve the deposition rate in the standard DC diode discharges magnets were placed behind a cathode [3]. This setup is known as magnetron sputtering. Permanent magnets placed behind a cathode provide closed magnetic field lines starting at the edge of a cathode and closing in the centre of a cathode. Secondary electrons ejected from the target, which serves as a cathode, are trapped by Lorentz force into a helical motion down the magnetic field lines. Helical motion forces the electrons to move in the target vicinity enhancing ionisation of gas atoms.

Commonly a DC power supply is applied to maintain a discharge and the deposition of a thin film. Main limitation of DC magnetron sputtering is low sputtering rate and low ion current density and low ionisation degree of the sputtered flux [2]. To increase the ionisation rate a radio-frequency (RF) field from an external coil placed in the region between the cathode and the anode, can be used to generate a highly ionized metal plasma discharge [4]. It has been found that the ionization, and therefore the ionization flux fraction, increases with increased RF power and pressure [5]. In 1999 Kouznetsov et al. [6] suggest a new method of increasing the metal particles ionisation named high power impulse magnetron sputtering (HIPIMS) for deposition of hard nanoscale coatings. They reported that HIPIMS produces a highly ionized flux of the target material and higher electron densities than standard DC magnetron sputtering. Highly ionized flux produces denser coatings and improved properties of the coating. HIPIMS is a proven technique in deposition of CrN [7] and TiN [8] hard thin films with applications in tribological protection of automotive engines and turning.

The wide application of HIPIMS for film growth requires understanding of plasma dynamics and influence of plasma parameters on the thin film properties. Understanding the properties of ions in the plasma could be helpful in controlling the flux of metal particles arriving at the substrate and therefore controlling growth of the coating and its properties such as microstructure density, surface roughness and lattice defect density.

The target power density in HIPIMS reaches 3000 Wcm^{-2} compared to < 30 Wcm^{-2} typical of conventional direct current magnetron sputtering (DCMS). Unlike DCMS where a constant voltage is applied, in HIPIMS voltage is applied in short pulses, typically around 100 µs long, with a long off time between pulses of 10 000 µs in order not to overheat the target. Increased power on the target leads to increased sputtering and ion density of >10^{19} m^{-3} in the vicinity of the target has been detected [6, 9] which in turn results in appreciable degree of ionization of the metal atoms sputtered from the target. Ionization degree of 90% in the HIPIMS discharge was reported [10].

The ionization mechanisms during a typical HIPIMS pulse evolution in time are governed by electron impact collision processes and depend strongly on the electron energy distribution function (EEDF). Langmuir probe

measurements of the EEDF in a similar system [11] - a pulsed magnetic multipole hydrogen discharge - showed that it changed from a non-Maxwellian distribution with high energy during the discharge to a Maxwellian distribution in the late post-discharge. The term Maxwellian distribution under the assumption that the plasma is in local thermal equilibrium is used. Similar results were reported in the HIPIMS discharge [12]. The work of Vetushka et al. [9] shows a high energy group during the ignition phase of the discharge and a low energy electron group at the end. It was found by Guimaraes et al [98][99] that EEDF in an Argon planar magnetron discharge with Mo target has nearly Maxwellian distribution at low energies but at energies higher than 15 eV the distribution is not Maxwellian than rather it has a high energy tail stretching up to 500 eV.

The HIPIMS plasma develops through several stages in time and the transport from the target to the substrate occurs not just during the pulse but also in the time between the pulses. Several phenomena have been uncovered to describe this behaviour. Gudmundsson et al. [12] have shown that the diffusion rates of plasma through the chamber are strongly influenced by the pressure of the process gas with speeds of 0.4 $cm\mu s^{-1}$ at 0.3 Pa and decreasing to 0.087 $cm\mu s^{-1}$ at 7 Pa, indicating that the diffusion is strongly dominated by elastic scattering. A number of works have distinguished two waves of plasma arriving at the substrate [13, 14, 15, 9] a gas plasma succeeded by a metal-rich plasma.

The HIPIMS plasma discharge undergoes several stages of development, as has been observed by optical emission spectroscopy (OES) [16, 17, 18], from gas dominated plasma to metal dominated plasma. The OES measurements of a HIPIMS plasma discharge of Ti [16] showed the existence of Ar^0, Ar^{1+}, Ti^0, Ti^{1+}, and Ti^{2+} species in the discharge. In the beginning of the pulse, the plasma is dominated by Ar neutrals and as the discharge current increases and the sputtering of metal vapour develops, Ti ions become the dominant species in the plasma. After the pulse, the relative emission intensity is decreasing, fastest for the Ti^{2+} and Ti^{1+} ions and at a slower rate for Ar^0 and Ti^0 atoms. These works have collectively pointed to the fact that at the substrate, gas plasma is firstly generated by quickly diffusing hot electrons and the bulk plasma generated at the target arrives at a later

3

stage, delayed by the diffusion process. In some cases a third peak may be detected attributed to reflection of plasma from the vessel walls [15, 16, 19].

De Poucques et al. [20] showed that in the post discharge titanium ions and electrons diffuse together from the magnetron cathode to the substrate obeying ambipolar diffusion. The ion energy distribution function (IEDF) is strongly affected by the diffusion of the discharge plasma through the chamber. The evolution of the electron density measured at different distances from the target at pressures from 0.3 Pa to 3 Pa shows that at high pressure the electron density decays slowly at all distances compared to sharp drop in density after switch off at low pressure [21]. In addition the measurements showed delayed arrival of peak electron density at longer distances and reduction of electron density peak travelling velocity with increased pressure. The results obtained with the Langmuir probe used to investigate the dependence of the electron density temporal evolution on the discharge power [19], show the increase in electron density with discharge power and delayed arrival of the electron density peak at longer distances from the target. Furthermore Langmuir probe was used to investigate the occurrence of the metal ions as a function of time and distance and as a function of time and pressure at 1.1 Pa [19]. The results show two waves of ions, first one arriving shortly after the end of the pulse and second wave arriving in the post-discharge reaching peak later for the longer distance from the target.

The ion saturation current measured at different distances from the target [22] showed that ions are able to leave the magnetized region and reach the substrate in greater numbers depending on the peak current, which is the consequence of the kinetic pressure exceeding the magnetic pressure.

The thermalisation of neutrals in a direct current (DC) magnetron sputtering plasma was investigated in detail by several authors [23, 24]. Simulations of particle transport [25] and the neutral particle flow in HIPIMS [26] add valuable information on plasma thermalisation and gas rarefaction. Several papers used mass spectrometry to describe the influence of pressure on the ion energy distribution function (IEDF) [27] and the influence of power on the IEDF [28, 29, 30]. Vlcek et al. [31] observed the dependence of the IEDF of Cu target in HIPIMS on pressure and distance from target. It was found that increasing the working gas pressure and distance from the target

the high energy tail of the metal IEDF was reduced and the low energy peak of the metal IEDF increased and narrowed as a result of thermalisation.

During the pulse a Thompson-like high energy tail distribution of metal IEDF with energies up to 100 eV has been reported [29, 32], whereas after the pulse metal ion IEDF comprised of a main low energy peak and a high energy tail, for measurements recorded in the vicinity of the target. Time resolved measurements comparing the rise of the discharge current to the end of the pulse have shown the existence of a single low energy peak in the post discharge [33, 28]. The mean energy was shifted towards higher values for measurement later in the pulse [33].

At higher pressure and lower peak power density Vlcek et al. [33] found that the intensity of the IEDF low energy peak is higher with higher discharge current and that peak position of the IEDF in the beginning of the pulse is at low energy and moves towards higher energies later in the pulse. Rao et al. [34] developed a technique for determining effective ion temperature in Townsend discharges from IEDF analysis of flux-energy distribution.

There are limited studies explaining the shape of measured IEDFs and the influence of power on the IEDF. Furthermore detailed study on the temporal and spatial evolution of ions and electrons in dependence on the external parameters such as applied power and working gas pressure in HIPIMS plasma discharges was missing. Time evolution and life-span of metal ions for different target materials in HIPIMS has not been reported yet.

This work investigates ion energy distribution in HIPIMS plasma discharges using three different target materials: Chromium (Cr), Titanium (Ti) and Carbon (C). Dependence of the IEDF on pressure and peak target current was measured. IEDFs comprised of a main distribution with low energy peak and a secondary distribution with high energy tail. Both experimentally determined distributions are fitted with analytical functions. The average ion energy and metal ion-to-gas ion ratio are evaluated. The results and discussion is presented in Chapter 4.1.

The temporal evolution of singly and doubly charged gas ion and metal ion energy distribution function in a HIPIMS discharge has not been studied in detail to date. Information on the lifespan of gas and metal particles and their energies especially between HIPIMS pulses is incomplete. The temporal

evolution of the gas, Ar^{1+} and Ar^{2+}, and metal, Cr^{1+} and Cr^{2+} IEDF at the position of the substrate using energy-resolved mass spectroscopy has been investigated. The ion saturation current was measured next to the mass spectrometer orifice to provide data on the total ion flux. The results and discussion is presented in Chapter 4.2.

Complete temporal and spatial variation of ion fluxes and ion energies impinging on the substrate during HIPIMS deposition hasn't been yet investigated. Temporal and spatial resolved measurements of the IEDF using plasma sampling mass spectrometer and spatial and temporal measurements of electron density using Langmuir probe have been performed to give an insight on plasma properties at different positions inside the deposition chamber. The results and discussion is presented in Chapter 4.3.

There are numerous materials used for thin film deposition. Each of materials has a specific mass, sputtering yield, binding energy and ionisation potential. In order to investigate the influence of these properties on the plasma properties the temporal evolution of metal and gas ions was investigated in the HIPIMS plasma discharge of C, Al, Ti, Cr, Cu and Nb. The result provided information about the correlation between sputtering yield and metal ion - to - gas ion ratio. The results and discussion is presented in Chapter 4.4.

In the final chapter the correlation between plasma properties, measured with plasma sampling mass spectrometer, and the properties of HIPIMS-deposited coating was given. Four CrAlSiN nanocomposite coatings were deposited, one with DC power supply connected on both Cr and AlSi target, and three with DC power supply connected to AlSi target and HIPIMS power supply connected to the Cr target. The power on the HIPIMS power supply was changed from 0.21 kW to 0.7 kW. Composition of the coating was investigated with Energy dispersive X-ray spectroscopy (EDX) and the surface of the coating was recorded using Scanning electron microscope (SEM) and Atomic force microscopy (AFM). The results and discussion is presented in Chapter 4.5.

CHAPTER 2

Literature review

This chapter consists of three sections; 2.1 comprise the basic principles and classification of discharges, 2.2 describes the principles of magnetron sputtering and various methods used for deposition of thin films, Section 2.3 is dedicated to the high power impulse magnetron sputtering (HIPIMS) and the final section 2.4 describes the interaction between plasma and surface of the coating.

2.1 The classification of plasma discharges

2.1.1 Electrical discharges

One of the basic types of discharges is the DC diode discharge. It consists of two electrodes at different potentials. The electrode with positive potential is anode and the electrode with negative potential is cathode. The air from the chamber is pumped by the vacuum pumps to achieve low pressures, for physical vapour deposition typically between 0.1 and a few Pa. Applying voltages on the electrodes, plasma discharge develops. To start the discharge and to start the current between electrodes it is necessary to have initial electrons and ions. Cosmic rays and natural radioactivity continually produce a small number of electrons and ions in the gas and this gives air a small conductivity. To maintain the discharge it is necessary to have a source of electrons since electrons are at least 1836 times lighter, and therefore more mobile than ions, to carry the majority of the current. Electrons can be created in the electron impact ionisation of the particles in the plasma [35, 36];

$$e^- + Ar \rightarrow Ar^+ + 2e^-$$

7
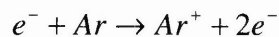
or ion impinging the cathode can create secondary electron from the cathode. Created electrons will diffuse to the anode, the ions to the cathode, and a small current will flow.

The collision between electrons and atoms or ions does not necessarily result in ionisation. Energy transferred from electron to atom or ion could be lower than the ionisation energy therefore the electron inside the atom is still orbiting the atom but in a higher energy level. Relaxation of the excited electron results in emission of a photon. Since energy levels are specific for each element, the light emitted from the plasma can be used to determine the composition of the plasma [36]. This is the main principle of optical emission spectroscopy that is described in more details in the chapter 3.3.2. In case of Ar gas, which is frequently used in the plasma discharges, first excited energy level of the Ar atom is 11.5 eV and spontaneous transition to the ground state is forbidden. These levels are called metastable states, which mean that a metastable atom may preserve the excitation energy for longer periods of time. The energy of a metastable state can be transferred to a different atom or ion by an inelastic collision [36].

The electrons, ions and neutrals are in constant thermal motion inside the plasma. In equilibrium, the velocities are distributed according to the Maxwell distribution [37];

$$f(v) = n \left(\frac{m}{2\pi kT} \right)^{3/2} exp \left(-\frac{mv^2}{2kT} \right)$$

(2.1)

where n is the plasma density, m is the mass of the particle and T is the temperature of the particles that is described by distribution. The diagnostic technique mass spectrometry used to measure ion energy distribution function is described in chapter 3.3.3.

At the point where the adequate amount of ions hitting the cathode produce a sufficient number of secondary electrons to maintain the discharge it becomes self-sustained. The voltage between the electrodes at which self-sustained discharge occurs is called breakdown voltage.

2.1.2 Discharge breakdown

The breakdown voltage is described by the Paschen law [100] and it is only dependant on the product of a pressure P and a gap distance between anode and cathode d. It is described by equation [38]:

$$V = \frac{A(Pd)}{B + lnPd}$$

(2.2)

A and B are experimentally determined constants that depend on the gas used in the discharge. The existence of the sparking potential minimum at Pd_{min} leads to unusual behaviour of the discharge. If the gap between electrodes is reduced and Pd product is lower than Pd_{min} then if the shape of the discharge chamber has a longer and shorter path between electrodes then the discharge will be created on the longer path since the breakdown voltage is lower. This indicates that bringing the electrodes closer together the discharge will require higher voltage to achieve a breakdown. The experimental result of the breakdown voltage in Ar for different cathode materials as a function of Pd product, was measured by Hassouba et al. [39] and it is presented on Figure 2.1.
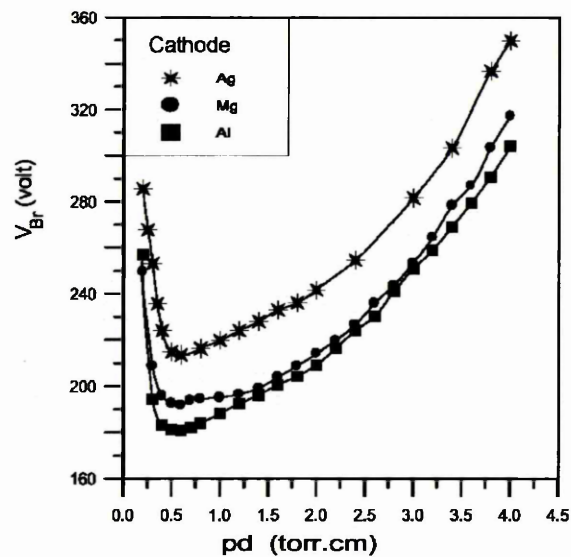
Figure 2.1 Breakdown voltage as a function of Pd (torr cm) product for different cathode materials. Adopted from [39]

9

2.1.3 Voltage current characteristic

Very comprehensive explanation of the voltage current characteristic of the discharges is given by Cobine [40]. The material and shape of the electrodes does not have an effect on the characteristics of the discharge. The voltage source with potential E is connected in series with a resistance R, therefore the voltage between anode and cathode is equal to V = E - IR, shown on Figure 2.2. Depending on the resistance R the current in the discharge and the properties of the discharge are changing. The irregular curve on Figure 2.2 is the voltage - current (V-I) characteristic of the device. The scale of the voltage and current has been distorted to show all stages of the discharge.

Point A on Figure 2.2 is a stable point of operation for R = R_1. It is a stable point since if the current I is slightly reduced the V increases, according to the load line, while the voltage between anode and cathode becomes smaller. The difference in voltage increases the current, restoring it to the value before the disturbance. If the current is slightly increased, a reduced voltage will tend to reduce the current again bringing the operating point back to the original place. At point A, the current is a few microamperes, the discharge is dark, it is not self-sustained and it is called the Townsend region.

Discharge Static V-I Characteristic
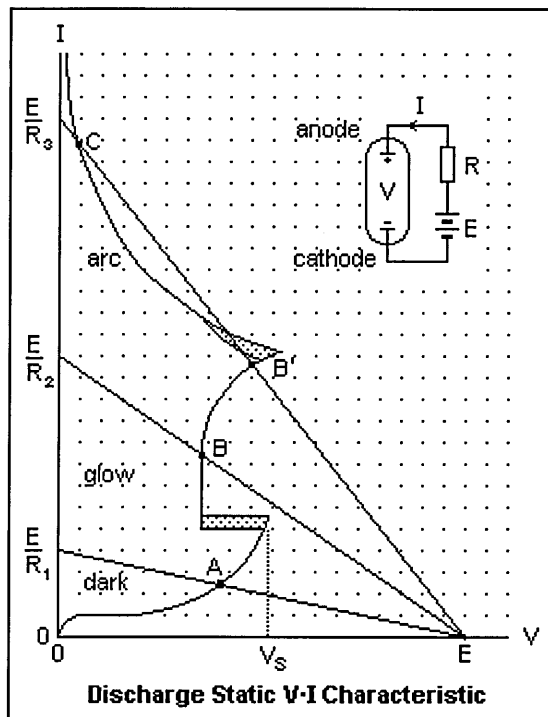
Figure 2.2 Discharge voltage current characteristic, adopted from [40]

10

Next stage occurs if the resistance is reduced from R_1 to R_2. The currents are higher and the discharge transits from Townsend discharge to a glow discharge. Operating point moves up the curve until the sparking potential V_S is reached. At the sparking potential the voltage is sharply reduced and the stable operating point is located at the position B. At this point the discharge is self-sustaining. The cathode heating is not sufficient to cause transition to an arc. If resistance R is decreased further, towards R_3, the discharge voltage increases until point B' is reached. To increase the current large increase in the voltage is needed. This is known as abnormal glow. If cathode heating is sufficient it will result in increase of the electrons and the discharge voltage will decrease. Reducing the voltage the discharge operating point moves to point C. At point C the voltage is low and current is considerably higher. At this point discharge is transformed to the arc. Further reduction of resistance R will result in target melting [40, 35, 38].

2.1.4 Glow discharge

Glow discharge in a tube and different regions of the glow discharge are shown and named on the Figure 2.3. It was found that if the tube is extended and the distance between electrodes is increased the negative glow and Faraday space do not expand while the positive column extends. To maintain the discharge it is necessary to have constant generation of ions and electrons. The whole process starts at the cathode where positive ions, mainly coming from the negative glow region, bombard the target and eject secondary electrons. The ions recombine at the cathode falling to the ground state with the emission of a photon. This light from the recombining ions produces the cathode glow, which is separated from the cathode by a very narrow space, the Aston dark space. Dark regions in the discharge are less luminous than brighter regions, such as cathode glow, negative glow and positive column. The Aston dark space has the strongest electric field in the discharge and most of the voltage between anode and cathode is lost in the cathode fall V_c near the cathode. Secondary electrons ejected from the cathode are accelerated in the cathode fall and by reaching negative glow the electrons acquire sufficient energy to ionize the atoms in the plasma. In the

11

negative glow space majority of ions necessary for the maintenance of the discharge are created. Once the ion is created it is accelerated towards the cathode and the whole process starts over again. The negative glow comprises of light emitted from excited neutrals and ions through collision with electrons. The electrons loose a substantial amount of their kinetic energy and drift out into the Faraday dark space. The density of ions is reduced in the Faraday dark space and electrons are accelerated in the electric field that is show on Figure 2.3 b). As the electrons accelerate towards anode their kinetic energy at this point is sufficient to excite atoms that emit photons as the electrons in the atom falls to a ground state. The space illuminated by these photons is called the positive column. The electrons carry most of the discharge current in the positive column [36, 38].
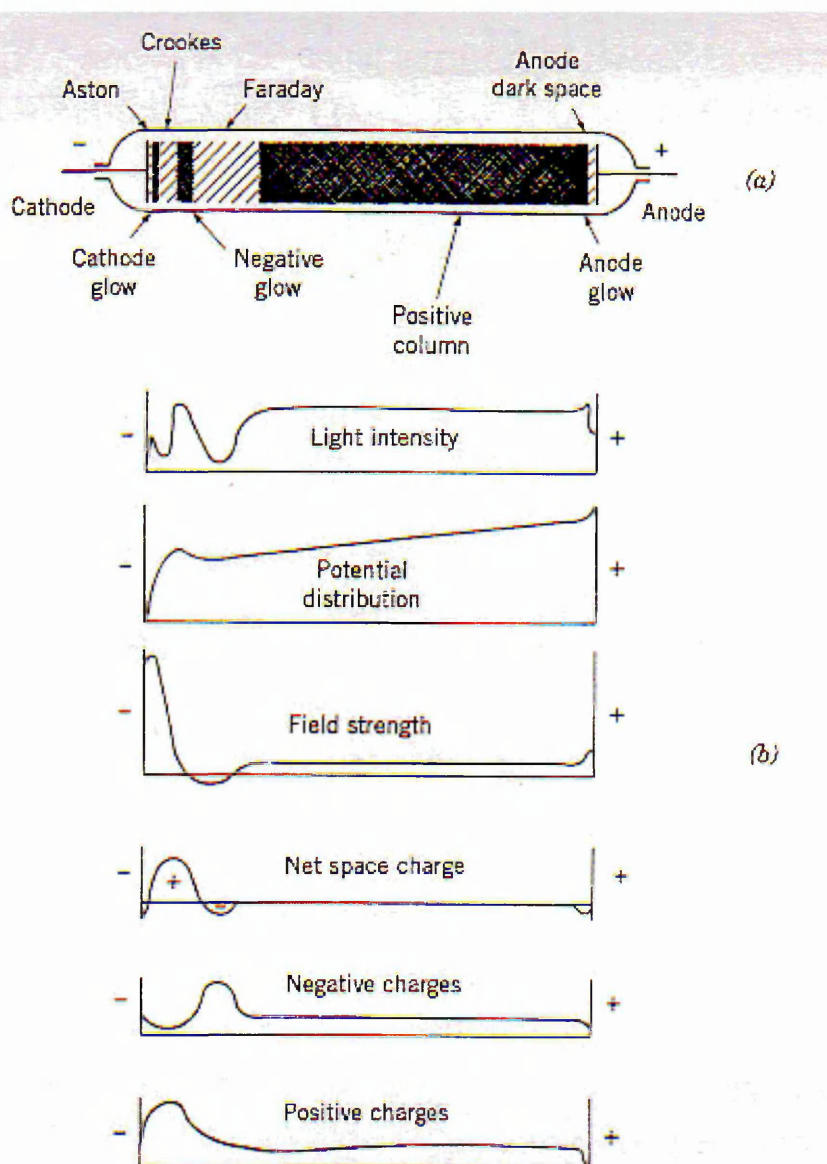
Figure 2.3 Qualitative characteristic of a DC glow discharge, adopted from [36]

2.1.5 Arc discharge

Increasing the temperature of the target by ion bombardment the discharge may turn into an arc. In the glow discharge the voltage drop is hundreds of volts while the arc requires few tens of volts. Difference in the voltage needed to sustain the discharge arises from the different cathode emission mechanism. In the arc the electrons are emitted thermionically from the cathode. High temperature of the arc cathode is a result of the cathode receiving energy from the current. Thermal effects play an important role in arcs. The cathode is heated by positive ion bombardment, where the effect of the ions is purely thermal and any electron emission induced by the bombarding ions is insignificant. Any spot that becomes hotter than its neighbour tends to become even hotter as the extra thermionic electrons attract the positive ions to the spot. The electrons are ejected either by thermionic emission, or by high-field emission. Materials such as tungsten have fixed cathode spot and electrons are ejected in thermofield emission, while low-melting-point cathodes have so called wandering cathode spot which is example of thermionic field emission. A typical current density for a thermionic cathode spot is 10^2-10^4 A/cm^2, and of a high-field spot, 10^4-10^7 A/cm^2 [38]. The arc spot in the thermionic field emission gets eroded and vaporised ejecting the cathode material into the chamber.

The arc consists of the cathode drop, the positive column, and the anode drop. The cathode drop is a little less than the ionizing potential of the gas or vapour. The width of the cathode drop region is little longer than a mean free path of an electron, so the cathode region is very thin. The anode drop occurs in a wider region, and resembles a probe sheath, as in a glow discharge [38].

2.1.6 Nano-pulsed discharges

A glow-type gas discharge with very short duration of the voltage pulse of few nanosecond creating homogeneous nanosecond discharge was investigated by Starikovskaia [41, 42, 43]. The discharge develops from a high-voltage to a low-voltage electrode when high voltage is applied to a

discharge gap. The displacement current closes the electric circuit during the discharge propagation along the discharge gap, while the conductive current closes the circuit after the discharge reaches the low-voltage electrode. Typical discharge is initiated by high voltage positive polarity pulses, where the pulse amplitude in the cable is between 10 and 15 kV, duration at half-height is 25 ns, rise time of 5 ns and repetitive frequency around 40 Hz. The typical discharge tube diameter was 5 cm and the distance between the electrodes was 20 cm. Spatial uniformity of nanosecond discharges has been proved by numerous images with the help of fast CCD cameras [41]. The maxima of plasma intensity are manifested near the electrodes, while, on the whole, the discharge develops uniformly. In cases where the constant high voltage pulse amplitude was maintained and the gas density was increased, the discharge transforms into a non-homogeneous streamer form. At the closing stage, the discharge current is rather high and reaches hundreds of Amperes. The peak of high reduced electric fields is not longer than 2–3 ns, as shown on Figure 2.4. Then the field rapidly decreases to the lower values. It is this narrow peak of high electric fields which is responsible for a uniform discharge development in space. High electric fields cause production of electrons with high energies that pre-ionize the gas in the vicinity of the front. The bulk of the required electron concentration and population of upper electronic levels take place behind the fast ionization wave front in the residual fields. These residual fields are comparable to the fields in the streamer head.
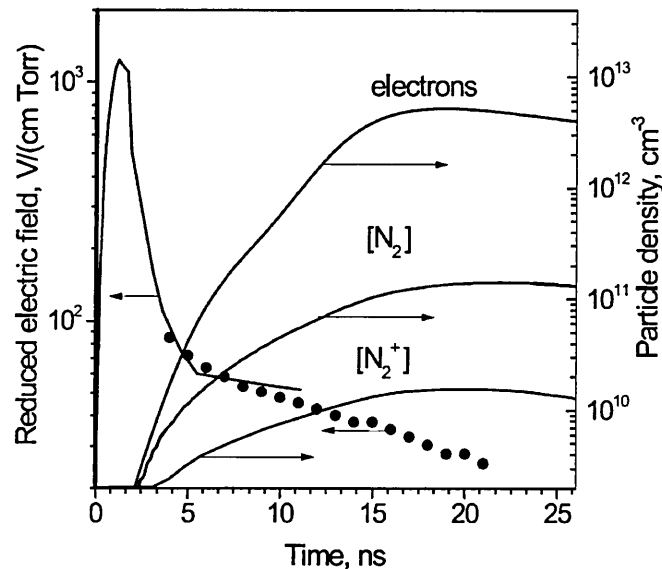
Figure 2.4 Temporal behaviour of the electric field, electron density and density of the electronically excited states in nano-pulsed discharges, from [42]

14

Figure 2.4, displays typical temporal behaviour of the electric field, electron density and concentration of the electronically excited states. The energy contributed to the plasma is mainly consumed for excitation of electronic states and the energy balance is shifted towards the high energy level states, including excited states of ions. The analysis based on time-resolved measurements of emission of two molecular bands showed that in the vicinity of the breakdown front the electron energy distribution function (EEDF) should be substantially overpopulated with high-energy electrons [42]. At the same time the conditions when nonstationary and nonlocal nature of EEDF may be neglected can be reached behind the fast ionization wave front. It was shown that formation of the EEDF in a fast ionization wave takes place as a result of interaction between two electron 'fluxes' oppositely directed along the energy axis. The electrons of energies of the order of kiloelectronvolts are produced in the fast ionization wave front lead to the formation of the secondary electron spectrum that decreases with energy in accordance with the power series law. On the other hand, heating of the electron ensemble by the electric field essentially affects formation of the EEDF in the region of elastic process thresholds.

A nanosecond discharge in the form of a fast ionization wave has a practical use in plasma assisted ignition and combustion. The benefits of nanosecond discharge are:

o plasma development during times significantly shorter than those typical for ignition

o produces a spatially uniform plasma

o excites high-energy levels of molecules causing dissociation at minimal gas heating.

2.2 Magnetron sputtering

Gas discharges can be initiated in the absence of an artificial source when the voltage across the electrode is equal to or exceeds the static breakdown voltage gap V. Increase in voltage results in an abrupt increase in current, which is accompanied with an increase in glow intensity in the gap.

DC glow discharges have long been used as sputtering sources for metallic materials. Figure 2.5 a) illustrates planar DC glow discharge driven by a constant current dc source [37]. The upper electrode, which is a cathode, serves as the target for ion impact sputtering. The substrate, on which the sputtered atoms are deposited, is placed on the lower electrode which is the anode.

(a)

(b)
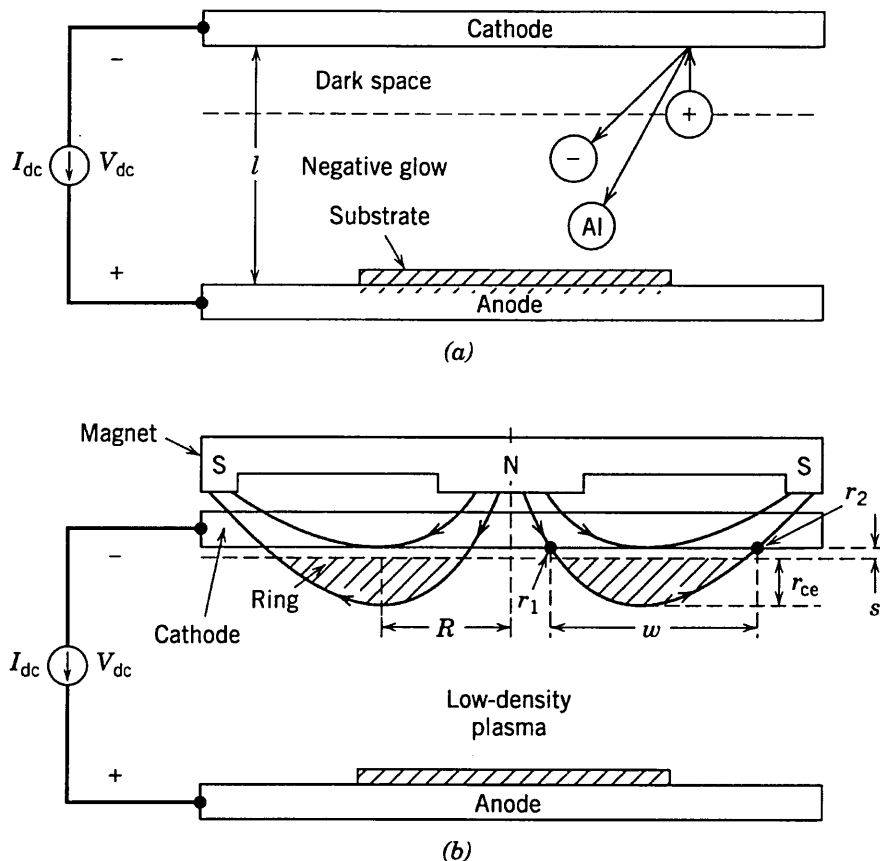
Figure 2.5 Schematic of a) DC glow discharge and b) DC magnetron discharge adapted from [37].

The discharge is maintained by secondary electron emission from the cathode, with the energetic secondary electrons providing the ionization required to maintain the discharge. However, operating pressures must be high enough, p > 30 mTorr, so that secondary electrons are not lost to the anode or side walls. This pressure is higher than optimum for deposition of sputtered atoms onto the substrate due to scattering of sputtered atoms. The drawback of the DC glow discharge is the low sputtering power efficiency, which is decreasing with increasing energy. It is necessary to operate a sputtering discharge at higher densities, lower voltages and lower pressures.

16

This has led to the use of a dc magnetic field at the cathode to confine the secondary electrons. An axisymmetric dc magnetron discharge configuration is shown on Figure 2.5 b). The permanent magnet placed at the back of the cathode target generates magnetic field lines that enter and leave through the cathode plate as shown. A discharge is formed when a negative voltage of 200 V or more is applied to the cathode. The discharge appears in the form of a high density brightly glowing circular plasma ring of width w and mean radius R that hovers below the cathode. The sputtering occurs in a corresponding track on the cathode. The plasma shields the electric field through most of the chamber and a cathode sheath of the order of $s = 1$ mm develops, which sustains most of the externally applied voltage. Due to high mass magnetic field doesn't confine Argon ions in the plasma which are accelerated toward the cathode and strike it at high energy. In addition to sputtering material, the impact of the ions produces secondary electron emission. These electrons are accelerated back to the plasma and are confined near the cathode by the magnetic field. The electrons undergo a sufficient number of ionizing collisions to maintain the discharge before being lost to a grounded surface [2, 35].

Both electric and magnetic field are present in a magnetron discharge. The electric field accelerates electrons away from the cathode and ions towards the cathode. Magnetic field has a circular shape from the edge towards the centre of the cathode. The Larmor orbit of electrons is small compared to curvature of the magnetic field, thus electrons follow magnetic lines and are being entrapped in the magnetic field. This enables longer path lengths of electrons and increases the number of ionisation collisions. The magnetic field lines of the magnetron could be set up as completely closed, known as balanced magnetron (Figure 2.6 a)), or closed in the middle and open at the edge of the magnetron, called unbalanced magnetron (Figure 2.6 b)). Balanced magnetrons have magnetically trapped electrons and low ion flux to the substrate, which is advantageous for deposition of thin films on plastic substrates since plastic cannot withstand high ion flux density create in the unbalanced magnetron. In the unbalanced magnetron ion flux to the substrate is increased as well as ionisation of metal atoms in vicinity of the substrate. It is a consequence of higher electron density in the substrate region that reaches the target following open magnetic field lines in direction

17

perpendicular to the target. Unbalanced magnetrons are advantageous for hard coatings [2].

a)

Magnetic field lines

Permanent magnets

Target

N   S   N

Water cooled cathode

b)

Magnetic field lines

Permanent magnets

Target

N   S   N

Water cooled cathode
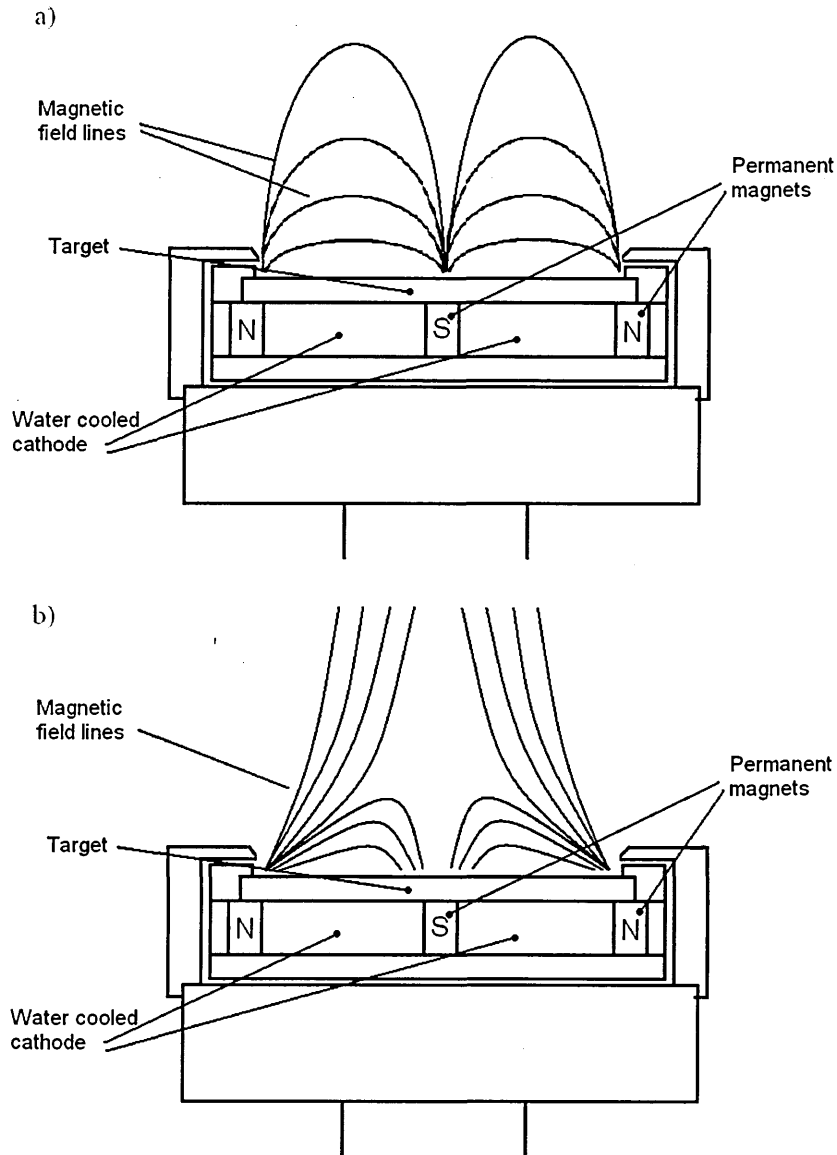
Figure 2.6 Schematic of the a) balanced magnetron, with closed magnetic field lines and b) unbalanced magnetron with magnetic field lines open at the edge of the target, from [37]

2.2.1 Direct current (DC) magnetron sputtering

Direct current (DC) magnetron sputtering is a sputtering technique that uses magnetic fields to enhance and confine the plasma, mainly electrons in the target vicinity. In a conventional DC plasma discharge, the cathode is kept at a constant negative voltage. Positive ions generated in the plasma are

accelerated towards the cathode, sputtering atoms and molecules from the target surface. DC magnetron sputtering is a line-of-sight process, since it generates mostly neutral atoms whose trajectory and energy cannot be easily controlled, therefore rather low pressures are used to minimize scattering of the sputtered atoms [37].

Diffusion of the electrons and ions in the DC magnetron sputtering through the chamber was simulated by Kwon et al. [44]. The result of the simulation, shown on Figure 2.7, shows similar spatial density distribution of electrons and ions that supports the theory of plasma quasi-neutrality. Highest density is calculated in the target vicinity reducing with increasing distance from the target due to diffusion. Yagisawa et al. [45] used a particle-in-cell/Monte Carlo model to investigate the spatial density of gas atoms, gas ions and metal atoms above the target. It was found that the density of sputtered metal atoms is four orders of magnitude lower than the density of gas atoms and peak density of metal atoms is one order of magnitude higher than peak Ar ion density. The metal density peaks in front of the target and decays exponentially due to collisional relaxation with surrounding Ar atoms.
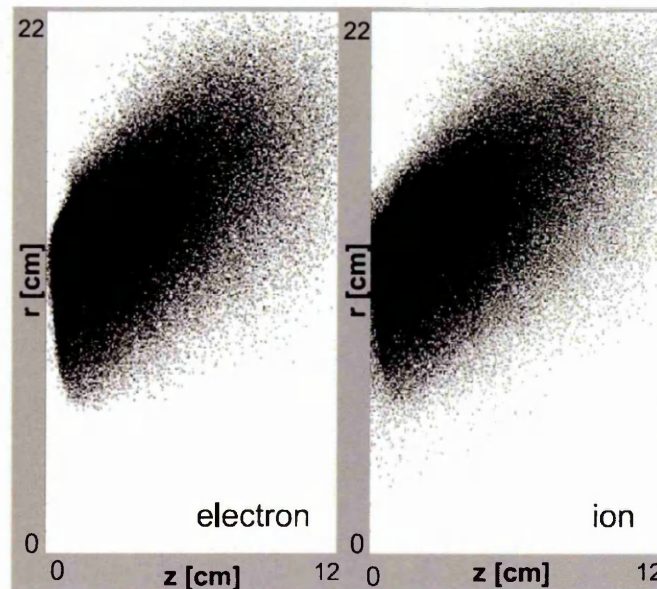
Figure 2.7 Simulated electron and ion distribution in the space near the target, from [44]

Several authors report the results of the ion energy distribution function (IEDF) in DC magnetron sputtering [46, 27, 30, 29]. The maximum reported ion energies were around 50 eV and the metal IEDF showed strong

19

dependence on pressure and the discharge current. Increasing pressure from 0.2 Pa to the values of 10 Pa the IEDF high energy tail reduced nevertheless the intensity of low energy metal ion signal increased with higher pressures. The increase in discharge current results in increase of both maximum energy and the intensity of the metal IEDF [30]. The main disadvantage of DC magnetron sputtering is low ionisation degree of the metal flux which is around 10^{-3} [36]. The energy and impact angle of the low ionised metal flux cannot be significantly altered. Therefore increasing the ionisation degree of metal flux would enable to tailor the properties of the metal flux and consequently to tailor the properties of the deposited film. First method used to increase ionisation degree in the metal flux is inductively coupled magnetron sputtering with a radio-frequency coil.

2.2.2 Inductively coupled magnetron sputtering

A radio-frequency (RF) field from an external coil placed in the region between the cathode and the anode, as shown on Figure 2.8 can be used to generate a highly ionized plasma discharge [4]. The inductive coil is generally driven at 13.56 MHz using a 50 Ω RF power supply through a capacitive matching network. It has been found that the ionization, and therefore the ionization flux fraction, increases with increased RF power and pressure. Inductively coupled discharges are commonly operated in the pressure range from 1 to 50 mTorr and applied power 200–1000 W resulting in an electron density in the range from 10^{16} to 10^{18} m^{-3}, generally found to increase linearly with increasing applied power [47, 5]. The atoms created at the magnetron and transiting the dense plasma, created by the RF coil, get ionized.
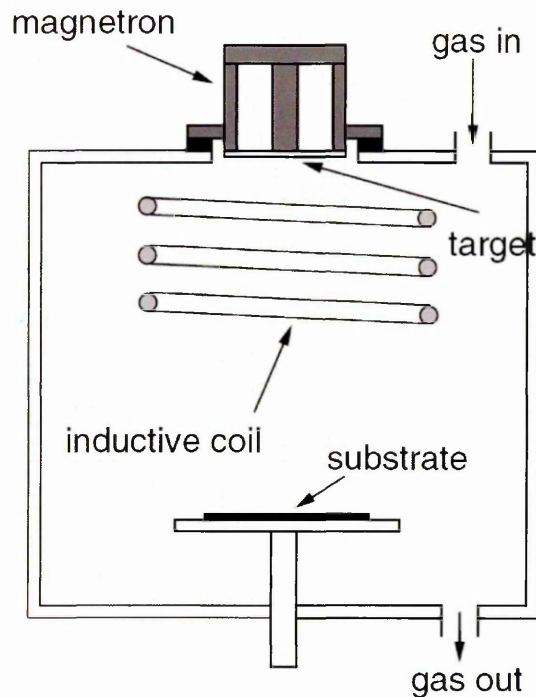
Figure 2.8 Schematic view of the inductively coupled magnetron sputtering, from [47]

Dony et al [48] compared DC and RF discharges and found the increase in density of Ar metastable and resonant atoms and metal atoms in the RF magnetron sputtering. Furthermore, a decrease of Ti atoms density with increase of RF power was reported and increase of Ti ion density with increase of RF power was observed using optical absorption spectroscopy in the RF assisted DC magnetron sputtering plasma discharge [49]. The reported degree of ionization, measured using optical absorption spectroscopy was suggested it could be up to 90%. Mass spectroscopy was used to measure the IEDF in the RF discharge of Al target in Ar atmosphere. It showed increase in the ion integrated intensity with RF power. The energy distributions showed similar high energy tails for Ar^+ and Al^+ energy distributions probably created through the collisions between gas and metal ions and atoms [50]. Fukushima et al. [51] studied ion energy distribution of Ti flux incident to substrate surface in RF-plasma enhanced magnetron sputtering. They have showed a clear dependence between energy of the IEDF main peak and plasma potential. A high ion fraction demonstrated a strong proportional correlation on electron density and temperature.

2.3 High power impulse magnetron sputtering (HIPIMS)

In 1999 Kouznetsov et al. [6] suggested a method where DC power supply would be replaced with pulsed power supply in combination with a standard circular flat magnetron source. Peak power density of 2800 W cm^{-2} was reported. Since many papers investigating novel method called high power impulse magnetron sputtering (HIPIMS) were published [31, 29, 33, 52, 53, 54]. Ehiasarian et al. [7, 52, 54] and Helmersson et al. [8] used HIPIMS to deposit hard CrN and TiN coatings with applications in tribological protection of automotive engines and turning. Konstantinidis et al. [53] report dense zinc-oxide films deposited using HIPIMS with application as a seed layer in low-emissivity windows.

The need for denser and thus harder coatings was the driving force behind developing the new technique. Denser coatings are achieved by increasing the ion to neutral ratio and by increasing the energy of ions. To increase ion production higher powers applied to target are needed. When the power on the target is increasing, the target is heating which could lead to melting of the target. One of solutions to produce more ions and to avoid melting of the target was to retain high power but to deliver it in short portions. That would increase ion to neutral ratio and ion energies but at the same time would prevent target from melting. Typical voltage and current profiles in dependence on time are shown on Figure 2.9. Usually a pulse of duration between 10 and 200 µs is used and repetition frequency up to 200 Hz [55].
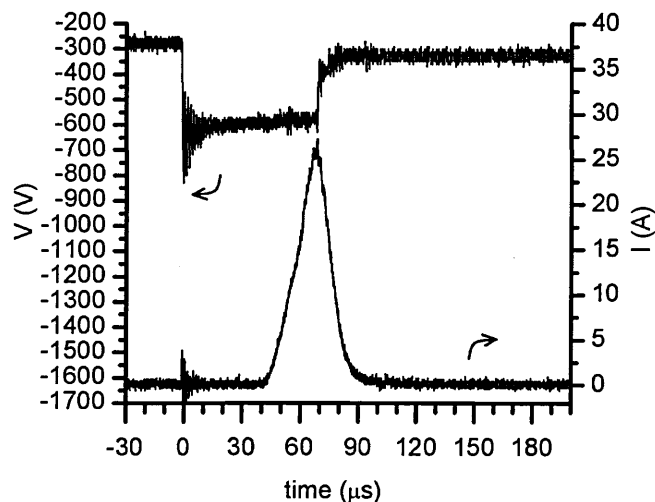
Figure 2.9 Voltage (up) and target current (down) as a function of time for HIPIMS of Ti at pressure of 0.27 Pa

The main advantage of HIPIMS over DC magnetron sputtering is increased ion to neutral metal ratio. Ehiasarian et al. [18] found increase in the ion to neutral ratio of Cr and increase in the ion current density and deposition rate with increase of target current, Figure 2.10. The increase in the ion to neutral ratio is the consequence of increased electron density in the target vicinity. The time and spatial evolution of the electron density was measured by Bohlmark et al. [15] measuring electron densities above 10^{19} m^{-3}. The results presented on Figure 2.11 show electron densities above 10^{18} m^{-3} in the chamber even at 640 µs from the start of the pulse.

High powers in the pulse result in amplified sputtering of the target. Increased density of sputtered material in the target vicinity leads to gas rarefaction. The effect of gas rarefaction was simulated by Kadlec [26] and the results are presented on Figure 2.12. The results show substantial gas rarefaction with gas density reduced tenfold in the close vicinity of the target.

23
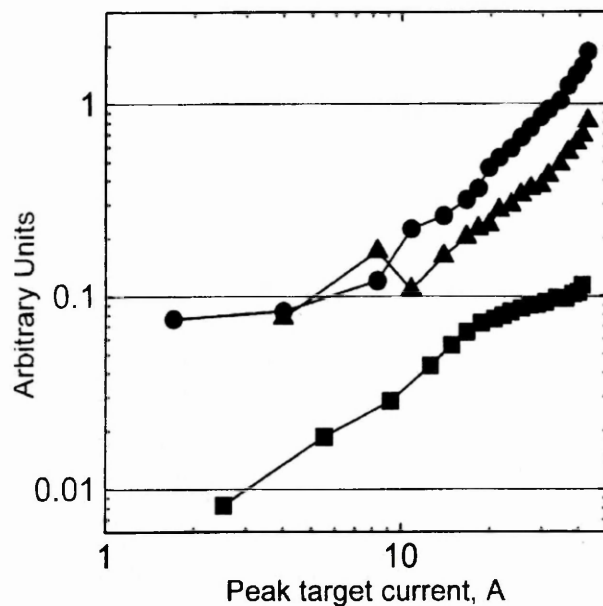
Figure 2.10 Ion to neutral ratio and deposition rate as a function of target current. Triangles represent $I(Cr^{2+})/(Cr^{0})$, circles represent $I(Cr^{+})/(Cr^{0})$ and squares represent the ratio of ion current density to deposition rate, from [18]
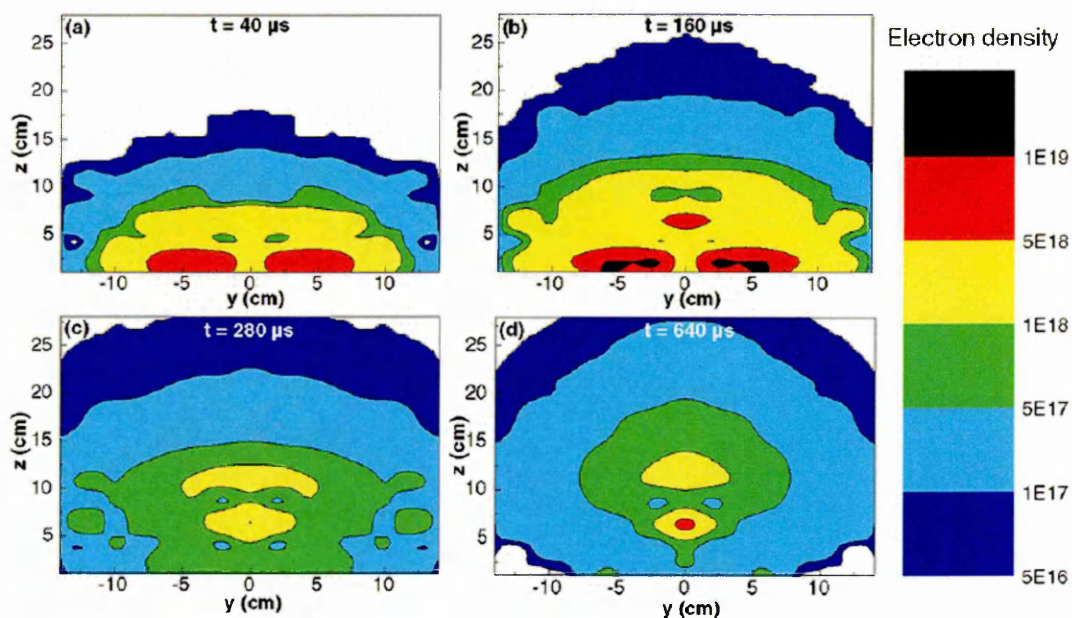
Figure 2.11 Temporal and spatial variation in the electron density below the target at 40, 160, 280, and 640 μs after pulse ignition in Ar atmosphere at pressure of 20 mtorr, from [15]
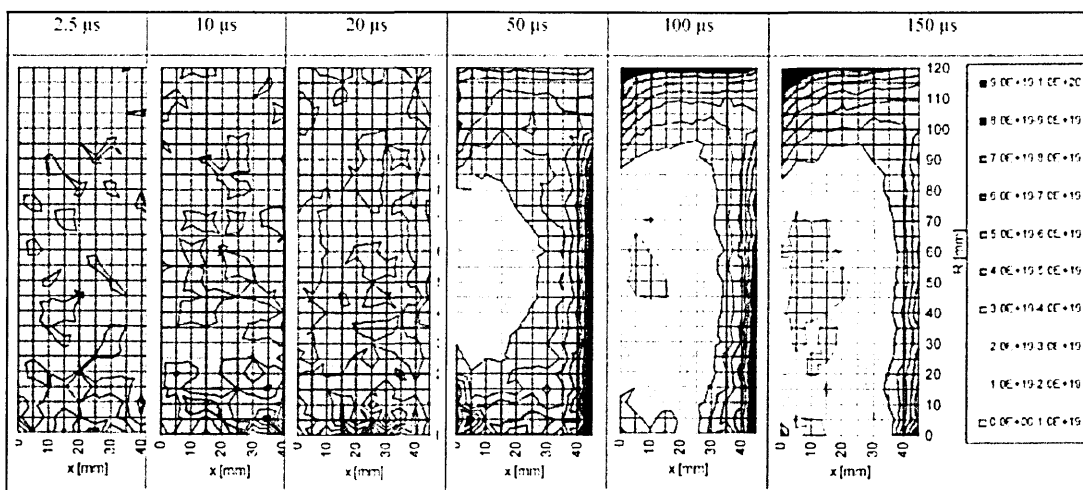
Figure 2.12 Time evolution of Ar gas density of in m^{-3}. The uniform number density of Ar at impulse start was 4.83×10^{19}m^{-3} at 0.2 Pa, from [26]

The ion energy distribution functions (IEDF) of metal and gas ions in HIPIMS obtained using plasma sampling mass spectrometry have been reported by various authors [29, 33, 32, 31, 28]. During the pulse, a Thompson-like high energy tail distribution of metal IEDF with energies up to 100 eV has been reported [29, 32], whereas after the pulse metal ion IEDF comprised of a main low energy peak and a high energy tail, for measurements recorded in the vicinity of the target. Time resolved measurements comparing the rise of the discharge current to the end of the pulse have shown the existence of a single low energy peak in the post discharge [33, 28]. The mean energy was shifted towards higher values for measurement later in the pulse [33]. Several papers used mass spectrometry to describe the influence of pressure on the ion energy distribution function (IEDF) [27] and the influence of power on the IEDF [28, 29]. Increasing the working gas pressure the high energy tail of the metal IEDF was reduced and the low energy peak of the metal IEDF increased and narrowed as a result of thermalisation.

The long lifespan of Ti neutrals and ions has been investigated showing that ions and electrons obey ambipolar diffusion in the post-discharge [20]. The evolution of the electron density measured at different distances from the target at pressures from 0.3 Pa to 3 Pa shows that at high pressure the electron density decays slowly at all distances compared to sharp drop in density after switch off at low pressure [21] In addition the measurements

showed delayed arrival of peak electron density at longer distances and reduction of electron density peak travelling velocity with increased pressure. The results obtained with the Langmuir probe used to investigate the dependence of the electron density temporal evolution on the discharge power [19], show the increase in electron density with discharge power and delayed arrival of the electron density peak at longer distances from the target. Furthermore Langmuir probe was used to investigate the occurrence of the metal ions as a function of time and distance and as a function of time and pressure at 1.1 Pa [13]. The results show two waves of ions, first one arriving shortly after the end of the pulse and second wave arriving in the post-discharge reaching peak later for the longer distance from the target.

The HIPIMS plasma discharge undergoes several stages of development as has been observed by optical emission spectroscopy (OES) [16, 17, 18]. The OES measurements of a HIPIMS plasma discharge of Ti [16] showed the existence of Ar^0, Ar^{1+}, Ti^0, Ti^{1+}, and Ti^{2+} species in the discharge. In the beginning of the pulse, the plasma is dominated by Ar neutrals and as the discharge current increases and the sputtering of metal vapour develops, Ti ions become the dominant species in the plasma. After the pulse, the relative emission intensity is decreasing, fastest for the Ti^{2+} and Ti^{1+} ions and at a slower rate for Ar^0 and Ti^0 atoms.

The OES measurements of HIPIMS of Cr [18] showed that, in the beginning of the pulse, the plasma is dominated by Ar^0 atoms and Ar^{1+} ions. At the peak of the discharge current Cr atoms and Cr^{1+} and Cr^{2+} ion signals appear. The intensity of the gas species signal drops with the discharge current and the Cr^{1+} signal dominates the end of the pulse. After the end of the pulse, the Cr^{1+} signal drops and the Cr^0 signal is dominant.

The ionization mechanisms during HIPIMS evolution are governed by electron impact collision processes and depend strongly on the electron energy distribution function (EEDF). The Langmuir probe measurements of the EEDF in a pulsed magnetic multipole hydrogen discharge that is similar to HIPIMS in term of pulse duration of 200 µs, discharge current of 2 A and pressure of 0.27 Pa, [11] showed that it changed from a non-Maxwellian distribution with high energy during the discharge to a Maxwellian distribution in the late post-discharge. We use the term Maxwellian distribution under the

26

assumption that the plasma is in local thermal equilibrium. Similar results were reported in the HIPIMS discharge [12]. The work of Vetushka et al. [9] shows a high energy group during the ignition phase of the discharge and a low energy electron group at the end. It was found by Vasina et al [101] that EEDF in HIPIMS with Cu target in Ar has Maxwellian distribution at low energies but at higher energies the distribution has a high energy tail stretching up to several hundreds of eV.

The ion saturation current measured at different distances from the target [22] showed that ions are able to leave the magnetized region and reach the substrate in greater numbers depending on the peak current, which is the consequence of the kinetic pressure exceeding the magnetic pressure.

Previous work by the present authors has suggested [28] that thermalisation of the metal ions occurs in the HIPIMS post-discharge. The thermalisation of neutrals in a direct current (DC) magnetron sputtering plasma was investigated in detail by several authors [23, 24]. Simulations of particle transport [25] and the neutral particle flow in HIPIMS [26] add valuable information on plasma thermalisation and gas rarefaction.

Conventional magnetron I-U characteristic follows a power law $I = kU^n$, where exponent n can be found in range 5 to 15 as reported by Rossnagel et al. [56]. Ehiasarian et al. [18] measured I-U characteristic of the HIPIMS plasma discharge and have found that it consists of two phases, Figure 2.13. At low currents the exponent is similar to the coefficient found in DC discharge. At the higher currents the exponent changes and additional increasing of target voltage are not accompanied with increase of discharge current.
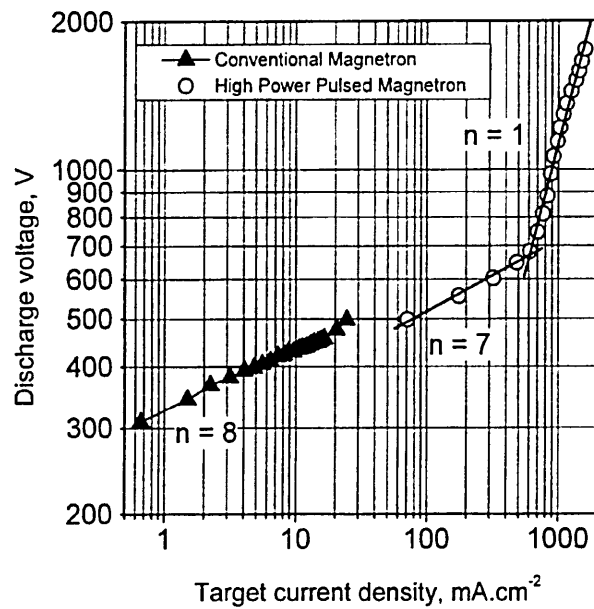
Figure 2.13 I-U characteristic of the conventional magnetron and pulsed discharge, from [18]

2.4 Plasma surface interactions

The interaction between the plasma and the surface of the coating is crucial in understanding the thin film growth process. The high energy plasma deposition method in which the surface of the sample is subjected to a flux of high energy ions and neutrals before and during deposition of the coating is called ion plating. The continuous bombardment of the substrate by these energetic ions and atoms, of both the coating material and the working gas, results in a wide variety of effects. There are four most important physical processes occurring during the ion plating process;

- o Substrate cleaning due to the removal of absorbed impurities from the substrate surface as a result of ion and atom bombardment
- o Ion penetration and entrapment in the substrate and coating
- o Ion-induced sputtering of substrate and coating atoms
- o Recoil displacement of substrate and coating atoms leading to their intermixing

28

The mentioned effects can be used to produce coatings with an excellent adhesion of the coating to the substrate, denser coating with little or no porosity and good chemical composition [1].

2.4.1 Sputtering

Sputtering is a process of ejecting material from the surface of a solid due to the exchange of the momentum related with surface bombardment by energetic particles. When an energetic ion or neutral atom hits the surface of the sputtering target (cathode) various complicated processes may occur simultaneously, in addition to the production of the secondary electrons. Sputtering is a statistical process which occurs as a result of a momentum-exchange collision cascade process at the target surface by an impinging energetic particle. Sputtering can not result from a single binary collision since the momentum vector of the struck target atom must be altered by more than 90°. The example of the simulated collision sequence is given in book edited by Bunshah [1]. The high energy ions that impinge on the cathode may sputter either cathode or contaminant atoms from the surface, or be reflected as high energy ion or neutral.

The sputtering process is measured in term of the sputtering yield. Sputtering yield is defined as the number of target atom ejected per incident particle. The sputter yield depends on the target species and the nature, energy and angle of incidence of the bombarding species. The sputter yield is greatest when the mass of the bombarding particle is of the same order of magnitude or larger than the mass of the target atoms. It is common to use inert gas to avoid chemical reactions at the target and substrate, therefore Ar is often used due to its mass compatibility with materials of engineering interest and its low cost. The dependence of the sputtering yield on the ion angle of incidence is shown on Figure 2.14. In glow discharge sputtering devices the ions generally approach the target in a direction normal to the target surface [35].
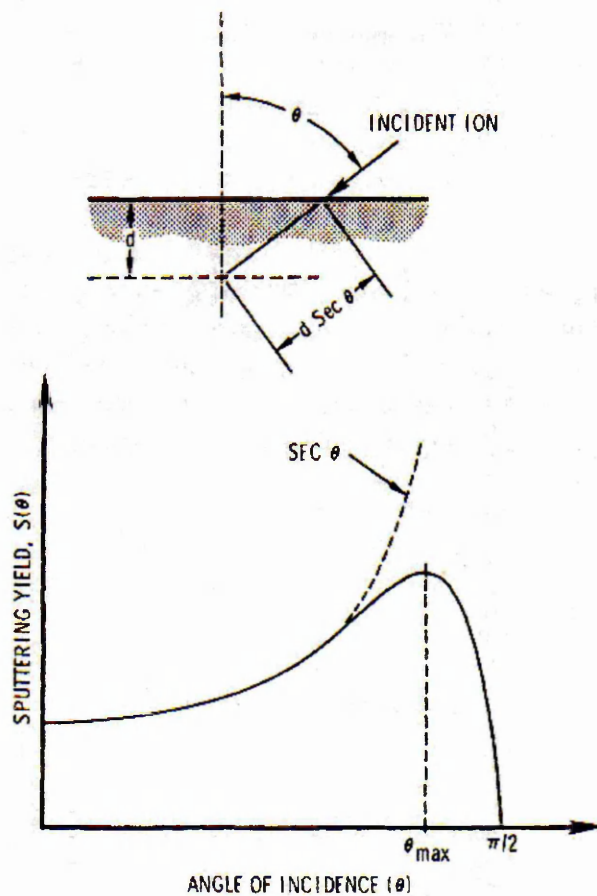
Figure 2.14 The sputtering yield as a function of the ion angle of incidence, from [1]

2.4.2 Bombardment effect on the substrate surface

In magnetron sputtering it is possible to influence the stress in the deposited films by adjusting the gas pressure in the sputtering chamber and therefore to alter the bombardment by the energetic particles. At low pressure high energy particles which are reflected as neutrals from the sputtering target provide particle bombardment of the growing film giving high compressive stresses. At higher gas pressure, the high energy particles are thermalised by collision before they can bombard the growing film and tensile stress is developed in the growing film [1].

Four regions affected by particle bombardment can be recognized. First region is the substrate surface exposed directly to the plasma. Below the surface there is surface region that is physically infiltrated by the bombarding particles that results in a collision cascade. Further inside the sample there is

the near surface region which is the region indirectly affected by bombardment through heating and diffusion. Finally bulk region is the material not affected by the impinging ions.

On Figure 2.15 effects of bombardment on the surface are presented. The most important effects on the surface are enhancing surface mobility of atoms on the surface and enhancement of the chemical reaction of impinging and adsorbed particles to produce condensed particles. In the near surface region following effects should be mentioned. The impinging particles can be physically implanted or they could cause a displacement of lattice atoms and lead to the creation of lattice defects. Particles from the surface may be implanted into the substrate lattice. Channelling process of the lattice could transmit these effects deeper into the surface [1].
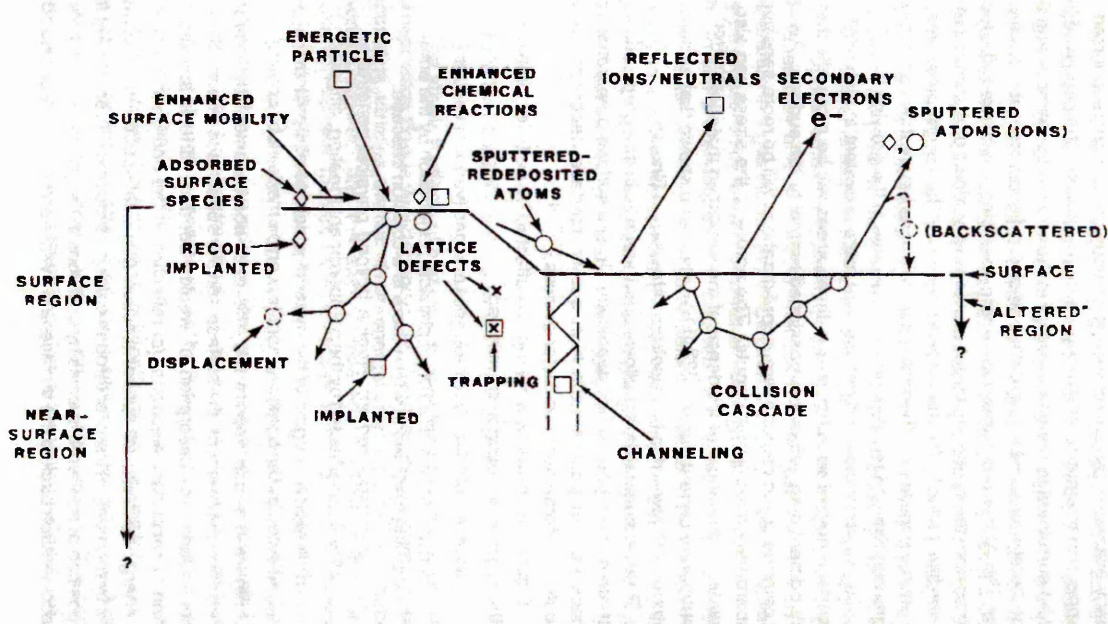
Figure 2.15 Schematic presentation of the surface and near surface region affected by ion bombardment, from [1]

2.4.3 Low energy ion influence on the film growth

Low energy ion bombardment of the substrate and growing film are likely to produce defects in the substrate surface. Produced defects could generate surface effects which are dependent upon the energy E, flux and mass of the incident particle, upon the growth temperature and the film to substrate combination. Krikorian and Sneed [57] have shown that variation of the energy of ions impinging on the substrate can be used to decrease or

31

increase the nucleation rate depending on the choice of the substrate temperature and substrate material.

The disordering of the crystalline substrate surface by ion bombardment at low temperatures prior or during the early stages of the deposition may lead to the production of new lower binding energy sites. It has been reported a decrease in island number densities in the presence of ion irradiation due to larger average island sizes, for a given nominal film thickness and hence larger ultimate grain size. One mechanism that could explain the increased average size is a depletion of small clusters by sputtering. The small clusters shrink which increases their mobility on the surface, increases diffusion and coalescence with large stable islands. Clusters reduced in size are energetically unfavourable and will spontaneously dissociate to form adatoms which diffuse to larger clusters. Ion bombardment of the large islands only results in a minor loss in material by sputtering [1].

Ion irradiation has been used to increase the density and the internal strength of the layers as well as to increase film to substrate adhesion. Drawback of the ion irradiation is the generation of very high compressive stress levels in the films which leads to spallation. Densification effect was nicely and for the first time demonstrated in work by Mattox and Kominiak [58] where they have observed the density of the deposited film as a function of negative bias voltage on the substrate. By increasing bias voltage from 0 to 500 V film density increased from 14.5 to 16.3 g/cm^3. The results are shown on Figure 2.16. Hakansson et al. [59] investigated the influence of ion bombardment on the film porosity. They have compared the TEM images of film deposited with different bias voltages. The growth conditions were the same except the bias voltage was changed from 0 to 250 V. The void density decreased with increase of bias voltage until bias voltage was set to 120 V or above, no voids could be detected. TEM images showed disruption of columnar structure, reduction of grain size and increase of the number density of defects such as dislocation loops.
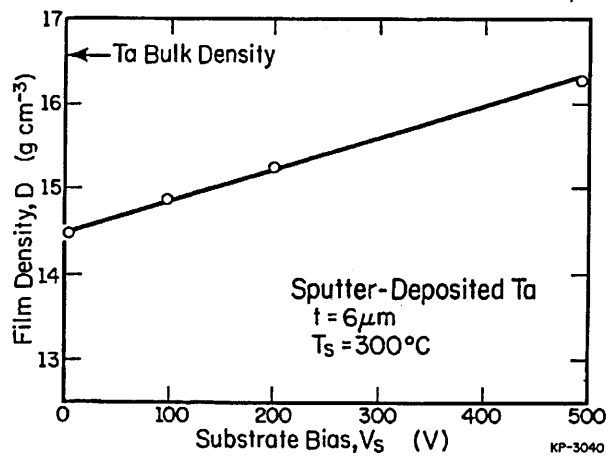
Figure 2.16 The density of the deposited film as a function of negative bias voltage on the substrate, from [58]

In the experiments where substrate was heated to temperatures higher than the room temperature, ion bombardment i.e. voltage bias of the substrate reduced the dislocation number density. Hultman et al. [60] reported an existence of optimal bias voltage V_s^* with minimum defect density. Increase of bias voltage strongly increased the defect density. It is suggested [1] that at lower biases, ion bombardment enhances adatom mobility and thereby accelerates the rate at which defects were annealed out during deposition. At higher bias voltages, the increased projected range of the impinging ions results in larger fraction of the irradiation induced defects being trapped in the growing film and therefore defect density becomes high enough that renucleation occurred during growth and polycrystalline films were obtained. Ideal deposition conditions would be low impinging energy, relatively high ion-to-neutral flux ratio and low deposition rates.

2.4.4 Effects of adatom migration

In his paper, Muller [61] reports results from research where adatom migration effects were included in a microstructure evolution growth simulation. Simulation allowed thermally active adatoms to move to empty neighbour sites of maximum coordination number. Boltzmann statistic was used to simulate fluctuations in adatom vibrational energy. Muller found that above a critical temperature range the porous columnar microstructure changes to a

configuration of maximum packing density. Example of the simulation is given on Figure 2.17. It shows a two dimensional microstructure simulation of Ni films deposited as a function of temperature. Film deposited at 350 K shows columnar structure. Increasing deposition temperature from 350 K to 420 K, film densifies but columnar structure is still visible. Increasing deposition temperature to 450 K fully dense film is deposited with local defects. Further simulations with different deposition rates showed increase of transition temperatures at increased deposition rates. These results are presented on Figure 2.18.
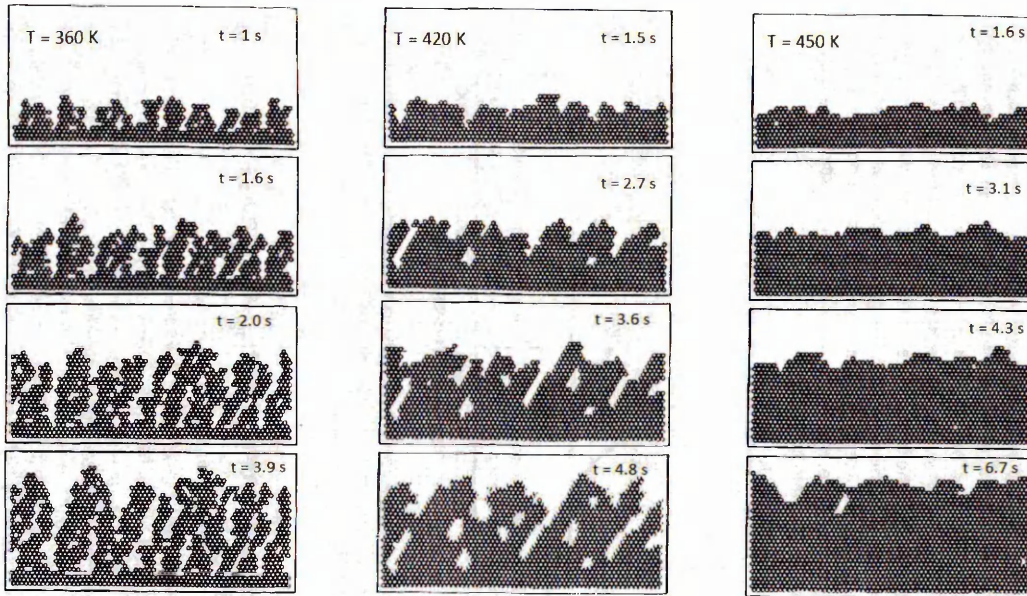
Figure 2.17 Two dimensional microstructure simulation of Ni films deposited as a function of temperature, from [61]
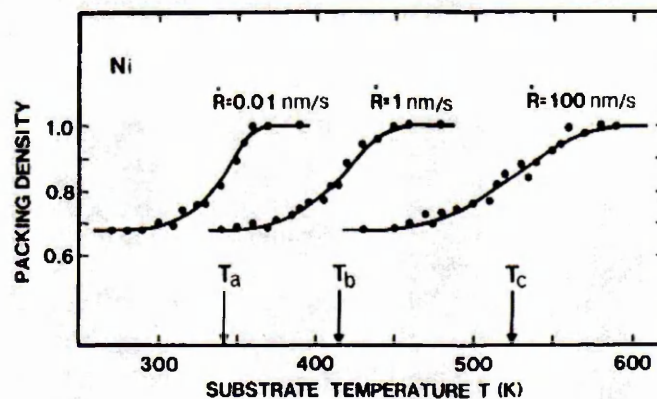
Figure 2.18 Simulations of the packing density with different deposition rates showing increase of transition temperatures at increased deposition rates, from [61]

34

2.4.5 Nucleation and film growth

The growth of the film starts with the ion flux impinging on the substrate surface and thermally settling with the substrate. The incident atom transfers its energy to the surface lattice and becomes a loosely bonded 'adatom'. The adatom than diffuses over the surface exchanging the energy with the lattice and other adsorbed species, until they either desorb by evaporation or back-sputtering from the substrate surface or become trapped at low energy sites. The process is shown on Figure 2.19. Fractions of the adatom cluster grow in size and become an island which coalesces to form a continuous film.

Nucleation and Growth Processes
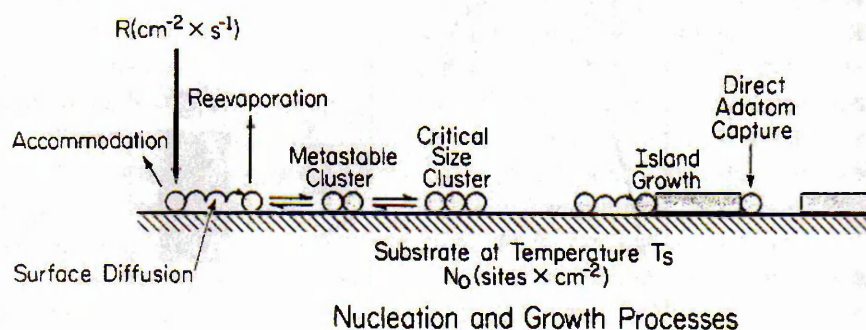
Figure 2.19 Nucleation and growth processes of the deposited coatings on the surface of the substrate, from [1]

Figure 2.20 shows a schematic illustration of sequential steps during nucleation of film in 3D film growth mode. In the beginning small size nuclei could be observed. As the time passes by, the size and number of nuclei increases. Continued deposition leads to coalescence of adjacent nuclei which exhibits behaviour of a liquid. Electron diffraction results show that coalescence is a solid state reaction. Capturing mobile adatoms and small clusters, large islands continue to grow. The coalescence of large islands with small islands and coalescence between large islands creates a semi continuous film with a network of channels and holes. Atoms impinging to a substrate could produce a secondary nucleation, nuclei growth and island coalescence in the voids, which are incorporated into a growing film.

35
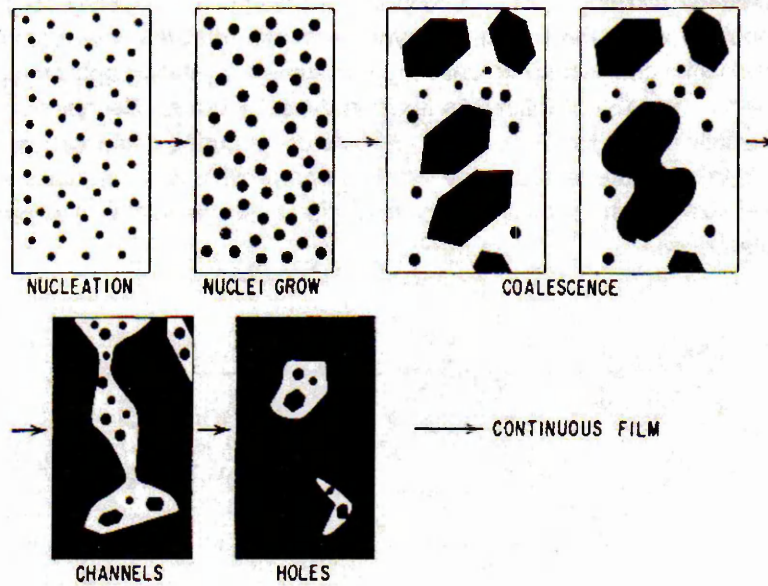
Figure 2.20 Schematic illustration of sequential steps during nucleation of film in 3D film growth mode, from [1]

Three modes of film growth on substrate are proposed. Volmar-Weber growth, also known as three dimensional (3D) islands growth start when small clusters are nucleated directly on the substrate surface. The cluster grow into islands which than coalesce to form a continuous film. If the film atoms are more strongly bounded to each other than to the substrate, 3D growth will occur. Frank-van der Merwe growth, or two dimensional (2D) layer-by-layer growths occurs when the binding between film atoms is equal to or less than between the film atoms and the substrate. The third growth mode, called Stranski-Krastanov, is a combination of 3D model and 2D model. In this mode, in the beginning film grows in a 2D layer and after few layers 3D islands start to form. All three modes are schematically presented on Figure 2.21 [1].

Figure 2.21 Three modes of the film growth, from [1]

36

In order to describe an influence of the substrate temperature on the morphology of the coating, Movchan and Demchishin [62] developed a structure zone model. Elevated substrate temperature increases surface mobility, enhances bulk diffusion and allows recrystallization to occur. Figure 2.22 represents Movchan and Demchishin structural zone model.
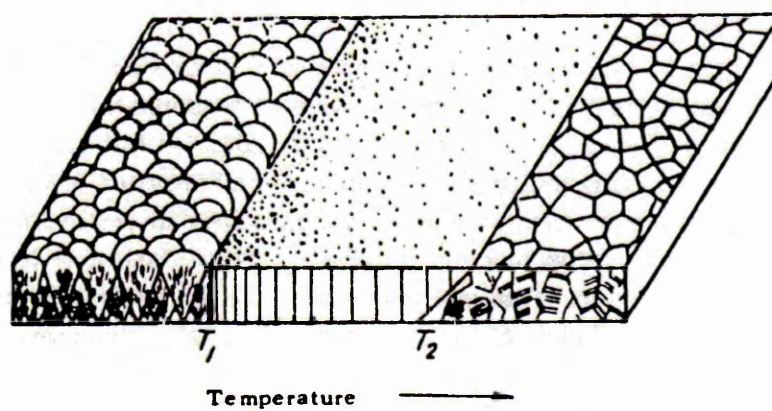
Figure 2.22 Movchan and Demchishin structural zone model for coating growth, from [62]

The model involves the formation of the three zones, which are determined by the ratio of the substrate surface temperature T to the melting point of the deposited material T_m. First zone occurs at $T/T_m < 0.3$ and results when adatom diffusion is not sufficient to overcome the effect of the shadowing, giving a columnar structure with low density boundaries between columns. The individual columns are polycrystalline and are usually highly defected with small grain size. It also contains a high dislocation density and has a high level of residual stress. The surface morphology is generally rounded.

Second zone occurs in the range $0.3 < T/T_m < 0.5$, where adatom diffusion dominates and the columnar structure consists of less defected and larger grains with higher density boundaries between the columns. The surface has smooth, matt appearance.

The third zone occurs in range $0.5 < T/T_m < 1$ and consists of equi-axed grains with a bright surface. Bulk diffusion and recrystallization dominate in this zone. The structure and properties in this zone correspond to a fully annealed metal.

Thornton [63] expanded the structural model by adding an additional axis to account for the sputtering argon gas in sputter deposition, where the effect of both temperature and argon pressure are showed in three dimensional diagram. The argon pressure indirectly influences the film microstructure. Decreasing Ar pressure increases the high energy ion bombardment that in turn leads to denser coatings. Increasing Ar pressure leads to shorter mean free paths of the elastic collisions between particles in the plasma and randomisation of the incident particle angle resulting in the zone 1 type of coatings. Thornton introduced a new zone T between first and second zone. Figure 2.23 shows a three dimensional structural zone model developed by Thornton.
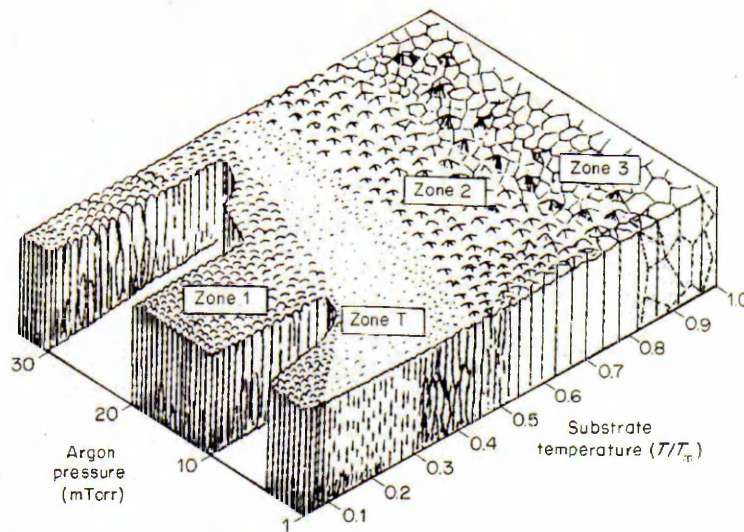
Figure 2.23 Thornton structural zone model for coating growth, from [63]

The structure in zone 1 is promoted by the substrate roughness, high argon pressure and an oblique component to the deposition flux. The transition zone T consists of a dense array of poorly defined fibrous grains without voided boundaries. Fibrous grains are tightly packed with weak grain boundaries. Second zone consists of columnar grains having highly faceted surfaces. At high T/T_m the surface are smooth, with grooved grain boundaries. Third zone consists of recrystallized grain structure and is characterized by bulk diffusion process.

Thornton's modification shows that the transition temperatures may vary significantly from those stated in Movchan and Demchishin model. In general, transition temperatures shift to higher temperatures as the gas

pressure in the synthesis process increase due to shorter elastic collision mean free path and tilted angel of the incident ion flux. Furthermore the transition from one zone to the next is not abrupt but smooth, hence the transition should not be considered as absolute, bat as guidelines. All zones are not found in all deposits. For example, zone T is not prominent in pure materials, but becomes more pronounced in complex alloys or in deposits produced at higher gas pressure. Zone 3 is not seen very often in materials with high melting points.

Continuous bombardment of the growing film with high energy charges or neutral atoms or molecules has been shown to cause changes in the film structure and result in density values near those of the compact materials. The effect of ion bombardment seems to increase nucleation density by causing surface damage and to enhance the mobility of adatoms by transferring kinetic energy to the atoms of the substrate surface. Ion bombardment during deposition suppresses the porous boundaries and results in a structure similar to zone T. Such an effect may be caused by the creation of the activation sites that simulate nucleation for the arriving coating atoms, or by eroding surface roughness peaks and redistributing material into valleys [1, 35].

CHAPTER 3

Methods and Materials

3.1 Experimental chamber

Kurt J. Lesker CMS 18 deposition system was used to investigate the influence of various external parameters on the plasma parameters. A picture of the chamber is shown on Figure 3.1. It has cylindrical shape and it is made from 304 stainless steel. The chamber top plate can be lifted and swung to enable installing experimental instruments and changing the targets. The experimental instruments used for plasma diagnostic are described in detail in chapter 3.3. The vacuum in the chamber is achieved with five vacuum pumps. One set consisting of roughing pump Leroy-Somer, backup turbomolecular pump Pfeiffer Vacuum TMH 071 P, with pumping speed 33 l/s, and main turbomolecular pump Pfeiffer Vacuum TMU 1601 P, pumping speed 970 l/s, evacuates the air directly from the chamber up to the base pressure of 10^{-7} mbar (10^{-4} Pa) measured using MKS SRG-2CE spinning rotor gauge. The other set consisting of roughing pump and turbomolecular pump Oerlikon Leybold Vacuum PT 50 is used to achieve high vacuum inside the mass spectrometer. The mass spectrometer and the experimental chamber are connected through the orifice of the mass spectrometer with 200 µm diameter.

Substrate can be loaded to the experimental chamber through a load lock mounted on the side of the chamber. The vacuum in the load lock is achieved with a set consisting of roughing pump Ulvac DIS-090, pumping speed 90 l/s, and turbomolecular pump Pfeiffer Vacuum TMH 071 P, pumping speed 60 l/s. Once substrate is mounted in the substrate holder it can be heated, biased and rotated to achieve uniform deposition.
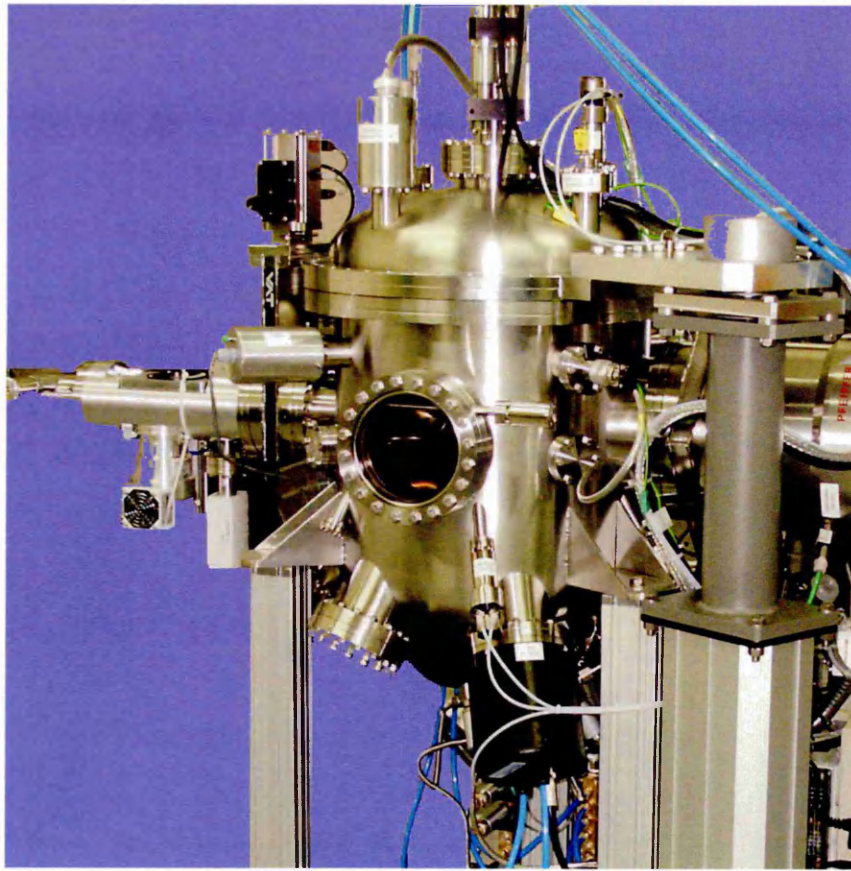
Figure 3.1 Photograph of the experimental chamber CMS 18

It is possible to mount up to 6 cathodes in the chamber. For all experiments only one cathode was used except the experiments described in chapter 4.5 when two cathodes were used. The cross-section of the chamber is shown on Figure 3.2 showing the position of cathode, substrate and plasma sampling mass spectrometer. Furthermore on Figure 3.2 two sets of vacuum pumps is shown, one used to achieve vacuum in main chamber and other one to achieve higher vacuum inside mass spectrometer. Main set of vacuum pumps is placed opposite mass spectrometer behind the cathode however for the simplified schematic view it is drawn on the bottom of the chamber. The surface of the cathode was placed under angle of 32° to the substrate surface. The cathode, fitted with a 3" target, could be connected to a DC or a HIPIMS power supply. The properties of used HIPIMS power supply Hüttinger HMP2/4 are described in chapter 3.2.
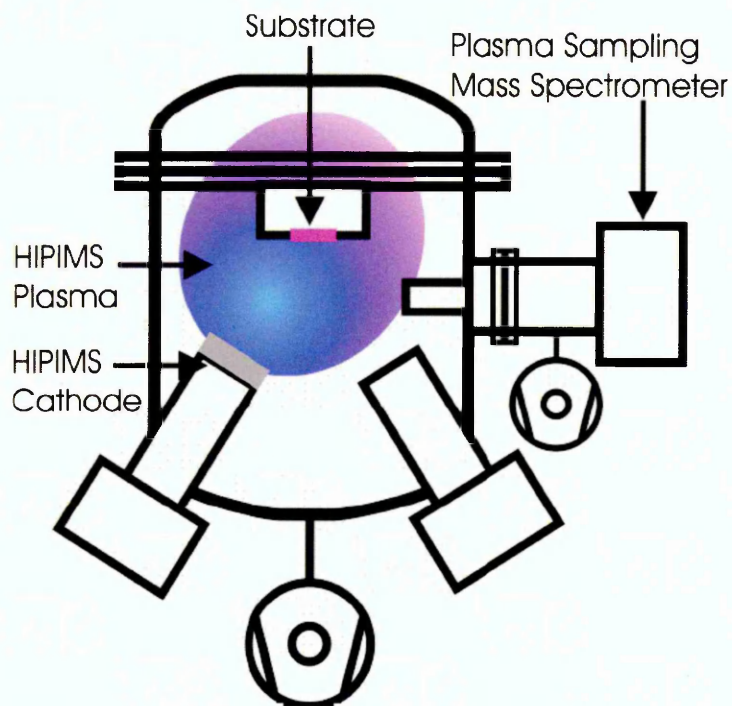
Figure 3.2 Schematic view of the experimental chamber cross section showing target, substrate and plasma sampling mass spectrometer

A position of the plasma sampling mass spectrometer with regard to the target is shown on Figure 3.2. A distance from the centre of the target and mass spectrometer (MS) orifice was 17 cm and the line of sight was placed below the substrate holder to investigate the ions reaching the substrate. MS was placed at an angle of 58° to the target normal. This setup has been used to perform measurements presented and discussed in chapters 4.1, 4.2, 4.4 and 4.5. Detailed description of the plasma sampling mass spectrometer is given in chapter 3.3.3.
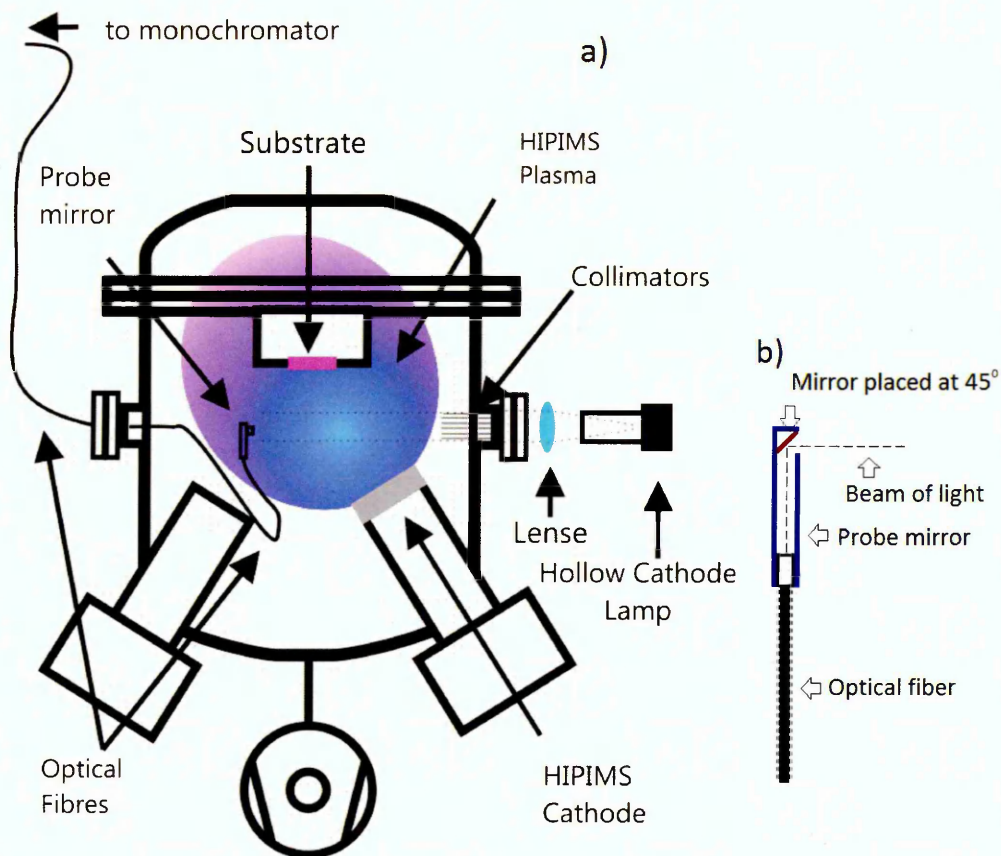
Figure 3.3 a) Schematic view of the experimental chamber cross section with atomic absorption setup showing target, substrate, optical fibre and hollow cathode lamp and b) detailed schematic of the probe mirror

The setup of the chamber with hollow cathode lamp and an optical fibre used for optical absorption and emission spectroscopy is shown on Figure 3.3 a). The optical fibre was mounted to a probe mirror to protect it from getting coated. Schematic of the probe mirror is shown on Figure 3.3 b). Probe mirror is a tube open on one end where the optical fibre is placed and on the other end the elliptical mirror is placed under the angle of 45°. On the side of the tube at the end where the mirror is placed is a hole. The hole is facing the window with collimator where the light from the lamp enters the chamber at distance of 30 cm. A light enters the probe mirror through the hole and reflects from the mirror directly to the optical fibre, Figure 3.3 b). Other end of the optical fibre is mounted on the holder facing quartz window. On the other side of the window is mounted another optical fibre that is connected to a monochromator. The optical fibres are mounted in the holders on both sides of quartz glass at the same point therefore no light is lost and the holders are made to perfectly fit the window so no external light can enter the fibre. A light

from hollow cathode lamp was transformed to a parallel beam with a lens and it entered the chamber through a quartz glass viewport. In front of the quartz glass, inside the chamber, set of glass tubes was mounted as a collimator and to prevent coating of the quartz glass. The path of the light from the hollow cathode lamp is marked with dashed line on the Figure 3.3 a). The results of the optical spectroscopy measurements are presented in chapter 4.1.
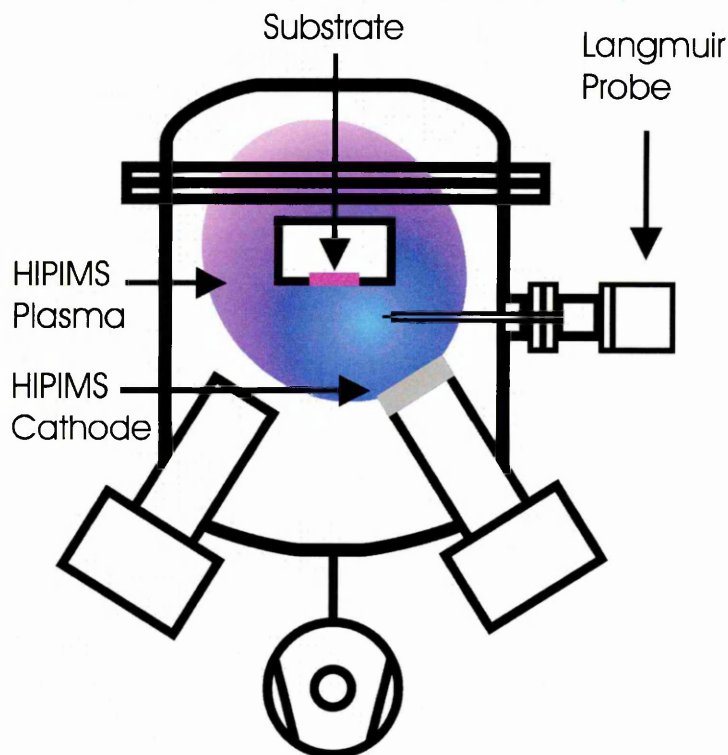
Figure 3.4 Schematic view of the experimental chamber cross section showing target, substrate and Langmuir probe

In addition to the mass spectrometer and the optical spectroscopy, Langmuir probe was used to investigate various plasma parameters. The probe was placed above the target at distance of 10 cm as shown on Figure 3.4. Further details about Langmuir probe are given in chapter 3.3.1. The results of the Langmuir probe measurements are presented in chapter 4.1.
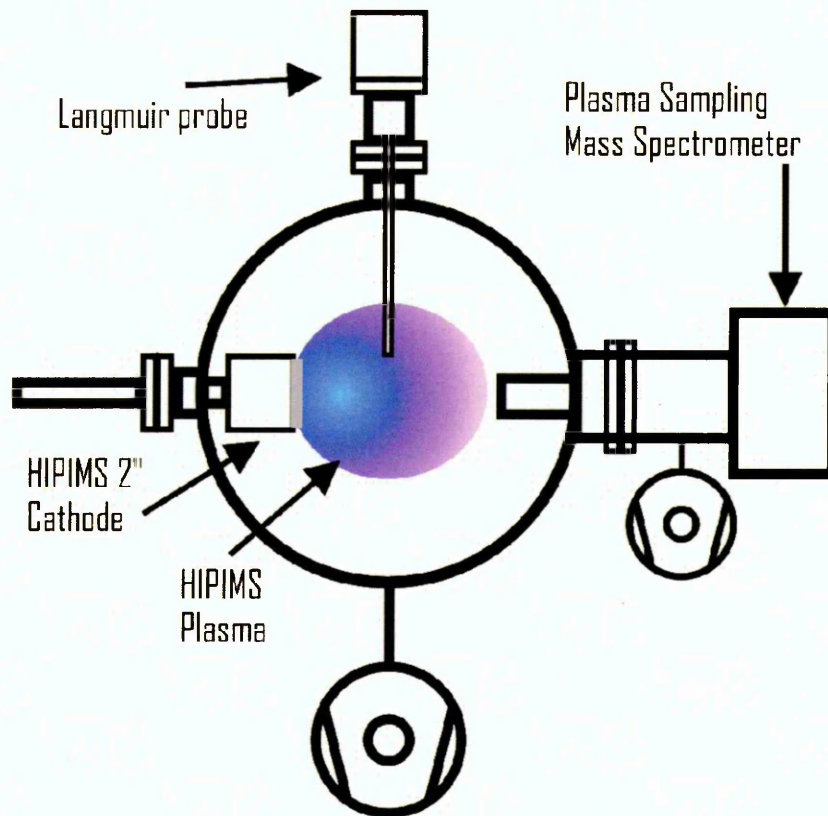
Figure 3.5 Schematic view of the experimental chamber view from the top showing target, plasma sampling mass spectrometer and Langmuir probe

To investigate the spatial evolution of plasma parameters, a 2" target mounted on a long arm was installed in the chamber. It was mounted through a feedthrough opposite mass spectrometer. A view from the top is shown on Figure 3.5. Long arm on which the target was mounted enabled to shift the target at various distances from the MS orifice from 2.5 cm up to 21 cm. Once the measurements with MS were finalized the Langmuir probe was mounted through a feedthrough perpendicular to the target normal. Due to its position the range of the target movement was restricted from 2.5 cm up to 15 cm. The results of the spatially resolved measurements are given in chapter 4.3.

3.2 HIPIMS power supply

Hüttinger power supply HMP2/4 is the power supply designed to power sputtering cathodes in the high power impulse mode. It consists of two units, the DC charging unit, upper unit showed on Figure 3.6, and the high impulse generator unit, shown on Figure 3.6 below DC unit.

Figure 3.6 Photograph of Hüttinger power supply HMP2/4

The power supply is controlled by 3 parameters; voltage, current and power. Control of power is necessary for the cathode performance and safety. In case of power exceeding the preset value the power controller will reduce the capacitor peak voltage. The voltage is important parameter in controlling the ignition of the cathode and shape of the pulse. Voltage is controlled and adjusted by the voltage controller. In case of peak capacitor voltage exceeds the preset value of the maximum voltage the current from DC current supply is reduced.

Maximum output voltage of the HMP2/4 power supply is 2000 V, with peak current of 4 kA and maximum total mean power of 20 kW. Frequency can be adjusted from 1 Hz to 500 Hz and pulse duration can be set from 10 µs up to 250 µs.

The high current of the pulse can sometimes lead to creation of arc. If the entire energy stored in the capacitors would be fed into the arc, this could cause a significant damage on the target surface. For this reason an arc detection feature has been implemented. The arc detection feature consists of a series semiconductor switch that turns off if the output pulse current exceeds a specified value. The discharge of the capacitor is stopped and only energy stored in the cable inductance is fed into the arc [64].

3.3 Plasma diagnostic techniques

Plasma diagnostics was performed using four techniques: Langmuir probe (LP), plasma sampling energy resolved mass spectrometer (MS), Optical emission spectroscopy (OES) and Optical absorption spectroscopy (OAS). Each technique provides information of different plasma parameter that creates complementary information of processes plasma is going through.

3.3.1 Langmuir probe

Langmuir probe is the plasma diagnostic instrument used to acquire the information about various plasma parameters; plasma potential, floating potential, electron density and electron temperature [38, 65, 37]. Langmuir probe consists of a piece of thin wire immersed in plasma and connected to a voltage power supply V (Figure 3.7). V is the potential difference between probe surface and a given reference point. In the experimental setup used in this work reference point is the grounded chamber itself.
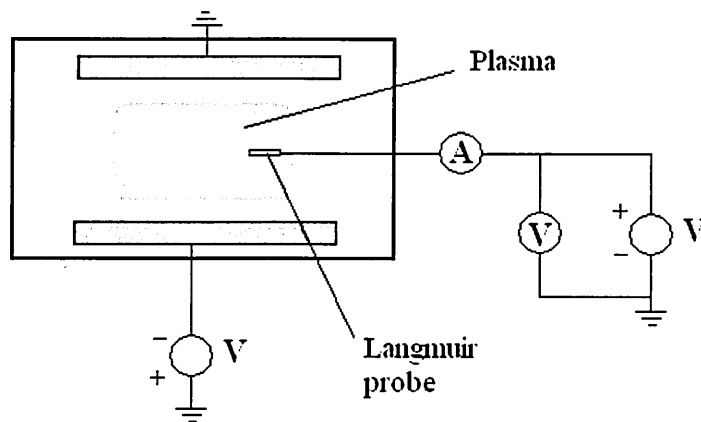
Figure 3.7 Schematic of the Langmuir probe inside the plasma

To obtain basic insight of Langmuir probe theories several assumptions are made [65];

- o the plasma is infinite homogenous and quasineutral in the absence of the probe

- o electrons and ions have Maxwellian velocity distribution and electron temperature T_e is greater than ion temperature T_i

47

- the mean free path of electrons λ_e and ions λ_i to be bigger than sheath thickness and larger than the probe radius
- each charged particle hitting the probe to be absorbed and not to react with the probe material
- existence of space charge sheath with well defined boundary
- the sheath thickness to be small compared to the dimension of the probe, hence edge effects can be neglected

The mean velocity of the electrons exceeds the mean velocity of the ions at least by a factor $(m_+/m_e)^{1/2}$ where m is the mass of the particle, that is in case of light Carbon equal to 148 and in case of Chromium is equal to 309, if we assume that the mean energies of the two kinds of charge carriers are equal. Furthermore, if we assume that the energy distribution of the particles is Maxwellian then the mean velocity of the particle is given by [65];

$$\bar{v} = \left(\frac{8k_B T}{\pi m}\right)^{1/2} \qquad (3.1)$$

where k_B is the Boltzmann constant, T is the temperature of the gas in Kelvin and m is the mass of the particle.

Outside the sheath the charge carrier density of electrons and ions is equal. Due to lighter mass, more electrons than ions hit the probe per unit of time and negative charge accumulates on the probe surface. This negative charge accelerates ions and repels electrons. Positive space charge sheath is formed in front of the probe which grows until a dynamic equilibrium between the two kinds of carrier currents I_i and I_e is achieved and no net current I_p flows to the probe. The probe is then at the floating potential V_f which is negative with respect to the sheath edge, i.e. to the undisturbed plasma (Figure 3.8).
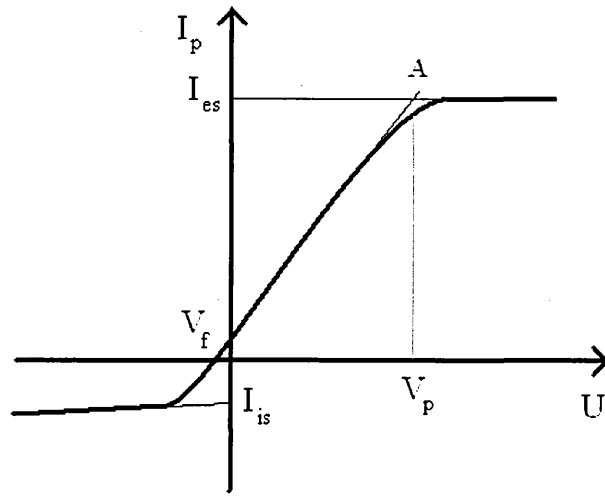
Figure 3.8 Typical voltage-current characteristic of the Langmuir probe

If the probe potential is sufficiently negative almost no electrons will reach the probe, while all ions passing the sheath in the probe direction are absorbed. The probe current is then equal to the ion saturation current I_{is};

$$I_{is} = \frac{1}{4} n_0 e \bar{v}_i A$$

(3.2)

where n_0 is the ion density in the plasma and A is the area of the probe. Raising V to values more positive than floating potential V_f, more and more electrons are able to overcome the retarding potential drop, first the faster electrons and at more positive values of V also the slow ones. The density distribution of Maxwellian electrons n_e in the positive sheath is governed by Boltzmann law [65];

$$n_e = n_0 \exp\left(\frac{eV_p}{kT_e}\right)$$

(3.3)

where V_p is the plasma potential and T_e is the electron temperature. The mean electron velocity at the sheath edge is equal to the velocity at the probe surface and using the analogy with eq. (3.3) electron current I_e is;

$$I_e = I_0 \exp\left(\frac{eV_p}{kT_e}\right)$$

(3.4)

When V approaches the plasma potential (V_p) the space charge sheath in front of the probe vanishes. Electron saturation current can be written;

$$I_e = \frac{1}{4} n_0 e \bar{v}_e A$$

(3.5)

The parameters n_{eo}, n_{io}, T_e and V_{sp} can now be readily derived from the probe characteristic. First measured value of I_{is} must be subtracted from the total probe current I_p in the region to the left of point A and obtains I_e as a function of V. The logarithm of I_e is plotted against V. If the electrons have a Maxwellian distribution the slope is constant and yields T_e;

$$\frac{d \ln I_e}{dU} = \frac{d \ln I_e}{dV_p} = \frac{e}{kT_e}$$

(3.6)

Using eq. (3.1) and inserting T_e into eq. (3.5) we evaluate n_{e0} from the measured electron saturation current I_{e0}. V_p is found as the abscissa of the intersection point of the exponentially increasing part of the characteristic as indicated.

Above analysis was done for the flat probe. To expand the theory on spherical and cylindrical probes one more assumption has to be made; the potential has to be symmetrical with respect to the centre and to be monotonically decreasing or increasing function of r between sheath edge and the probe surface, where r is the radial distance from the centre of the probe. Differential equation describing the particle orbit is [65];

$$\dot{r} = \frac{v}{r}\left[r^2\left(1 - \frac{2qV(r)}{mv^2}\right) - p^2\right]^{1/2}$$

(3.7)

where p stands for impact parameter, v and q are the velocity and the charge of the particle, respectively. For given impact parameter p and initial velocity v the probe centre is reached by particle when its radial velocity $\dot{r}$ is equal to zero;

$$p_g^2 = r_p^2\left(1 - \frac{2qV_p}{mv^2}\right)$$

(3.8)

and it intersects the probe if

$$r_m < r_p \quad \text{or} \quad p < p_g.$$

Electric field surrounding the sheath can be either retarding ($qV_p > 0$) or accelerating ($qV_p < 0$). In case of retarding field only particles fulfilling following two conditions reach the probe; particles with velocity $v \geq \left(\frac{2qV_p}{m}\right)^{1/2}$ and the impact parameter p should be bigger than zero and smaller than $p_g = r_p$, where r_p stands for probe radius.

50

In the case of accelerating field ($qV_p < 0$) the behaviour of the particle is dependant on whether the initial particle velocities v are smaller or larger than a certain critical velocity v_c which is defined by

$$v_c = \left(\frac{2qV_p}{m} \middle/ \left(\frac{r_s^2}{r_p^2} - 1 \right) \right)^{1/2}$$

(3.9)

- v < v_c, all particles with impact parameter $p \leq r_s$ are collected by the probe, where r_s is the sheath radius. The motion of the particle is called "sheath limited"

- v > v_c, only particles with $p \leq p_g < r_s$ arrive at the probe. The motion of the particle is called "orbit limited".

These were basics of Langmuir probe theory for Maxwellian energy distribution of electrons. The energy distribution of electrons collected by Langmuir probe in experiment conducted in this work is not Maxwellian. It is either double Maxwell distribution or Druyvesteyn distribution and the analysis is dependent on the plasma density. Criterion for plasma density is determined by the ratio of probe radius r_p and Debye length λ_D. Plasma where the ratio of probe radius and Debye length is higher or equal to 1 is called high density plasma and plasma with $r_p / \lambda_D < 1$ is called low density plasma. Debye length λ_D is defined as a distance at which mobile charge carriers, i.e. electrons, shield the potential of the positive ion. It is given by expression [66];

$$\lambda_D = \left(\frac{\varepsilon_0 k_B T}{n_e e^2} \right)^{1/2}$$

(3.10)

where ε_0 is the vacuum permittivity, k_B is the Boltzmann constant and T is the temperature of the gas in Kelvin. n_e is the electron density and e is the elementary charge. The probe radius r_p is 75 μm and Debye length is calculated to be below 10 μm, thus HIPIMS plasma is high density plasma. Ion saturation current was derived from the Bohm criterion [65];

$$I_i = 0.6 n_0 eA \left(\frac{2kT_e}{m_i} \right)^{1/2}$$

(3.11)

The electron density was calculated using following expression [67];

$$n = \int_0^\infty F(\varepsilon) d\varepsilon$$

(3.12)

51

where $F(\varepsilon)$ stands for electron energy distribution function (EEDF). EEDF was calculated using $f(\varepsilon)$ which is the electron energy probability function (EEPF). EEPF is related to EEDF through the expression $f(\varepsilon) = \varepsilon^{-1/2} F(\varepsilon)$. EEPF can be calculated using expression [67];

$$f(\varepsilon) = \frac{2\sqrt{2m_e}}{e^3 A} \frac{d^2 I_p}{dV^2}$$ (3.13)

Effective electron temperature is calculated using the expression [67];

$$T_{eff} = \frac{2}{3}\langle\varepsilon\rangle = \frac{2}{3n}\int_0^\infty \varepsilon F(\varepsilon)d\varepsilon$$ (3.14)

On Figure 3.9 all stages of analysis of the Langmuir probe V-I characteristic is given. The analysis is performed using Matlab program developed by A. Vetushka. As a result it gives four parameters; floating potential, plasma potential, electron density and electron temperature. Figure 3.9 a) shows measured V-I characteristic. The voltage where the curve intersects the current axis is the floating potential, for given measurement it is 2.5 V. Figure 3.9 b) shows second derivative of the V-I characteristic. The voltage where the second derivative intersects the current axis is the plasma potential, for given measurement it is 6.15 V. Next step in calculating the electron density and the electron temperature is to remove the ion current. It is done by fitting a straight line on the ion current, as shown on Figure 3.9 c) and deducting it from measured V-I characteristic. The V-I characteristic without ion current is shown on Figure 3.9 d). Finally on Figure 3.9 e) the electron energy distribution function is shown and using equations (3.12) and (3.14) it is possible to calculate electron density and electron temperature.
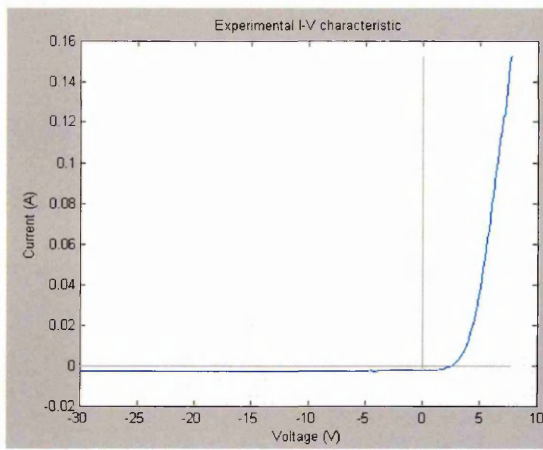
a)
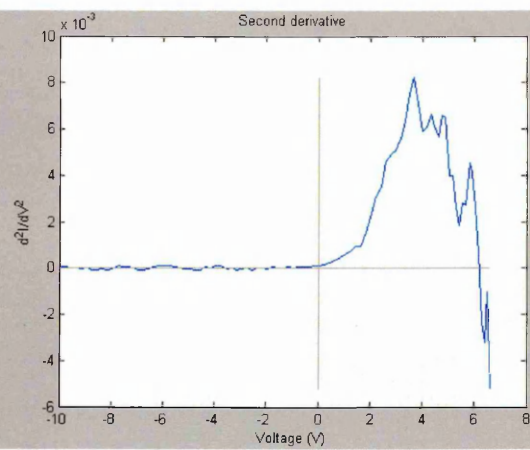
b)
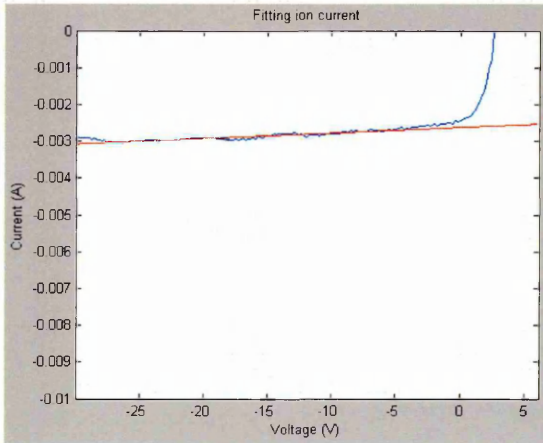
c)
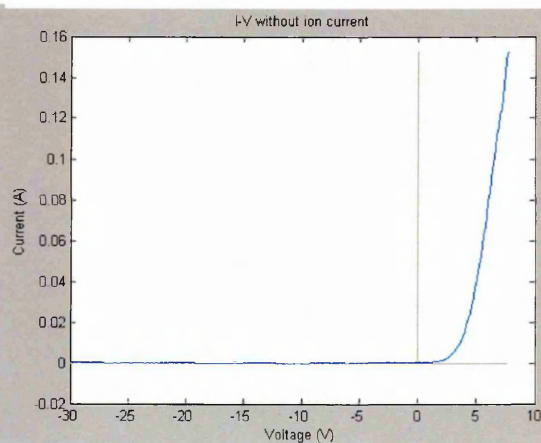
d)
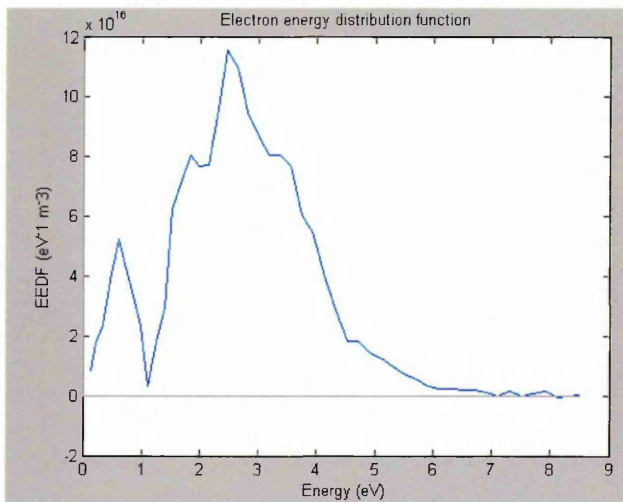
e)

Figure 3.9 All stages of Langmuir probe V-I characteristic analysis a) measured V-I characteristic, b) second derivative of the V-I characteristic, c) fit for the ion current, d) V-I characteristic without ion current, e) electron energy distribution function

3.3.1.1 Langmuir probe measurements specification

Hiden Analytical ESPion Langmuir probe with 0.15 mm in diameter and 10 mm long tip was used to perform the measurements. The measurements obtained and presented in this work use the same setup. The V-I curve was measured from -30 V up to 20 V with resolution of 0.2 V. Each point was averaged over 60 pulses. Between measurements Langmuir probe tip was cleaned by applying voltage of -150 V for 1 ms. while the probe was idle the same voltage was applied to prevent deposition of the material on the probe tip. All measurements are taken in time resolved mode with trigger supplied from the power supply. Once the measurement reached 20 V new V-I curve commenced delayed in time by 20 μs. First measurement was done when power supply triggered the measurement and consequent measurements were delayed by the internal trigger.

3.3.2 Optical spectroscopy

Light emitted from the excited atom or ion is unique for every element. Observing the light emitted from the plasma, it is possible to obtain information about the elements in the plasma. Atoms and ions get excited through collisions with other particles in plasma, atoms, ions and electrons. Therefore the information of presence and the density of ions can be obtained.

The light from the atom is emitted when electrons transition between different energy levels. For example when the atom collides with a free electron in a non-elastic collision an electron inside the atom is excited to a higher energy level. The electron relaxing to initial level emits a photon of light. The wavelength of the photon is unique for each element. The possible excitation levels and corresponding wavelengths of photons are usually given in a Grotrian diagram. Examples for Grotrian diagram are given on Figure 3.10 made on the National Institute for standards and Technology [68].
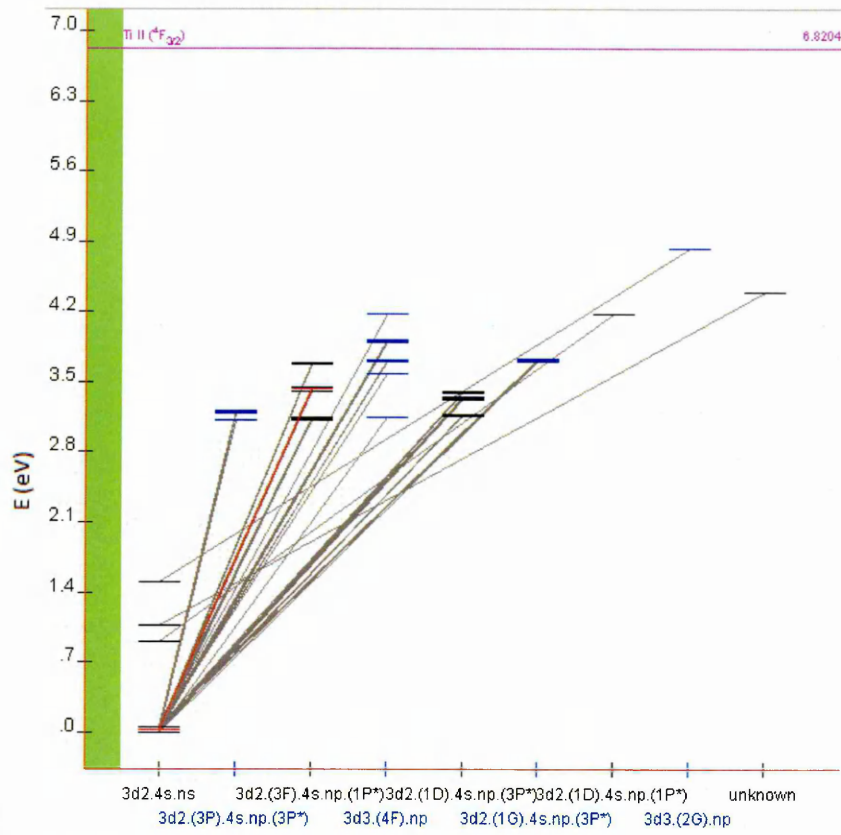
a)
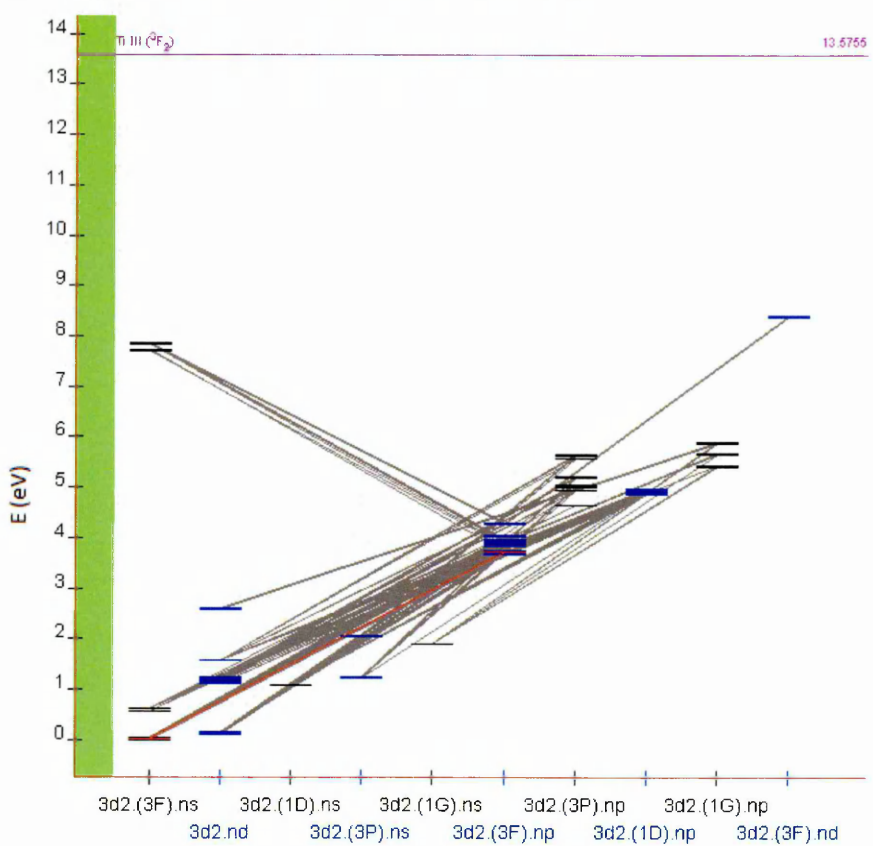
b)

Figure 3.10 Grotrian diagram of Titanium representing possible relaxation transitions between excitation levels of a) Ti^0 and b) Ti^{1+}, from [68]

On Figure 3.10 it can be seen that not all transitions are possible. Every level has its quantum number. The notation of quantum numbers is nicely described in D.J. Griffiths book [69], where the quantum number is presented in following form; $^{2S+1}L_J$. S stands for total spin, which in this case is equal to 1/2. L is the total orbital angular momentum, where L = 0 is marked as S orbital, L = 1 is marked as P orbital etc. J is the grand total angular momentum, J = L + S, thus J = 1/2 + 0 = 1/2 .Conservation of the angular momentum allows only transitions where the difference between initial and final quantum number obeys following conditions; ΔJ =0, ±1 and ΔL = ±1. The electron in the Ti atom jumps from $3d^24s4p$ to $3d^24s^2$, the transition occurs from the orbital 4p to orbital 4s, therefore ΔL = +1. On Figure 3.10 a) the transition occurs between levels with total angular momentum J_{upper} = 4 J_{lower} = 3 so the other condition is fulfilled ΔJ = +1. In case of Ti ion the transition is from $3d^24p$ (J = 9/2) to $3d^24s$ (J = 7/2) and the conditions are as in the Ti atom case ΔL = +1 and ΔJ = +1.

The optical emission spectrum of the plasma is acquired using a monochromator. Figure 3.11 shows a schematic of a monochromator. The light collected with an optical fibre is brought to the entrance slit of the monochromator. A collimating mirror reflects the light to a parallel beam which is then diffracted on the diffraction grating. The diffraction grating splits the light in the same manner as a prism. Parallel beam of diffracted light is focused using a mirror to an exit slit. Exit slit is ~10-100 micrometer wide which enables only the light with selected wavelength to pass through it whereas the light with longer and shorter wavelengths hits the wall and doesn't get detected in a photomultiplier. The width of the slit sets the resolution of the monochromator. The photomultiplier is a device in which the incident light ejects electrons from the photo emissive cathode, which are then multiplied through series of dynodes. The amount of current at the exit of photomultiplier is proportional with the amount of light that enters the photomultiplier. Rotating the diffraction grating it is possible to select the wavelength of the light that is detected in the photomultiplier. If the grating is rotated in a short turns the whole spectrum in the visible light can be recorded [70].
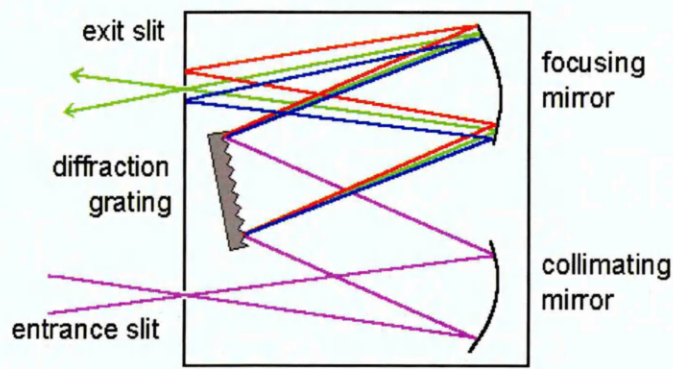
Figure 3.11 Schematic of a monochromator used to measure spectrum from the plasma, adapted from [71]

3.3.2.1 Optical emission spectroscopy

Optical emission spectroscopy (OES) is a plasma diagnostic technique where a spectrum of the plasma is recorded and no artificial source of light is used as a stimulus. An example of emission spectrum with identified spectral lines is given on Figure 3.12. The OES method provides information about atoms and ions detected in the plasma however the ratio of detected particle density cannot be calculated.
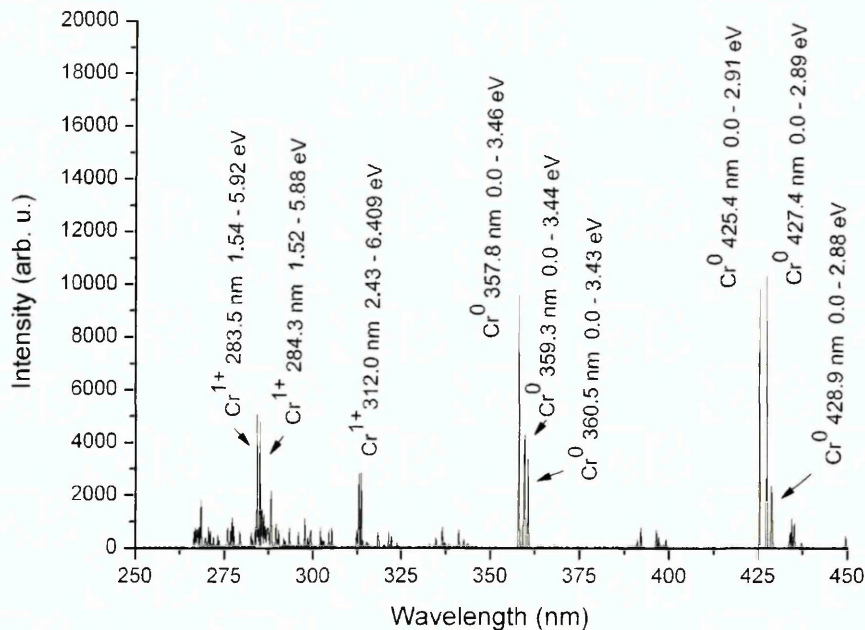
Figure 3.12 Spectrum of HIPIMS with Chromium target with identified spectral lines of Cr^0 and Cr^{1+}

57

3.3.2.2 Optical absorption spectroscopy

In order to find the ratio of the ion and neutral density the optical absorption spectroscopy (OAS) is used. The atoms and ions can be excited by an external source, e.g. the light with matching wavelength. In OAS a lamp is used to excite the atoms and ions in order to observe the particles even when particles do not emit the light. The optical absorption spectroscopy provides one of the best means for obtaining species number density in plasma without perturbing the mechanism of the plasma. The absorption coefficient A_L, along a distance L, is defined as [49];

$$A_L = 1 - \frac{I_{lp} - I_p}{I_l} \qquad (3.15)$$

where I_l is the lamp intensity without the plasma, I_p is the plasma intensity with the masked lamp and I_{lp} is the intensity of the lamp and plasma together. Distance L is a length between the collimator and the optical fiber, a distance where the light from the lamp is absorbed by the particles in the plasma. Measuring each of the above mentioned intensities and using equation (3.15) it is possible to calculate absorption coefficient. The density of the absorbing ions can be calculated using following expression [49];

$$k_{\sigma_0} L = 8.25 \times 10^{-13} \frac{fL}{\delta\sigma_p} n \qquad (3.16)$$

where k_{σ_0} is the absorbing coefficient at the centre line wave number, f is the oscillator strength, n is the density of the absorbing gas and $\delta\sigma_p$ is the plasma half-intensity width given by expression [72];

$$\delta\sigma_p = 7.16 \times 10^{-7} \frac{1}{\lambda} \left(\frac{T}{M} \right)^{1/2} \qquad (3.17)$$

where λ is a wavelength, T is the gas temperature and M is the unified mass of the element, e.g. $M_{Cr} = 52$. The plasma linewidth ($\delta\sigma_p$) and optical depth ($k_{\sigma_0} L$) can be found from the following equations [49];

$$A_L = \sum_{m=1}^{\infty} \frac{(-1)^{m+1} (k_{\sigma_0} L)^m}{m! (1+m\alpha^2)^{1/2}} \qquad (3.18)$$

where factor α represents the ratio of optical source($\delta\sigma_s$) and plasma linewidths ($\delta\sigma_p$). The absorption coefficient A_L is related to an absorbing gas

density through absorbing coefficient k_{σ_0} from equation (3.16). Therefore the ratio of calculated A_L for the ion and neutral lines is the ratio of ion and neutral density.

3.3.2.3 Optical absorption spectroscopy measurements specification

The light from the S&J Juniper Hollow Cathode Lamp, operated in a pulsed mode in order to generate the wavelengths of both ion and neutral lines, was transformed to a parallel beam using fused silica spherical plano-convex QuantaGlas lens. Parallel beam entered the chamber through a quartz glass. The light was collected with an optical fibre as described in chapter 3.1. Other end of the optical fibre was connected to the Jobin Yvon-SPEX Triax 320 monochromator. The monochromator has 320mm focal length, dispersion is 2.64nm/mm, resolution 0.12nm and grating has 1200 grooves/mm. The output of the PMT was measured and recorded in the Stanford Research Systems SR400 photon counter.

The measurements are performed for the HIPIMS plasma discharge with Ti target. Wavelengths 336.1 nm for Ti^{1+} and 364.3 nm for Ti atom were chosen. Transition in the Ti^{1+} ion from $3d^2(^3F)4p$ to $3d^2(^3F)4s$, i.e. from energy level of 3.715595 eV to the level of 0.027987 eV, resulted in the emission of light with wavelength of 336.1 nm. Transition in the Ti atom from $3d^2(^3F)4s4p(^1P^{\circ})$ to $3d^24s^2$, i.e. from energy level of 3.4237821 eV to the level of 0.0210937 eV, resulted in the emission of light with wavelength of 364.3 nm. The lines are chosen according to their lower energy level that is very close to the ground level, and the lines are relatively close on the wavelength scale so that monochromator response curve can be excluded from data analysis [68].

The monochromator was fixed on the selected wavelength and 5 measurements were performed to obtain mean value and standard deviation for each intensity. Intensity of plasma only, intensity of lamp only and intensity of plasma and lamp was measured. The mean value of the absorption coefficient for Ti ions and atoms was calculated using equation (3.15). The standard deviation was calculated using following equation:

$$M_A = \left(\left(\frac{M_{ILP}}{I_L} \right)^2 + \left(\frac{M_{IP}}{I_L} \right)^2 + \left(\frac{I_{LP} - I_P}{I_L^2} M_{IL} \right)^2 \right)^{1/2} \quad (3.19)$$

where M_A, M_{ILP}, M_{IP}, and M_{IL} are standard deviation of the absorption coefficient, the lamp + plasma intensity, the plasma intensity and the lamp intensity, respectively. I_{LP}, I_P and I_L are the lamp + plasma intensity, the plasma intensity and the lamp intensity, respectively.

During the pulse the intensity of plasma is few orders of magnitude higher than the intensity of lamp therefore the standard deviation of the calculated absorption coefficient was comparable with mean value. Calculating ion to neutral ratio the standard deviation turned out to have bigger value then the signal. For this reason ion to neutral ratio could be calculated only in the post-discharge when the signal from the plasma was comparable to the signal from the lamp. On Figure 3.13 an example of the measurement is given. It shows the measured intensity from lamp + plasma, lamp only and plasma only. With a blue line discharge current is shown to demonstrate the duration of the pulse. Since red circles, intensity of lamp + plasma, have lower intensity than black squares, intensity of lamp without plasma, it is possible to conclude that plasma exist for times up to 1 ms as only the light from the lamp can be absorbed by the particles in the plasma. Results of the OAS measurements are presented in chapter 4.1.1.
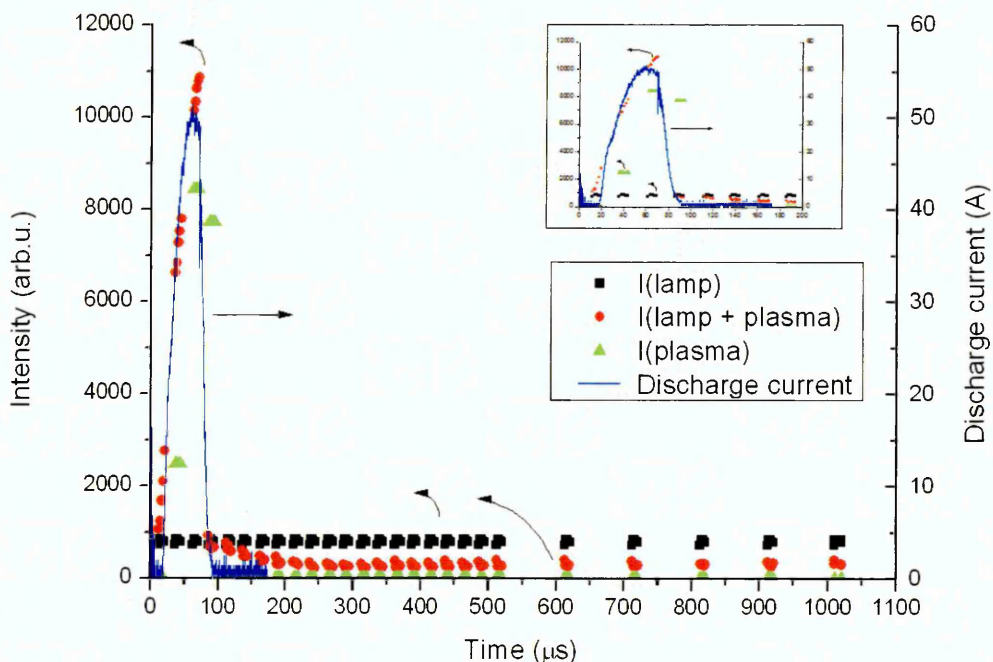
Figure 3.13 Example of the OAS measurement showing data for intensity from lamp + plasma (red circles), lamp only (black squares), plasma only (green triangles) and discharge current (blue line). The inset shows the same data from 0 to 200μs.

3.3.3 Plasma sampling mass spectrometer

The mass and relative concentrations of atoms, ions and molecules and their energy distribution is measured using plasma sampling mass spectrometer. Schematic picture of plasma sampling mass spectrometer is shown on Figure 3.14.
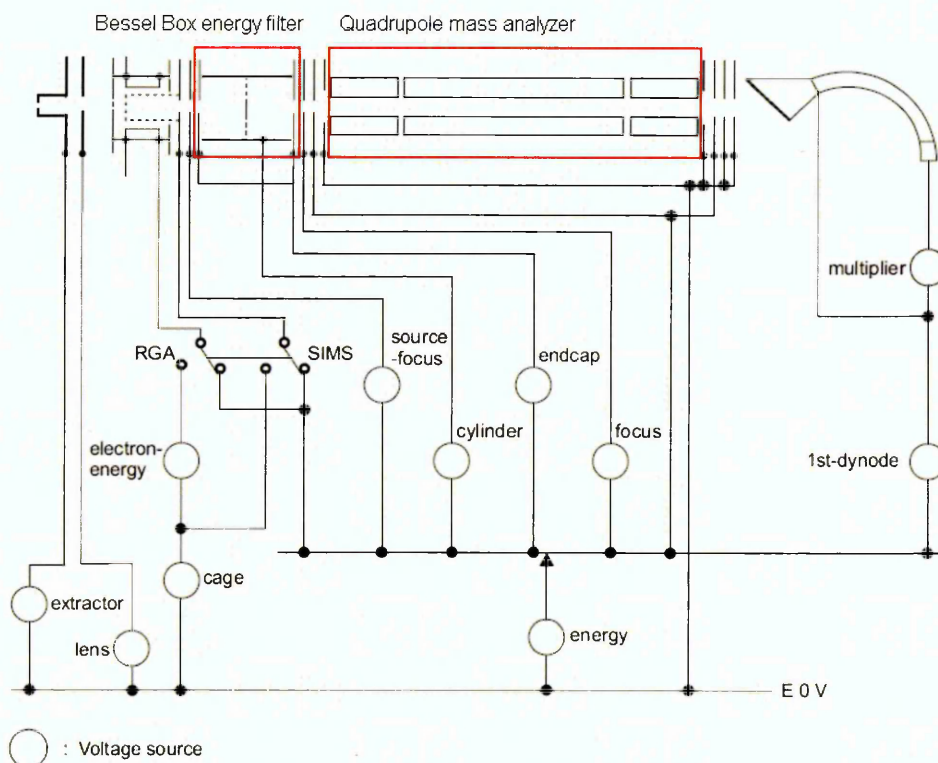
Figure 3.14 Schematic of the mass spectrometer [73]

The ions are extracted from the plasma and focused by applying direct current voltage on the extractor electrode and by the lens electrode. Voltages on the extractor electrode and on the lens electrode are around -10 V and -79 V, respectively. Negative voltage on the extractor is used to repel electrons and accelerate ions. In the next step it is possible to choose Residual Gas Analysis (RGA) mode that uses internal impact ionisation source for ionisation of neutrals from the plasma. In this work RGA mode was not used since only ions generated in the plasma were analysed. The ions from the extraction electrodes are then filtered by their energy in the Bessel box. Remaining ions are further filtered by their mass-to-charge ratio in the quadrupole mass analyzer (QMA). Ions with the selected mass-to-charge ratio enter the detector. The secondary electron multiplier (SEM) is used as an ion detector. A

secondary electron multiplier consists of a series of electrodes called dynodes, each connected along a string of resistors. One signal output end of the resistor string is attached to the positive high voltage and the other end of the string is grounded. The dynodes maintained at increasing potential create a series of amplifications. When a particle, e.g. ion, strikes the first dynode it generates secondary electrons. The secondary electrons are then accelerated into the next dynode where each electron produces more secondary electrons, thus generating a cascade of secondary electrons. Typical amplification is of order 10^6 generated electrons per one incoming particle [70, 74].

Mass analyzer separates the ions according to their mass-to-charge ratio. All mass spectrometers are based on the dynamics of charged particles in electric and magnetic fields in the vacuum where the Lorentz law:

$$\vec{F} = q\vec{E} + q\vec{v} \times \vec{B} \qquad (3.20)$$

and Newton second law applies:

$$\vec{F} = m\vec{a} \qquad (3.21)$$

where $\vec{F}$ is the force applied to the ion, q is the ion charge, $\vec{E}$ is the electric field, $\vec{v} \times \vec{B}$ is the vector cross product of the ion velocity and the magnetic field, m is the mass of the ion and $\vec{a}$ is the acceleration. Equating the eq. (3.20) and eq. (3.21) the expressions for the force applied to the ion yields;

$$\frac{m}{q}\vec{a} = \vec{E} + \vec{v} \times \vec{B} \qquad (3.22)$$

where m/q is called mass-to-charge ratio. Initial conditions of the particle and equation (3.22) are completely determining the particle motion in space and time. Two particles with the same mass-to-charge ratio (m/q) behave the same. This is the basic principle of mass spectrometry.

The quadrupole mass analyzer (Figure 3.15) consists of four parallel metal rods. Each opposing rod pair is connected together and a radio frequency (R.F.) voltage is applied between one pair of rods, and the other. A direct current voltage is then superimposed on the R.F. voltage. Ions travel between the rods and through the quadrupole. Only ions of a certain mass-to-charge ratio will reach the detector for a given voltage parameters. Other ions will be lost due to collisions with rods and the wall of QMA. This allows selection of a particular ion, or scanning by varying the voltages.
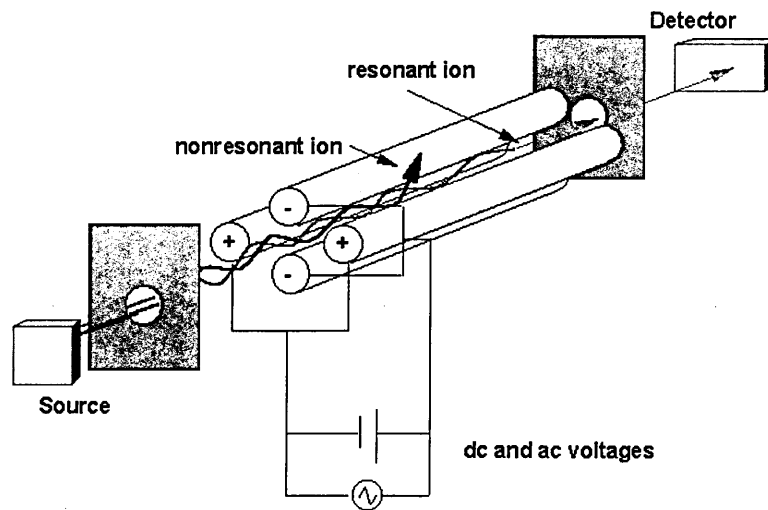
Figure 3.15 Schematic of the quadrupole mass analyzer showing resonant ion passing the analyzer and reaching the detector and nonresonant ion scattered in the analyzer [75]

Energy resolution of the ions is obtained using Bessel box. Schematic of a Bessel box is shown on Figure 3.16. The Bessel box energy filter has a cylindrical geometry and is situated prior the quadrupole. The centre stop and cylinder electrode are driven by direct current voltage with value of 0 V. Endcap electrodes are round plates with a hole in the middle situated at the ends of the energy filter. Direct current voltage on the endcap electrode is around -20 V.
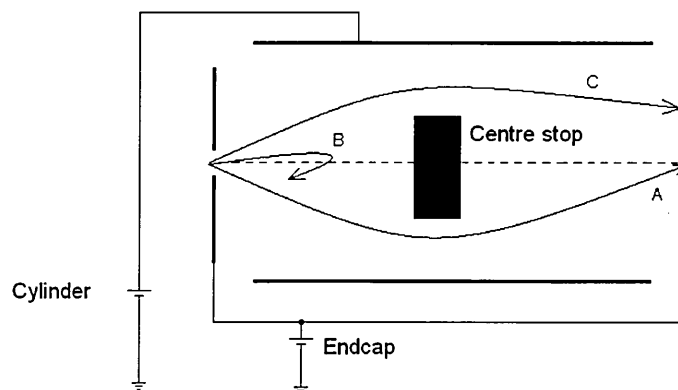
Figure 3.16 Schematic of the Bessel box showing the trajectory of the particle with adequate energy passing through the filter (A), and two particles with excessive (C) and insufficient energy (B), not passing the filter (adapted from [73])

Ion marked with A on Figure 3.16 will have sufficient energy to pass straight through the filter. The ions with excessive energy will follow trajectory C on Figure 3.16. The ions with insufficient energy, e.g. trajectory B on Figure 3.16, will be mirrored back. In this way the Bessel box achieves a high and low energy cut-off. The main advantage of the Bessel box analyzer is possibility of direct analysis of energy spectrum and the drawbacks are low transmission and narrow angular acceptance ($2.5° < \theta < 9.5°$). The velocity of ions through the energy analyser can be approximated by the expression [29];

$$v = \sqrt{\frac{2e\left(V_{endcap} - V_{cylinder} - K_{ion}\right)}{m}} \qquad (3.23)$$

where V_{endcap} and $V_{cylinder}$ are voltages on the endcap and cylinder, respectively, K_{ion} is kinetic energy of ion and m is the mass of the ion.

Takahashi et al. [76] used quadrupole mass spectrometer (QMS) with Bessel-box type energy analyzer. Signal strength and signal to noise ratio for conventional QMS and QMS with Bessel-box was compared. The results are shown in Figure 3.17.
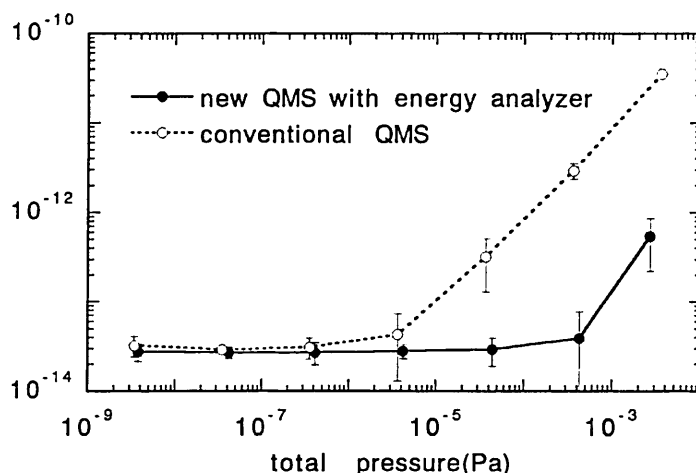
Figure 3.17 Change of the background noise as a function of Ar pressure. Error bars are the fluctuation factors of noise intensity [76]

In this work the plasma mass spectrometer was used for two purposes. First was measuring mass spectrum of the plasma. Second was measurement of the ion energy distribution. An example of a mass spectrum of a HIPIMS of Cr discharge is shown in Figure 3.18.
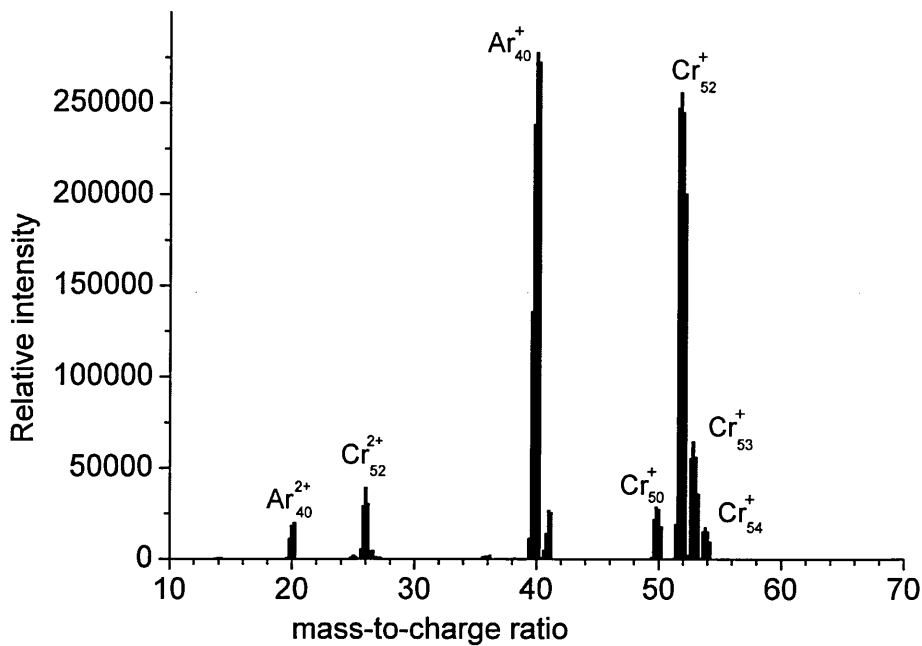
Figure 3.18 Mass spectrum of HIPIMS plasma discharge for Cr target in Ar atmosphere taken at an ion energy of E = 0.5 eV at pressure of p = 0.29 Pa

Mass spectrum is measured by setting a fixed voltage on the Bessel box to define the ion energy and changing the voltage on the QMA, therefore scanning through the mass-to-charge ratio. On Figure 3.18 it is possible to recognize main isotopes of chromium, Cr^+ at m/q = 52 and Argon, Ar^+ at m/q = 40. The unified mass unit of Cr isotope is 52 and once ionized Cr ion has q = +1, thus mass-to-charge ratio, m/q for Cr^+ is equal to 52. On Figure 3.18, one can recognize stable Chromium isotopes Cr_{53} (m/q = 53) and Cr_{54} (m/q = 54) and long life isotope Cr_{50} (m/q = 50) with half-life of 1.8 e+17 y [77]. Twice ionized ions have q = +2, thus Cr^{2+} has m/q = 26 and Ar^{2+} has m/q = 20. On Figure 3.18 peaks for Cr^{2+} with m/q = 26 and Ar^{2+}, with m/q = 20 can be seen.

The energy distribution of Cr^+ ion is measured by setting QMA to enable only ions with m/q = 52 and then scanning all energies using the Bessel box. Figure 3.19 shows an example of the Cr^+ ion energy distribution in Ar atmosphere at pressure of 0.29 Pa.
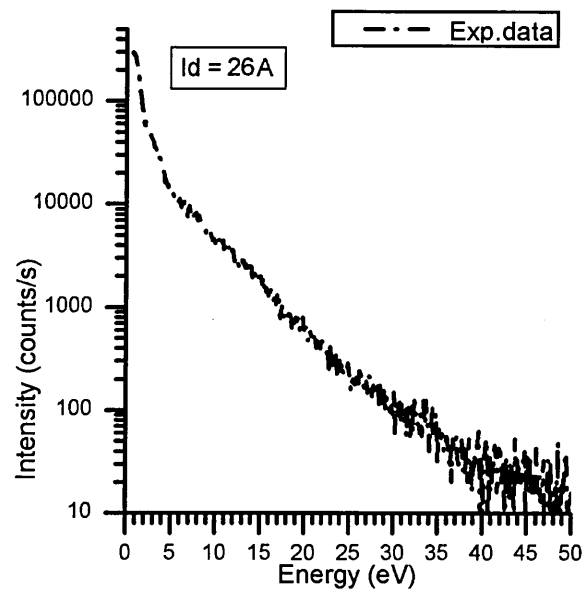
Figure 3.19 Ion energy distribution function for Cr^+ in Ar atmosphere at pressure p = 0.29 Pa

Ion energy distribution function (IEDF) for gas ions differ from metal ion energy distribution. Gas ion energy distribution function is a Maxwellian. On the other hand metal atoms sputtered from the target have Thompson distribution [31] near the target. Metal atoms are ionized through electron impact ionisation. Diffusing from the target metal ions collide among themselves and with gas ions and atoms resulting in the thermalisation of metal ions.

The energy scale measured by mass spectrometry is represented in volts. To change the energy scale to eV it is necessary to multiply it by the charge of the particle, e.g. in case of doubly charged ions the energy scale should be multiplied by two to obtain the energy scale in eV.

3.3.3.1 Time averaged mode

Mass spectrometer acquires data at certain energy for a specified length of time. Changing the acquisition time it is possible to measure the IEDF in time averaged and time resolved mode. In the time averaged mode the acquisition time was 300 ms meaning the detector was collecting the ions arriving to the detector for 300 ms which is around 30 pulses. The amount of ions detected at certain energy represents the number of ions detected both during and between the pulses. The IEDF measured in the time averaged

mode gives information of ions arriving to the substrate during deposition. The origins of comprising parts of the time averaged IEDF is given in chapter 4.1.

3.3.3.2 Time resolved mode

In the time resolved mode the acquisition time was 20 μs and the detector was triggered from the power supply trigger. From the orifice of the MS till the detector the ions need to go through the different parts of the MS and the required time is called a time of flight, TOF_{ms}. The TOF_{ms} through the spectrometer is determined by the velocity of ions through its separate sections which are characterised by different accelerating or decelerating voltages. Bohlmark et al. [29] give an equation to calculate the time of flight through each section of the mass spectrometer;

$$TOF_{ms} = d_{ext} \frac{\sqrt{2m}}{\sqrt{e(K_{ion} - V_{ext})} + \sqrt{|eV_{endcap}|}} + d_{en} \sqrt{\frac{m}{|2e(V_{endcap} - V_{cylinder} - K_{ion})|}}$$
$$+ d_{mass} \sqrt{\frac{m}{|2eV_{te}|}} + d_{det} \sqrt{\frac{2m}{|eV_{dyn}|}} \tag{3.24}$$

where d_{ext}, d_{en}, d_{mass} and d_{det} correspond to the length of the extractor, the energy filter, the mass filter and the detector, respectively. The values for the above lengths are; d_{ext} = 4 cm, d_{en} = 3.756 cm, d_{mass} = 20 cm and d_{det} = 1.6 cm. V_{ext}, $V_{cylinder}$, V_{dyn} and V_{endcap} are potentials applied to different sections of the mass spectrometer, to the extraction system, cylinder, multiplier and endcap, respectively. The voltages were as follows; V_{ext} = -10 V, $V_{cylinder}$ = -0.4 V, V_{dyn} = 2100 V and V_{endcap} = -20 V. K_{ion} is the initial ion energy and m is the ion mass. The TOF_{ms} was calculated with respect to masses of the Ar^{1+}, Cr^{1+}, Ar^{2+} and Cr^{2+} particles and with respect to the energies of the particles entering the mass spectrometer. Expected particle energies are between 0 eV and 50 eV and therefore the TOF_{ms} is calculated as a range. Substituting in equation (3.24), the TOF_{ms} for Ar^{1+} is between 58 and 61 μs, for Cr^{1+} it is between 66 and 70 μs, for Ar^{2+} it is between 41 and 43 μs and for Cr^{2+} it is between 47 and 49 μs. Taking into account that particles spend most of their time in the mass filter, where they have the same energy, and that acquisition time is 20 μs, which is much longer than the variation in the TOF_{ms}, we used an average value for the TOF_{ms}. That is 60 μs for Ar^{1+}, 68 μs for Cr^{1+}, 42 μs for Ar^{2+} and 48 μs for Cr^{2+}.

The position of the mass spectrometer with regard to the target is shown on Figure 3.2. The exact value of the TOF_c of ions through the experimental chamber is determined by a multitude of factors. The TOF_c depends on the distance between the ion start position, the mass spectrometer orifice and the energy of ion. The TOF_c as a function of distance and energy of ions is plotted on Figure 3.20 in a first approximation assuming that no collisions or external fields alter the speed of ions.
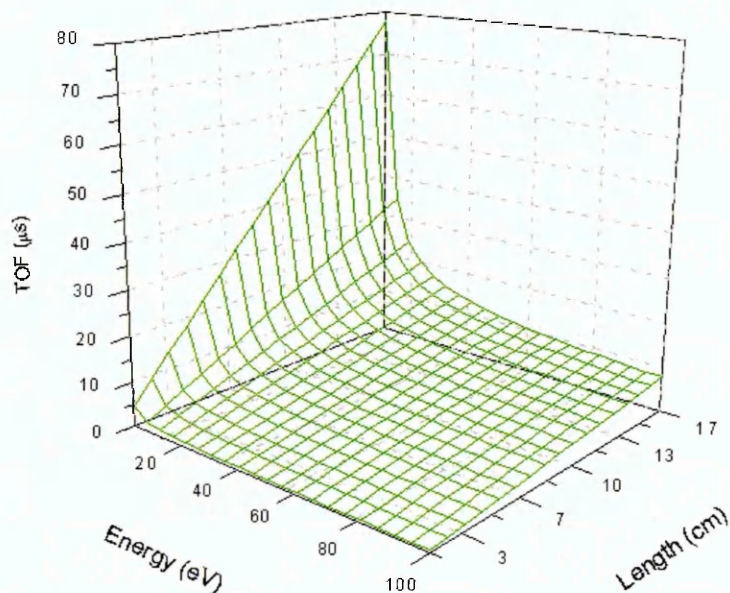
Figure 3.20 Time of flight from target to the mass spectrometer orifice as a function of distance and ion energy

The figure illustrates that the time resolved measurements, especially at long distances from the target, are governed by the diffusion of ions through the chamber and are not necessarily influenced by fast processes occurring at the target. Nevertheless, the measurements accurately portray the deposition conditions at the substrate.

3.3.3.3 Mass spectrometer measurements specification

Hiden Analytical Ltd. Plasma sampling mass spectrometer PSM003 with a 200μm diameter grounded orifice was used to measure the mass spectrum and ion energy distribution function.

The tuning of the mass spectrometer was needed to obtain highest intensity of the ion signal. To obtain the tuning that is not dependant on target

material and to achieve highest possible intensity even for the low density ions, the tuning was performed on Ar^{2+} ions in the DC plasma discharge, since pulsed nature of HIPIMS plasma discharge didn't provide constant influx of ions to the mass spectrometer. The tuning comprise of varying the voltage on 4 parameters to obtain the setup where the signal of Ar^{2+} ions was strongest. Energy scan ranged from -5 V to 40 V. Voltage on the lens electrode and focus electrode ranged from -100 V to 0 V and cylinder electrode voltage was varied from -10 V to 10 V. The highest intensity of the signal was obtained at voltage of -78 V, -18 V and -0.4 V applied on the lens electrode, focus electrode and cylinder electrode, respectively.

3.3.4 Scanning electron microscope (SEM)

Scanning electron microscope (SEM) is an electron microscope that creates a micrograph of the sample surface by scanning it with a high-energy beam of electrons. The electrons interact with the atoms of the sample surface and produce electrons, X rays and in case of some materials secondary fluorescence. Figure 3.21 shows a cross section of the sample surface as the electron beam strikes the surface and the volume origin of signals from the sample. Secondary electrons are generated near the surface and the area generating secondary electrons is equal to the size of the beam. Secondary electrons are produced throughout the interaction volume, but have very low energies and can only escape from a thin layer near the sample's surface. Observing secondary electron SEM can resolve surface morphology details about less than 1 to 5 nm in size. Due to the very narrow electron beam, SEM micrographs have a large depth of field yielding a characteristic three-dimensional appearance useful for understanding the surface structure of a sample [78, 79].

Back-scattered electrons (BSE) are beam electrons that are reflected from the sample by elastic scattering and provide the information from the volume below the surface. Back-scattered electrons signal intensity is strongly dependant on the atomic number of the specimen and therefore BSE images provide information about the distribution of different elements in the sample. BSE together with characteristic X rays are often used as analytical tool in

SEM. Characteristic X-rays are emitted when the electron beam removes an inner shell electron from the sample, causing a higher energy electron to fill the shell and release energy specific for each element. Since energies of the X rays are specific for each element it is possible to identify the composition and measure the abundance of elements in the sample.

electron
beam

10Å Auger electrons

Sample

50-500 Å secondary electrons

backscattered
electrons

characteristic
x-rays

$E = E_c$

$E = 0$

continuum x-rays

secondary fluorescence
by continuum and
characteristic x-rays
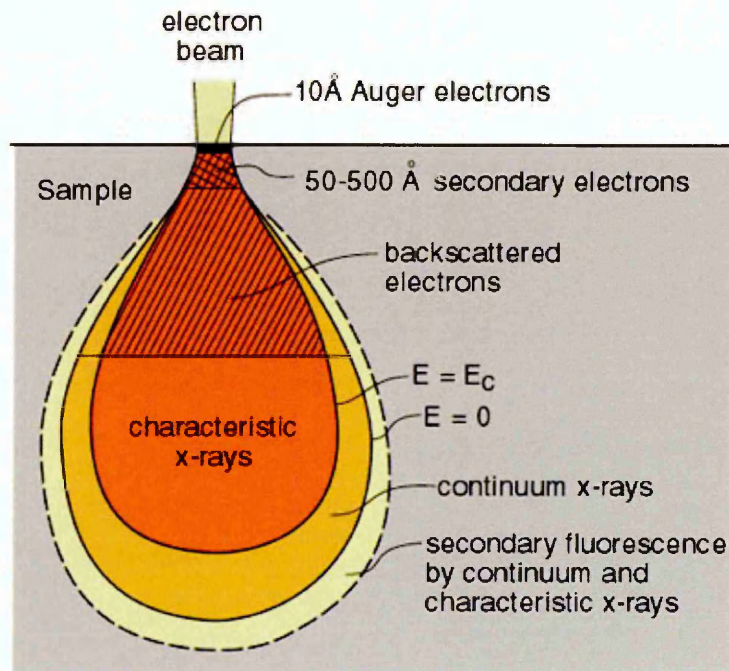
Figure 3.21 The interaction diagram of the electron beam with surface of the sample, adopted from [80]

The schematic view of the SEM is shown on Figure 3.22. Electrons are generated in the electron gun which is usually a filament made of various types of materials. Typically filament is a loop of tungsten which functions as the cathode. A voltage is applied to the loop, causing it to heat up. The anode which is positive with respect to the filament attracts electrons causing electrons to accelerate toward the anode. The air from the SEM interior is evacuated using a vacuum pump that allows electrons to reach the sample without colliding with gas molecules and atoms. When the electron beam passes the anode it reaches the condenser lenses that focus the beam through scanning coils onto the sample surface. Scanning coils is a set of magnets used to deflect the electron beam in x and y directions performing two dimensional scan over the sample surface. The secondary electrons and back scattered electrons created in the interaction between sample surface

70

and electron beam are detected in the SE detector and BSE detector shown on Figure 3.22.
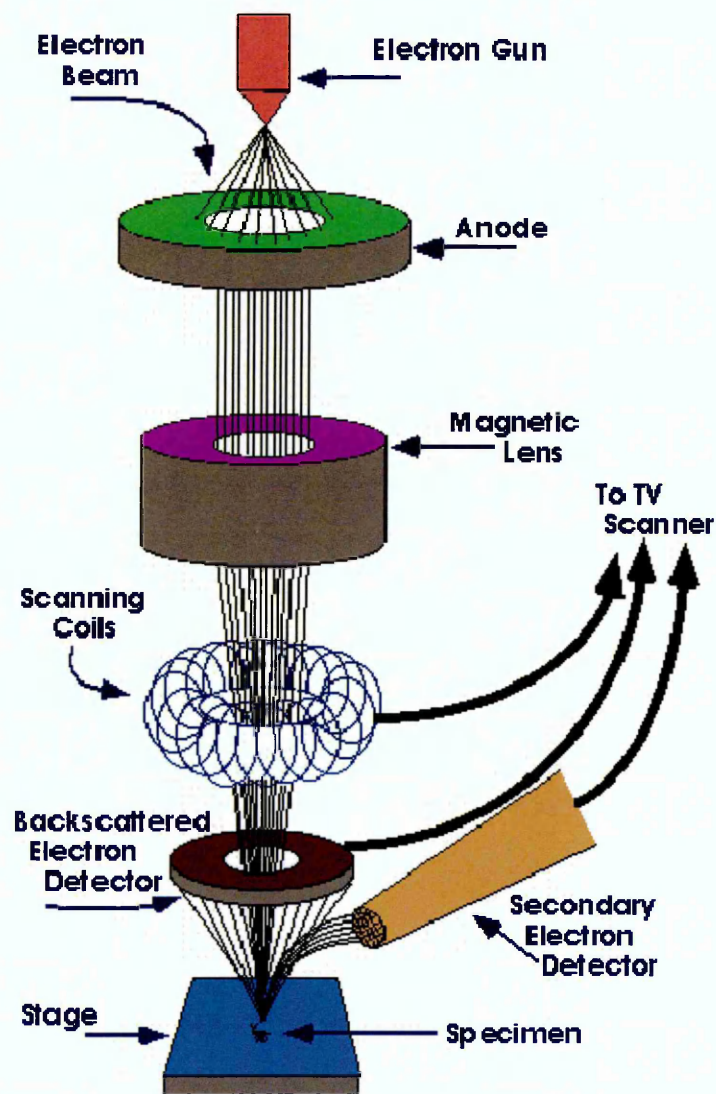
Figure 3.22 Schematic view of the SEM, adopted from [80]

Together with SE and BSE, X rays are emitted from the sample during the interaction between electron beam and sample surface. Apparatus used to measure the energy and intensity of the emitted X rays is energy dispersive X-ray spectroscopy (EDX). EDX is an analytical technique used for the elemental analysis or chemical characterization of a sample. EDX collects the X rays emitted from sample surface, sorts and plots them by energy. Since each element emits X rays at specific set of energies and the intensity of signal is proportional to the number of atoms on the observed surface, it is possible to indentify the elements on the surface and provide quantitative composition of the surface.

Scanning electron microscope FEI Nova NanoSEM was used to record the micrograph of the sample surface. It operates at a low-vacuum using field emission gun to generate electrons. Typical gun voltage was 20 kV and the working distance was 5.7 mm. Results of EDX analysis of deposited coatings and obtained SEM micrographs are presented in chapter 4.5.

3.3.5 Atomic force microscopy
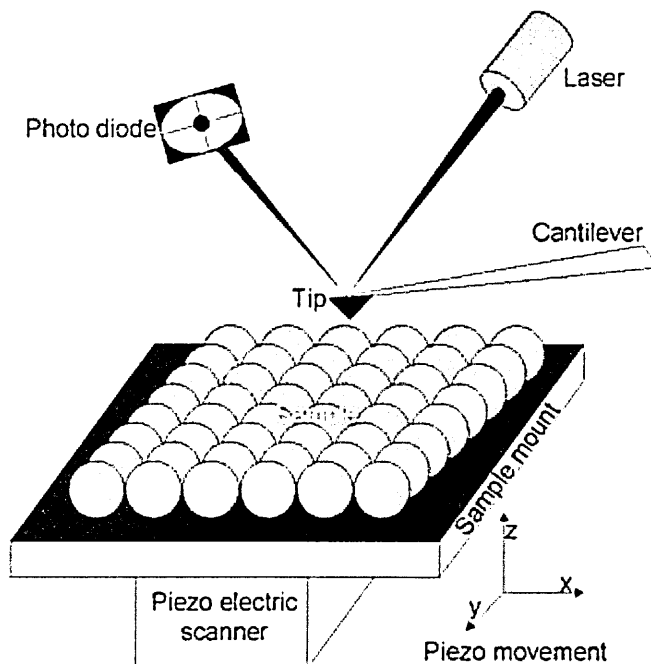
Figure 3.23 Schematic view of the basic working principle of the atomic force microscope, adopted from [82]

Atomic force microscopy (AFM) is a scanning technique used to provide topographic information of the scanned sample surface. AFM can be used to evaluate surface roughness of the sample and to control surface profiles of thin film and coatings. This technique is especially useful for imaging nanoscale surface features as well as accurately measuring their dimensions. The AFM consists of a very fine sensor tip mounted to the end of a small deflecting cantilever that is brought into contact with the sample surface, Figure 3.23. The cantilever has a tip radius of curvature on the order of nanometres. When the tip is brought into proximity of a sample surface, forces between the tip and the sample lead to a deflection of the cantilever. Typically, the deflection is measured using a laser spot reflected from the top surface of

the cantilever into an array of photodiodes. A feedback loop is used to maintain a constant interaction between the probe and the sample. The sensor tip is moved across the surface in order to produce a three-dimensional image of the surface with ultra high resolution using piezoelectric ceramics. The position of the probe and the feedback signal are electronically recorded to produce a three dimensional map of the sample that is either a three dimensional image of the surface or a line profile with height measurements [74, 81].

Atomic Force Microscope mounted on the CSM Indentation Tester was used to record the topography of the sample surface. Observed area was 4.5 µm times 4.5 µm recorded with best available resolution of 512*512 pixels. Results obtained using AFM are presented in chapter 4.5.

CHAPTER 4

Results

4.1 Influence of power on the plasma parameters in HIPIMS plasma discharge

The influence of power on plasma parameters in the HIPIMS plasma discharge was investigated. In order to show the influence of the power on the time evolution of particles and ion to neutral ratio the optical absorption spectroscopy in time resolved mode was used. To understand the influence of power on ion energy distribution function (IEDF) for both metal and Ar ions mass spectrometer was used in both time averaged and time resolved mode. The measurements in time averaged mode provide information on the energies of ions that are constantly arriving to the substrate while time resolved mode provides more fundamental information about the origins of the IEDF shape and the information on each particle life-span between the pulses. A more complete understanding of temporal evolution of ion energies and fluxes in the HIPIMS plasma discharge and knowledge about the influence of power on the HIPIMS plasma discharge demands studies of the fundamental plasma parameters such as plasma and floating potential, and the electron energy distribution function. The latter set of information was measured using Langmuir probe.

Typical discharge current and voltage curves of the HIPIMS plasma discharge are presented on Fig 4.4.1. It shows the typical voltage and target current of the pulse measured at the power supply output as a function of time for the HIPIMS plasma discharge of Ti. The high oscillations of the voltage profile at the start of the pulse appear due to electrical switching and subsequent high frequency ringing sustained by small parasitic capacitance

74

and inductance in the system. The noise picked up 'by the current profile measurement yields the high oscillations of the current profile at the start of the pulse. The time delay between the application of the voltage and the current rise is the so-called statistical time lag before full plasma breakdown can develop [38].
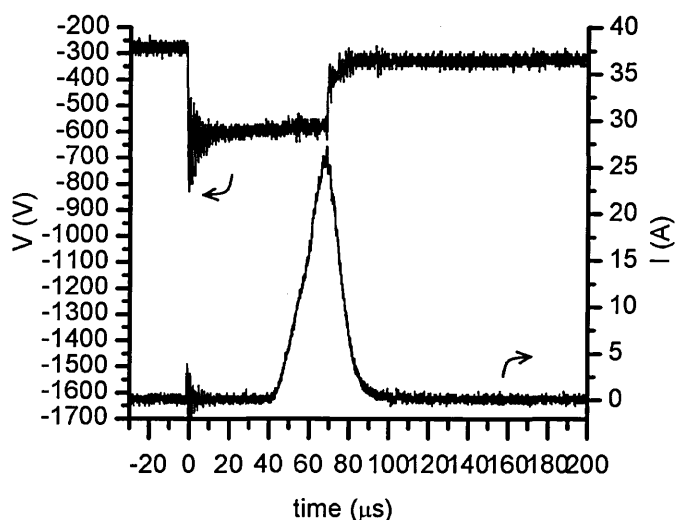
Fig 4.1.1 Typical discharge current (bottom) and voltage (top) curves of the HIPIMS plasma discharge as a function of time, showing HIPIMS plasma discharge of Ti target in Ar at pressure of 0.3 Pa

4.1.1 Dependence of the ion to neutral metal ratio on power in HIPIMS plasma discharge

Optical absorption spectroscopy was used in HIPIMS of Titanium plasma discharge to investigate the time evolution of the metal ion to neutral ratio. The ion to neutral ratio carries information about the ionisation of the plasma and consequently information about the density of the deposited coating. The time resolved measurement of the ion to neutral ratio of Ti provides information about particles impinging on the substrate during the pulse and in the post-discharge.

The results are shown on Figure 4.1.2 as a function of time and for four different peak discharge currents. Ion to neutral ratio was measured from the end of the pulse up to 1 ms from the start of the pulse. The pulse length was 70 μs for measurements up to peak current $I_P = 100$ A and for the $I_P = 150$ A the pulse length was reduced to 50 μs due to restrictions on the power load

onto the target. Discharge currents were 0.6 Acm^{-2} (I_P = 25 A), 1.25 Acm^{-2}(I_P = 50 A), 2.5 Acm^{-2} (I_P = 100 A) and 3.75 Acm^{-2}(I_P = 150 A).

The ion to neutral ratio for the discharge with peak current of 25A up to 150 μs has a value of 3 with large error bars and after 150 μs the value including the error bars is between 1 and 2. After 600 μs neutral Ti becomes dominant species and the ratio falls below 1 reaching 0.5 at 1 ms. Discharge with peak current of 50 A up to 150 μs has a value between 3 and 4 and in the period from 150 μs to 1 ms it is reduced from 2 to 1. The results for the discharges with peak current of 100 A and 150 A are very similar probably due to limit of the power supply that limited the duration of the pulse to 50 μs during the discharge with peak current of 150 A that resulted in equal amount of power delivered into the system for these two plasma discharges. From 100 μs up to 800 μs the ion to neutral ratio decreases from 3 to 2, indicating that shortly after the pulse the ionisation is 75% and at 800 μs from the start of the pulse the ionization of the metal particles is 66%. At last measured point at 1 ms the ratio was 1.5 for peak current of 150 A discharge and 1.8 or peak current of 100 A discharge.

The ion to neutral ratio is higher due to high density of electrons created as secondary electrons emitted from the target during the pulse. High density of electrons increases the ionisation process resulting in high density of ions and high ion to neutral ratio. In the post-discharge the metal ions obey ambipolar diffusion [20] and are being lost to the chamber walls reducing the density of metal ions resulting in lower ion to neutral ratios in the post discharge. Increasing the discharge power the density and energy of secondary electrons is increased leading to higher ion density with higher peak discharge currents.

The high error bars of the results shortly after the end of the pulse are consequence of high intensity of light from the plasma. During the pulse intensity of plasma is few orders of magnitude higher than intensity of lamp therefore the standard deviation of the calculated absorption coefficient was comparable with mean value. Calculating ion to neutral ratio the standard deviation turned out to have bigger value then the signal. For this reason ion to neutral ratio could be calculated only in the post-discharge when the signal from the plasma was comparable to the signal from the lamp.
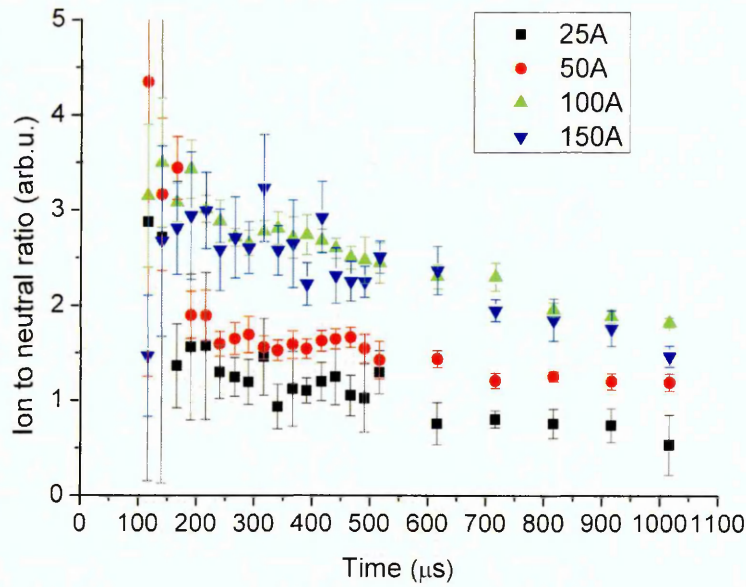
Figure 4.1.2 Ion to neutral ratio as a function of time for four peak discharge currents in HIPIMS plasma discharge of Ti at pressure of 2.7 Pa

4.1.2 The influence of power on ion energy distribution function (IEDF) in HIPIMS plasma discharge and origins of the IEDF constituents

The origins of the IEDF shape were suggested in literature [46, 31]. A low energy main peak originates from completely thermalised ions collected with an energy given by the difference between the plasma potential and the ground potential of the orifice. A high energy tail originates from sputtered metal ions or could be generated by reflection from the target. A first attempt to simulate experimental data with a sum of Maxwell and Thompson distributions is given in Figure 4.1.3. Maxwell and Thompson distributions are chosen since it was suggested by Thompson [83] that energy of atoms sputtered from the target has distribution;

$$F_T(\varepsilon) \approx \frac{\varepsilon E_b}{(\varepsilon + E_b)^3}$$

$$(4.1.1)$$

where E_b is the binding energy of metal atoms within the target and ε is the ion kinetic energy. Maxwellian distribution [37];

$$F_M(\varepsilon) \approx C \sqrt{\frac{\varepsilon}{(k_B T)^3}} \exp(-\varepsilon/k_B T)$$

$$(4.1.2)$$

77

is a distribution of thermalised Ar atoms, where k_B is the Boltzmann constant, T is temperature of the thermalised Ar gas and C is the constant. The IEDF should comprise of metal ions with Thompson distribution sputtered from the target and Maxwell distribution of metal ions thermalised through elastic collisions with Ar particles.
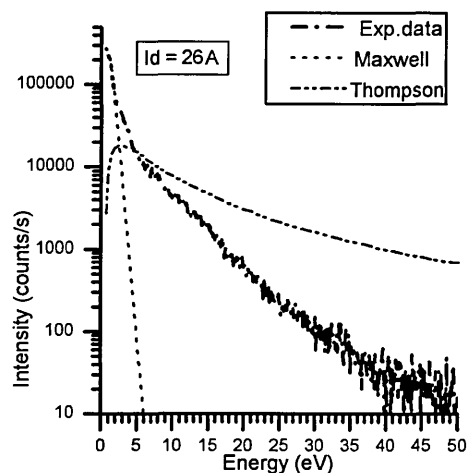
Figure 4.1.3 Ion energy distribution function for Cr^+ ions fitted with sum of Maxwell and Thompson measured in HIPIMS plasma discharge of Cr in Ar at pressure of p = 0.29 Pa, peak current 26 A and pulse duration 70 μs

Figure 4.1.3 shows that the main peak could be fitted accurately to a Maxwellian distribution up to 5 eV. However at higher energies, the experimental data had a much steeper fall-off than predicted by the Thompson distribution for the given parameters. The mass spectrometer orifice is situated 150 mm away from the target and the mean free path of chromium ions is around 70 mm, signifying that each ion undergoes at least 2 collisions before it is detected in the mass spectrometer. In these conditions, we could expect a partially thermalised, i.e. randomized, Thompson distribution. Depending on the reduced mass ions will need more collisions to thermalise. Taking this conclusion into account it should be possible to fit the experimental data with the sum of two Maxwell distributions.

The IEDFs of the single and double charged metal and Ar ions were measured. The origin of both can be explained as follows. Metal atoms are sputtered from the target as a result of the impact of Ar and metal ions. The sputtered metal atoms then diffuse away from the target and, due to collisions with electrons trapped in the magnetic field of the magnetron, are ionized in the dense plasma region. The resulting ions have practically the same energy as the atoms prior to ionisation. The IEDF of metal ions is thus partly

78

determined by the sputtering process. The energy distribution of sputtered metal atoms is described by the Thompson distribution (Eq. 4.1.1). Sputtered metal ions travelling from the target to the substrate undergo elastic collisions with Ar atoms and ions, which have kinetic energy equal to the room temperature, whereby metal ions lose kinetic energy and thermalise. The mean free path for metal ion-gas atom collisions can be estimated as 70 mm at 0.29 Pa and 7 mm at 2.67 Pa.

Gas atoms are thermalised and therefore the expected IEDF is given by the Maxwellian:

$$F_M(\varepsilon) \approx C_1 \sqrt{\frac{\varepsilon}{(k_B T)^3}} \exp(-\varepsilon / k_B T)$$

(4.1.4)

where C_1 is a constant. To successfully reproduce experimental data with a Maxwell distribution, $k_B T$ and constant C_1 must be known or derived from fitting. The quantity $k_B T$ could be defined as "effective ion temperature". In order to reduce the number of fitting parameters, we have determined $k_B T$ from the probability function. The procedure was proposed by Godyak et al. [67] who performed similar analysis for an electron energy probability function. Rao et al. [34] proposed a similar technique for IEDF analysis to determine effective ion temperature. The ion energy probability function (IEPF) is given by expression

$$f(\varepsilon) = \varepsilon^{-1/2} F(\varepsilon)$$

(4.1.5)

where $F(\varepsilon)$ is the ion energy distribution function (IEDF). Assuming a Maxwellian IEDF and combining (4.1.4) and (4.1.5), the logarithm of equation (4.1.5) is given by a linear expression

$$\ln f(\varepsilon) = \ln c - 1.5 \ln k_B T - \varepsilon / k_B T$$

(4.1.6)

where c is a constant. $k_B T$ can be determined from the slope of the straight line $\ln(f(\varepsilon))$ vs. ε.

Values of effective ion temperature $k_B T$ are then inserted in Equation 2 and the constant C_1 is determined by a least squares fit to the experimental data.xperimental data containing two ion distribution functions may be approximated by the sum of two Maxwellian distributions;

$$F(\varepsilon) \approx C_1 \sqrt{\frac{\varepsilon}{(k_B T_1)^3}} \exp(-\varepsilon / k_B T_1) + C_2 \sqrt{\frac{\varepsilon}{(k_B T_2)^3}} \exp(-\varepsilon / k_B T_2)$$

(4.1.7)

4.1.2.1 Influence of peak current and pressure on the IEDF of metal ions

Measured IEDFs of Cr^+ ions for three different peak currents are shown in Figure 4.1.4 (at low pressure p = 0.29 Pa) and Figure 4.1.5 (at high pressure p = 2.67 Pa). The calculated fitted curves comprising the two Maxwellian functions as well as the individual functions are given as well. Pulse duration of 70 µs and frequency of 100 Hz was kept constant for all discharges presented in this section.

Figure 4.1.4 Ion energy distribution functions for Cr^+ ions at the lower pressure of p = 0.29 Pa for different peak target currents a) 14 A, b) 26 A and c) 40 A. The thick dash-dot line represents experimental data. The thick solid line represents the sum of two Maxwell distributions; the thin short dashed for the first Maxwellian and the thin dash dot line for the second Maxwellian.

Figure 4.1.5 Ion energy distribution functions for Cr^+ ions at the higher pressure of p = 2.67 Pa for different peak target currents a) 14 A, b) 26 A and c) 40 A. Legend is as for Figure 4.1.4.

By increasing the peak current from 14 A to 40 A and the voltage from 788 to 1489 V, the relative number of high energy ions compared to low energy peak is increasing steadily with current as shown for low pressure in Figure 4.1.4. However, the effective ion energy (slope and peak position) of the high energetic group does not change significantly. Thus the average energy of IEDF increases with peak current due to the increased number of high energy ions. The values of average energy will be shown and discussed in subsequent sections. At high pressure (Figure 4.1.5) the increase of high energy tail with increasing peak current can still be observed, but to a lesser

extent than for the low pressure. The width of main peak goes up to 5 eV for low pressure (Figure 4.1.4) but only up to 2 eV for high pressure (Figure 4.1.5).

To further clarify the origins of the IEDF of metal ions, time resolved measurements were analysed at low pressure, p = 0.29 Pa, and at 40 A peak current. Figure 4.1.6 shows a comparison of time-averaged measurement and two time-resolved measurements taken close to the peak of the pulse (100-120 μs after voltage pulse) and in the afterglow (at a time delay of 320-1200 μs). At the time when the peak current reaches its highest value, between 60 and 80 μs the IEDF of Cr^{1+} ions consists of only high energy tail with average energy of 13 eV. In contrast, at 320 μs after the start of the pulse, the IEDF of Cr^{1+} ions consists of only low energy peak with a slope quite similar to the slope of the time-averaged measurements. The IEDF diminishes steadily until no more Cr^{1+} ions are detected at 1200 μs after the start of the pulse. This comparison clearly demonstrates that ions generated during the pulse contribute to the high energy tail. Ions detected in the after-glow contribute to the low energy main peak.

Figure 4.1.6 Time resolved measurements of the HIPIMS Ion energy distribution functions for Cr^+ ions at 0.29 Pa and 40 A peak current, compared with time-averaged measurement. Hollow circles represent Cr IEDF between 100 and 120 μs after the start of the pulse, hollow squares represent Cr IEDF between 230 and 1200 μs and hollow triangles represent time-averaged Cr IEDF.

It is apparent from Figure 4.1.4 and Figure 4.1.5, that calculated sum of two Maxwell distributions (equation (5)) fits well with the experimental data. At higher currents, however a small portion of highly energetic ions (up to 1000 counts/s) is detected which cannot be described by two Maxwellian distributions. Time-resolved studies have shown that these high energy ions are generated during the pulse indicating that they gain energy in the cathode voltage fall. These ions may stem from a number of sources. For example, ions accelerated in the cathode fall due to high electrical fields may be neutralised upon contact with the surface [36] or they may be reflected into the chamber with high energies. The probability of reflection is proportional to the reduced mass of the incident ion and target and is 0.18 for Ar ions on W target [2]. In the case of self-sputtering, characteristic of HIPIMS, the reduced mass is lower and the probability of reflection may be reduced. These fast neutrals may then be ionised when passing through the dense plasma region with a low probability due to the short time they spend in the dense plasma region. Such reflected and ionised species may indeed retain a relatively high energy during transport to the substrate and mass spectrometer and could be a reason.

The low energy peak originates from metal ions that are completely thermalised in collisions with Ar atoms and ions. The energy of the main peak maximum is known to be strongly dependent on plasma potential [27, 51]. Time resolved Langmuir probe measurements near the substrate at low pressure (Figure 4.1.7) show that, at its peak value, the plasma potential is approximately +3 V and quickly falls to +1 V after the pulse. The maximum in plasma potential occurs simultaneously with the maximum in discharge current (Figure 2.9) signifying that the majority of ions are generated at maximum plasma potential. The energy of the IEDF peak in measurements presented in this work agrees well with the measured plasma potential.
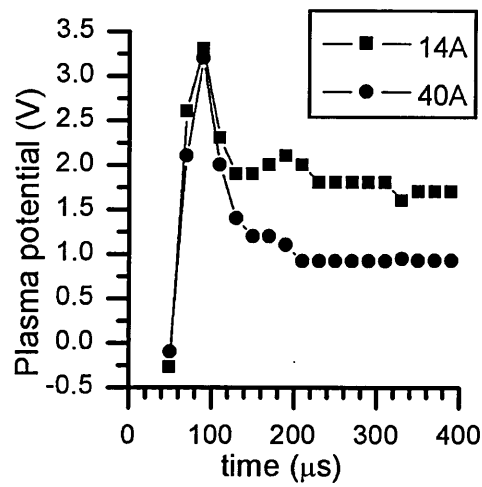
Figure 4.1.7 Plasma potential as a function of time, of Ti HIPIMS at low pressure of 0.29 Pa for two peak currents 14A and 40A

The values of effective ion temperature for first Maxwell distribution, marked as k_BT_1, are given in table 4.1.1. Comparing values of the first Maxwell distribution for Cr^+ and Ar^+ at high pressure it can be seen that the effective ion temperatures are very similar which indicates complete thermal equilibrium with the two ions due to the high number of collisions. At low pressure k_BT_1 for Cr^{1+} is factor 3 greater than for Ar^{1+} pointing to a highly non-equilibrium plasma.

The high energy tail of the IEDF can be approximated with a second Maxwell distribution with k_BT_2 with typical values of 3 eV as given in Table 1. High energy ions are created by electron impact ionisation from sputtered atoms that have a Thompson energy distribution upon ejection from the target. Passing through the plasma, ions are thermalised through collisions with other atoms and ions. The second Maxwell distribution could be attributed to partially thermalised sputtered metal ions. A significant drop in second Maxwellian distribution function can be seen as the pressure is increased. At high pressure ions undergo more collisions than at low pressure and by the time they reach the mass spectrometer, ions are almost completely thermalised.

The clear separation between the hot and cold distributions could be explained by their origin in the different temporal stages of the pulse. Since the measurements are time averaged, ions detected both during the pulse and between pulses are recorded. The distance from the target to cathode is 150 mm and, as mentioned before, the mean free path for metal ion-Ar ion collision is about 70 mm at p = 0.29 Pa, and 7 mm at p = 2.67 Pa . During the pulse,

84

there is significant rarefaction of the process gas close to the target due to the high applied power [26]. Thus metal ions diffusing from the target probably collide more often with metal atoms and ions than with Ar atoms and ions. Collisions between metal atoms and ions result in a small energy loss because energy distribution of metal atoms and metal ions is similar. Energy loss in metal-Ar collisions is greater since the IEDF of Ar atoms and ions doesn't contain high energy tail. Thus, during the pulse, metal ions are being partially thermalised therefore retaining the high energy tail described with the second Maxwellian distribution. This is consistent with measurements of Böhlmark et al [29]. After the pulse, equal gas pressure is restored inside the chamber. Thermalised metal ions collide equally with Ar and metal atoms and ions. The collision energy loss is greater, hence metal ions reaching and detected by the spectrometer produce the main low energy peak.

Langmuir probe measurements [9] suggest that the density of metal ions at high pressure is slightly abating after the pulse and the density of metal ions at low pressure is maintained at some 10% of peak value at 330 µs after the pulse. Comparing effective ion temperatures of Cr^+ and Ar^+ ions in table 4.1.1, it can be seen that, for high pressure, the values of effective ion temperature are similar, but at low pressure the values of k_BT are higher for metal ions than for Ar ions. Metal ions at high pressure have long lifetimes and undergo many collisions. On the other hand, metal ions at low pressure have shorter lifetimes due to less frequent collisions at lower pressure which may lead to greater losses to the chamber walls.

Low pressure (p = 0.29 Pa)			High pressure (p = 2.67 Pa)		
$I_d(A)$	k_BT_1 (eV)		$I_d(A)$	k_BT_1 (eV)	
	Cr	Ar		Cr	Ar
14	0.347	0.168	14	0.128	0.130
26	0.436	0.147	26	0.127	0.150
40	0.383	0.321	40	0.160	0.187
$I_d(A)$	k_BT_2 (eV)		$I_d(A)$	k_BT_2 (eV)	
	Cr	Ar		Cr	Ar
14	3.563	2.618	14	1.032	not detected
26	4.200	2.530	26	1.061	not detected
40	4.878	2.049	40	1.115	not detected

Table 4.1.1 Values of effective ion temperature for the first Maxwell distribution (k_BT_1) and for the second Maxwell distribution (k_BT_2) for three different peak currents (14 A, 26 A and 40 A) and for low pressure (p = 0.29 Pa) and high pressure (p = 2.67 Pa)

4.1.2.2 Influence of peak current and pressure on the IEDF of Ar gas ions

A high energy tail can be observed in the Ar^+ IEDF at low pressure (Figure 4.1.8). High pressure measurements of the Ar^+ IEDF show no high energy tail (Figure 4.1.9). In contrast to IEDF for metal ions, an additional "shoulder" is seen. This shoulder exists both at low and high pressure (Figure 4.1.8 and Figure 4.1.9) and can be described with third Maxwell distribution. A similar shoulder was observed in other works as well [29, 31, 46].
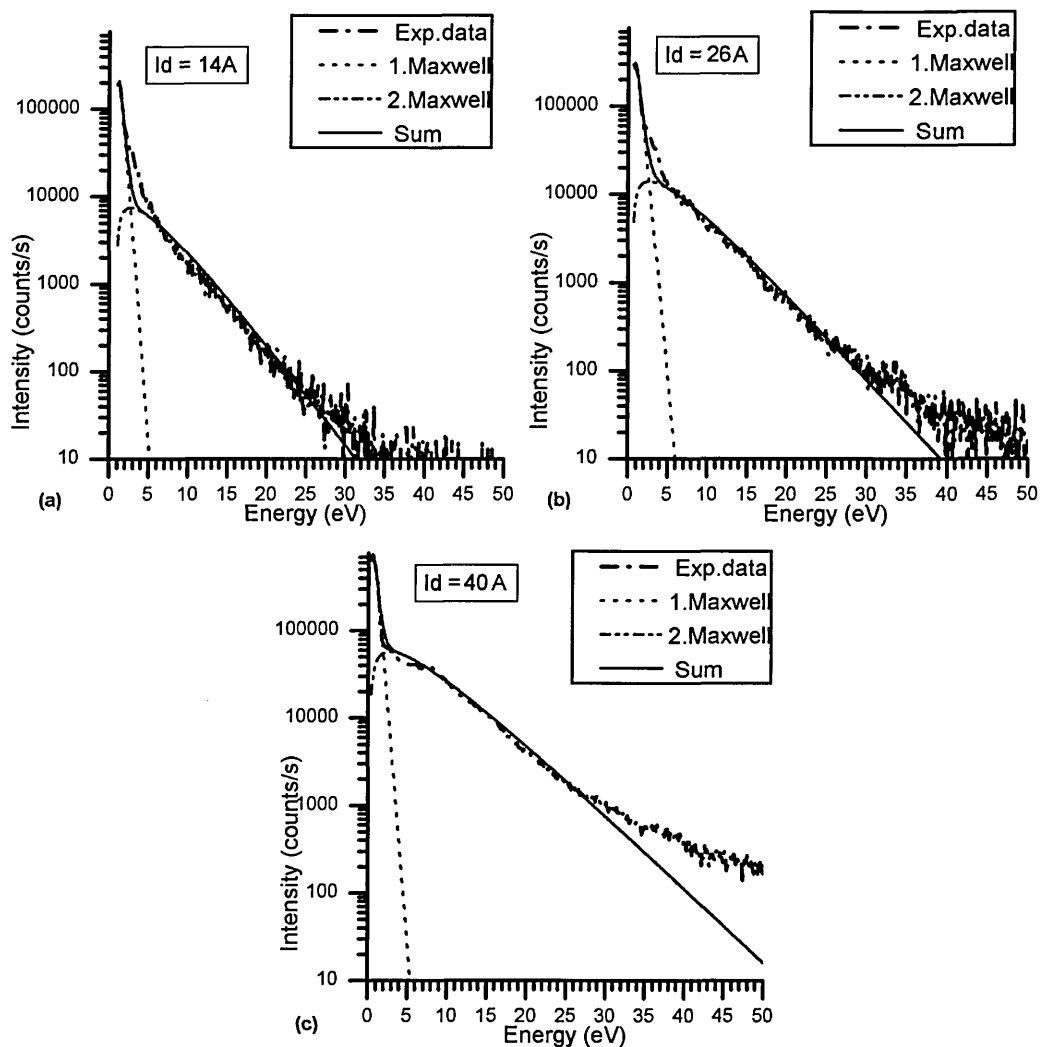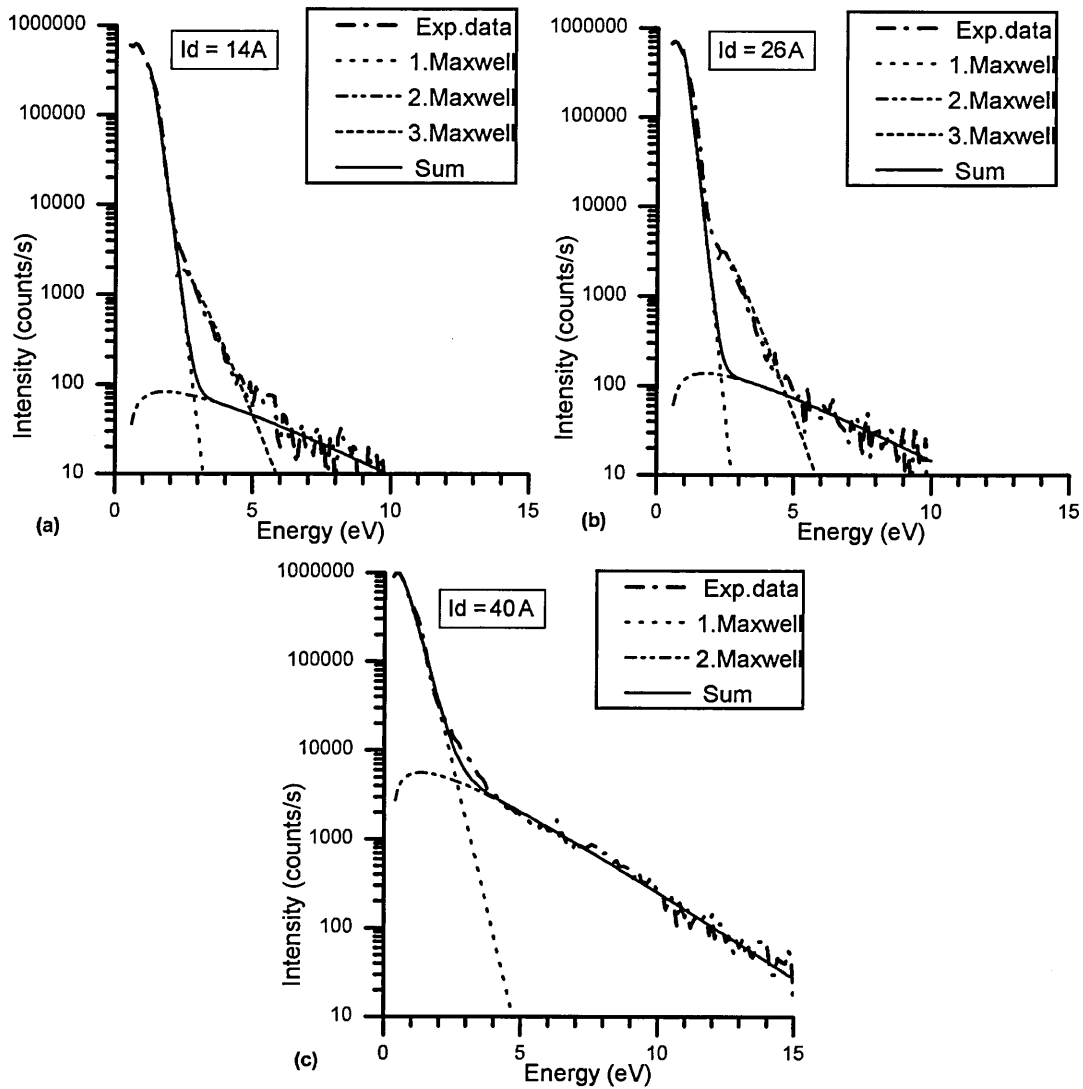
Figure 4.1.8 Ion energy distribution functions for Ar$^+$ ions at the lower pressure of p = 0.29 Pa for different peak target currents a) 14 A, b) 26 A and c) 40 A. Legend is as for Figure 4.1.4.
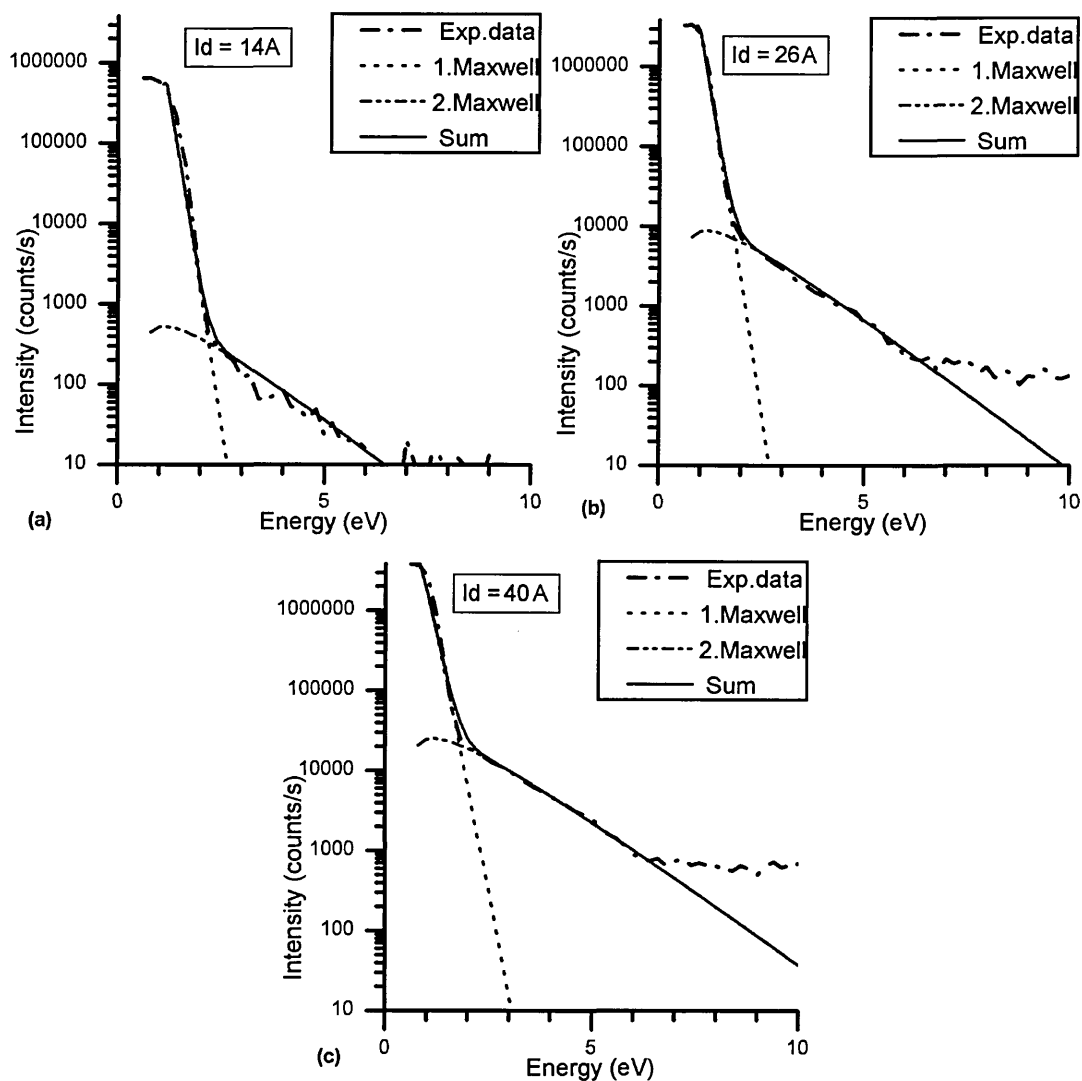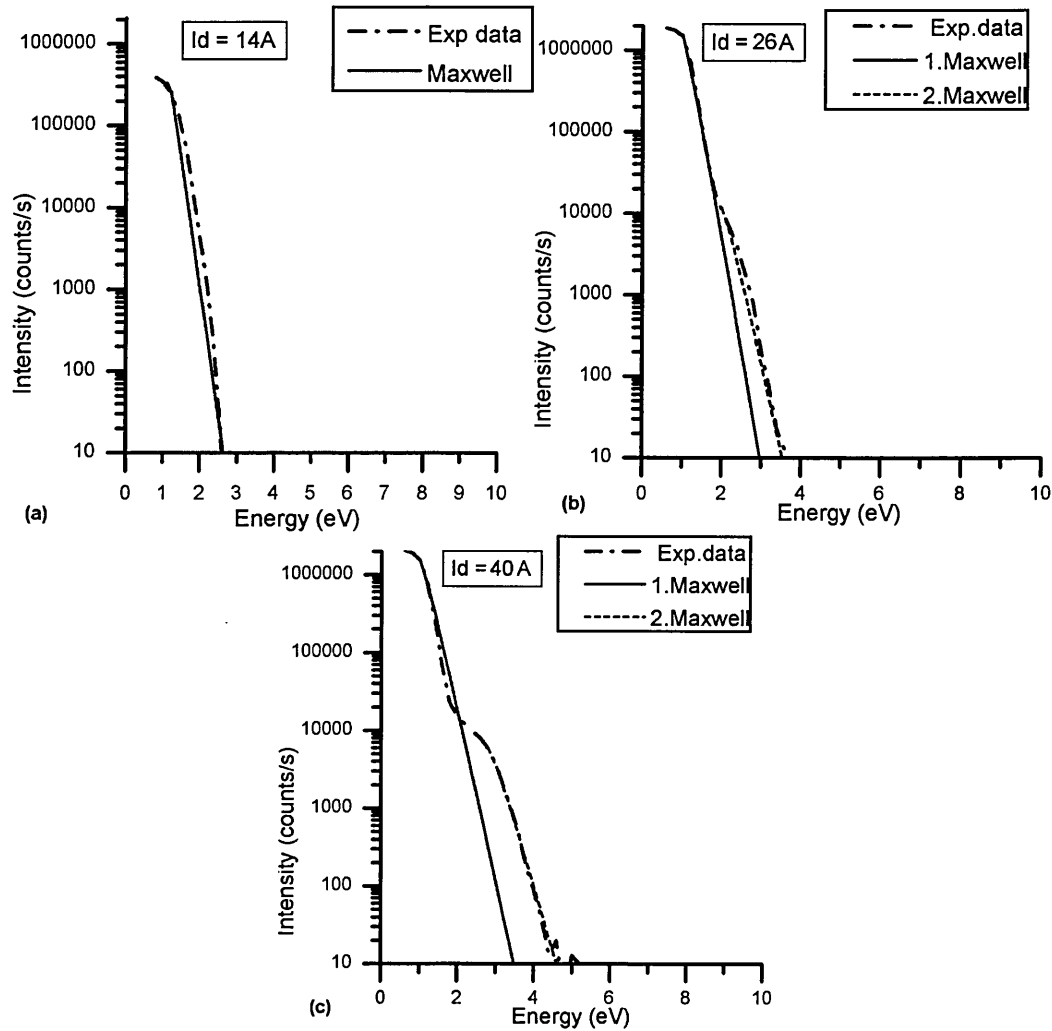
Figure 4.1.9 Ion energy distribution functions for Ar^+ ions at the higher pressure of p = 2.67 Pa for different peak target currents a) 14 A, b) 26 A and c) 40 A. Legend is as for Figure 4.1.4.

To understand the origin of the shoulder time resolved measurements were made. On Figure 4.1.10 time-averaged measurements are compared with time-resolved measurement done at low pressure, p = 0.29 Pa, and at 40 A peak current. The figure shows that the shoulder at ~2 eV and high energy tail in the time-averaged IEDF originates from the period spanning the beginning and shortly after the pulse, 100 µs to 120 µs, and is a result of a shockwave from gas rarefaction [26, 19]. The energy tail detected up to 12 eV in the time 100-120 µs can be attributed to gas heating due to interaction with the sputtered metal and by reflected neutrals. The energy of the peak of the IEDF of ~2 eV is relatively high and can be attributed to the partial thermalisation of the high energy tail. This effect is additionally slowed down by gas rarefaction. It is important to note that this value also corresponds to

the plasma potential determined by Langmuir probes at that time shown in Figure 4.1.7. Within the next 60 µs, the Ar IEDF at 220 µs to 240 µs transforms into a single low energy distribution indicating that the ions have been thermalised. This could be attributed to a fast energy relaxation afforded by the fact that the power input to the plasma and the corresponding heating of ions have ceased. The low-energy IEDF was observed up to 5 ms in the post-discharge.
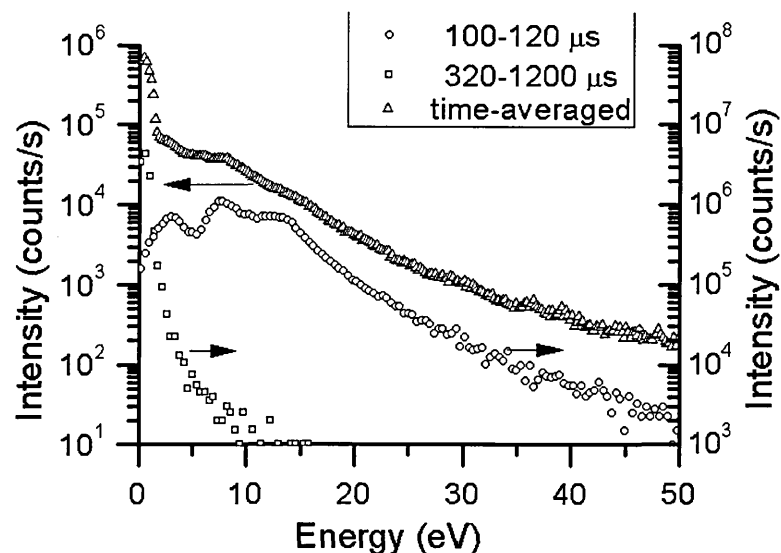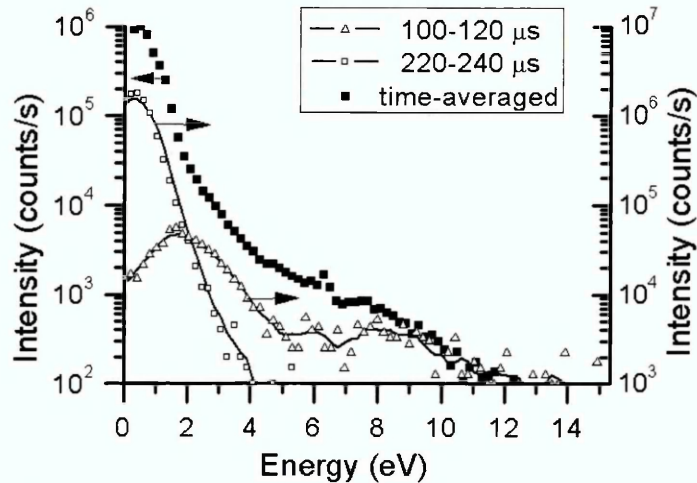

Figure 4.1.10 Time resolved measurements of the HIPIMS Ion energy distribution functions for Ar+ ions at 0.29 Pa and 40 A peak current, compared with time-averaged measurement. Hollow triangles represent Ar IEDF between 100 and 120 µs after the start of the pulse, hollow squares represent Ar IEDF between 220 and 240 µs and solid squares represent time-averaged Ar IEDF. Time resolved measurements are connected with the smoothing line to ease the data recognition on the figure.

4.1.2.3 Influence of power on the average energy of ions and metal ion-to-gas ion ratio

Figure 4.1.4 indicates that the number of high energetic ions and maximum value of Cr+ IEDFs is increasing with increasing peak current. To clearly demonstrate the increases of proportion of high energetic ions it is convenient to plot the ratio of second Maxwell distribution integral to the integral of the whole IEDF as a function of peak current. A second method is to plot the average energy of an experimental data as a function of peak current.
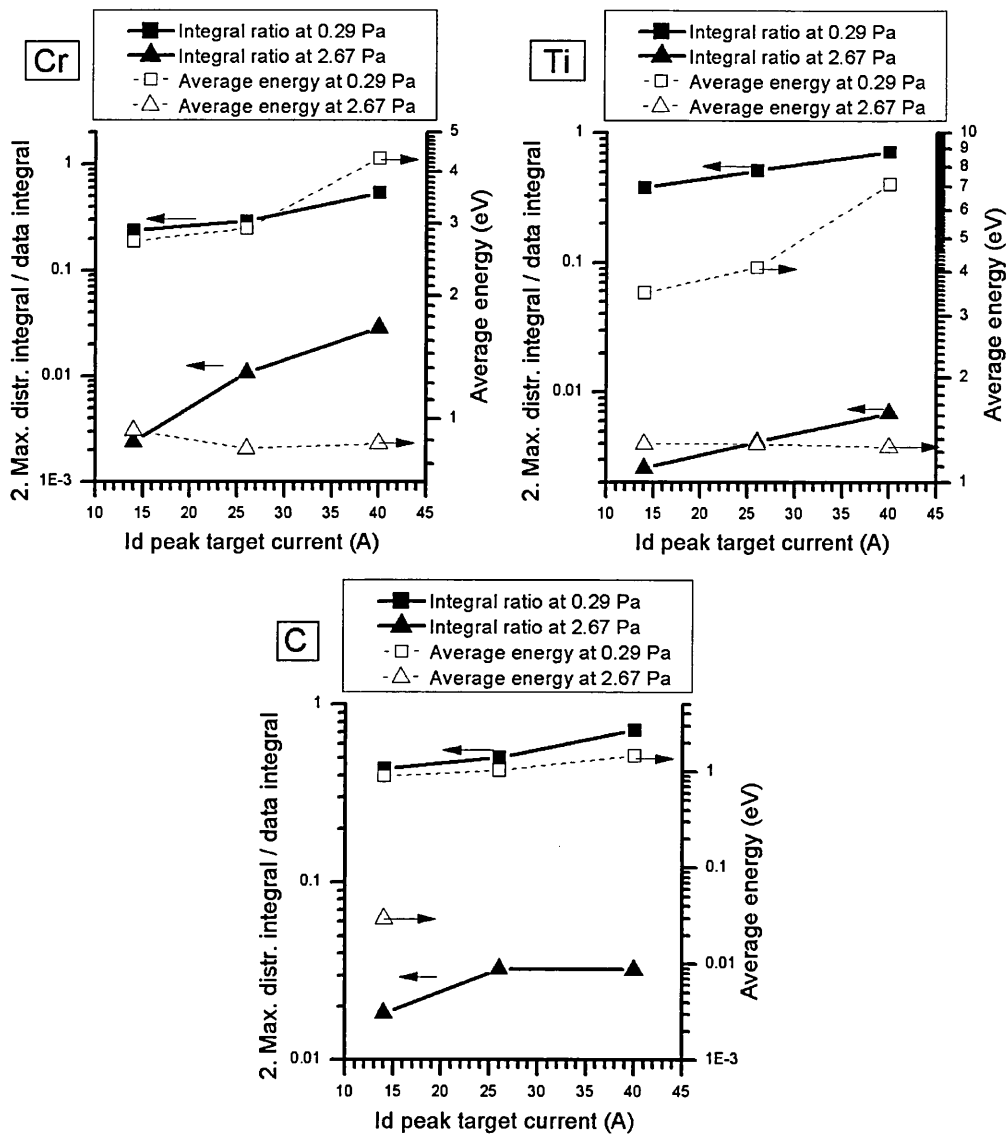
Figure 4.1.11 Ratio of second Maxwell distribution integral to experimental data integral (solid line) and average energy of experimental data (dashed line) as a function of the peak target current for three different targets a) Chromium, b) Titanium and c) Carbon

Figure 4.1.11 a, b, and c, show the integral ratio and average energy as a function of peak current for Chromium, Titanium and Carbon respectively. Squares represent data at lower pressure (p = 0.29 Pa) and triangles represent data for high pressure (p = 2.67 Pa). For Cr and Ti at low pressure, an increase of both integral ratio and average energy with higher current is visible. This could be attributed to gas rarefaction that is increasing as a function of power and thus reduces collisional losses of sputtered atoms and ions and promotes their transport to the substrate. Another possibility is that the ions reflected from the target contribute to the high energy tail and thus

increase the average energy. These results indicate that by increasing the power, the energy delivered to the growing films by ion bombardment is increased. The average energy of C ions is significantly lower indicating their quick thermalisation on account of their small reduced mass in collisions with Ar. The influence of discharge current is negligible as this case is completely dominated by collisional cooling. A similar effect is observed for all materials at high pressure - IEDFs appear thermalised and again no effect of current can be recognized.

Important parameter information for film growth is the proportion of metal ions to gas ions in plasma. Figure 4.1.12 shows the metal ion-to-gas ion ratio ($J(Me^+)$ / $J(Ar^+)$) as a function of peak current, for three different materials. The proportion of metal ions in the plasma is rising exponentially with peak current.
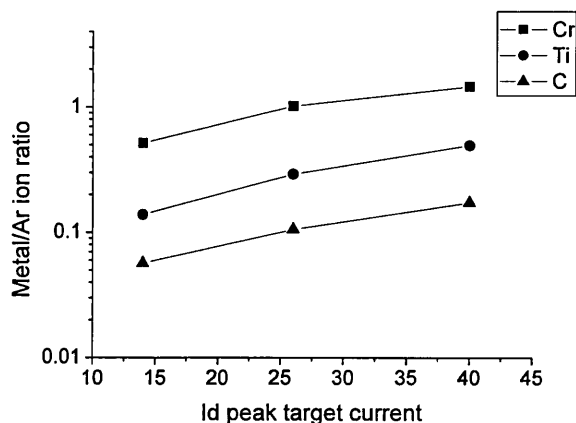
Figure 4.1.12 Metal ion-to-gas ion ratio as a function of peak current at low pressure for three elements (Cr, Ti and C)

Chromium has the highest $J(Me^+)$ / $J(Ar^+)$ ratio of 1 at Id = 40 A and Carbon has the lowest $J(Me^+)$ / $J(Ar^+)$ ratio of 0.09 at Id = 40 A. The sputter yield for Chromium is 1.18, for Titanium is 0.51 and for Carbon is 0.12, for Ar^+ ions at 500 eV [36]. Since metal ions and carbon have lower ionisation potential (6.76 eV, 6.82 eV and 11.26 eV for Cr, Ti, and C respectively) than Ar (IP = 15.76 eV), they are ionised readily in the plasma. If the sputter yield is high, the relative density of metal atoms and ions is increased whilst the density of Ar ions and atoms remain constant or are depleted due to rarefaction. Thus elements with higher sputter yield will have higher $J(Me^+)$ /

91

$J(Ar^+)$ ratio which is in agreement with the experimental observation. The error of presented measurements is in range ± 8 %.

4.1.3 Plasma parameters dependence on power and pressure measured with electrostatic probes

The influence of power and working gas pressure on ion current arriving to the substrate was measured using flat probe. The ion saturation current was evaluated using time resolved measurements with a flat probe positioned next to the entrance of the mass spectrometer at distance of 17 cm from the target. Measurements were performed for two pressures, 0.29 Pa and 2.90 Pa. Pulse duration was set to 70 μs and frequency was 100 Hz.

The results of the ion saturation current at high pressure are presented on Figure 4.1.13 a). As expected the peak ion current grows with the power reaching the maximum of 6 mA at 40 A peak discharge current. The shape of ion current resembles the shape of the current discharge on the target, shown on Figure 4.1.14 a). The position of the ion current peak in time depends on the power. At lowest measured power of 10 A the peak was reached at the end of the pulse at 70 μs while at 40 A the peak was reached at 35 μs from the start of the pulse. The position of the peak could be explained with the shape of discharge current that shows has a peak value at around 60 μs at 10 A discharge and at 40 A discharge the peak occurs at 40 μs. It indicates that the ion saturation current closely follows the shape of the discharge current.

Figure 4.1.13 b) shows ion saturation current at low pressure. The ion saturation current doesn't follow the shape of the discharge current, shown on Figure 4.1.14 b), but it arrives to the flat probe shifted in the time for 10 μs after the end of the pulse. The position of the ion energy peak in time does not change with power, rather the intensity shows strong dependence on power increasing from 4 mA at 10 A peak discharge current up to 13 mA at 40 A.
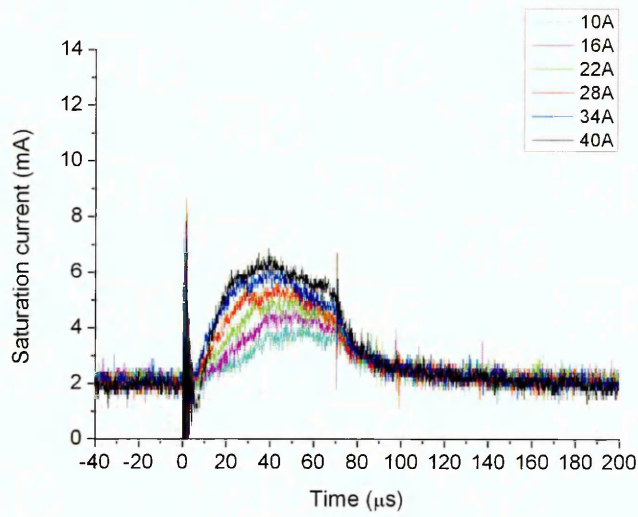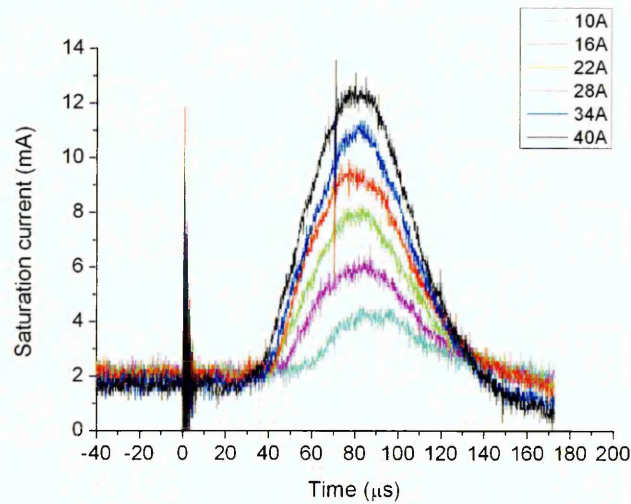
Figure 4.1.13 Ion saturation current measured with flat probe at a) pressure of 0.29 Pa and b) pressure of 2.9 Pa as a function of peak current, in HIPIMS plasma discharge with Cr target

One possible explanation for the different ion saturation current shapes at low and high pressure could be that the transport of the ions strongly depends on the existence of ions in the space between target and substrate, postulated by Konstantinidis et al. [14]. It could be that at high pressure ions from preceding pulse can be still found in the plasma that enables fast transport of ions and rise of ion saturation current with discharge current. At low pressure, in the beginning of the pulse no ions from preceding pulse lead to reduced transport and delayed start of saturation current compared to discharge current. Second explanation is that the ions collected with the flat probe at high pressure, due to high rate of collisions with surrounding gas, are

found at the position of the flat probe simultaneously with discharge current that is proportional to the rate of sputtering process at the target. The position of the probe is not directly in direction of sputtered particle velocity direction defined by cosine law. At low pressure the mean free path of ions is around 7 cm therefore the bulk of ions need more time to change their velocity direction to arrive to the region where the flat probe is positioned.

a)

b)
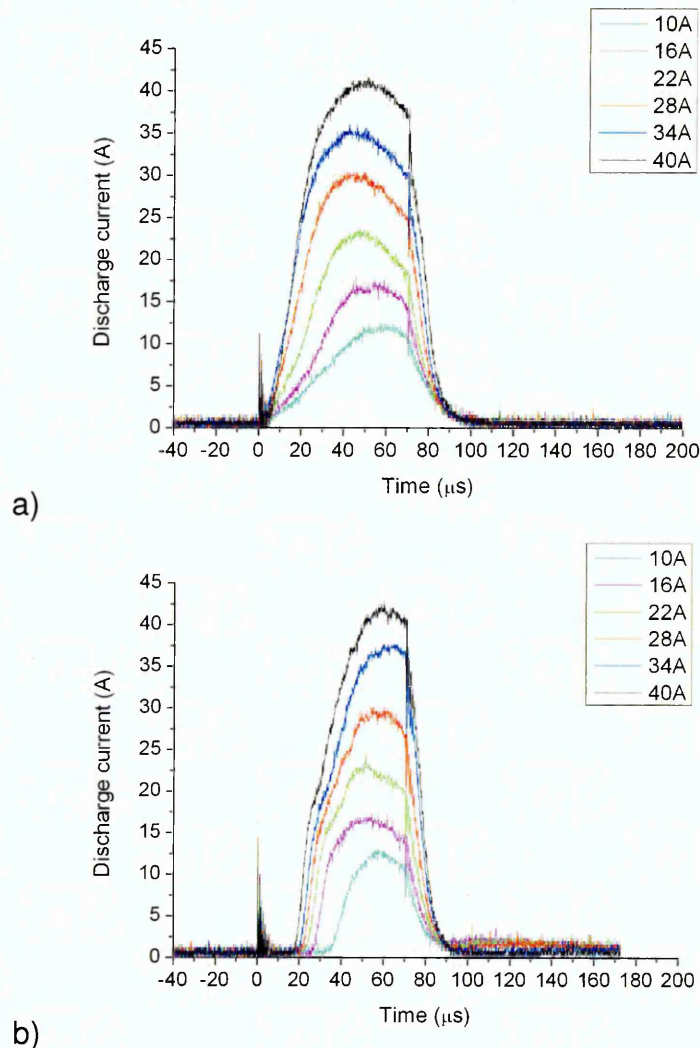
Figure 4.1.14 Discharge current for different peak currents as a function of time at a) 2.9 Pa and b) 0.29 Pa, in HIPIMS plasma discharge with Cr target

During the HIPIMS discharge with peak current of 10 A the ion saturation current at both low and high pressure was 4 mA. Increasing the peak current up to 40 A at high pressure the ion saturation current increased up to 7 mA while at low pressure ion saturation current increased to 13 mA. Lower saturation current at high pressure compared to low pressure measurements could be the consequence of higher thermalisation and

deflection of metal ions due to high pressure of working gas and short mean free path which is calculated to be around 1 cm.

Disconnecting the flat probe from the power supply and record the output of the flat probe it was possible to measure the floating potential of the plasma. Figure 4.1.15 shows the floating potential in the HIPIMS plasma discharge at high pressure of 3 Pa. The floating potential drops with the increase of the discharge current and reaching -11 V at peak discharge current of 10 A at 44 μs from the start of the pulse, up to -12 V at peak discharge current of 40 A at 18 μs from the start of the pulse. Apart from the change of the floating potential peak time with power, the rate of floating potential increase in the post discharge is faster at high powers and slow at low powers.
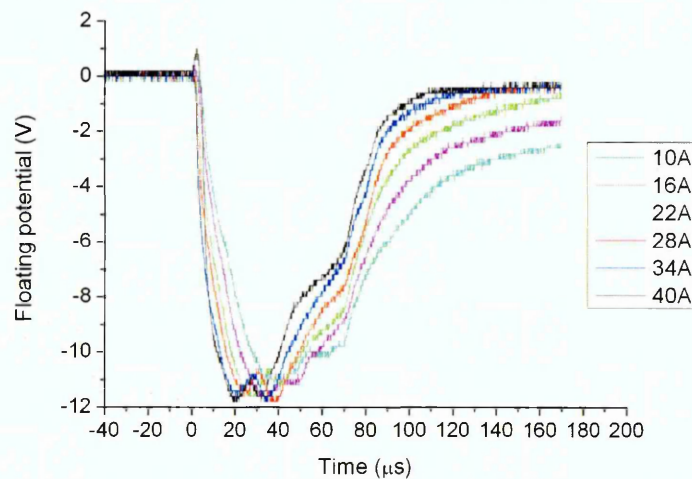
Figure 4.1.15 Floating potential as a function of time for various peak currents measured with flat probe at pressure of 3 Pa, in HIPIMS plasma discharge with Cr target

The dependence of the floating potential at low pressure on the power is shown on Figure 4.1.16. The floating potential sharply drops at the start of the discharge to values between -1 V and -1.5 V and than within 10 μs increases to values up to 1 V after which it steadily falls to 0 V after the end of the pulse. The start of the drop is at 15 μs for 40 A peak discharge current and at lower power it is at 33 μs at 10 A peak discharge current. The peak of floating potential is -1.8 V at high power and -1.1 V at low power. After pulse switch off time the floating potential steadily falls to 0 V at the same rate not depending on power.
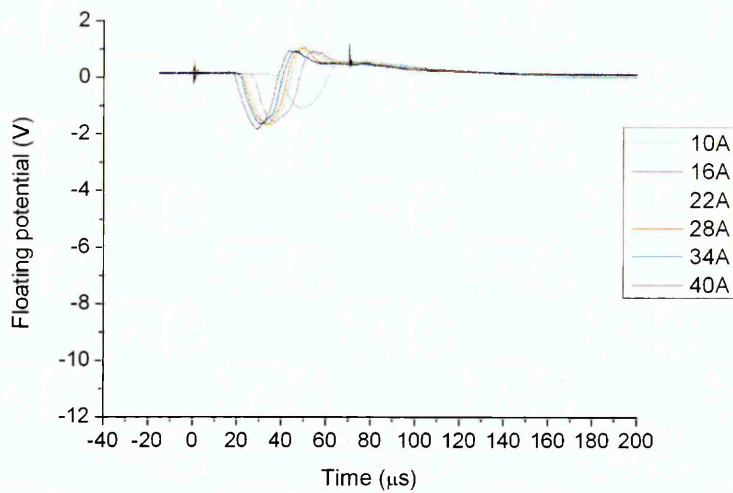
Figure 4.1.16 Floating potential as a function of time for various peak currents measured with flat probe at pressure of 0.3 Pa, in HIPIMS plasma discharge with Cr target

The influence of plasma parameters; floating potential, plasma potential, plasma density and electron temperature on discharge power and working gas pressure was investigated using Langmuir probe. Time resolved Langmuir probe measurements in a HIPIMS plasma discharge with Ti target in Ar atmosphere were carried out. Langmuir probe was positioned 100 mm away from the cathode above the race track. Measurements were averaged over 50 pulses. Measurements were performed for two pressures, 0.29 Pa and 2.67Pa. Pulse duration was set to 70 µs and frequency was 150 Hz, equivalent to 1% duty cycle. Measurements were time resolved with 20 µs between the measurements. First measurement was done at the start of the pulse and last measurement was done 390 µs after the start of the pulse for low pressure and 450 µs for high pressure measurements.

At low pressure the plasma is ignited some 40 µs after the voltage is applied to the target therefore the measurements below 50 µs give no signal since there is no plasma in the chamber. At higher pressure the time between the rise of voltage and the start of the discharge is shortened, thus the data at 30 µs already give information about plasma parameters.

Floating potential, calculated as the voltage at which current goes from negative value to positive value from the I-V characteristic, and presented in Figure 4.1.17, is very similar to the floating potential measured with the flat

96

probe with a difference that calculated result has a lower time resolution and longer detection time.
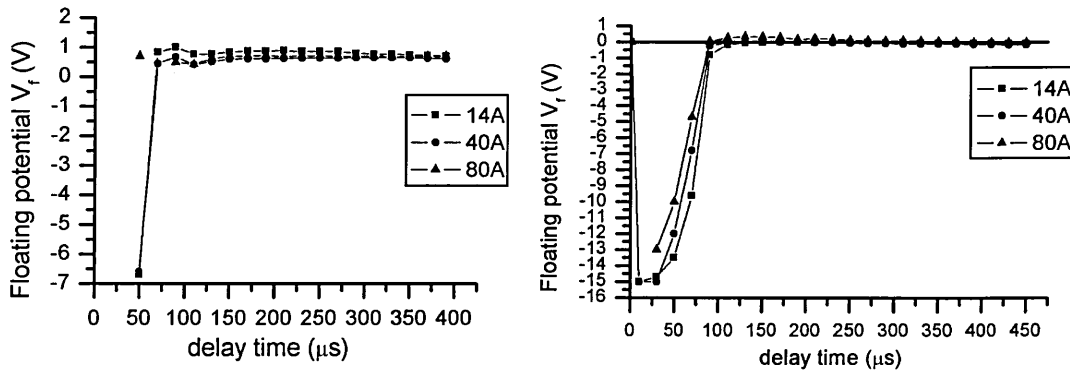
Figure 4.1.17 Time evolution of the floating potential for three peak discharge currents measured using Langmuir probe at 10 cm away from the target at a) low pressure 0.3 Pa and b) high pressure 2.67 Pa
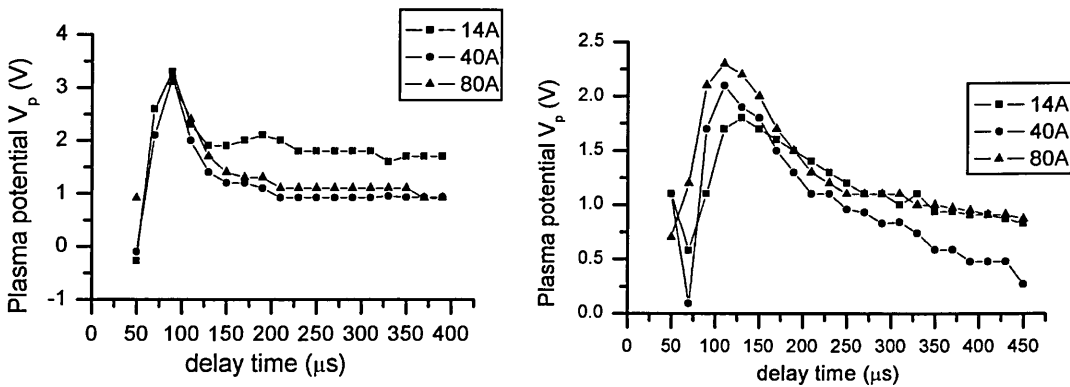
Figure 4.1.18 Time evolution of the plasma potential for three peak discharge currents measured using Langmuir probe at 10 cm away from the target at a) low pressure 0.3 Pa and b) high pressure 2.67 Pa

At low pressure the plasma potential inside and shortly after the pulse is similar for all three measurements as shown on Figure 4.1.18 a). In the beginning of the pulse plasma potential has a value around 0 V than raises to a maximum of 3 V and then slowly diminishes to around 1 V for 40 A and 80 A discharge and to 2 V for 14 A discharge. The plasma potential of the 80 A discharge at 50 µs is 1 V which can be attributed to earlier start in the current rise, as shown on Figure 4.1.19. The maximum of plasma potential is at 90 µs that is 20 µs after the end of the pulse. It could be due to the time necessary for particles to diffuse from the target region to the probe positioned at distance 100 mm from the target.

The plasma potential at high pressure, Figure 4.1.18 b), reaches its maximum at 110 μs, at 2.3 V for 80 A discharge, 2.1 V for 40 A discharge and 1.7 V for 14 A discharge. After the pulse the value of plasma potential falls down to 1 V at 450 μs after the start of the pulse.
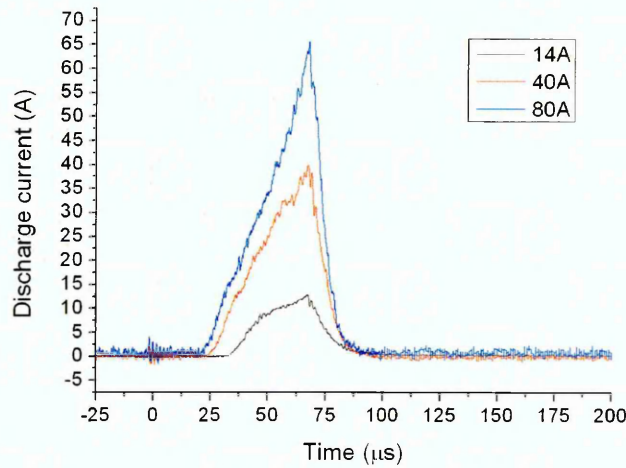
Figure 4.1.19 Discharge current as a function of time for HIPIMS discharge with Ti target for different peak currents at pressure of 0.3 Pa
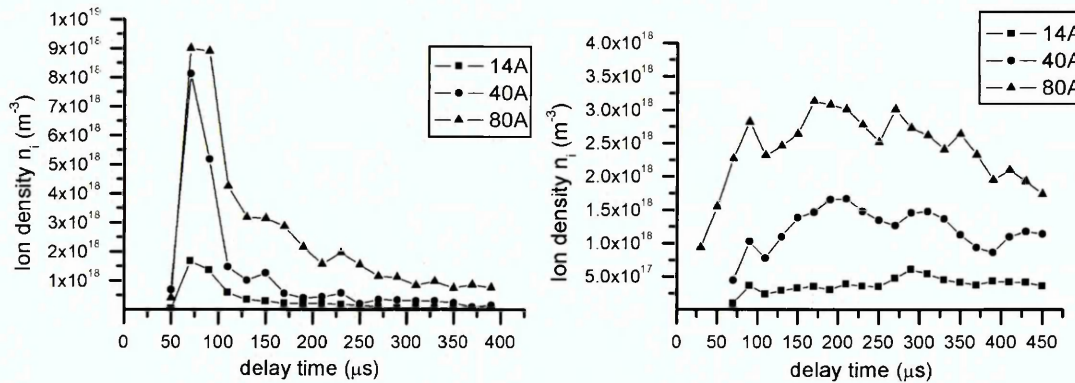
Figure 4.1.20 Time evolution of the plasma density for three peak discharge currents measured using Langmuir probe at 10 cm away from the target at a) low pressure 0.3 Pa and b) high pressure 2.67 Pa

The calculated ion density at low pressure shown on Figure 4.1.20 a), reaches a maximum at 70 μs after the beginning of the pulse, at the same time when the discharge achieves peak current. Peak of the ion density is at $9*10^{18}$ m^{-3} for discharge with 80 A peak current, $8*10^{18}$ m^{-3} for discharge with 40 A peak current and lowest $2*10^{18}$ m^{-3} for discharge with 14 A peak current. Results show increase of ion density with increase of peak discharge current. By increasing the discharge current the number of ions striking the target

increases which results in increased number of sputtered atoms and accordingly the number of secondary electrons. Higher density of electrons leads to higher ionisation of particles in the plasma resulting in the increased plasma density.

The time evolution of the ion density at high pressure, Figure 4.1.20 b), is not as straightforward to analyze as the result at low pressure. At low pressure the peak at 70 µs consists of both Ar and metal ions as shown in chapter 4.2.4. At high pressure there are at least three peaks. The first peak appears shortly after the end of the pulse, at 90 µs and is probably comprised of Ar ions. Due to the high pressure, electrons diffuse faster and ionize Ar ions in the vicinity of the probe. Metal ions arrive some 100 µs after the end of the pulse which can be seen as second peak at around 200 µs. Equally as at the low pressure the plasma density at high pressure increases with power. The highest density of ions is for 80 A discharge with maximum of $3*10^{18}$ m^{-3}, at 40 A discharge the maximum of ion density is at $1.5*10^{18}$ m^{-3} and for 14 A discharge it is $5*10^{17}$ m^{-3}. The linear dependence of the peak plasma density on the peak discharge current is shown on Figure 4.1.21.
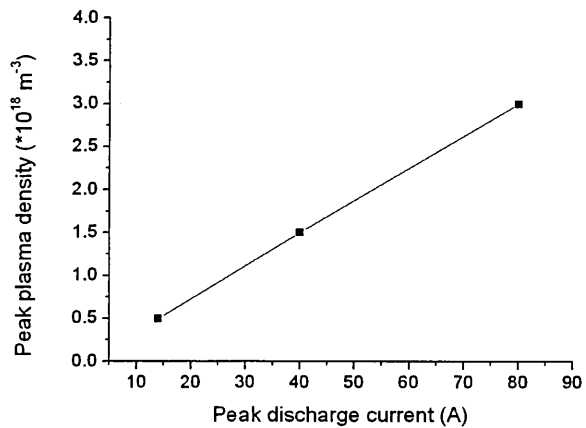
Figure 4.1.21 Dependence of the peak plasmas density measured with Langmuir probe on the peak discharge current in HIPIMS plasma discharge with Ti target at pressure of 0.3 Pa
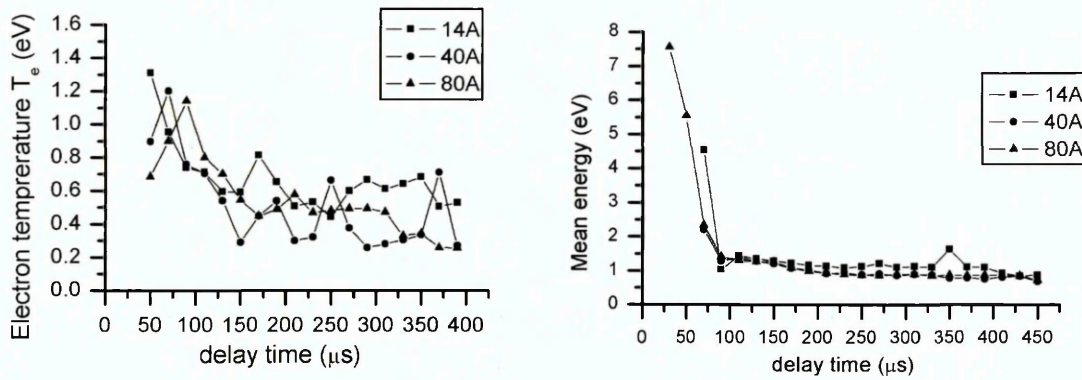
Figure 4.1.22 Time evolution of the electron temperature for three peak discharge currents measured using Langmuir probe at 10 cm away from the target at a) low pressure 0.3 Pa and b) high pressure 2.67 Pa

The electron temperature exhibits maximum inside the pulse, shown on Figure 4.1.22 a), for all three measured peak currents, of around 1.2 eV and slow decline towards approximately 0.5 eV at 400 µs after the beginning of the pulse. The mean electron energy has a maximum value of 7.5 eV inside the pulse for 80 A discharge and falls down to around 1eV at 100 µs after the beginning of the pulse. The electron temperature time dependence profile for 40 A discharge follows the profile for 80 A discharge. In contrast, the 14 A discharge profile has a peak of 4.5eV at 70 µs which could be due to later creation of discharge current due to lower voltage applied to the cathode.

On the Figure 4.1.22 the results for electron temperature at low pressure are given and for high pressure measurements the results for mean electron energy are stated. Both of these two values describe the energetic state of electrons in the plasma and the difference results from different data analysis. Mean electron energy $\langle\varepsilon\rangle$ is calculated using following equation [67];

$$\langle\varepsilon\rangle = \frac{\int_0^\infty \varepsilon F(\varepsilon)d\varepsilon}{\int_0^\infty F(\varepsilon)d\varepsilon} \qquad (4.1.8)$$

where ε is the energy of the electron and $F(\varepsilon)$ is the electron energy distribution function calculated from the V-I characteristic of the Langmuir probe explained in the chapter 3.3.1 and electron temperature is calculated using following equation [67]; $\qquad T_{eff} = \frac{2}{3}\langle\varepsilon\rangle \qquad (4.1.9)$

100

4.1.4 Summary

The measurements of the ion to neutral ratio show that the ionisation of the plasma increases with power. The ion to neutral ratio, in the period shortly after the end of the pulse, increases from 1.5 to 3.5 by increasing the peak power from 25 A to 100 A. At 1 ms from the start of the pulse at the lowest power (discharge current of 25 A) an ionisation of 33 % is detected and at higher power (discharge current of 100 A) the ionisation was 64 %. Higher power leads to increased sputtering of the target and increased plasma density that in turn results in higher ionisation rates of sputtered metal atoms.

The ion energy distribution function for three elements (Cr, Ti and C) was successfully measured using a plasma sampling mass spectrometer in HIPIMS plasma discharge. The time-averaged metal ion flux comprised high- and low- energy particles whose combined IEDF could be described by a sum of two Maxwellian distributions. The main energy peak showed no dependence on target current as it originated from the post-discharge plasma. The high energy tail increased with increasing target current and could be attributed to the power applied in the pulse. By increasing power sputtering from the target increased resulting in enhanced gas rarefaction. Decreased gas density in the target vicinity lead to reduced thermalisation of the metal particles sputtered from the target with Thompson distribution resulting in higher intensity of the high energy tail.

The IEDFs of Ar ions have significantly different shapes for different pressures. At low pressure, the IEDFs exhibited two Maxwellian distributions similar to the ones found for metal ions but had lower effective temperature. The high energy tail comprised gas ions heated up through collisions with sputtered atoms. At high pressure, the gas IEDF comprised only a single low-energy peak. The average energy of metal ions was found to increase monotonically from 2.7 eV to 4.3 eV (Cr), from 3.5 eV to 7 eV (Ti) and from 0.8 eV to 1.5 eV (C) as the discharge current was increased from 14 A to 40 A. The metal ion-to-gas ion ratio was higher for target materials with high sputter yield.

Electrostatic probe measurements show higher ion saturation current at low pressure compared to high pressure measurements. Lower saturation current at high pressure could be due to higher thermalisation and deflection

of metal ions due to high pressure of working gas and short mean free path that is around 1 cm. At both pressures the ion saturation current increased linearly with power. The electron density calculated from Langmuir probe measurements at low pressure consists of one peak appearing shortly after the end of the pulse with its peak increasing with the power. At high pressure measurements the electron density comprises three peaks increasing with power and reaching the maximum at around 200 μs. The delay of the electron density peak at high pressure could be attributed to the short mean free path and suppressed diffusion of metal ions in the plasma.

4.2 Temporal evolution of the ion energy distribution function (IEDF) in HIPIMS plasma discharge

In Chapter 4.1 it has been shown that the high energy tail of the ion energy distribution function (IEDF) is created during and shortly after the pulse and that low energy peak originates from period after the end of the pulse. To expand the understanding of time evolution of the metal and gas ions near the substrate, time resolved measurements from the start of the pulse up to the beginning of the next pulse have been performed. The time resolved measurements of the IEDF have been performed using energy resolved mass spectrometer, and the ion saturation current has been measured using flat probe positioned next to the entrance of the mass spectrometer. Pressure in the experimental chamber was 0.3 Pa, pulse duration was set to 70μs, repetition frequency was 100 Hz and peak discharge current was 40 A.

4.2.1 Temporal evolution of the metal IEDF in HIPIMS plasma discharge with Cr target

The time averaged measurements of the Cr^{1+} IEDF are shown in Figure 4.2.1 and show a low energy main peak and a high energy tail reaching up to 60 eV. It has been suggested [28] that ions in the high energy tail are created during the pulse whilst the low energy main peak originates from the time after the end of the pulse.

Figure 4.2.1 Time averaged measurements of the Cr^{1+} ion energy distribution function in a HIPIMS plasma discharge with Cr target in Ar atmosphere at pressure of 0.3 Pa

The time resolved measurements of the Cr^{1+} IEDF are presented in Figure 4.2.2. In Figure 4.2.2 a) the time scale is shown ascending to show the IEDF in the start of the pulse, whereas on Figure 4.2.2 b) the scale is shown descending to show the end of the pulse. The time scale is plotted from the start of the pulse at 0 µs to the 5000 µs from the start of the pulse. From 0 µs to 220 µs, the time scale is linear with 20 µs step, to demonstrate the IEDF time evolution inside the pulse and shortly after the pulse. These are followed by three measurements at 320 µs, 420 µs and 520 µs, showing the time evolution of the IEDF in the post discharge. Finally, to demonstrate the lifespan of ions in the discharge, the last three time scale points are 1.2 ms, 2.5 ms and 5 ms. The time when the pulse is on, from 0 µs to 70 µs, is shaded gray on the figures.

Figure 4.2.2 a) and b) show that high energy ions originate from the time inside and shortly after the end of the pulse, while the main low energy peak originates from the time after the pulse. In detail, three phases of development can be identified. The first phase is a discharge ignition and development from 0 to 120 µs during which the highly energetic ions are detected. Second is the post-discharge phase from 120 µs until 420 µs specified with the dominance of the low energy group of ions and a decreasing high energy tail. Finally is the off-time phase where only a thermalised low energy peak is observed until the last detected metal ion signal at 2.5 ms from the start of the pulse.

1) *Discharge ignition and development:* At 40 μs from the start of the pulse (Figure 4.2.2 a), two energy-groups of Cr^{1+} ions are detected, a low energy group of ions with a peak at 3 eV and a high energy group of ions with a peak at 14 eV. From 60 μs until 100 μs, the high energy tail is growing strongly both in intensity and in energy and accounts for the majority of Cr^{1+} ions. At the same time a low energy group of ions is seen to develop slowly with intensity remaining lower than the high energy group of ions. The highest energy of ions detected from 40 μs until 80 μs, increases from 25 eV to 70 eV however the peak value is decreased from 14 eV to 8 eV. The ions with energy of 70 eV are detected for a short period of time some 20 μs after the end of the pulse.

A third IEDF with an intermediate energy of 8 eV is seen to develop together with the low energy group of ions with peak at 0.8 eV. There are two possible explanations of its origin. The most probable explanation is that the Cr^{2+} ions undergo either a process of charge exchange with the Ar atoms or a process of electron-ion recombination to become Cr^{1+} ions. The experimental data for the charge transfer cross section [37], 40×10^{-16} cm^2, and the electron-ion recombination cross section calculated from a recombination rate coefficient data [84], 0.2×10^{-16} cm^2, indicate a higher probability of Cr^{1+} ions being created by charge exchange collisions between Cr^{2+} ions and Ar atoms. The ionisation potential of Cr^{2+} and Ar atoms are 16.49 eV and 15.76 eV, respectively [85], therefore the energy defect of +0.73 eV for this reaction is quite low, indicating that the probability for this charge exchange reaction is very high. The peak of high energy Cr^{2+} IEDF has a peak around 8 eV (Figure 4.2.5) which corresponds to the peak of intermediate IEDF. It should be mentioned that the probability of charge exchange during the pulse is lowered due to gas expansion and rarefaction [26] but, after the switch off, the Ar diffuses back towards the target and the probability increases.

Another possibility is that the intermediate energy IEDF is a result of a wave created due to a sharp drop in the plasma potential and electron temperature observed during the initial ignition and build-up of the discharge current phase [9].

In subsequent experiments (see Chapter 4.3 for details) the metal IEDF was measured at different distances from the target. The third peak was detected even at very short distances therefore it is not a result of metal ions

being reflected from the substrate holder or similar obstacles in the chamber. The long lifespan of high energy ions, up to 320 μs, could be attributed to the long lifespan of plasma in the region next to the target reported in the work of Bohlmark et al. [15]. Due to the heavy gas rarefaction in the vicinity of the target [26] metal ions collide only with high energy metal particles and significant high energy group of ions has been detected. At 320 μs only a weak high energy tail is detected (Figure 4.2.2 b) which indicates that the metal ions are completely thermalised with the Ar particles that have diffused into the space near target.

The high energy tail originates from atoms sputtered from the target with a Thompson distribution [83] and ionized near the target through electron impact ionisation. The increase in maximum energy of detected ions with time and discharge current could be partially attributed to increased rarefaction of the metal vapour due to the high instantaneous power. A partial breakdown of magnetic confinement promoting ion transport can be expected as well.

2) *Post-discharge:* At times above 120 μs (Figure 4.2.2 b), the low energy peak increases in intensity and prevails over the high energy tail which decreases both in intensity and in the highest energy of detected ions. The highest intensity of the low energy group of ions with the peak at 0.8 eV is measured at 180 μs after which it slowly decreases.

3) *Off-time:* At 420 μs after the start of the pulse only a weak signal of the high energy tail can be detected. In contrast, the low energy peak is maintained up to 2.4 ms after the pulse start. Therefore the metal ions could be detected 2.4 ms from the start of the pulse demonstrating that ions are present in the system much longer than the duration of the pulse.

The plasma potential measured in similar plasma discharges [12] had a peak value of around 5 V during the pulse and a value of 1 V in the post-discharge. The low energy peak group of ions had a peak at 3 eV during the pulse and in the post-discharge the value was below 1 eV. The low energy peak had a value equal to the difference between the plasma potential and the ground potential of the orifice.

The high energy tail diminishes faster than the low energy group of ions due to termination of the sputtering process (voltage off), high loss rate to the wall and collisions with Ar particles. The low energy group of ions loss rate to

106

the wall is lower, due to long drift time, and constant repopulation with thermalised high energy ions.

a)

b)

Figure 4.2.2 Temporal evolution of Cr^{1+} IEDF from the start of the pulse until 5ms from the start of the pulse in a) ascending scale and b) descending scale in HIPIMS plasma discharge of Cr at pressure of 0.3 Pa

4.2.2 Temporal evolution of the Ar IEDF in HIPIMS plasma discharge with Cr target

The time averaged measurement of the Ar^{1+} IEDF, presented in Figure 4.2.3, show similar shapes to the Cr^{1+} IEDF (Figure 4.2.1) with two groups of ions, a very narrow low energy peak and high energy tail. However the

detected ion energies were significantly lower with a maximum reaching only 12 eV. The main peak probably originates from thermalised Ar atoms ionized near the target through electron impact ionization. The high energy tail could originate from ions that gained energy through collision with the high energy metal ions and atoms. It has been suggested [28] that the high energy tail is generated over a short period of time. To investigate the time origin of the high energy tail, time resolved measurements of Ar^{1+} IEDF were performed and are shown on Figure 4.2.4.
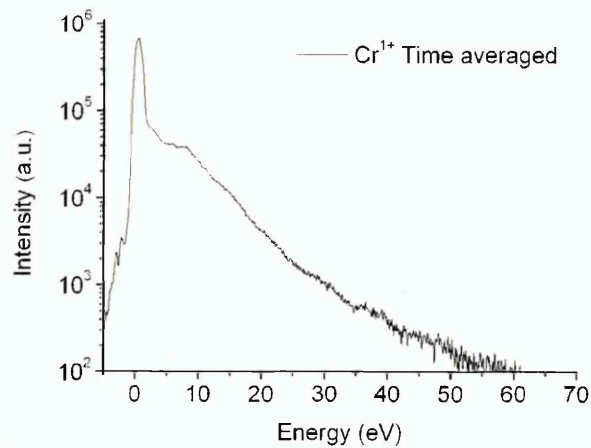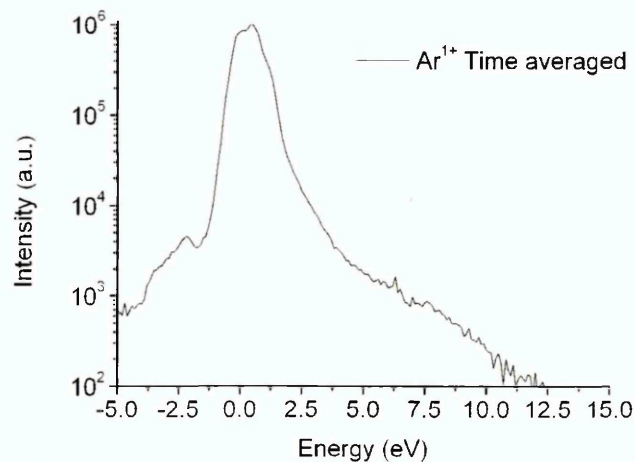

Figure 4.2.3 Time averaged measurement of the Ar^{1+} ion energy distribution function in the HIPIMS plasma discharge with Cr target

The first signal from Ar^{1+} ions is detected 20 μs after the start of the pulse (Figure 4.2.4 a). Energies of ions are below 5 eV. From 60 μs to 120 μs after the start of the pulse, two groups of ions can be recognized. The first group of ions consists of a high intensity low energy peak with mean energy at around 2 eV. The second group of ions has higher energies of up to 16 eV and a peak at around 8 eV. The high energy tail of the Ar^{1+} IEDF is detected at the same time as the highest intensity of the high energy tail of Cr^{1+} IEDF, between 60 μs and 120 μs. Therefore the second group of ions could be due to Ar^{1+} ions involved in elastic collisions with metal ions or atoms that have energies of up to 60 eV. Another possibility is that the highly energetic Ar^{1+} ions originate from neutrals reflected from the target (so called back-reflected fast neutrals), ionized and detected in the mass spectrometer [46].

108

a)

b)

Figure 4.2.4 Temporal evolution of Ar^{1+} IEDF from the start of the pulse until 5 ms from the start of the pulse in a) ascending scale and b) descending scale in HIPIMS plasma discharge of Cr at pressure of 0.3 Pa

From 120 μs to 220 μs after the start of the pulse (Figure 4.2.4 b) the intensity of the low energy group of ions increases while the position of the peak decreases from 2 eV to 0.5 eV. The high energy group of ions is decreasing both in intensity and energy after 120 μs and completely disappears at 220 μs after the start of the pulse. The intensity of the low energy group of ions reaches a peak at 420 μs and then slowly decreases until 5 ms after the start of the pulse when only a weak signal could be measured. The energy of the Ar^{1+} IEDF peak in measurements presented in this paper agrees well with the reported plasma potential [12].

These results show that metal and Ar ions can be detected in the plasma a long time after the end of the pulse. The Ar^{1+} ions have the longest

life-span of all ions detected in our experiment, twice the life-span of metal ions. The long life-span of ions could contribute to reduction of stress in the coating and reduction of contaminants in the coating. Reduction of stress was demonstrated in the work by Nakajima et al [86] that showed a decrease of stress with an increase of the number of ions impinging on the substrate which is comparable with the long life-span of ions. The microstructure of deposited films has been shown to improve with reduced oxygen to aluminium flux ratio, where oxygen was observed as a contaminant [87].

4.2.3 Temporal evolution of the doubly charged IEDF in HIPIMS plasma discharge with Cr target

The energy scale measured by mass spectrometry is represented in volts. To change the energy scale to eV it is necessary to multiply it by the charge of the particle, e.g. in case of doubly charged ions the energy scale should be multiplied by two to obtain the energy scale in eV.

The first Cr^{2+} ions are detected 40 µs after the start of the pulse and exhibit only one IEDF with a peak at 8 eV and ions with energies of up to 40 eV (Figure 4.2.5 a). The Cr^{2+} IEDF comprises only one group of ions until 120 µs when two groups of ions can be recognized, a low energy main peak and a high energy tail. From 120 µs after the start of the pulse (Figure 4.2.5 b) the main low energy group of ions with peak at 2 eV slowly decreases in intensity, while the high energy tail diminishes until 220 µs when a single group of ions at low energy can be measured. The high energy group of ions originates from atoms sputtered from the target having a Thompson distribution [83] and ionised through electron impact ionisation. It is also possible that doubly charged ions are created through a process of direct double ionisation process or a fast two step process resulting in ejection of inner-shell electron and Auger electron. This process requires highly energetic electrons, which are reported to exist during the pulse in the negative magnetized glow [98].

a)

b)
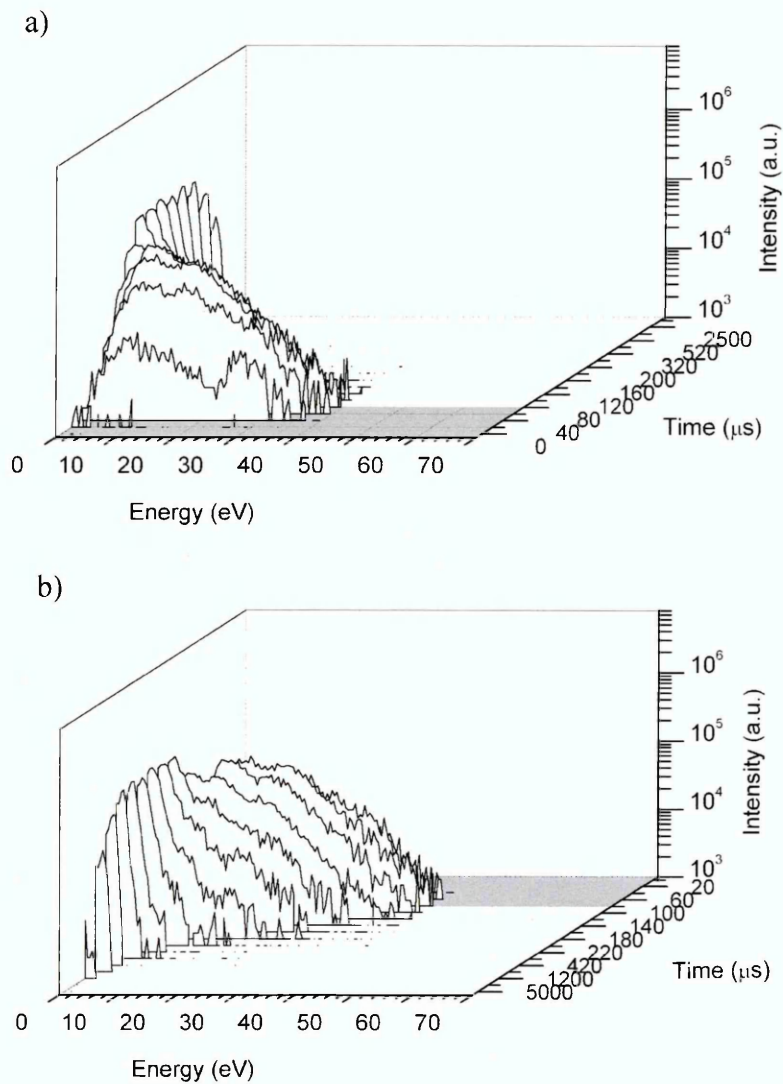
Figure 4.2.5 Temporal evolution of Cr^{2+} IEDF from the start of the pulse until 5ms from the start of the pulse in a) ascending scale and b) descending scale in HIPIMS plasma discharge of Cr at pressure of 0.3 Pa. The energy scale measured by mass spectrometry is represented in volts, to obtain it in eV it was multiplied by two for doubly charged ions.

After voltage switch-off at the end of the pulse, the generation of high energy atoms from the target is terminated. Cr^{2+} ions go through a process of charge exchange with Ar atoms, whereby Ar atoms are ionized and Cr^{2+} ions lose a charge and convert to Cr^{1+} ions, as described in section 4.2.1. Additionally, Cr^{2+} goes through elastic collisions with low energy ions and atoms of the working gas which results in thermalisation. The effect of the thermalisation is the appearance of a low energy peak and a fast reduction of the high energy tail. The mean free path of the elastic collision of Cr^{2+} ions is

approximately 7 cm. After 220 μs the ions are lost to the chamber walls or less probably undergo through the processes of charge transfer and become Cr^{1+} ions. The mean free path of charge transfer is around 1 m. This leads to the reduction in intensity of the main peak up until 1.2 ms from the start of the pulse when only a weak signal of Cr^{2+} ions could be detected in the plasma.

From the first signal of the Ar^{2+} IEDF measured at 20 μs until 100 μs, the Ar^{2+} IEDF consists only of high energy ions with considerable energy of up to 25 eV and peak at 10 eV (Figure 4.2.6 a). After 120 μs the intensity and the highest energy of the high energy tail decreases and the low energy peak intensity increases until 180 μs when the Ar^{2+} IEDF consists of only low energy peak (Figure 4.2.6 b). The high energy tail could be created in the same way as Ar^{1+} high energy tail, which is through collisions with the highly energetic metal ions. The Ar^{2+} ions from high energy tail thermalise after the end of the pulse to contribute to a low energy main peak which is shown in Figure 4.2.6 b. The main peak reaches the highest intensity around 200 μs and completely disappears 1.2 ms after the start of the pulse. For both Cr^{2+} and Ar^{2+} IEDF the low energy peak in the post-discharge has a value of 2 eV which corresponds well with the value of the plasma potential in the post-discharge of 1 V multiplied by two for doubly charged ions.
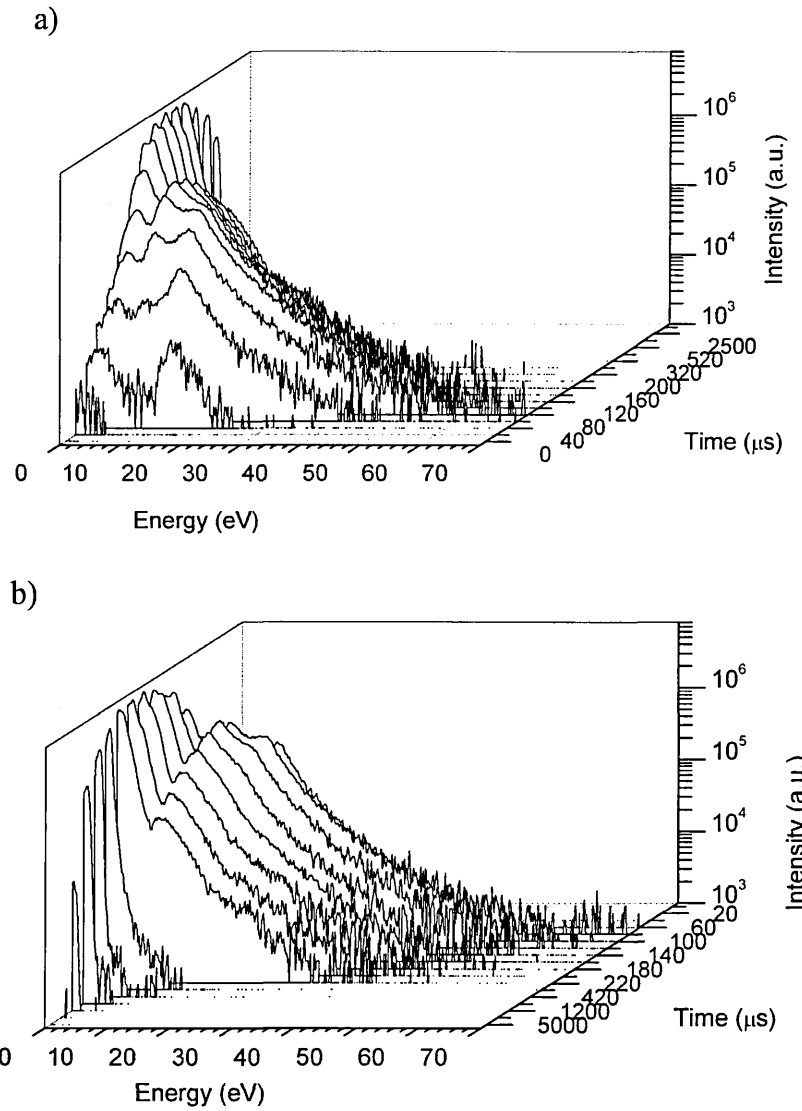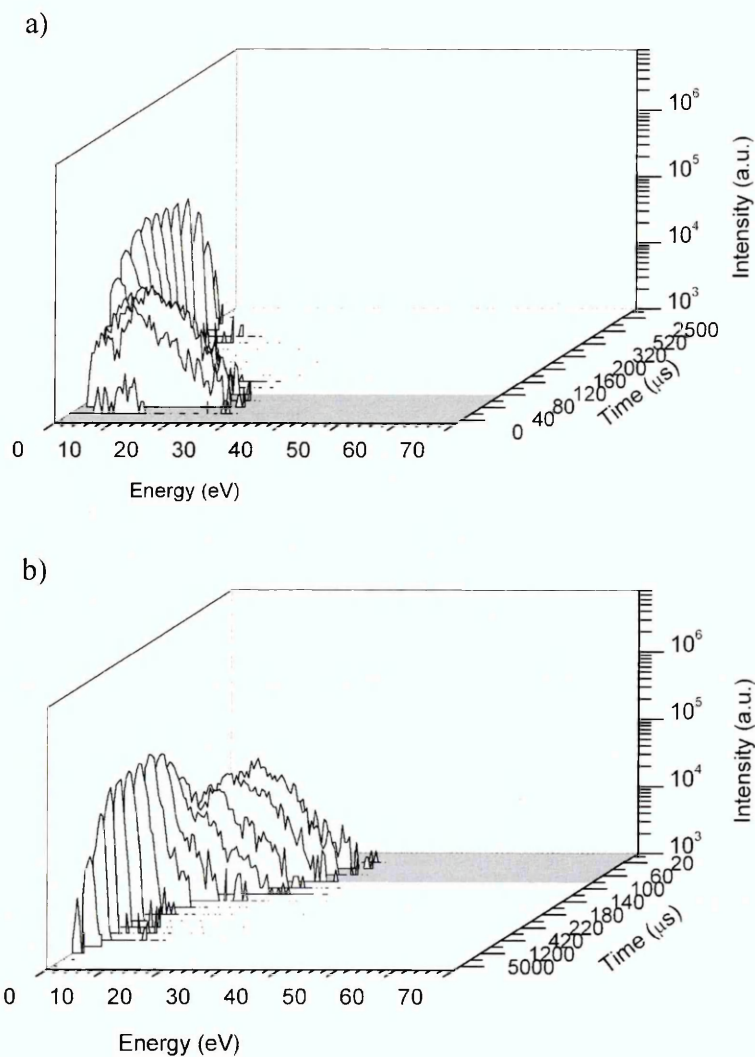
112

a)

b)

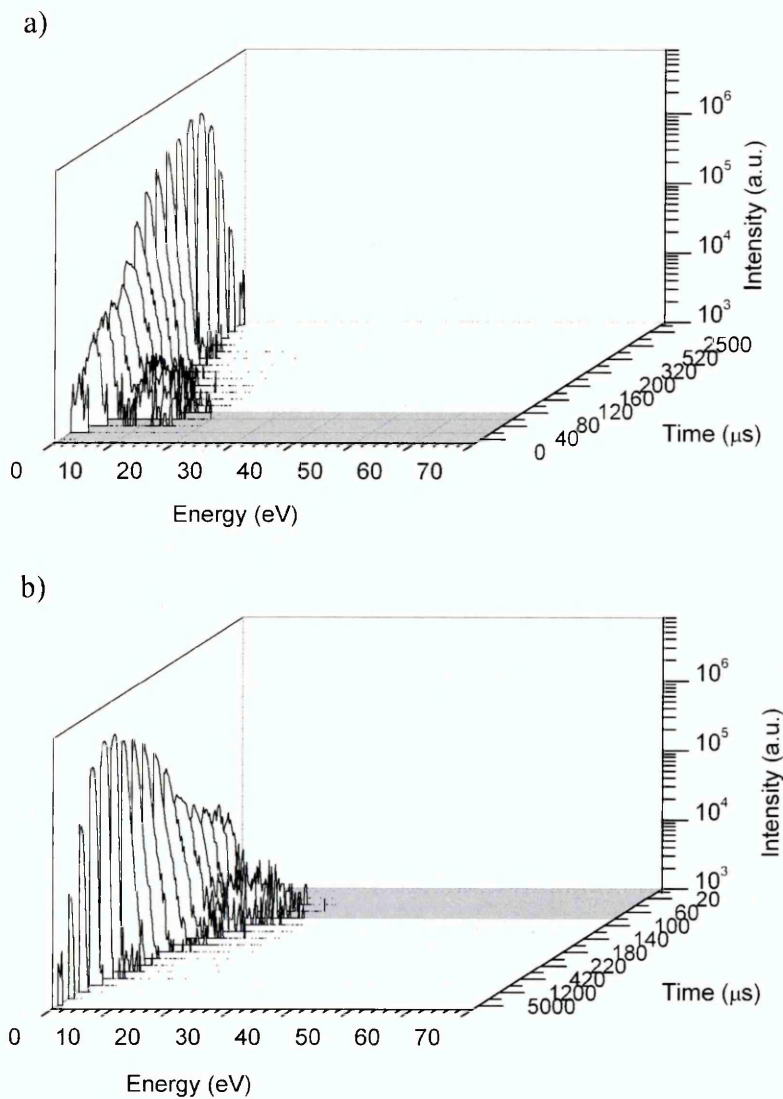Figure 4.2.6 Temporal evolution of Ar^{2+} IEDF from the start of the pulse until 5ms from the start of the pulse in a) ascending scale and b) descending scale in HIPIMS plasma discharge of Cr at pressure of 0.3 Pa. The energy scale measured by mass spectrometer is represented in volts, to obtain it in eV it was multiplied by two for doubly charged ions.

The higher energy observed for Ar^{2+} ions of 25 eV compared to Ar^{1+} ions (10 eV) could be attributed to charge exchange collisions. The Ar^{1+} can undergo charge exchange collisions with Ar^0 which has a very low energy (equivalent to room temperature), and a high density of 8.0×10^{19} m^{-3} at 0.3 Pa. These collisions convert slow neutrals into slow Ar^{1+}. Because the density of Ar^0 is so high, the frequency of the process is high and the resulting decrease in energy is fast. In contrast, Ar^{2+} can only undergo charge exchange collisions with Ar^{1+} since the process with Ar^0 is not energetically favourable. Because the density of Ar^{1+} is much lower than the density of

113

neutrals, the frequency of collisions is much lower and energy losses are reduced allowing Ar^{2+} to maintain its initial energy. The last detection time of the Ar^{2+} ions is 1.2 ms from the start of the pulse.

4.2.4 Temporal evolution of the Ion saturation current

The ion saturation current has been measured with a flat probe placed next to the mass spectrometer orifice. Results presented on Figure 4.2.7 show a steady rise from 40 µs reaching a peak at 85 µs and decay until 140 µs. The ion saturation current peak value is 13 mA and the current density is 4 mA/cm^2.
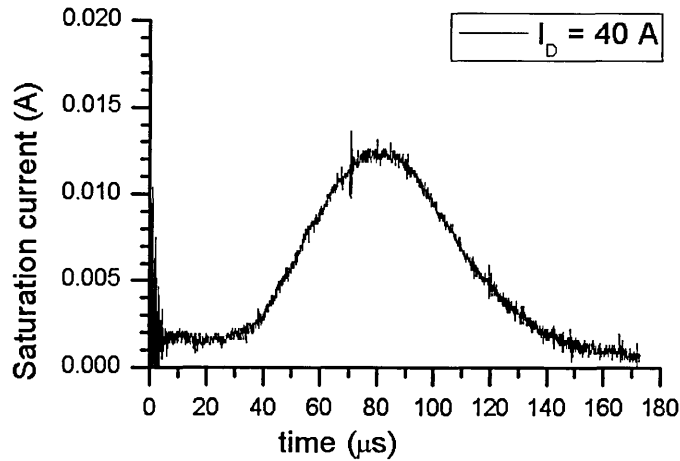
Figure 4.2.7 Ion saturation current of HIPIMS plasma discharge with Cr target at pressure of 0.3 Pa and peak current of 40 A

The ion saturation current, I_S, is given by the expression [65].

$$I_S = \frac{1}{4} n_0 e v_+ A \qquad (4.2.1)$$

where n_0 is the plasma density, e is the elementary charge and A is the surface of the probe that is 3.14 cm^2 for Langmuir probe used in our experiment. v_+ stands for the velocity of ions which is proportional to the square root of average energy of the IEDF.

The average energy of the IEDF is presented in Figure 4.2.8. The focus of comparison between the ion saturation current and the average energy will be on the Cr^{1+} ions since mass spectroscopy measurements showed that these ions constitute the majority of ions in the pulse. The integrals of the ion energy distribution functions, as a measure of number of ions entering the mass spectrometer with 3° acceptance angle i.e. arriving flux of ions, are shown on Figure 4.2.9.
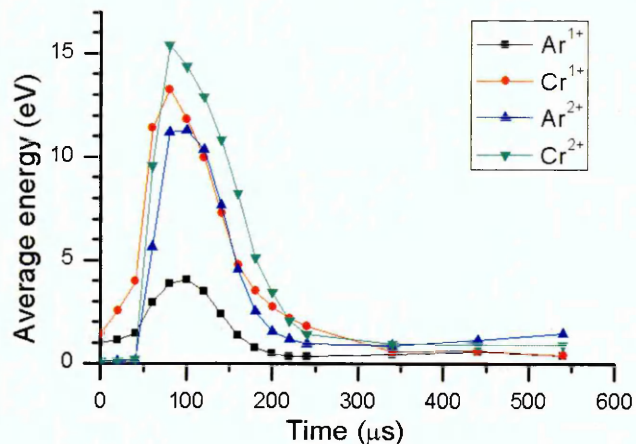
114

Figure 4.2.8 Average energy of species measured in HIPIMS plasma discharge with Cr target at pressure of 0.3 Pa and peak current of 40 A
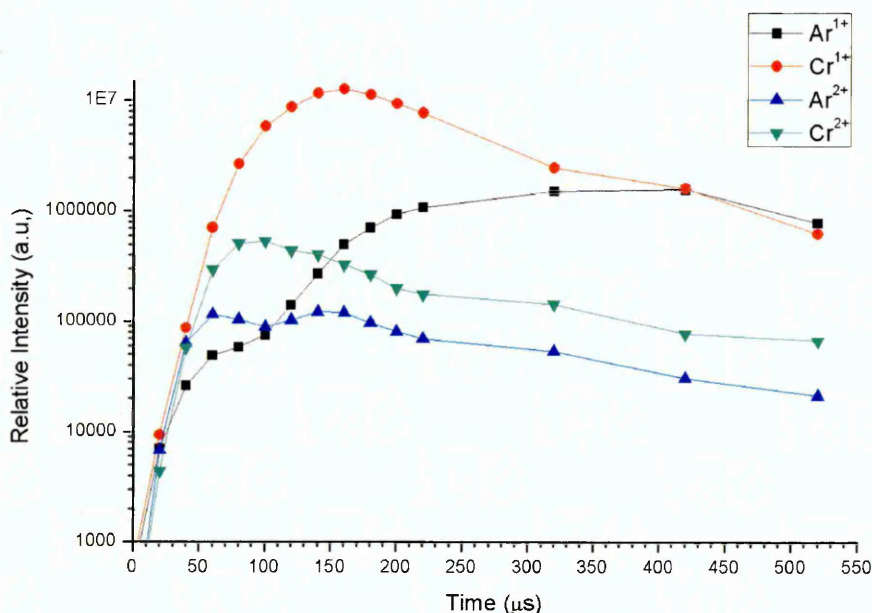
Figure 4.2.9 Integral values of the ion energy distribution function in HIPIMS plasma discharge with Cr target at pressure of 0.29 Pa and peak current of 40A

The Cr^{1+} flux dominates the figure from the start of the pulse until 420 µs after the start of the pulse when more Ar^{1+} ions are being detected in the mass spectrometer. At 420 µs after the start of the pulse the flux of the Ar^{1+} ions reaches a maximum. The peak of the Cr^{1+} ion flux at 160 µs is ten times the peak of the Ar^{1+} ions. The flux of Cr^{2+} ions reaches a maximum at 100 µs and slowly diminishes. The peak of the metal IEDF integrals compared to a peak of the ion saturation current is shifted by a 100 µs probably due to the low angle acceptance of the mass spectrometer.

115

The ions created during the pulse fly straight to the sample due to the cosine distribution of sputtered particles and only a small portion is detected. The number of ions entering the mass spectrometer during the pulse is low since sputtered particles ejected from the target following the cosine law have velocity vectors pointed towards the substrate. As the particles in the plasma collide the velocity vectors of particles change direction and more particles enter the mass spectrometer. After the pulse ions thermalise and their velocities are less oriented therefore a substantial fraction of ions reaches the detector. Nevertheless the IEDF of the particles entering the mass spectrometer during all of the measuring time could be considered correct since the IEDF of particles that enter the mass spectrometer during the pulse reflects the IEDF of ions in the plasma but at reduced intensity. Therefore we believe that the information about average energy is correct.

The flux of Ar^{2+} ions seems to have two maxima arriving in two waves, first one coming at the same time with metal ions and the second one at 140 μs coming with the Ar^{1+} flux. First wave could originate from an energy transferred from sputtering particles to a nearby Ar particles and second wave could be from particles arriving to the mass spectrometer from near the target region.

The rise of average energy of the Cr^{1+} IEDF starts at 30 μs, the peak of 13 eV is reached at 90 μs. At 250 μs after the start of the pulse the value of average energy is below 2 eV. Since the ion saturation current and the average energy of collected ions have been measured it is possible to calculate the density of ions at the position of mass spectrometer rearranging equation (4.2.1) to

$$n_i = \frac{I_S}{\sqrt{E_{AV}}} \frac{4}{eA} \sqrt{\frac{m_i}{2}} \qquad (4.2.2)$$

where m_i is the mass of the Cr^{1+} ion and E_{AV} is the average energy given on Figure 4.2.8. The calculated ion density is shown on Figure 4.2.10. The calculated value of ion density at the start of the pulse is probably not correct since the measured saturation current is a consequence of the static noise caused by switching on of the pulse. The peak value of 1.5×10^{17} m^{-3} is reached at 80 μs after the start of the pulse. The measured ion density in the vicinity of substrate is consistent with reported plasma densities [12, 10, 22, 88]. After the peak, the ion density decreases strongly until 140 μs, after which

116

the decrease is slower until last measured value of 1.5×10^{16} m^{-3} 180 µs after the start of the pulse.
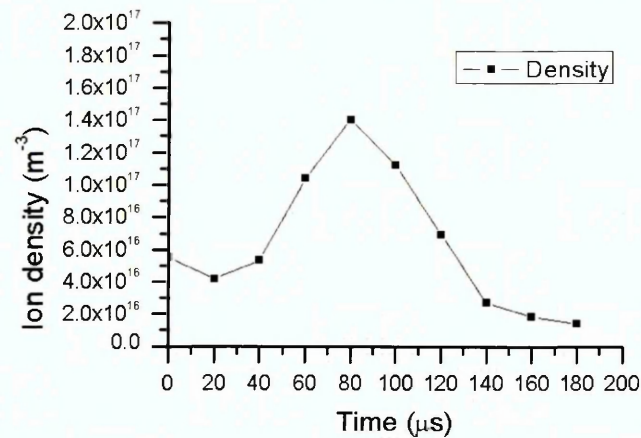
Figure 4.2.10 Ion density of the HIPIMS plasma discharge with Cr target at pressure of 0.29 Pa and peak current of 40 A at the position of the mass spectrometer

The peak ion density is detected at 80 µs and coincides well in time with the peak in discharge current at 70 µs. This indicates that the bulk plasma diffuses in ~ 10 µs through the chamber volume.

It is interesting to note that the maximum density also coincides with the maximum energy of ions. This is then followed with a very long period between pulses where the ion energy is very low and the density is reduced but still at a relatively high level of 10^{16} m^{-3}. This has implications on the growing film. For example, for the particular case of Cr, it indicates that in every pulse, the film is deposited in two stages. In the first stage, the film is bombarded with a high flux of highly energetic ions containing predominantly Cr metal ions. The initial stage lasts as long as the pulse duration. This is then followed by a second stage where the instantaneous bombardment flux is lower, but still significant, and the ion energy is also very low. Metal ion bombardment is observed for up to 2 milliseconds whereas Ar bombardment continues up to several milliseconds after the pulse. The long duration of the second stage means that the deposited material (total dose) may be equal or greater than the material deposited during the peak of the pulse. This has implications for films deposited under these conditions. For example the continuous bombardment by low energy ions between pulses may result in densification of the film and annealing of lattice defects. Furthermore, the

replenishment of the surface with metal may reduce the relative flux of impurities incorporated in the coatings.

4.2.5 Summary

The ion energy distribution function of Cr^{1+}, Cr^{2+}, Ar^{1+} and Ar^{2+} ions in the HIPIMS plasma discharge at different times inside and after the pulse has been successfully measured. The time evolution and the lifespan of each species have been demonstrated. The ion energy distribution function of metal ions inside and shortly after the end of the pulse showed existence of highly energetic ions with energies of up to 70 eV and 40 eV for Cr^{1+} and Cr^{2+} ions, respectively. The metal ions originated from atoms sputtered from the target with Thompson distribution function [83] that are ionized in the vicinity of the target by electron impact ionization. At the same time Ar ion energy distribution function comprising a main low energy peak and small high energy group of ions that is probably created through collisions with high energy metal ions.

After the pulse, the high energy tail of the metal ion IEDF slowly diminished with time as a result of absorption by the substrate and surrounding walls, collisions with the surrounding low energy Ar particles. The low energy part of the IEDF is thus preserved over longer times. The high energy tail of Ar IEDF was found to disappear shortly after the end of the pulse and only the low energy peak was detected. The long lifespan of ions in the plasma, 1.2 ms for Cr^{2+} and Ar^{2+}, 2.5 ms for Cr^{1+} and 5 ms after the start of the pulse for Ar^{1+} showed that ion existence is not limited to only the period inside and shortly after the pulse but that ions exist long after the power supply is switched off. The long lifespan of ions impinging on the substrate could be beneficial to reduce residual stresses and inhibit the incorporation of contaminants in the coating.

4.3 Temporal evolution of plasma parameters at various distances from the target in HIPIMS plasma discharge

The time resolved measurements of the ion energy distribution function (IEDF) presented in Chapter 4.2 present ion energies at a fixed distance of 17 cm from the target. In the industrial size machine the sample rotates inside the chamber changing the position inside the chamber and the distance from the target. The time averaged and time resolved measurements of the IEDF presented in this chapter have been performed at 5 different distances from the target to investigate the influence of distance on ion fluxes and ion energies in the HIPIMS plasma discharge. The ion energy distribution function has been measured using an energy resolved mass spectrometer. A Langmuir probe was placed perpendicular to target normal at 4 different distances to measure the time evolution of the electron density.

Magnetron with diameter of 2" mounted on a stem tube was used to perform spatially resolved measurements. At the time measurements were performed only available 2" target was Ti target. Therefore in this chapter presented results are measured in the HIPIMS plasma discharge with Ti target in Ar atmosphere.

4.3.1 Temporal evolution of electron density at distances between 2.5 cm and 15 cm from the target

The LP measurements of the electron density are presented in Figure 4.3.1 a) and b) for Ar pressure of 1 Pa and 3 Pa respectively. At pressure of 1 Pa the plasma density increases sharply during the pulse and reaches a peak of 2.5×10^{17} m^{-3} which occurs at the same time as the peak discharge current (Figure 2.9). After pulse switch-off, the plasma decays, however the density remains at a relatively high level of 5×10^{16} m^{-3} up to very long times > 600 µs. It is interesting to note that this density is comparable to conventional sputtering plasmas and is sustained for a large proportion of time between pulses. The results presented in Figure 4.3.1 allow studying the spatial distribution of the plasma at different times in the pulse.

At very short times of < 50 μs after pulse ignition, the plasma density is high near the target and significantly lower at long distances. As the plasma density reaches its peak at later times > 70 μs, it is observed to be homogeneously distributed throughout the chamber at all distances from 2.5 to 15 cm.
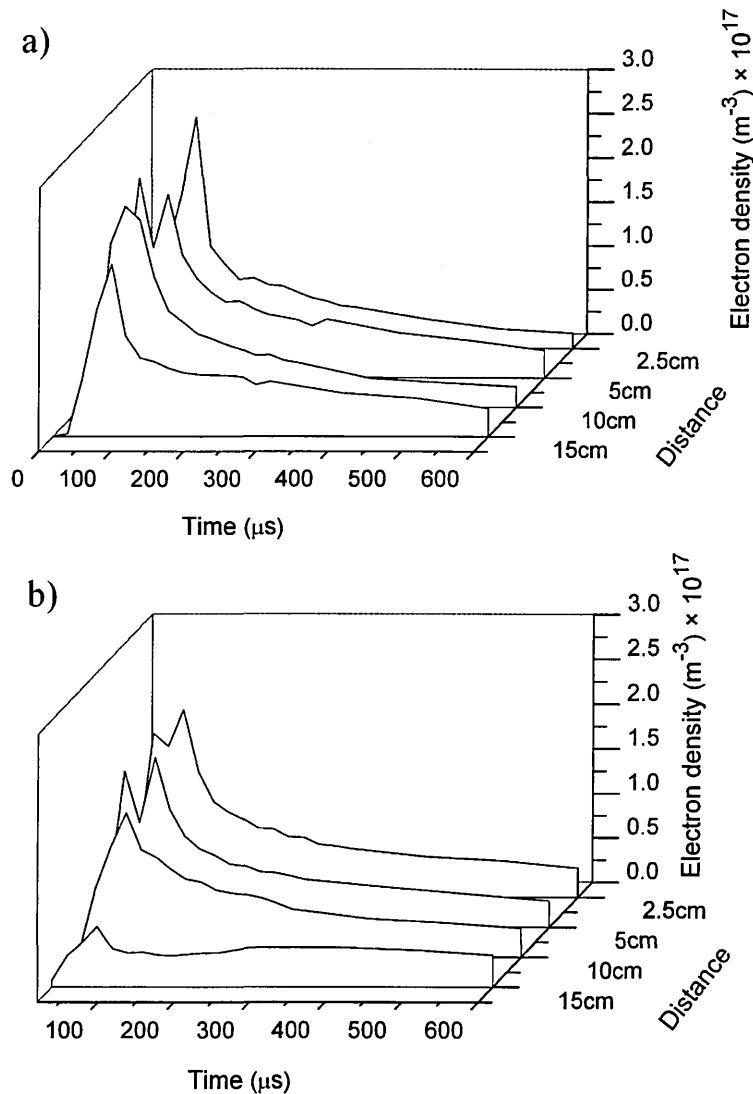
Figure 4.3.1 The electron density as a function of time and distance from the target at a) pressure of 1 Pa and b) pressure of 3 Pa, in HIPIMS plasma discharge with Ti target

At pressure of 3 Pa it is observed that the evolution of the plasma density strongly depends on the distance from the target. During the pulse, at distances below 5 cm, the density is two to three times higher compared to 10 cm and 15 cm, respectively. At the end of the pulse at 70 μs, the highest density of 2.2×10^{17} m^{-3} is detected at 2.5 cm with linear decrease in peak

value with distance (Figure 4.3.1 b). A spatial difference in plasma density is observed up to 300 µs when the plasma distributes itself homogeneously across the chamber with a relatively high density of 5×10^{16} m^{-3}. This indicates that the plasma requires several tens of microseconds to diffuse within the chamber volume, however it then remains homogeneous with distance for several hundreds of microseconds. In contrast, as MS measurements will show in the following sections, the plasma composition depends strongly on distance.

4.3.2 The spatial distribution of the time averaged measurements of IEDF

The spatial resolved time averaged IEDFs of Ti1+ and Ar1+ have been measured to show the ion energies present at the different distances from the target. The first set of measurements was done at pressure of 1 Pa and the second set of measurements was done at pressure of 3 Pa.

The IEDF of Ti1+ ions comprises of two distributions, low energy peak and high energy distribution at low pressure. It has been demonstrated that the high energy tail originates from the period when the pulse is on and shortly after the end of the pulse [89]. The high energy distribution of the metal ions comes from electron impact ionisation of the sputtered metal atoms which have a highly energetic Thompson distribution [83]. At all distances ions with energies up to 100 eV have been detected nevertheless the peak of the high energy distribution, i.e. the number of high energy ions, is reducing with the distance as showed on Figure 4.3.2 a). The reason is that at longer distances the probability of elastic collision between metal and Ar particle increase and consequently the thermalisation of metal particles increases. This is demonstrated by the increase of the main low energy peak with distance as shown on Figure 4.3.2 a).

At lower pressure of 1 Pa the Ar1+ IEDF, shown on Figure 4.3.2 b), contains a small portion of ions with energies up to 80 eV at 2.5 cm and 5 cm distances. At 10 cm distance the highest detected ion energy is 30 eV and at 15 cm and 21 cm it falls below 10 eV. At 2.5 cm distance the IEDF comprises two distributions, low energy peak and high energy distribution. At 5 cm an intermediate distribution is detected. The intermediate distribution is detected at 10 cm and 15 cm, while at 21 cm only a shoulder is detected at the energies

121

of the intermediate distribution. The intermediate distribution could be a demonstration of the gas rarefaction [26]. The low energy peak comprises thermalised ions and the high energy distribution ions are probably created through a process of elastic collisions with the high energy sputtered metal atoms and ions. The energy of the maximum of the low energy peak corresponds well with the plasma potential measured using Langmuir probe [28].
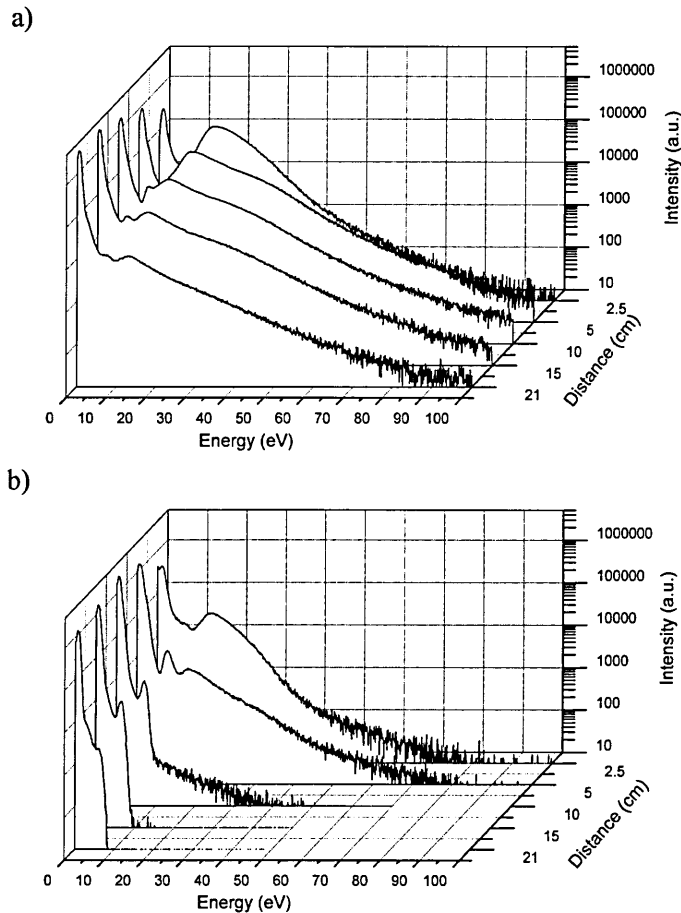
a)

b)

Figure 4.3.2 Time averaged ion energy distribution (IEDF) of a) Ti^{1+} ions and b) Ar^{1+} ions as function of distance at pressure of 1Pa

The IEDFs of Ar1+ and Ti1+ ions measured at various distances at pressure of 3 Pa, shown on Figure 4.3.3, exhibit a different shape compared to low pressure measurements. The high energy distribution is reduced to a shoulder rather than separate distribution. The high energy distribution of the Ti1+ IEDF, shown on Figure 4.3.3 a), strongly reduces with distance. At 21 cm distance the Ti1+ IEDF is a narrow peak comprising ions with energies below 10 eV. At low pressure the mean free path for elastic collisions of metal ions is 1.5 cm and at high pressure it is 0.5 cm. For this reason at high pressure ions

with energies up to 100 eV are detected only up to 5 cm but at longer distance the maximum ion energy is 60 eV, 30 eV and 10 eV at 10 cm, 15 cm and 21 cm, respectively. Mean free path was calculated using equation , where ng is the density of the working gas and σ is the cross section for the elastic collisions [37].

The maximum energy of Ar1+ ions at 5 cm is now reaching 20 eV compared to 80 eV at low pressure at the same distance. From 10 cm distance until 21 cm, the Ar1+ IEDF comprises only one low energy distribution with ions up to 6 eV. Due to the high pressure, the high energy shoulder of the Ar1+ IEDF is detected only at distances of 2.5 cm. Substantially lower Ar1+ ion energies are a consequence of the high density of thermalised Ar particles and high probability of resonant charge exchange.
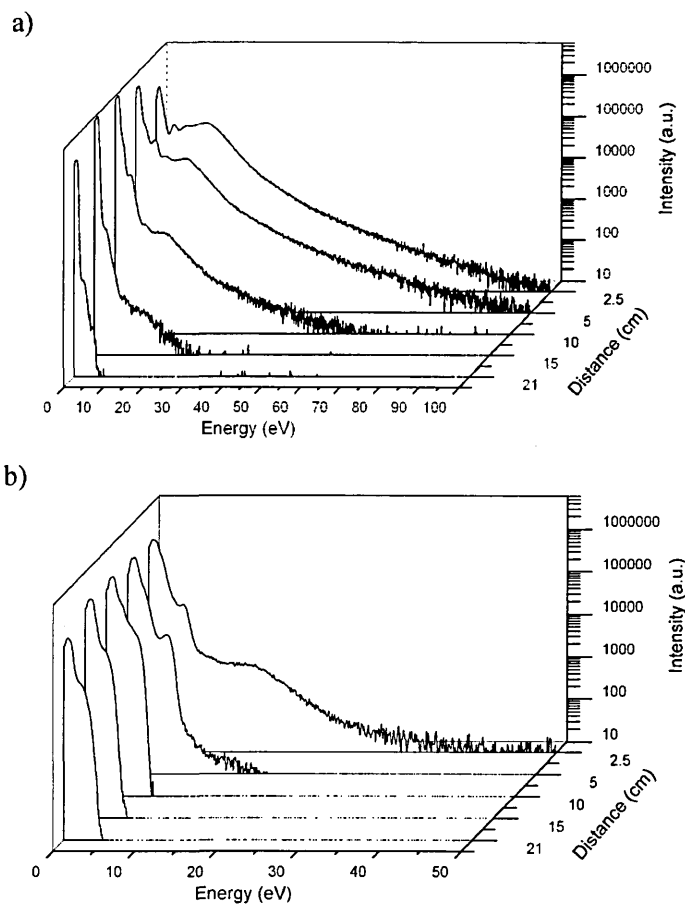
Figure 4.3.3 Time averaged ion energy distribution (IEDF) of a) Ti^{1+} ions and b) Ar^{1+} ions as function of distance at pressure of 3Pa

The flux of Ar^{1+}, Ti^{1+}, Ar^{2+}, Ti^{2+} ions presented at various distances from the target, calculated as integral of IEDF, is shown on Figure 4.3.4. Figure 4.3.4 a) shows that the ion flux measured at low pressure comprises both single and double charged ions and that metal ions are dominant at all

distances. The highest amount of metal ions, both Ti^{1+} and Ti^{2+}, at low pressure measurements is detected at distance of 15 cm. The flux of the Ar^{1+} and Ar^{2+} ions reaches the maximum at 10 cm. Metal to Ar ion ratio at distances up to 10 cm is around 1.5, whereas at distances above 15 cm it is 2.5.
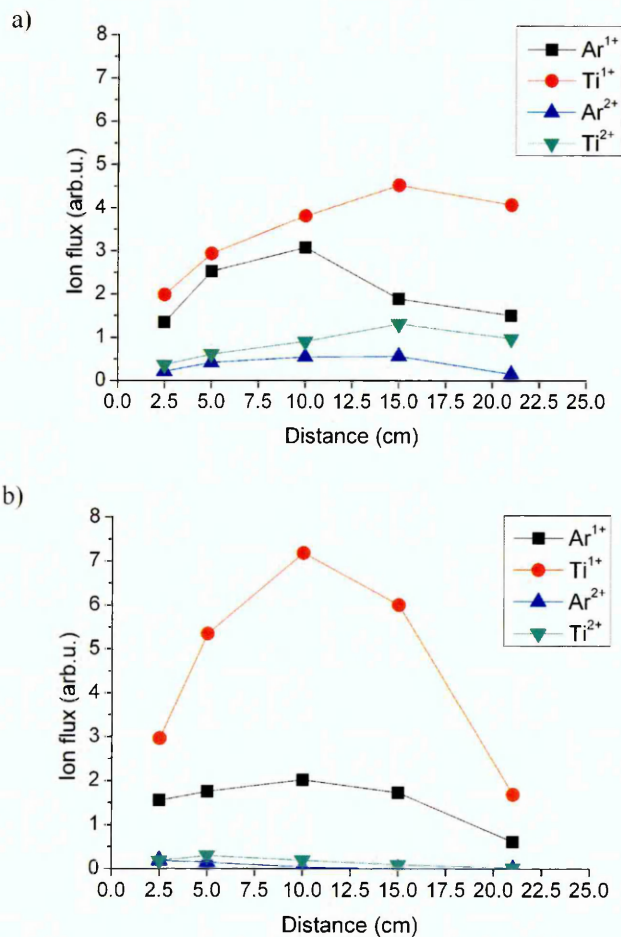
Figure 4.3.4 The ion flux of Ar^{1+}, Ti^{1+}, Ar^{2+}, Ti^{2+} ions as a function of distance for a) pressure of 1 Pa and b) pressure of 3 Pa in HIPIMS plasma discharge

The ion flux measured at high pressure, Figure 4.3.4 b), shows very small representation of doubly charged ions compared to low pressure results. The peak of ion flux is reached at 10 cm, both for metal and Ar singly charged ions. Metal to Ar ion ratio is considerably higher with maximum of 3.5 at 10 cm distance.

The results show that the metal ion-to-Ar ion ratio varies strongly as a function of distance from the target. This could have implications on film growth conditions. Metal ion rich regions would promote film growth with a higher density microstructure due to a high mobility of depositing species.

Regions with high content of Ar ions would experience lower deposition rates due to the low incorporation probability for inert gas.

4.3.3 Temporal and spatial evolution of the ion fluxes in dependence on pressure

The IEDF of Ti^{1+} and Ar^{1+} ions in time resolved mode has been measured at five distances from the magnetron target. Each IEDF provided information about the ion flux, calculated as the integral of the IEDF from 0 to 100 eV, and about the average energy of IEDF. Calculated data of the metal and Ar ion flux as a function of space and time are presented on Figure 4.3.5, measured at pressure of 1 Pa, and Figure 4.3.7, measured at pressure of 3 Pa. The distance scale goes from 2.5 cm to 21 cm, representing the distance from the target, with step of 2.5 cm. The time period is taken from the start of the pulse until 1200 µs from the start of the pulse. The z axis is presented in arbitrary logarithmic units of the measured ion flux. Average energy of the metal and Ar IEDF as a function of time is presented on Figure 4.3.6 and Figure 4.3.8, for pressures of 1 Pa and 3 Pa, respectively. The time scale starts at the beginning of the HIPIMS pulse and ends at 600 µs since after 600 µs the average energy does not change significantly.

At low pressure, during the pulse on-time the measured flux of metal ions is high not just at short distances but also at long distances from the target, Figure 4.3.5 a). At short distances the ion flux is high since metal ions are created as a result of the electron impact ionisation of the metal particles sputtered from the target. Reasonably high metal ion flux measured at long distances from the target could be interpreted as a result of substantial amount of metal ions with high kinetic energies reaching the distance of 21 cm from the target in short time. Average energy of the metal IEDF presented on Figure 8 shows average energy of metal ions of 27 eV at distances from 10 to 21 cm during and shortly after the pulse. After the end of the pulse, the ion density in the vicinity of target has a steep fall, probably due to the proximity of the grounded MS body that acts as a sink for the electrons. At distances from 5 cm to 21 cm metal flux is homogeneously distributed in space. Homogeneous spatial distribution of metal ion flux is detected up to 1200 µs with relatively higher density around 15 cm.
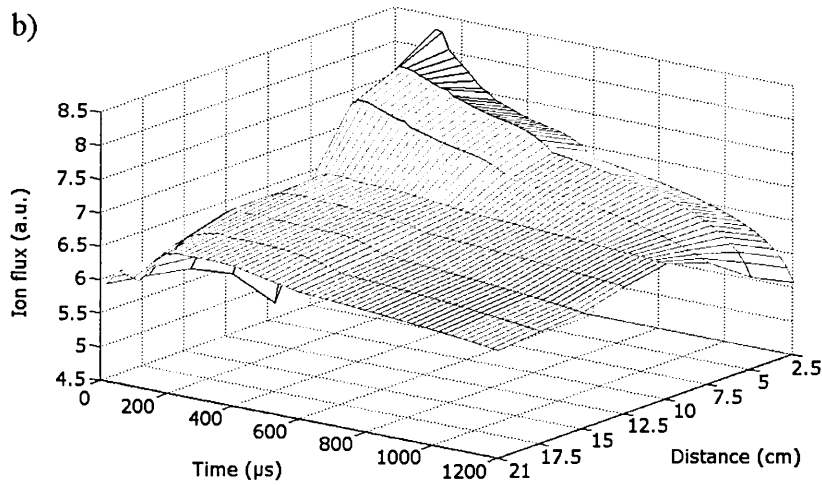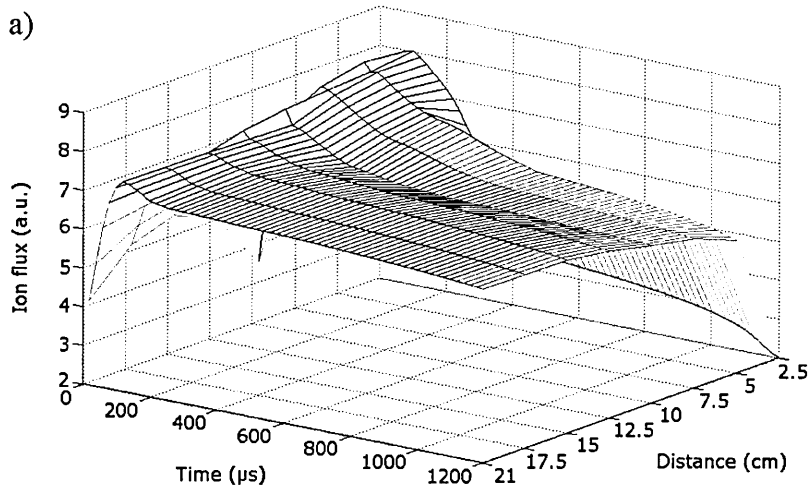
a)

b)

Figure 4.3.5 The ion flux of a) Ti^{1+} and b) Ar^{1+} as a function of time and distance at pressure of 1 Pa in HIPIMS plasma discharge with Ti target

The time evolution of the Ar^{1+} ion flux at 1 Pa, Figure 4.3.5 b), shows a high density of Ar^{1+} ions near the target region during the pulse on-time and substantially lower density at longer distances. In the post discharge the density of Ar^{1+} ions is steadily falling, faster in the near target region and slower at longer distances. At 1200 μs the highest density of Ar ions is present at 10 cm that indicates long lifespan of Ar ions that could be the explanation for the high Ar $^{1+}$ ion flux at 10 cm measured by the time averaged measurements on Figure 4.3.a).

Figure 4.3.6 The average energy of a) Ti^{1+} IEDF and b) Ar^{1+} IEDF as a function of time at different distances from the target at pressure of 1 Pa

Figure 4.3. represents the average energies of the Ar and metal IEDFs. The average energy of Ti^{1+} ions, Figure 4.3.6 a), indicates that the high ion flux observed at longer distances (Figure 4.3.5 a)) is a result of high energy ions that travel with high velocity. Average energy of metal ions at distances above 10 cm at the end of the pulse is around 26 eV and at distances up to 5 cm it is below 18 eV. Explanation for this unusual result could be due to chamber setup. The orifice of the mass spectrometer was positioned facing the centre of the magnetron target, where the erosion rate is smallest, and not facing the racetrack therefore at small distances only sputtered metal particles deflected

in a collision with surrounding particles entered the mass spectrometer. This could be the reason for the low values of average energy at short distances observed in Figure 4.3.6 a).

The average energy of Ar ions shows strong dependence on the distance, shown on Figure 4.3.6 b). The peak average energy at distances of 2.5 cm and 5 cm is 11 eV and 7 eV, respectively, while at longer distances it is below 4 eV. Higher Ar ion energies arise from elastic collision with sputtered material in the target vicinity where the density of sputtered material is higher due to gas rarefaction.
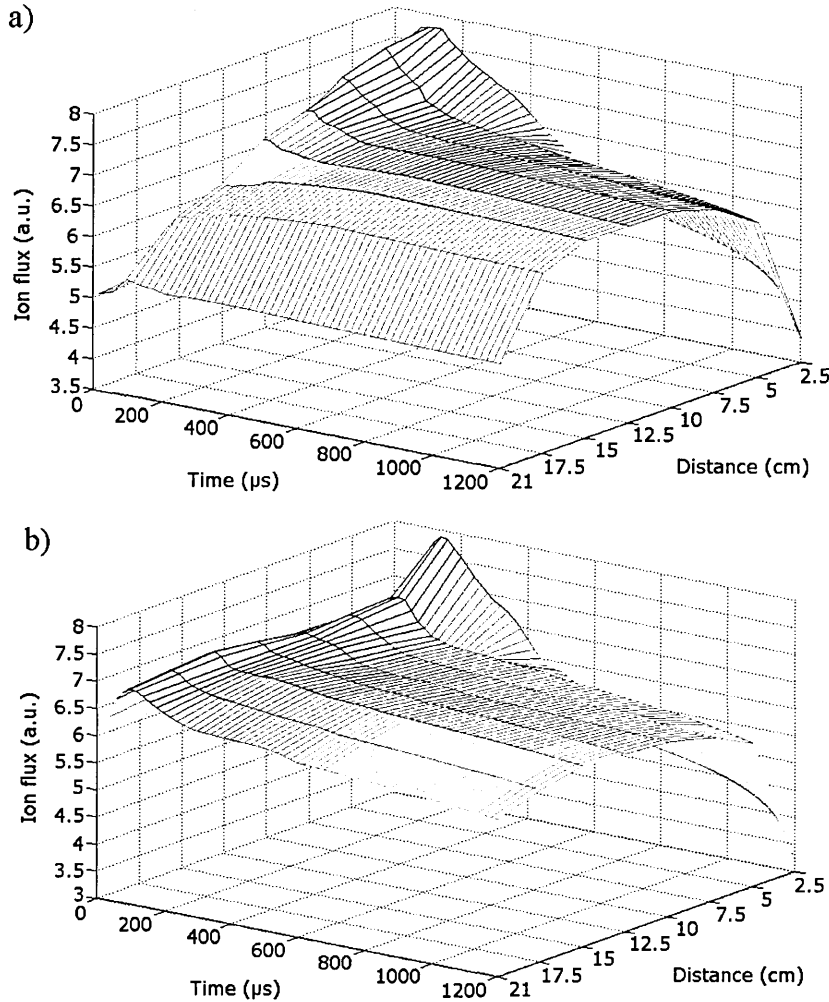
Figure 4.3.7 The ion flux of a) Ti^{1+} and b) Ar^{1+} as a function of time and distance at pressure of 3 Pa in HIPIMS plasma discharge with Ti target

The metal ions diffusion is influenced by the high working pressure as shown on Figure 4.3.7 a). During the pulse metal ion flux is high in the vicinity of the target and as the distance increases the ion flux linearly decreases. It is in contrast with the low pressure measurements, where high energy ions were able to diffuse faster. Due to the high pressure and short mean free path of 0.5

128

cm, high energy ions are localized to the near target region during the pulse, as shown on Figure 4.3.8 a). On Figure 4.3.8 a) the time evolution of the average energy of metal ions for five distances from the target at pressure of 3 Pa is shown. It is shown that the average energy of metal ions strongly depends on the distance. At distance of 2.5 cm, 5 cm and 10 cm the peak average energy is reached at 70 μs and the peak value is 12 eV, 10 eV and 6 eV, respectively. At distances of 15 cm and 21 cm the peak of 3 eV and 2 eV is reached at 90 μs from the start of the pulse.

The measurements of the ion flux at high pressure for Ar^{1+} ions, Figure 4.3.7 b), show a considerably different spatial evolution. The density of Ar^{1+} ions is very high at 2.5 cm, whereas at 5 cm the density is reduced and remains constant until 21 cm. This could be attributed to mobile electrons reaching a distance of 15 cm during the pulse on phase. Figure 4.3.9 compares the electron density and ion flux densities, at pressure of 3 Pa and at 80 μs. The electron density linearly decreases with distance, whereas the metal ion flux is exponentially reduced with distance. This indicates a possibility that an almost constant Ar ion flux density in space originates from electrons that, due to higher mobility, reach distances above 10 cm and ionize Ar atoms that are present there. At the same time, the metal ion content is low due to their slower diffusion from the target vicinity. The electron density shows peak electron density of 1.5×10^{17} m^{-3} at distances up to 10 cm, and peak density of 7×10^{16} m^{-3} at 15 cm. Ideally the sum of Ar and Ti ions should be equal to the total density of electrons. The discrepancy could not be explained and requires additional work. In the post-discharge, the Ar ion flux, constituted thermalised ions as shown on Figure 4.3.8 b), is detected in region from 5 cm to 15 cm. Again the long lifespan of ions in this region corresponds well with the shape of ion flux from the time averaged measurements on Figure 4.3.4 b).

The distribution of the metal ion flux at low pressure and Ar ion flux at both low and high pressure in the post discharge is homogeneous, only the distribution of metal ion flux at high pressure shows a highly localized character. The long life span of both metal and Ar ions measured with MS and reasonably high electron density up to 1 ms after the start of the pulse measured with LP indicates it is not a consequence of mistake caused by longer lifespan of ions in the MS or electrical interference in the LP. The long

life span at distance between 10 cm and 21 cm is very hard to explain with a simple diffusion.
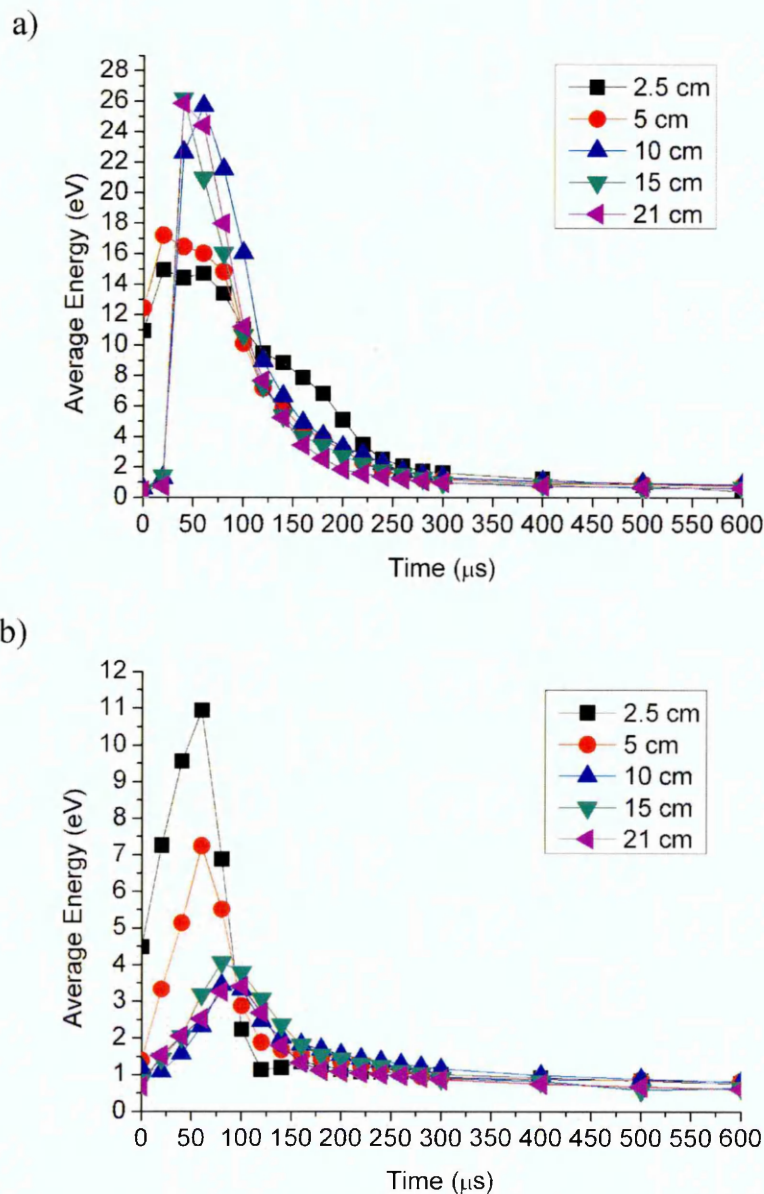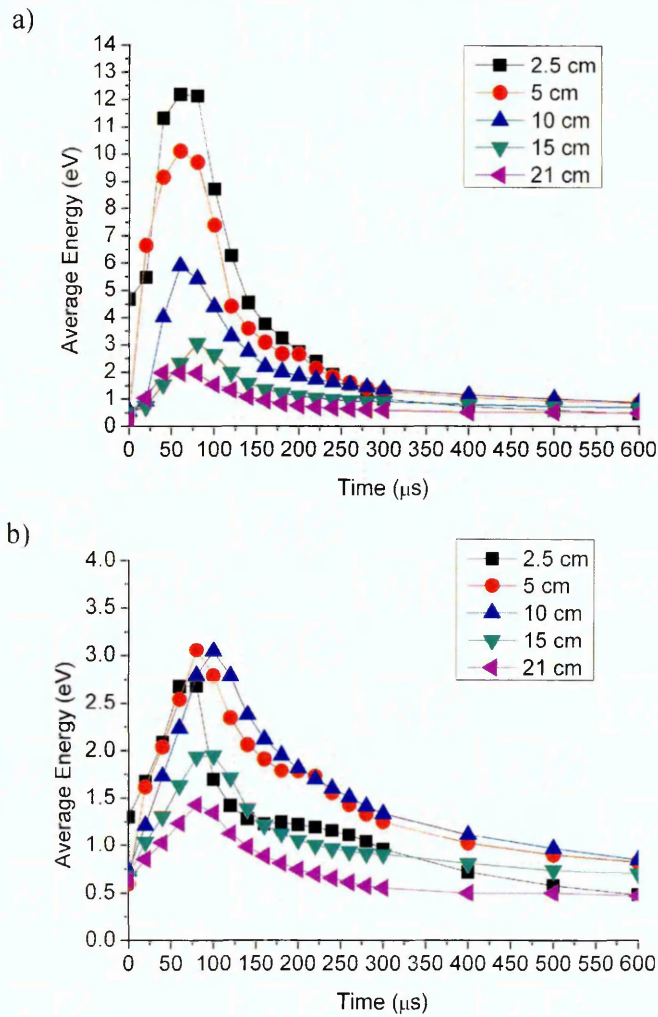
a)

b)

Figure 4.3.8 The average energy of a) Ti^{1+} IEDF and b) Ar^{1+} IEDF as a function of time at different distances from the target at pressure of 3 Pa
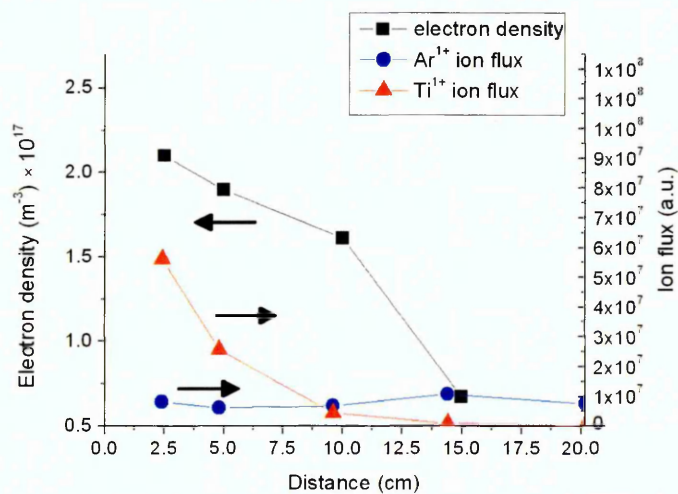
Figure 4.3.9 Comparison of the spatial distribution of the electron density and ion fluxes at pressure of 3 Pa and at 80 μs

4.3.4 Temporal and spatial evolution of the IEDF of metal and Ar ions at pressure of 1 Pa

In the previous chapter temporal and spatial evolution of plasma parameters, such as ion flux and average energy, during and after the pulse was presented. This chapter contains the results from the life-span and time evolution of metal and Ar ion energy distribution function (IEDF) measured at different distances from the target. The evolution of metal IEDF is presented on the Figure 4.3.10 with ascending time scale and on Figure 4.3.11 with descending time scale. The evolution of Ar IEDF is presented on the Figure 4.3.12 with ascending time scale and on Figure 4.3.13 with descending time scale. Figures with descending time scale are shown in order to present the reduction of the intensity of the IEDF in the post-discharge.

The metal IEDF comprises of two groups of ions, low energy group with peak between 1 and 2 eV and high group with peak at 15 eV. In the beginning of the pulse IEDF mainly comprises of high energy group while after 80 μs IEDF is dominated by low energy group. Group of ions with high energies originate from Thompson distribution of sputtered metal [83] atoms and low energy group originates from metal ion thermalisation in collisions with Ar particles that have energies below 1 eV. The effect of thermalisation of the metal IEDF at short distances is visible only after the end of the pulse due to gas rarefaction [26] in the vicinity of the target during the pulse. At the end of the pulse, Ar diffuses towards the target and the thermalisation takes place. At longer distances, where the Ar rarefaction is reduced, the thermalisation is visible during the pulse. The peak of the low energy group of ions is in good agreement with Langmuir probe measurements of the plasma potential presented in Chapter 4.1.3.

131
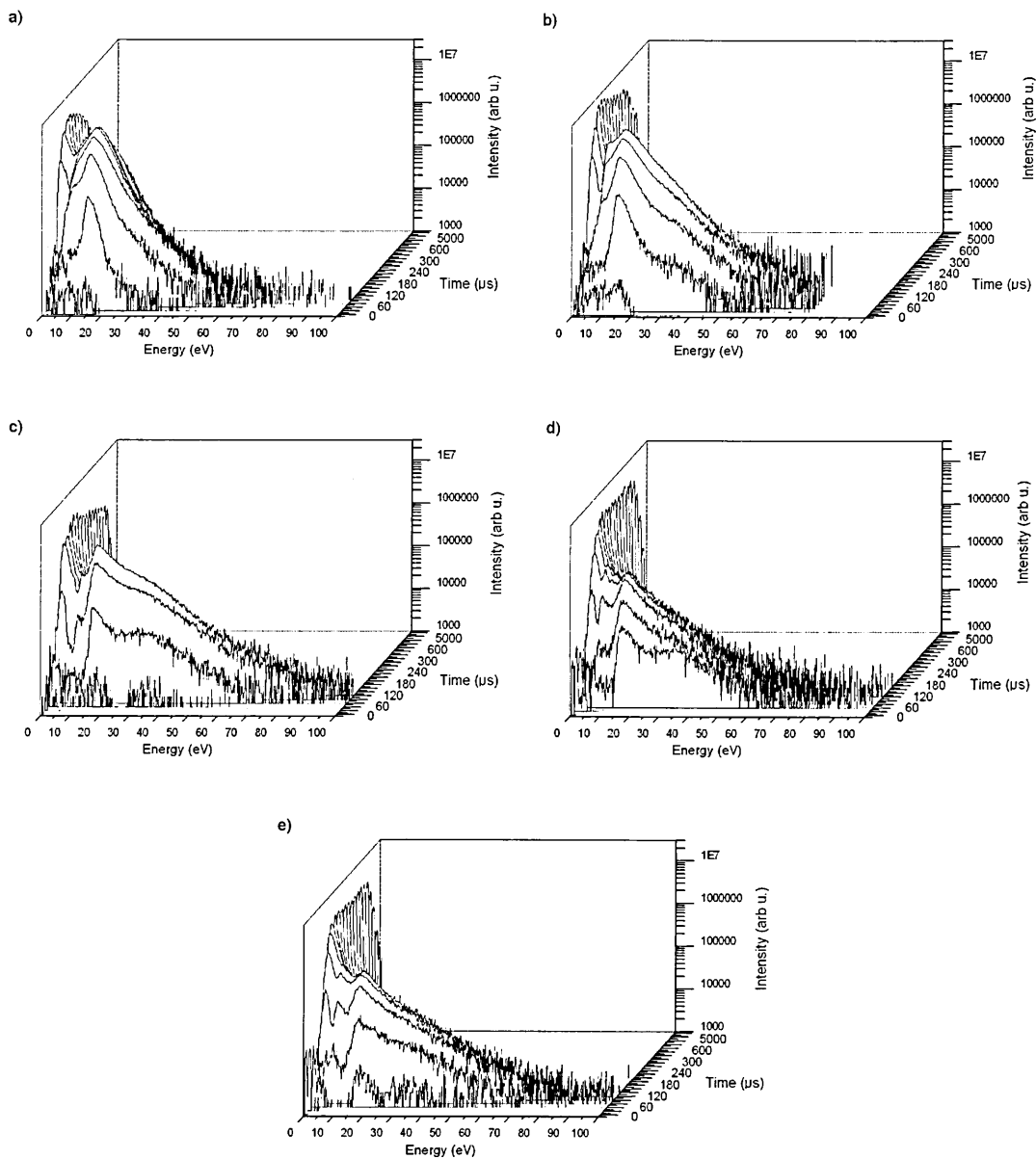
Figure 4.3.10 The temporal evolution of the ion energy distribution function of the Ti^{1+} ions at pressure of 1 Pa during HIPIMS of Ti, at different distances from the magnetron target; a) 2.5 cm, b) 5 cm, c) 10 cm, d) 15 cm and e) 21 cm

After the end of the pulse, both low and high energy group of ions exponentially decrease with time, as shown on Figure 4.3.11 at all distances. The high energy group decays at a faster rate compared to the low energy group. Furthermore the peak of the high energy group shifts from around 15 eV to 7 eV . Last detection time of Ti^{1+} ions at short distances is 400 μs at 2.5 cm and 1200 μs at 5 cm distance. At longer distances from the target the last detection time is increased and it is 5 ms at distance of 10 cm, and for 15 cm

and 21 cm distance a small signal of Ti^{1+} ions is detected at 9900 µs that is 10 µs before the start of the consequent pulse.

Figure 4.3.11 The temporal evolution of the ion energy distribution function of the Ti^{1+} ions at pressure of 1 Pa during HIPIMS of Ti, at different distances from the magnetron target; a) 2.5 cm, b) 5 cm, c) 10 cm, d) 15 cm and e) 21 cm with descending time scale
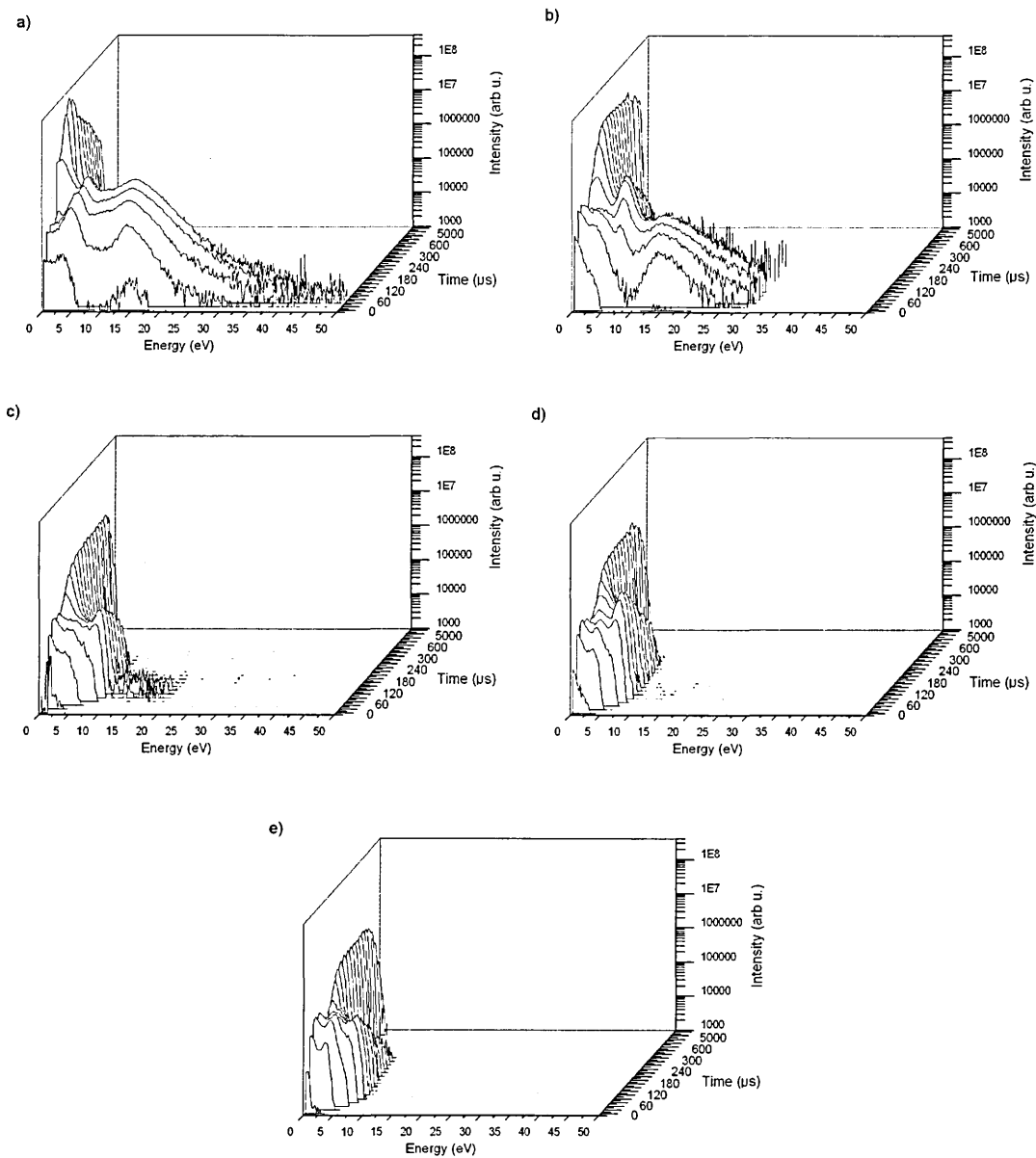
Figure 4.3.12 The temporal evolution of the ion energy distribution function of the Ar^{1+} ions at pressure of 1 Pa during HIPIMS of Ti, at different distances from the magnetron target; a) 2.5 cm, b) 5 cm, c) 10 cm, d) 15 cm and e) 21 cm

The life-span and time evolution of Ar ion energy distribution function (IEDF) arriving at different distances from the target is shown on Figure 4.3.12 with ascending time scale. The shape and maximum energy of Ar ions strongly depends on distance. At short distances up to 5 cm Ar ion IEDF comprises of low energy and high energy group with ions with energy up to 50 eV while at longer distances two groups of ions are still visible but negligible amount of ions with energies above 10 eV is detected. High energy group of

134

ions originate from collisions of Ar ions with highly energetic metal particles in which Ar ions gain kinetic energy. High intensity of high energy Ar ions in target vicinity stem from increased probability for collision with high energy particles since the highest amount of high energy metal ions is detected in the region up to 5 cm from the target, as shown on Figure 4.3.10.

Figure 4.3.13 The temporal evolution of the ion energy distribution function of the Ar^{1+} ions at pressure of 1 Pa during HIPIMS of Ti, at different distances from the magnetron target; a) 2.5 cm, b) 5 cm, c) 10 cm, d) 15 cm and e) 21 cm with descending time scale

On Figure 4.3.13 the decay of the Ar IEDF intensity is shown. After the end of the pulse Ar IEDF is dominated with low energy thermalised group of ions. Low energy group of ions with energies below 1 eV is a product of

135

thermalisation of Ar ions through collisions with Ar atoms that have energy equivalent to room temperature. The position of the peak of the low energy group of ions is in good agreement with Langmuir probe measurements of the plasma potential presented in Chapter 4.1.3.

The last detection time of Ar ions at 2.5 cm distance is 600 µs. At 5 cm it is 1.2 ms and at 10 cm the last ion is detected at 5 ms. For distances of 15 cm and 21 cm small signal of Ar ions could be detected up to 9.9 ms that is 10 µs before the start of the subsequent pulse. The reason for short lifespan of Ar ions at short distances could be the proximity of mass spectrometer that is connected to the ground and acts as an anode that attracts the electrons and reduces the life-span of ions at short distances.

4.3.5 Temporal and spatial evolution of the IEDF of metal and Ar ions at pressure of 3 Pa

The conditions in plasma at high pressure are considerably different than at low pressure. At high pressure of 3 Pa the density of Ar atoms that have room temperature energies is greater. The mean free path of metal ions is shorter and consequently lower energies at longer distances can be expected. High pressure conditions are reducing the speed of the ion diffusion in the chamber and reducing the losses to the walls thus possibly leading to the longer life-spans.

The temporal evolution of Ti^{1+} IEDF at five distances from the target is presented on the Figure 4.3.14 . In the vicinity of the target, up to 5 cm, the energies of the Ti^{1+} ions reach up to 80 eV. At longer distances both intensity and highest energy of metal ions of the high energy group is reduced compared to short distances. At distance of 2.5 cm the high energy ions are measured at times between 60 µs and 80 µs i.e. at the end of the pulse. At distance of 5 cm, 10 cm and 15 cm high energy ions are detected in the time interval between 80 µs and 120 µs. Delayed detection of high energy ions could be attributed to the diffusion time so the bulk of the plasma is reaching longer distances at later times. At short distance two groups of ions are detected during first 80 µs. At distance of 10 cm and 15 cm the high energy group of ions doesn't have a separated peak rather it is a shoulder of the low energy group. At longest distance no high energy group of ions is detected.
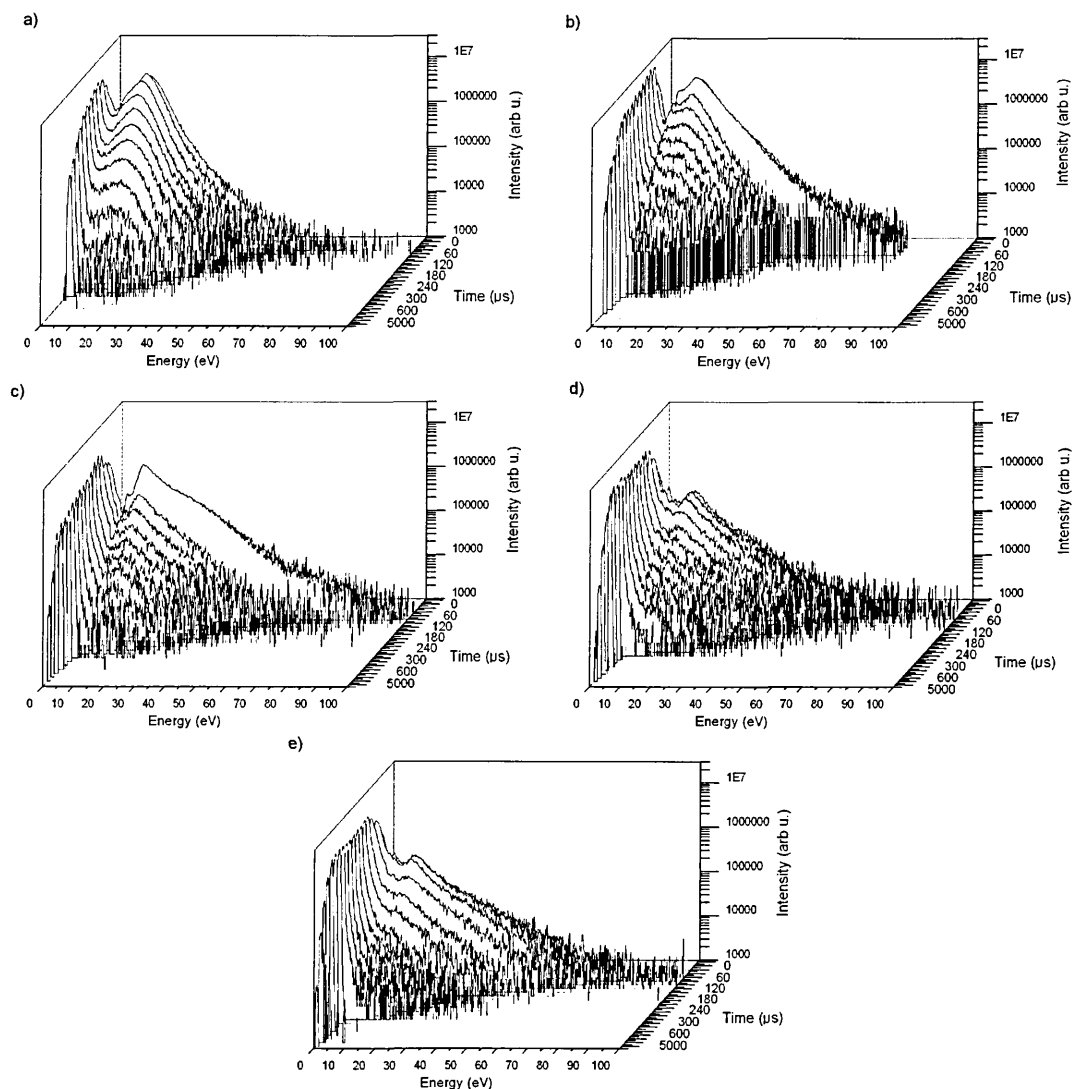
136

Figure 4.3.14 The temporal evolution of the ion energy distribution function of the Ti^{1+} ions at pressure of 3 Pa during HIPIMS of Ti, at different distances from the magnetron target; a) 2.5 cm, b) 5 cm, c) 10 cm, d) 15 cm and e) 21cm

Figure 4.3.15 represents measured temporal evolution of the Ti^{1+} IEDF at pressure of 3 Pa with time scale in descending order to demonstrate the post-discharge of the Ti^{1+} IEDF. In the post-discharge the high energy ions decay exponentially in time. At distance of 2.5 cm last detection time of the Ti^{1+} ions is 600 µs and at distance of 5 cm it is 5 ms from the start of the pulse. At distances longer than 10 cm metal ions are detected 10 µs before the start of the next pulse.
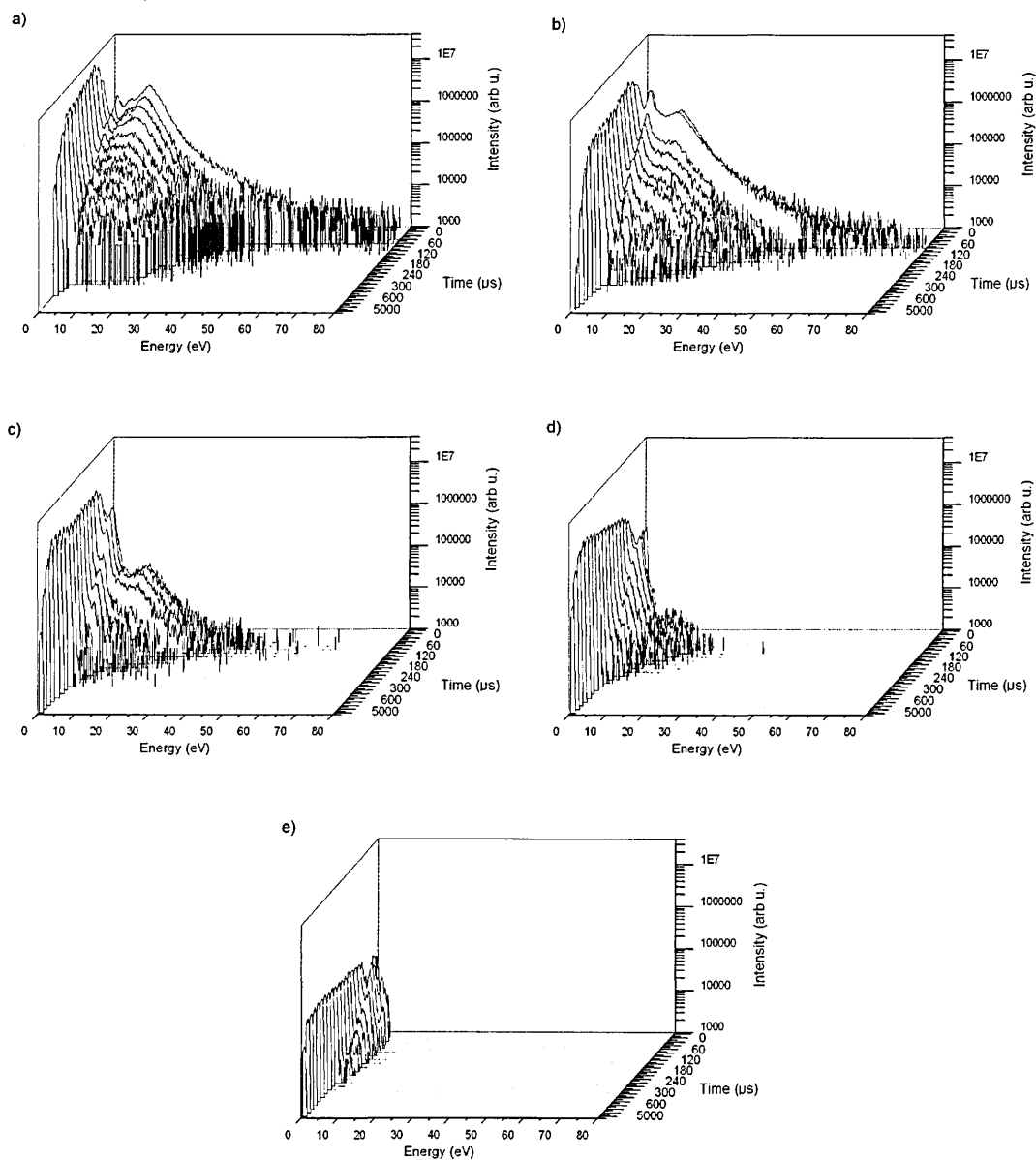
Figure 4.3.15 The temporal evolution of the ion energy distribution function of the Ti^{1+} ions at pressure of 3 Pa during HIPIMS of Ti, at different distances from the magnetron target; a) 2.5 cm, b) 5 cm, c) 10 cm, d) 15 cm and e) 21 cm with descending time scale

The intensity of metal ion signal at 9.9 ms, at distance of 21 cm is 20 % of the maximum intensity detected during the pulse at this distance. At distance of 15 cm and 10 cm the intensity at the end of the pulse is 5 % and 1 % of maximum intensity detected at each distance, respectively. In Figure 4.3.15 d) it can be seen that the intensity of metal ions detected at distance of 15 cm at 9.9 ms is higher than intensities of metal ions at the same time at

distances of 10 cm and 21 cm. The intensity is exactly 4.5 and 7 times higher at 15 cm than at 10 cm and 21 cm, respectively.

This data indicate that diffusion of metal particles at high pressure of 3 Pa is slowed sufficiently that 1 % of maximum intensity of metal ions is detected at the beginning of the consequent pulse. The existence of ions in the chamber up to 10 ms could enhance the diffusion of the ions generated in the consequent pulse. This has been demonstrated using an additional plasma source to create background plasma by Konstantinidis et al. [14]. Furthermore the impinging of the metal particles not just during the pulse but equally between the pulses could be beneficial to reduce residual stresses and inhibit the incorporation of contaminants in the coating [57].

Figure 4.3.16 shows the temporal evolution of Ar^{1+} IEDF at pressure of 3 Pa, at different distances from the target. Ar IEDF comprises mainly of low energy ions with exception of IEDF at distance of 2.5 cm where small signal of high energy ions is detected during the pulse. Due to high pressure of 3 Pa the gas rarefaction effect is less pronounced and even at distance of 5 cm maximum energy of ions is 10 eV compared to 30 eV at the same distance at pressure of 1 Pa.

It is interesting to note that first weak signal of low energy ions is detected in the first 20 μs from the start of the pulse at all distances. These ions could be created by the electron impact ionisation by the electrons that are created in the start of the pulse as secondary electrons that could reach up the distance of 21 cm from the target following magnetic field lines of the unbalanced magnetron.
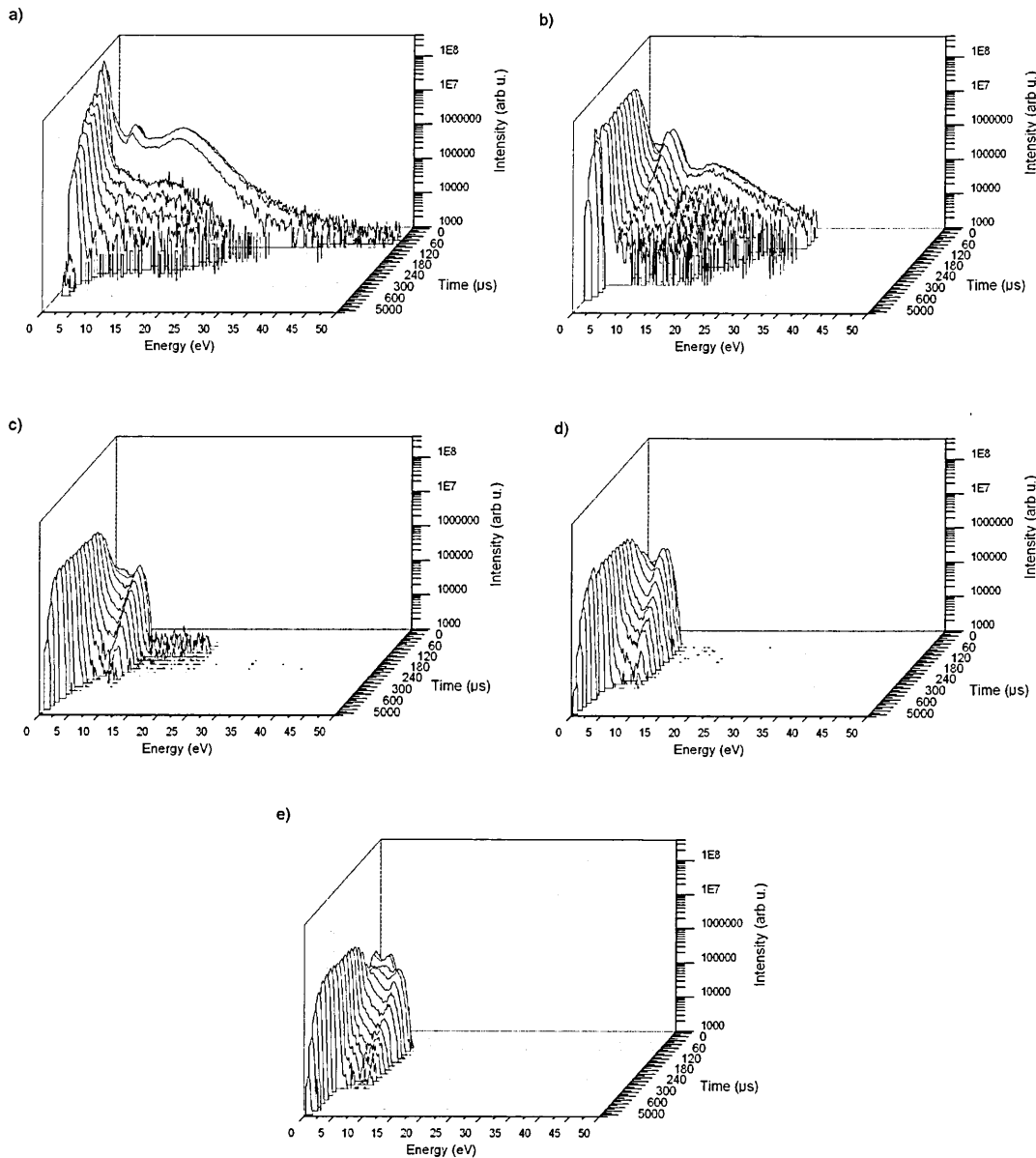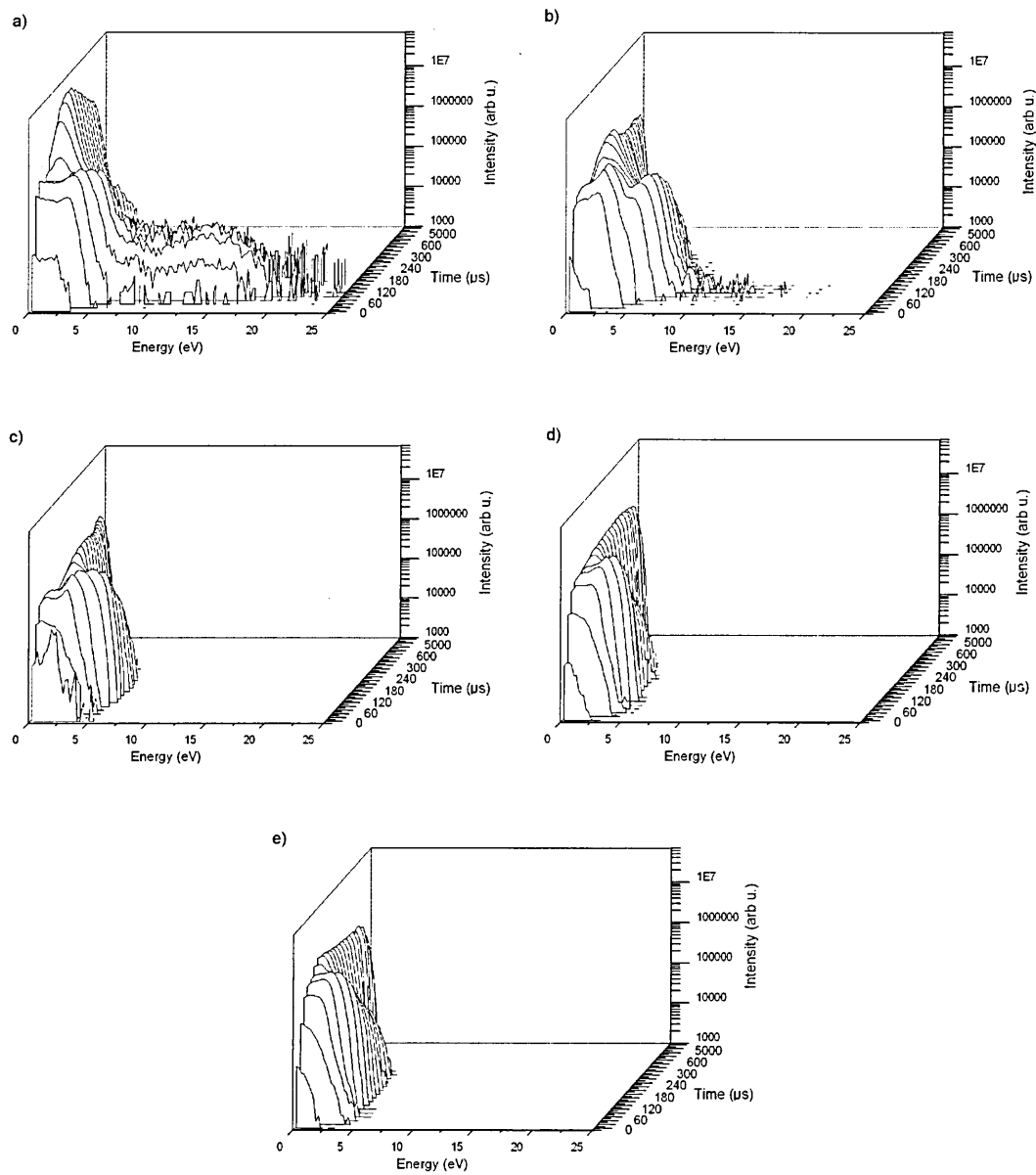
Figure 4.3.16 The temporal evolution of the ion energy distribution function of the Ar^{1+} ions at pressure of 3 Pa during HIPIMS of Ti, at different distances from the magnetron target; a) 2.5 cm, b) 5 cm, c) 10 cm, d) 15 cm and e) 21cm

Figure 4.3.17 shows the temporal evolution of the Ar^{1+} IEDF with time scale in descending. After the end of the pulse both low energy group of ions and high energy group of ions decrease exponentially with time. Last signal of Ar IEDF at 2.5 cm is detected at 600 μs from the start of the pulse and at distances of 5 cm and 21 cm small signal is detected at 5 ms. Last signal of Ar ions at distances of 10 cm and 15 cm is detected at 9.9 ms.
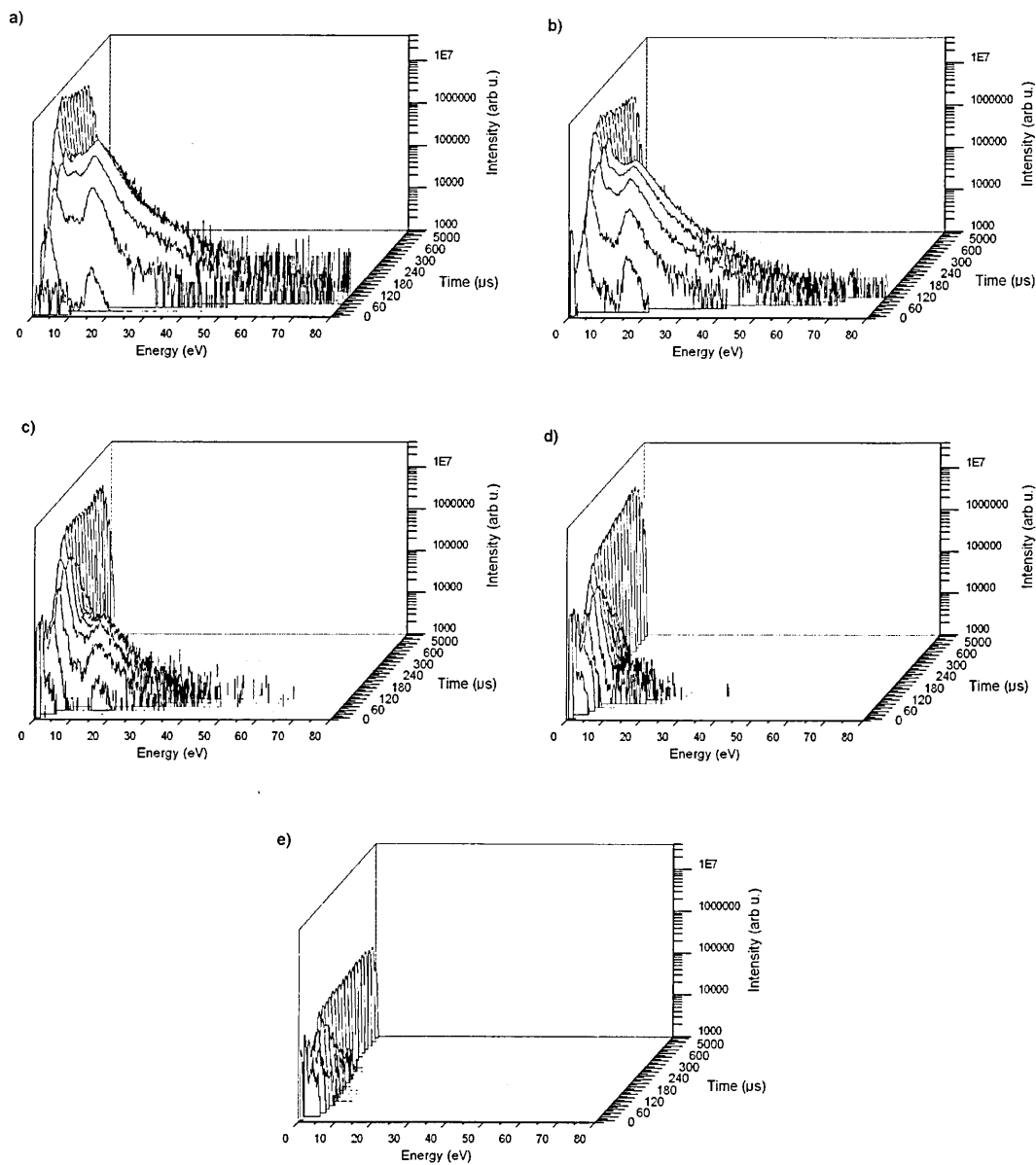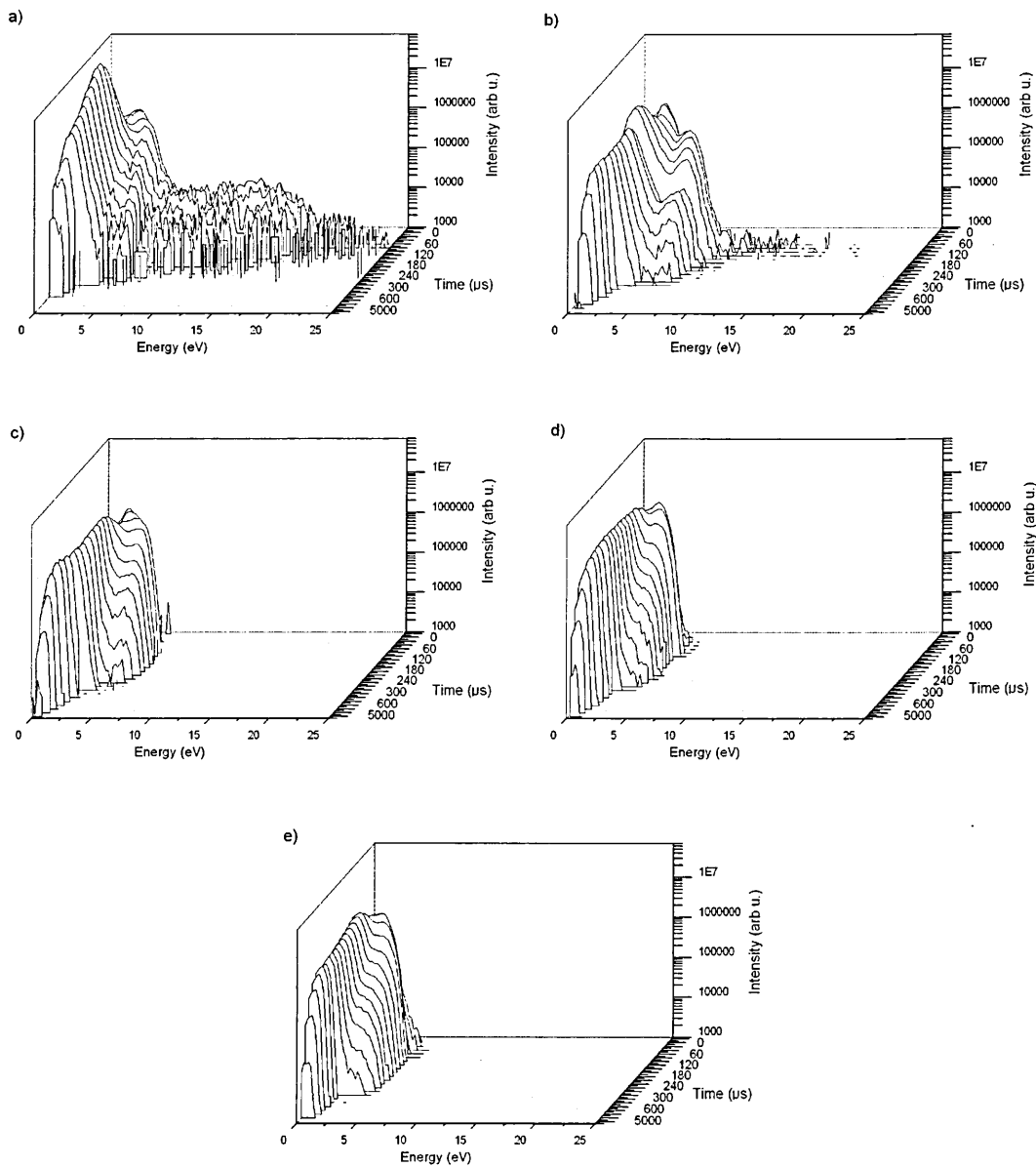
Figure 4.3.17 The temporal evolution of the ion energy distribution function of the Ar^{1+} ions at pressure of 3 Pa during HIPIMS of Ti, at different distances from the magnetron target; a) 2.5 cm, b) 5 cm, c) 10 cm, d) 15 cm and e) 21 cm with descending time scale

The time resolved measurements of the IEDF show the temporal evolution of the ion energies at different distances from the target and the life span of metal and Ar ions between the pulses. Low pressure measurements show high energy metal ions with energies up to 100 eV detected at all distances while energies of metal ions at high pressure showed a strong dependence on distance due to short mean free path of 0.5 cm. The IEDF of Ar ions at low pressure and at short distances comprise two group of ions, low

141

energy and high energy group with ion energies reaching 50 eV. At high pressure low energy group has intensity two orders of magnitude greater than high energy group of ions with maximum energy of ions of 25 eV. High energy tail of Ar ions is consequence of gas rarefaction in the target vicinity and elastic collision with hot sputtered material. At low pressure the target vicinity is mainly populated with sputtered particles and Ar ions thermalise with hot metal particles resulting in high energy tails while at distances longer than 10 cm gas rarefaction is less distinct and ions have energies up to 10 eV. The gas rarefaction at high pressure is less apparent and energies of Ar ions are lower.

4.3.6 Summary

The ion energy distribution function of Ti^{1+}, Ti^{2+}, Ar^{1+} and Ar^{2+} ions with a spatial and temporal resolution was successfully measured. The time averaged measurements show the dominance of the metal ions in the plasma at all distances both for low and high pressure. At low pressure both single and double charged metal and Ar ions are detected while at high pressure only single charged metal and Ar ions are detected. The peak of the total ion flux has been detected in the region between 10 cm and 15 cm. The long lifespan of ions in that region, measured with the time resolved measurements, could lead to high ion fluxes in that region. The long lifespan of the ions could be beneficial for the coating deposition through long period of ions impinging on the substrate reducing the stress and reducing the deposition of contaminants.

The spatial distribution of Ar^{1+} ion flux has been found to be homogenous at both pressures in the post discharge. In contrast, the spatial distribution of Ti^{1+} ion flux depends on pressure. At low pressure it is homogeneous. At high pressure metal ions appear with high concentration at intermediate distances and decrease sharply near the chamber walls.

The lifespan of metal and Ar ions at low pressure is up to 5 ms at distances below 15 cm, whilst at distances above 15 cm a small signal of ions is detected before the start of consequent pulse. The long lifespan of Ar and metal ions at low pressure are in good agreement with highest ion fluxes measured in a time averaged mode presented in chapter 4.3.2. Long life-

spans up to the consequent pulse are measured in high pressure measurements at distance 10 cm and 15 cm for Ar ions and at distance above 10 cm for metal ions. The intensity of last metal ions signal at distance of 15 cm is 5 % of maximum intensity detected at particular distance. The long life spans of ions in the time resolved measurements are in good agreement with ion fluxes calculated from time averaged measurements. The constant bombardment of metal particles not just during the pulse but equally between the pulses could be beneficial to reduce residual stresses and inhibit the incorporation of contaminants in the coating.

4.4 Temporal evolution of the ion fluxes in dependence on pressure for various elements in HIPIMS plasma discharge

In chapter 4.2 the life-span of metal ions in the high power impulse magnetron sputtering (HIPIMS) was measured up to 5 ms from the start of the pulse. To investigate the influence of the ion mass, ionisation energy and sputter yield on the time evolution and life span of singly and doubly charged metal and Ar ions in the HIPIMS plasma discharge the most frequently used materials for thin film deposition Carbon (C), Aluminium (Al), Titanium (Ti), Chromium (Cr), Copper (Cu) and Niobium (Nb) have been used. The ion energy distribution function (IEDF) of each material was measured using energy resolved mass spectrometer in time resolved mode. The targets used in HIPIMS plasma discharges had a purity of 99.9 % and the setup of the mass spectrometer was the same for all materials. To investigate the influence of working gas pressure on the time evolution of ion fluxes, measurements have been performed at two pressures, 0.3 Pa and 3 Pa.

The pulse length was 70 µs and the repetition frequency was 100 Hz. The peak discharge current was kept constant for all measurements at 40 A that is equivalent to a current density of 1 A/cm^2. The target discharge current and voltage for each element are shown on Figure 4.4.1 for low pressure measurements and on Figure 4.4.2 for high pressure measurements. Figure 4.4.2 shows that the shape of the discharge voltage is the same since it is regulated by the power supply. The shape and the ignition time of the discharge current is different for each element. For most of the materials, the current starts to rise around 20 µs from the start of the pulse except for Ti where the discharge started with delay of 40 µs from the start of the pulse. Time resolved measurements obtained using optical emission spectroscopy by Ehiasarian et al. [18, 16] showed that the discharge goes from Ar plasma phase to a metal plasma phase. Short time of the HIPIMS pulse with Ti target could lead to lower metal density due to shorter time between end of the Ar plasma phase and end of the pulse. Consequently it is possible to expect lower intensity of Ti ion flux. The discharge current shape can be described as a triangle with exponential rise of the current until 70 µs, when at the end of

144

the pulse the voltage is turned off, when the current reaches peak discharge current of 40 A. After the end of the pulse the current linearly reduces to zero within 15 μs. The shape of discharge current for the high pressure measurements differs from the low pressure measurements. The rise of the current occurs within 10 μs from the start of the pulse. For Al, Cr, Cu and Nb target material the shape of the discharge current indicated that saturation has occurred. After initial rise up to value of 40 A the current saturates until the end of the pulse when it is reduced linearly to zero. For C and Ti the discharge current has a triangular shape as at low pressure measurements.
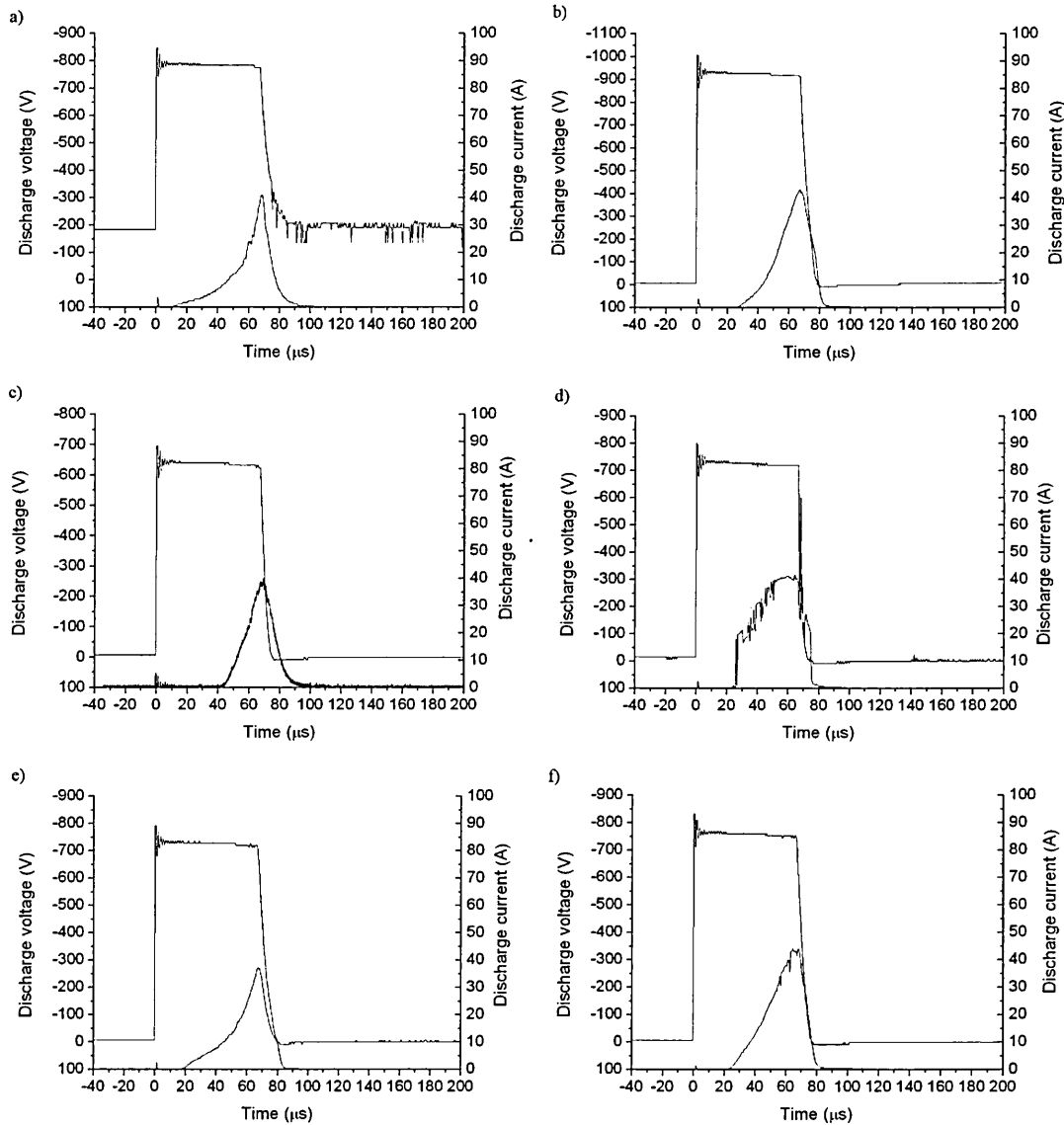
Figure 4.4.1 The discharge current and voltage during HIPIMS plasma discharge for a) C, b) Al c) Ti, d) Cr, e)Cu and f)Nb target at pressure of 0.3 Pa
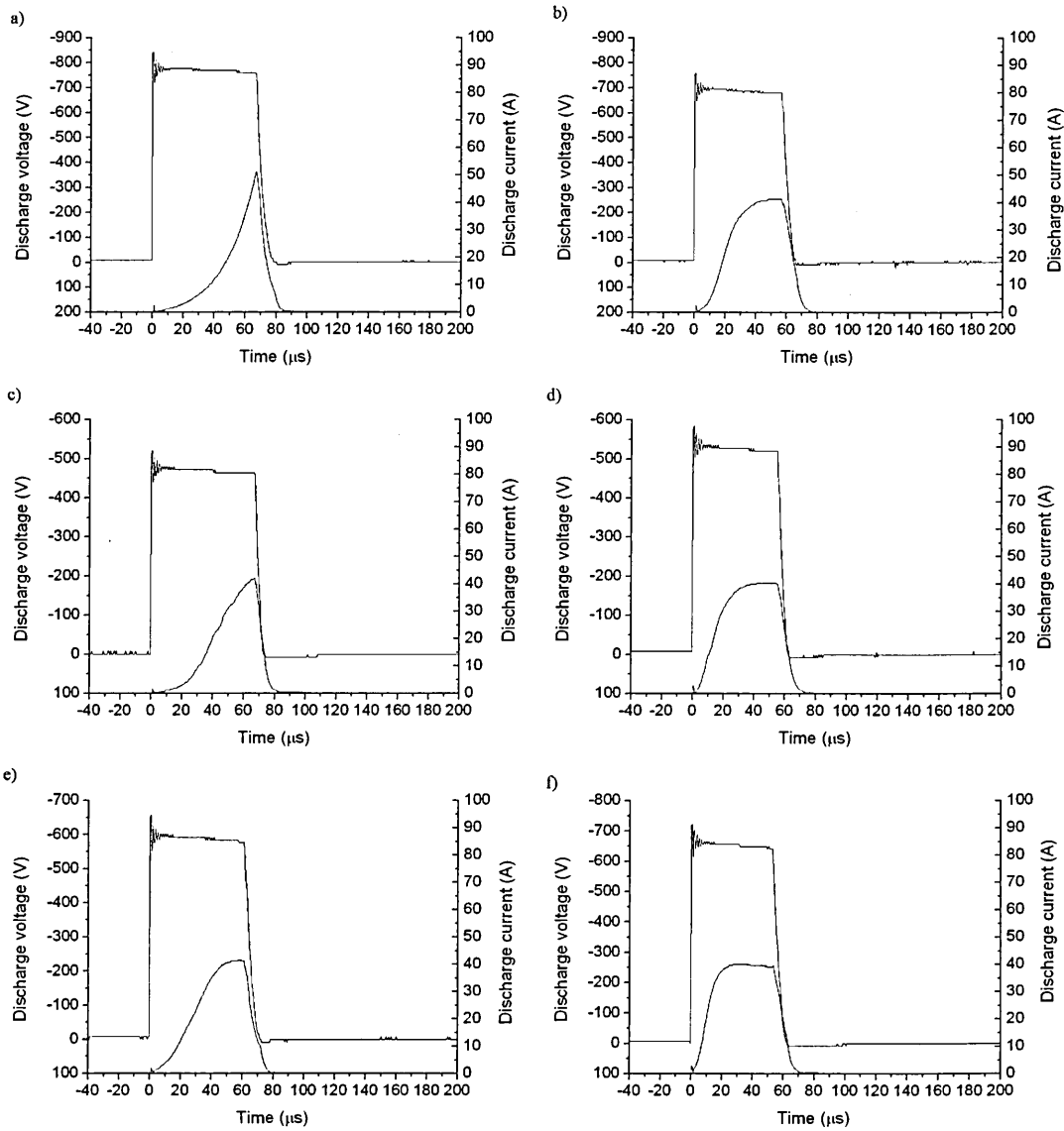
Figure 4.4.2 The target discharge current and voltage during HIPIMS plasma discharge for a) C, b) Al c) Ti, d) Cr, e) Cu and f) Nb target at pressure of 3 Pa

4.4.1 Temporal evolution of metal and Ar ion fluxes of various elements at pressure of 0.3 Pa

4.4.1.1 Singly charged ions of various elements

The time evolution of the singly charged ion fluxes for different materials at pressure of 0.3 Pa is presented on Figure 4.4.3. The x axis of Figure 4.4.3 represents the time between pulses of 10 ms and the y axis is the ion flux calculated as the integral of the ion energy distribution function. For all elements the peak in ion flux intensity is detected at 150 µs from the start of the pulse, i.e. 80 µs after the end of the pulse. The highest intensity of the ion

146

flux is measured for Cr and Nb. The peak intensity can be correlated to the integral of the power during the pulse, i.e. energy delivered to the system.

The peak intensity as a function of energy delivered to the system is plotted on Figure 4.4.4 and it shows an increase of the peak intensity with delivered energy. The energy introduced into the system is calculated as the integral of power with respect to time from the start of one pulse to the beginning of the consequent pulse. The energy in the system is primarily distributed as thermal energy to neutrals, ions and electrons in the plasma, and higher thermal energy of electrons leads to increased ionisation, e.g. higher ion fluxes.
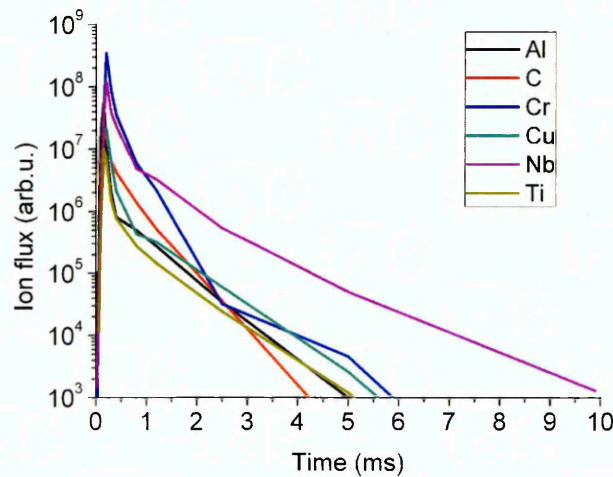
Figure 4.4.3 The time evolution of the single charged ion flux of different elements at pressure of 0.3 Pa
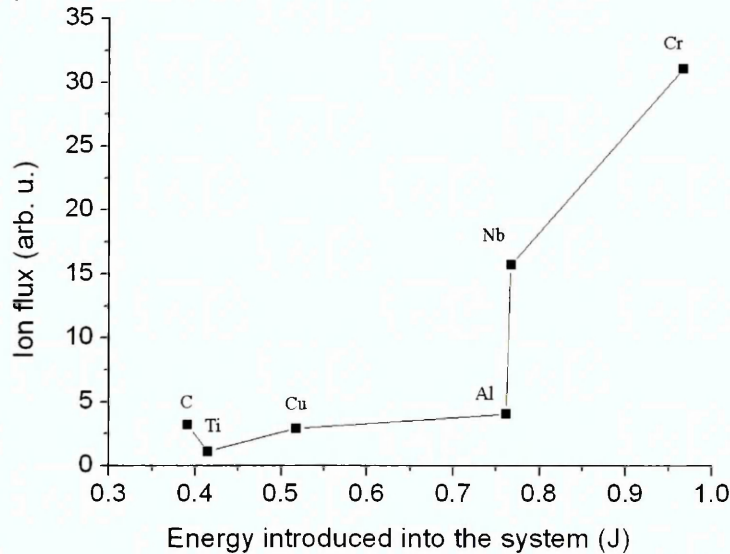
Figure 4.4.4 The dependence of the peak intensity of the ion flux on the energy introduced to the system during the pulse period at pressure of 0.3 Pa

Figure 4.4.3 shows that from 150 µs up to 1 ms the reduction of the ion flux intensity for all elements is exponential in time and very sharp, whereas

after 1 ms the decrease of intensity is exponential at slower rate. After the initial peak, the ion fluxes decrease up to a time of 5 ms when the last signal is detected for all elements. A notable exception is Nb for which a small signal of metal ions is detected at 9.9 ms. The quantity of ions detected at 5 ms for each element is plotted on Figure 4.4.5 as a function of the atomic mass number. The ion flux is higher for heavier elements Nb, Cu and Cr and the ion fluxes reduce for lighter elements Ti, Al and C.
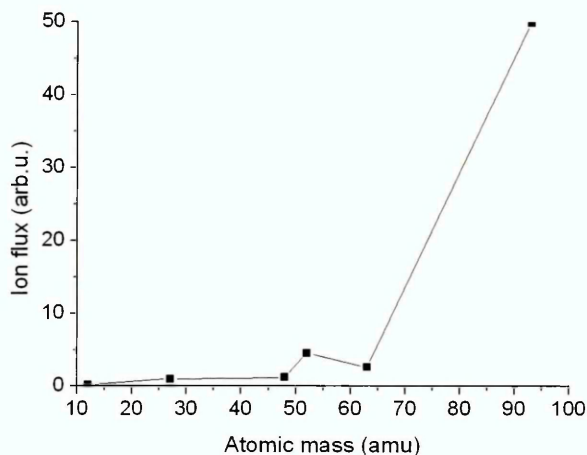
Figure 4.4.5 The dependence of the ion flux intensity as a function of element mass at 5 ms from the start of the pulse at pressure of 0.3 Pa

Figure 4.4.6 represents the average energy of ions as a function of time. Average energies of up to 8 eV have been detected at the end and shortly after the pulse at 70 μs and 100 μs. High average energies of ions originate from particles sputtered from the target with Thompson distribution [83]. After the end of the pulse, the flux of sputtered material is stopped and metal ions are loosing energy through collisions with Ar atoms and ions. Ar particles have thermal energy equivalent to room temperature. After 400 μs, all metal ions are thermalised, as shown in chapter 4.2.1, and have an average energy below 1 eV that is equivalent to the plasma potential, in chapter 4.1.3 plasma potential measurements are presented and the value of plasma potential is 1 V at pressure of 0.3 Pa in the post discharge at 400 μs from the start of the pulse.
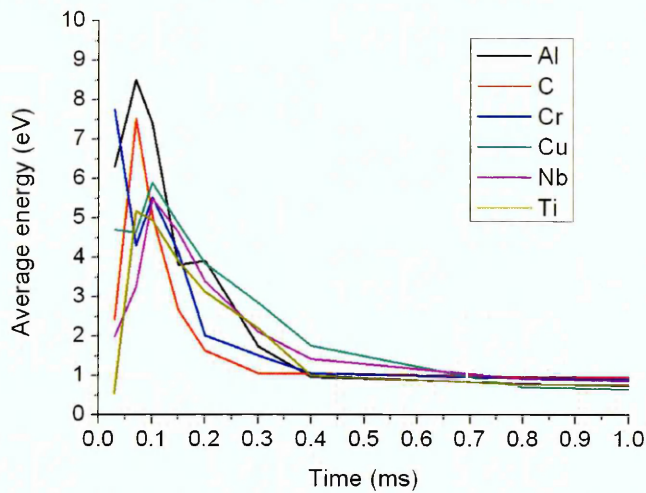
Figure 4.4.6 The average energy of element ions at low pressure of 0.3 Pa

4.4.1.2 Doubly charged ions of various elements

The temporal evolution of doubly charged ions of various elements is shown on Figure 4.4.7. The temporal evolution of doubly charged ions follows the temporal evolution of single charged ions presented on Figure 4.4.3. The ion flux of all elements has a peak at 150 µs followed by an exponential decrease in time. The life span of doubly charged ions for C, Al and Cu is around 1 ms. In HIPIMS of Cr and Ti discharges, the life span is 2.5 ms and for Nb discharge the doubly charged ions are detected up to 5 ms. Long life span of Nb, Cr and Ti ions could be due to high intensity of ion fluxes detected shortly after the end of the pulse. The highest intensity of ion flux is detected for Nb, Cr and Ti elements. The high amount of doubly charged ions detected after the end of the pulse for these elements is probably due to heavy mass of ions and due to low ionisation potential of singly charged ions, which is 13.58 eV for Ti, 14.32 eV for Nb and 16.5 eV for Cr. Furthermore Cr and Nb have the highest quantity of singly charged ions in the same period as shown on Figure 4.4.3. The lack of Cu doubly charged ions could be explained by high second ionization potential which is 20.3 eV.

149
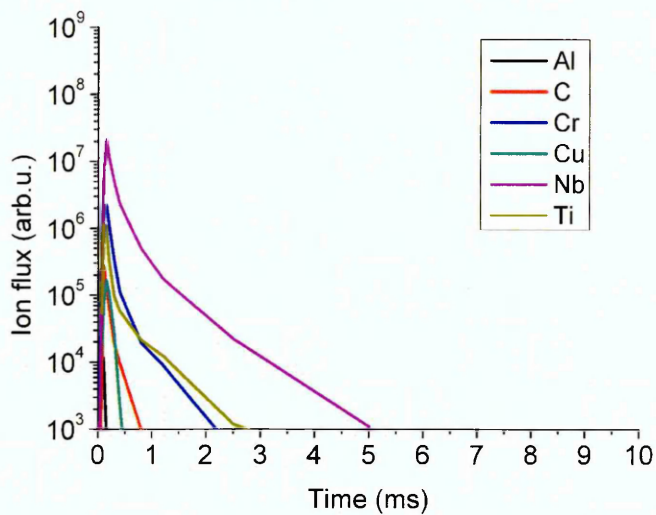
Figure 4.4.7 The time evolution of the doubly charged ion flux of different elements at pressure of 0.3 Pa

4.4.1.3 Singly charged Ar ions

In addition to singly and doubly charged ions of various elements, the singly charged ions of Ar are measured during the discharge of each element and the results are shown on Figure 4.4.8. The temporal evolution of Ar ions is similar to the temporal evolution of metal ions on Figure 4.4.3. Peak intensity of the Ar ions flux is reached shortly after the end of the pulse at 200 μs. After the peak the ion flux of Ar ions reduces exponentially in time until 5 ms when the last Ar ions are detected. At the last measuring point at 9.9 ms only a single signal was detected. Highest intensity of Ar ion flux is detected for Nb, C and Cr discharges. The HIPIMS discharges of Nb and Cr targets yield a high intensity of metal ions, as shown on Figure 4.4.3, producing equal number of electrons that could ionise Ar atoms explaining the high intensity of Ar ions. The high amounts of Ar ions in the Carbon discharge could be explained by the high ionisation potential of C atoms. As C atoms are sputtered from the target into the plasma, the plasma electrons are cooled less compared to metals and the ionisation of Ar is more efficient producing higher number of Ar ions.
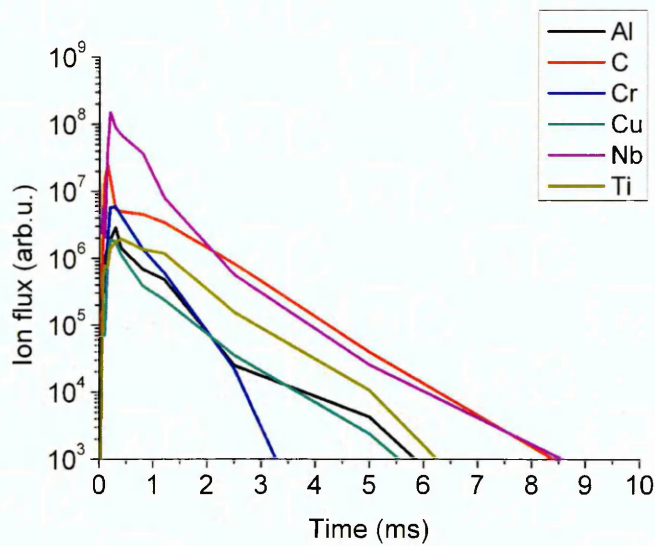
Figure 4.4.8 The temporal evolution of the Ar ion flux at HIPIMS discharge of different elements at pressure of 0.3 Pa
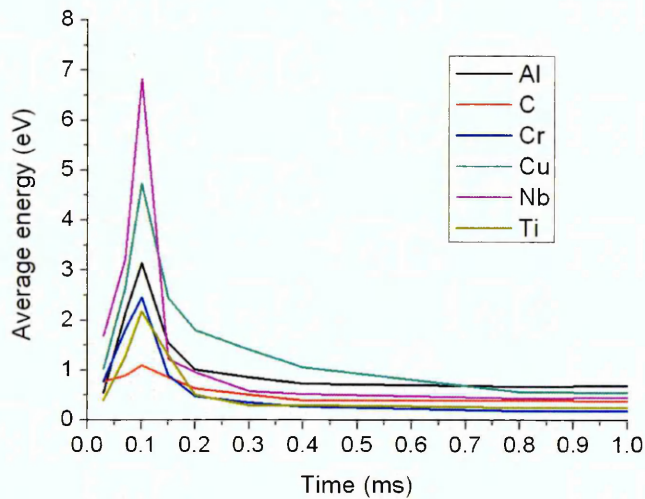
Figure 4.4.9 Average energies of the Ar ions for HIPIMS plasma discharges of various elements at pressure of 0.3 Pa

Figure 4.4.9 shows the average energy of Ar ions for different target materials. The figure shows increase in average energy during the pulse and peak at 100 μs. Increased average energy above values of plasma potential are due to collisions with hot metal particles ejected from the target in target vicinity. After termination of the pulse the Ar ions loose their kinetic energy in collisions with thermalised Ar particles within next 100 μs. After 200 μs Ar ions for all discharges are below 1 eV which is equal to plasma potential measured and presented in chapter 4.1.3. Average energy of 6.8 eV and 4.7 eV are calculated in plasma discharges of Nb and Cu. The kinetic energy transferred to Ar ions in elastic collision with heavy Nb and Cu ions and atoms is significant and therefore the average energy of Ar ions in mentioned

discharges is high. The lowest average energy is detected in C discharge and following the same argument as in case of heavy elements the kinetic energy transferred to Ar ions in collision with light C particles is insignificant. Maximum energy transferred from C particle to Ar particle in the elastic collision, assuming elastic collision between 'billiard balls', is only 35 % of the C particle kinetic energy, compared to above 60 % for other elements.

4.4.2 Temporal evolution of metal and Ar ion fluxes of various elements at pressure of 3 Pa

4.4.2.1 Singly charged ions of various elements

In chapter 4.3.5, time and spatial resolved measurements are presented measured at pressure of 3 Pa. The measurements show the life-span of metal ions up to the start of consequent pulse at distances above 10 cm. The measurements presented on Figure 4.4.10 are measured at distance of 17 cm from the target and at pressure of 3 Pa therefore long life-spans are expected. The x axis represents the time scale from the start of the pulse until the start of the following pulse at 10 ms and y axis is the ion flux calculated by integrating the IEDF of each element. The ion flux scale on Figure 4.4.3 and Figure 4.4.10 is same to ease the comparison. Instead of only one peak and following decay the high pressure measurements show existence of two peaks, first one occurring at the end of the pulse and second one at around 1.2 ms from the start of the pulse.

At the end of the pulse the highest intensity is detected for elements Cu and Nb, probably due to heavy atomic mass and high amount of energy introduced into the system during the pulse. The element to Ar mass ratio is 2.3 and 1.6 for Nb and Cu ions means that due to heavy mass the change of the ion trajectory angle is small in the elastic collisions with Ar atoms and ions, and more ions are reaching the mass spectrometer orifice at given time. Furthermore the energy introduced into the system, presented in Table 4.4.1, has a high values for Nb and Cu discharges. During the discharge of Al the energy introduced into the system is also high but the peak value of ion flux is lower compared to Nb and Cu due to the low mass of Al ions. Al to Ar mass

152

ratio is 0.68 and the change of the Al ion trajectory angle, in other words - scattering, is significant in the elastic collisions with Ar particles.
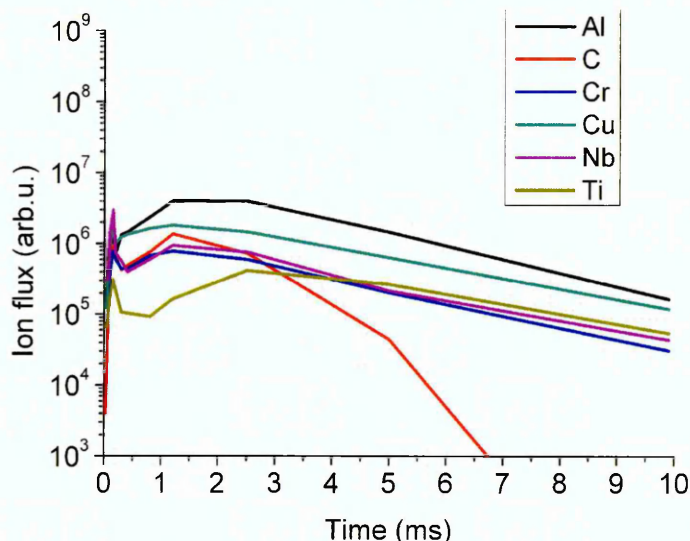
Figure 4.4.10 The time evolution of the single charged ion flux of different elements at pressure of 3 Pa

Element	E(J)
Ti	553207
C	790944
Cu	885664
Cr	905086
Al	1119128
Nb	1178179

Table 4.4.1 The energy introduced into the system calculated as integral of Power integrated from 0 μs to 70 μs, i.e. during the pulse.

A second peak is detected for all elements and it is highly reproducible. For all elements it has a peak at 1.2 ms except Ti discharge when the peak is detected at 2.5 ms. The intensity of second peak for light elements is higher than first peak. On the table 4.4.2 the intensity of first and second peak for each elements and the percentage of change of the second peak intensity compared to first peak intensity is given. It is clear that for light elements the second peak intensity is increased whereas it is reduced for heavier elements.

The first peak probably comprises of hot and fast ions created during the pulse that fly directly to the mass spectrometer and due to heavy mass, high amount of Cu and Nb ions reaches the mass spectrometer. Second peak

comprises of thermalised ions that are diffusing through the chamber obeying ambipolar diffusion [20] and arriving 1.2 ms from the start of the pulse to the mass spectrometer. Light elements C and Al loose more energy in collisions with Ar atoms and ions during the pulse and therefore the ion flux reaching mass spectrometer is reduced in the peak after the end of the pulse. The thermalised ions diffuse slowly reaching the mass spectrometer 1.2 ms from the start of the pulse in greater numbers compared to first peak. On the other hand the number of thermalised heavy element ions during the pulse is smaller and the ion flux at 1.2 ms is reduced compared to the first peak.

Slow diffusion of metal ions at pressure of 3 Pa leads to a long life-span until the start of consequent pulse for all elements except C. The ion flux of elements at 9.9 ms is around 10 % of maximum value for each element indicating a reasonably high amount of ions impinging on the substrate at high pressure.

Element	1. peak intensity (arb. u.)	2. peak intensity (arb. u.)	% of change in intensity of 2. peak compared to 1. peak
C	936100	1373500	46.7
Al	1614000	3985600	146.9
Ti	309200	414300	33.9
Cr	772900	789000	2.0
Cu	1970200	1825500	-7.3
Nb	2977900	943600	-68.3

Table 4.4.2 The intensity of the first and second peak for each element and percentage of change in intensity of the second peak compared to first peak

Figure 4.4.11 shows the average energy of IEDF for each element as a function of time. Only first millisecond is shown since no change in average energy occurs after that time. Somewhat surprisingly highest average energy is detected for C ions followed by heavy elements Cu and Nb. Due to their mass heavy elements loose less kinetic energy in collisions with thermalised Ar particles and this could explain somewhat higher average energy. Lowest average energy is measured for Ti, Al and Cr and it could be that elements with mass similar to Ar loose more kinetic energy in collisions with Ar. The dependence of the peak average energy on element to Ar mass ratio is plotted

on Figure 4.4.12. It shows that elements that have similar mass to the mass of cold Ar gas can only maintain a lower average energy while heavy elements Cu and Nb retain higher average energy.
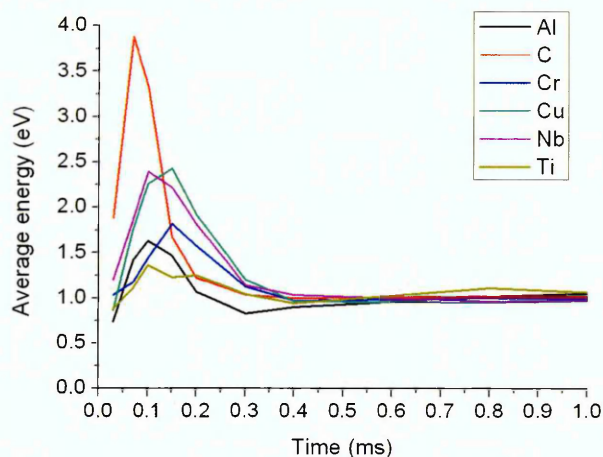
Figure 4.4.11 The average energy of singly charged ion flux of different elements at pressure of 3 Pa
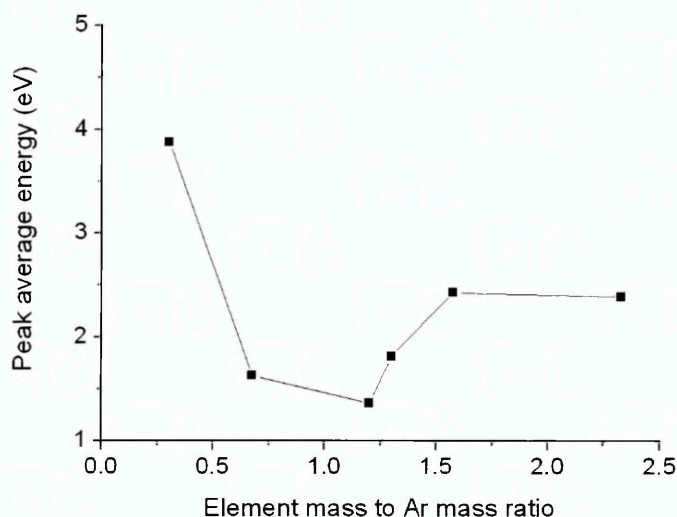
Figure 4.4.12 The peak average energy plotted as a function of element mass to Ar atomic mass ratio at pressure of 3 Pa

The high average energy of C ions could be explained by low energy transfer factor to Ar particles as mentioned in section 4.4.1.3. The elastic collision cross section of C is so small that it can maintain its high initial energy of sputtering much better the rest of the atoms considered.

4.4.2.2 Doubly charged ions of various elements

The flux intensity of singly charged ions at high pressure is two orders of magnitude lower compared to low pressure measurements. The intensity of doubly charged ion flux is also two orders of magnitude lower. Therefore at the

155

high pressure, only a weak signal of Nb, Cr and Ti ions has been detected, shown on Figure 4.4.13. Peak of the ion flux for all three elements is detected at 150 μs from the start of the pulse. After the peak Nb^{2+} ion flux has a shoulder similar to Nb^{1+} ion flux but at lower intensity and with life-span until 2 ms. Cr^{2+} ion flux peaks at ~0.8 ms and then falls to zero after 1.2 ms. The peak of Ti^{2+} ions is detected with life-span of only 200 μs. Longer lifespan ions are probably below the detection limit of the spectrometer. The peak of doubly charged ions consists of fast ions reaching the mass spectrometer shortly after the end of the pulse. The average energies of doubly charged ions are plotted as a function of time on Figure 4.4.14. The average energies are lower compared to low pressure measurements since the energy of the metal ions is lost in elastic collisions with the surrounding thermalised Ar particles due to short mean free path of 0.5 cm. The shoulder of Nb^{2+} and reappearance of Cr^{2+} ions could be a result of thermalised plasma reaching the mass spectrometer. As shown on Figure 4.4.14, after 400 μs all doubly charged ions are thermalised with surrounding gas. After 1.2 ms no doubly charged ion flux is detected at high pressure probably as a result of doubly charged ions being lost to the walls.
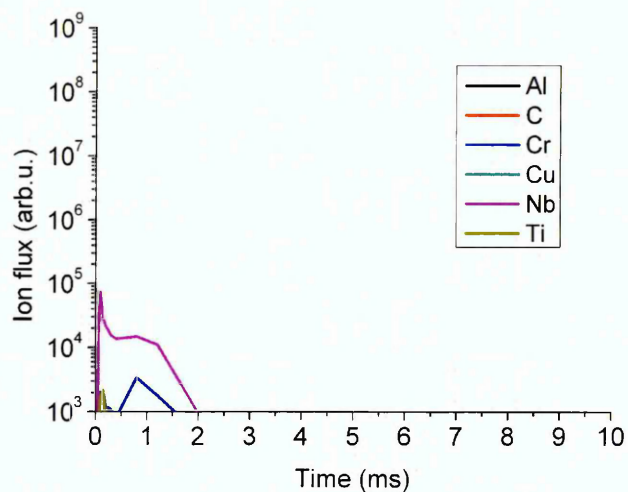
Figure 4.4.13 The temporal evolution of the doubly charged ion flux of different elements at pressure of 3 Pa
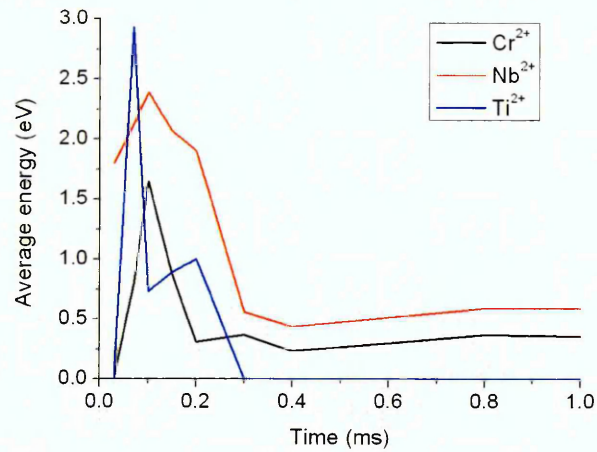
Figure 4.4.14 The average energy of doubly charged ions at pressure of 3 Pa

4.4.2.3 Singly charged Ar ions

The measurement of Ar ion flux for various target materials at high pressure is shown on Figure 4.4.15. The ion flux of Ar ions has a peak shortly after the end of the pulse at 100 μs. After the peak, in HIPIMS plasma discharges of Cu and Cr, Ar ion flux decays exponentially in time. For other materials the ion flux decays exponentially for a short period of time until 300 μs when the decay is halted. The Ar ion flux is almost constant from 300 μs until 2.5 ms after which the exponential decay continues. This continuous influx of Ar ions arriving to the mass spectrometer between 300 μs and 2.5 ms coincides in time with second peak of the ion flux of various elements show on Figure 4.4.10. The first peak comprises of Ar ions ionised by electrons produced during the HIPIMS pulse. In chapter 4.3.3 it is shown that Ar ions are detected at all distances early in the pulse as a result of higher mobility of electrons compared to ion mobility due to high pressure and short mean free path of metal ions.
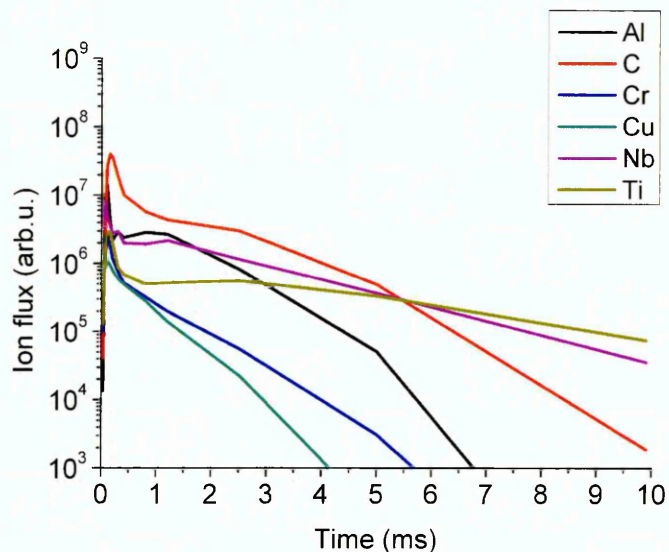
Figure 4.4.15 The temporal evolution of the Ar ion flux at HIPIMS discharge of various elements at pressure of 3 Pa

The highest density of Ar ions after the pulse is detected for HIPIMS plasma discharge of C. The high amounts of Ar ions in Carbon discharge could be explained by high ionisation potential of C atoms. As C atoms are sputtered from the target into the plasma, the plasma electrons are cooled less compared to metals and the ionisation of Ar is more efficient producing higher number of Ar ions. Second and third highest density of Ar ions detected after the pulse is for the HIPIMS discharges of Al and Nb. During Al and Nb discharges the high amount of energy is introduced into the system during the pulse, calculated as integral of power during the pulse and presented in Table 4.4.1. This high energy is transferred to all particles in the system and increased energy and number of electrons could lead to higher amounts of Ar ions detected in the discharges with Al and Nb target.

element	sputter yield	1. to 2. peak ratio
C	0.12	0.11
Ti	0.51	0.18
Nb	0.6	0.26
Al	1.05	0.19
Cr	1.18	0.07
Cu	2.35	0.08

Table 4.4.3 The ratio of the first peak and shoulder intensity of the Ar ion flux in a relation to a sputter yield of element

The shoulder on the Ar ion flux in the post-discharge comprises of Ar ions arriving to the mass spectrometer together with the bulk metal plasma. After 2.5 ms the density of ions in the bulk plasma reduces due to losses to the wall and the density of Ar ions is reduced accordingly. In the HIPIMS plasma discharges of Cu and Cr the shoulder of Ar ion flux does not exist. Cu and Cr are materials with high sputter yield, 2.35 and 1.18, respectively and the gas rarefaction in the target vicinity is emphasized. The bulk plasma reaching the mass spectrometer at 1.2 ms is mostly composed of metal ions, 80% and 92 % of the ions flux are metal ions for discharge of Cr and Cu, respectively. For this reason the life span of Ar ion flux in Cu and Cr HIPIMS plasma discharges is up to 5 ms and for other materials it is up to 9.9 ms before the start of consequent pulse.

In the table 4.4.3 the ratio of the first peak and shoulder intensity of the Ar ion flux in a relation to a sputter yield of element is presented. For high sputter yield elements Cu and Cr the shoulder has below 8% of intensity while for elements with lower sputter yield Ti, Al and Nb the ratio is between 0.18 and 0. 26. For elements with lower sputter yield gas rarefaction is less emphasized and both Ar and metal ions can be found in bulk plasma arriving around 1.2 ms to the mass spectrometer. C has a lowest sputter yield of 0.12 and the ratio is only 0.11 however it can be excluded from this discussion due to high intensity of Ar ion flux created during the pulse due to higher efficiency of Ar ionisation as mentioned in previous section.

On the Figure 4.4.16 the average energy of Ar ion flux is presented. The average energy for all elements is below 1.2 eV indicating high thermalisation of Ar ions in the plasma.
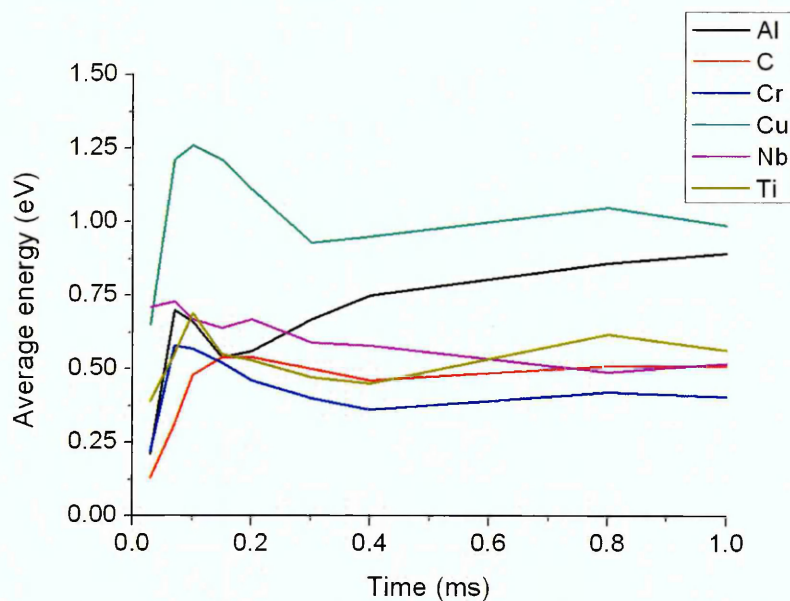
Figure 4.4.16 Average energies of Ar ions for HIPIMS plasma discharges of various elements at pressure of 3 Pa

4.4.3 Influence of properties of elements on the plasma properties

The nature of the sputtered material seems to be an overbearing factor that determines the metal-to-gas ion ratio as well as the ion flux. The trends are preserved regardless of the gas pressure.

Figure 4.4.17 shows the metal to gas ion ratio extracted from the integral values of the metal and ion fluxes. At both low and high pressure the metal ion to gas ion ratio increases with sputter yield of the element. This behaviour is expected since in the plasma discharge with high sputter yield elements density of metal particles is higher compared to discharge with low sputter yield elements, plus higher density of sputtered material leads to emphasized gas rarefaction further reducing the density of Ar ions and increasing metal to gas ion ratio. In Figure 4.4.17, the increase is constant for high pressure measurements however at low pressure the metal to gas ion ratio increases for Cr (Sputter yield is 1.18) and then is reduced to a value of 4 for Cu(sputter yield is 2.35). The reason for such behaviour could be an associated decrease in power for Cu and high intensity of Cr ions proportional to higher energy introduced into the system during the pulse.
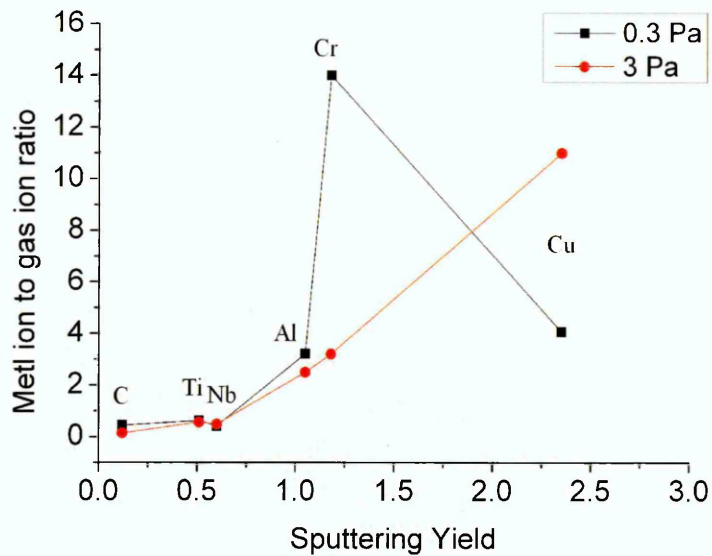
Figure 4.4.17 The metal to gas ion ratio as a function of sputtering yield for different elements at pressure of 0.3 Pa and 3 Pa

The average energy of ions for different elements from time averaged measurements as a function of atomic mass is presented on Figure 4.4.18 at pressure of 0.3 Pa. The increase in average energy of ions with increase in atomic mass of the element shows that the effect of thermalisation is stronger for lighter particles.

Figure 4.4.19 shows the average energy of ions for different elements as a function of atomic mass at high pressure of 3 Pa. On this figure the average energy is decreasing from 0.8 eV to 0.58 eV as the atomic mass increases from 12 amu for C to 93 amu for Nb. The decrease in average energy for heavier elements could be due to shorter mean free path for larger particles. The mean free path is reversely proportional to the product of gas pressure and elastic collision cross section, $\lambda = 1/(n_g\sigma)$ [37]. The elastic collision cross section is proportional to the size of the ion therefore bigger ions have shorter mean free path and thermalisation is enhanced.

The average energy as a function of ion radius is presented on Figure 4.4.20 and it shows a decrease in average energy with increase in ion radius. This effect has less impact on the ions at the low pressure since at low pressure the mean free path is 10 times longer and it is around 7 cm therefore, on average, an ion will collide two to three times before entering the mass spectrometer at 17 cm away from the target. At high pressure of 3 Pa the ion

has an average of twenty to thirty collisions before entering the mass spectrometer.
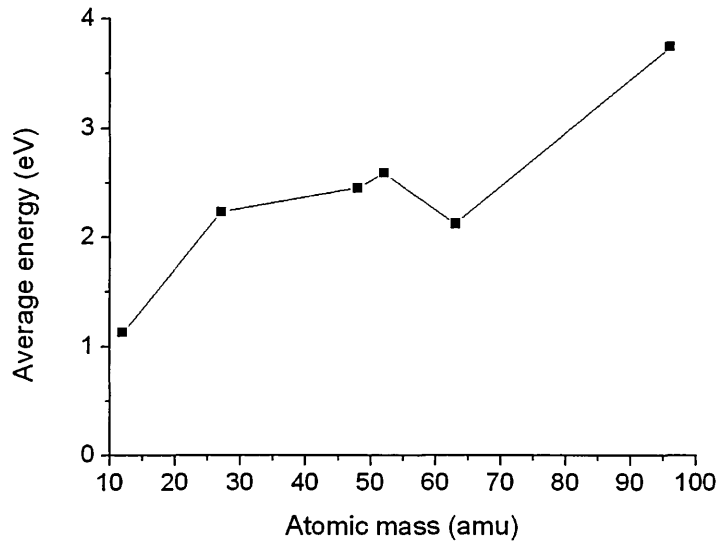
Figure 4.4.18 The average energy of singly charged ions of the various elements as a function of element atomic mass number at pressure of 0.3 Pa
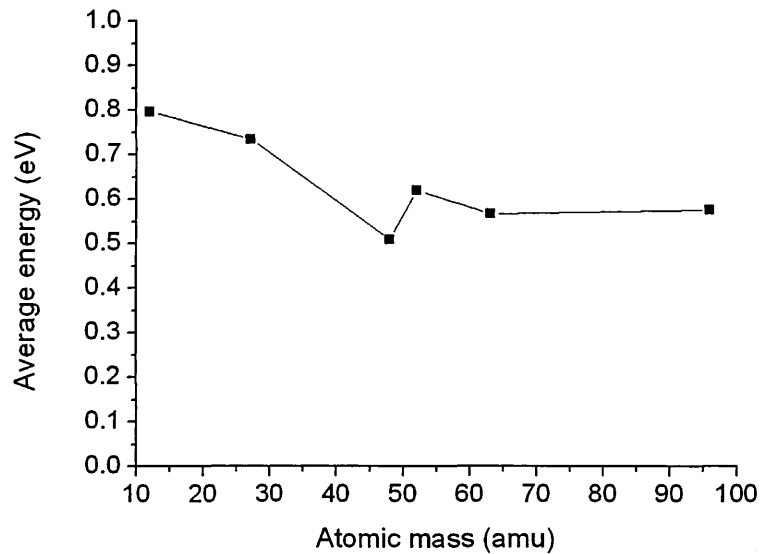
Figure 4.4.19 The average energy of singly charged ions of the various elements as a function of element atomic mass number at pressure of 3 Pa
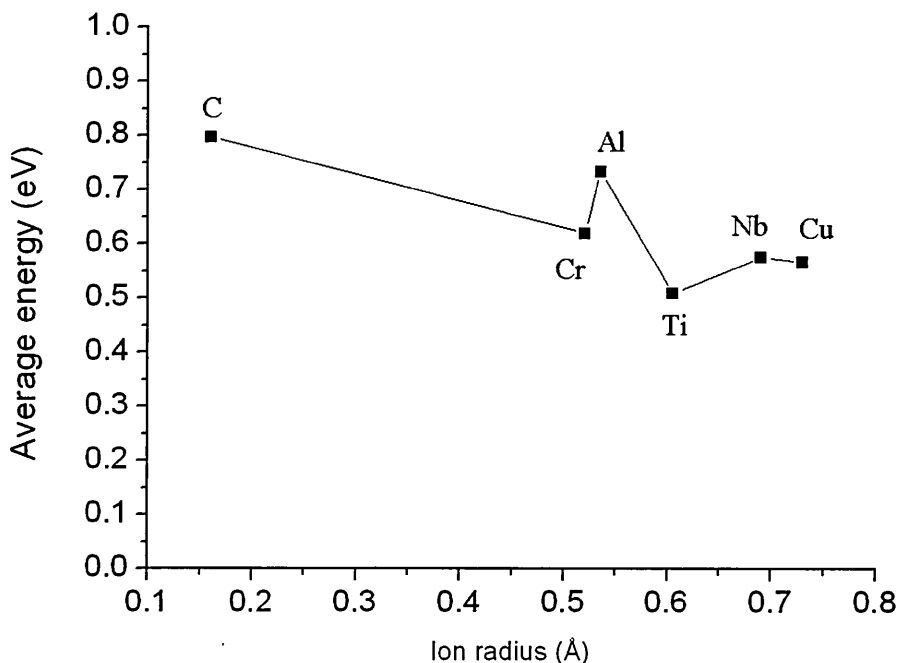
Figure 4.4.20 The average energy of singly charged ions of the various elements as a function of ion radius at pressure of 3 Pa

The effect of the binding energy of the element on the ion density is shown on Figure 4.4.21 for the low pressure measurements. The high pressure measurements are presented on Figure 4.4.22. The ion density is calculated as an integral of the IEDF measured in time averaged mode. The particles are sputtered from the target with Thompson distribution [83]. Thompson distribution has a dependence on the binding energy E_b as $f_T \approx 1/E_b^2 + 1/E_b$. The shape of the curves on Figure 4.4.21 and Figure 4.4.22 match the dependence of the Thompson distribution on the binding energy. The elements with low binding energy Cu and Al have higher intensities and the elements with higher binding energy such as C and Nb have lower intensities. On the Figure 4.4.21 and Figure 4.4.22 calculated Thomson distribution for binding energy is plotted for comparison.
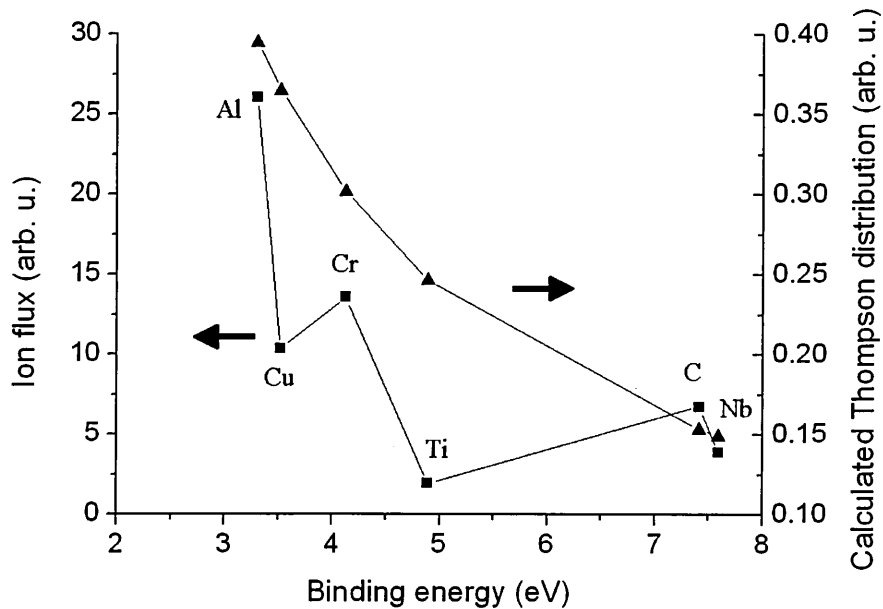
Figure 4.4.21 The ion flux of elements as a function of binding energy measured at low pressure of 0.3 Pa compared with calculated Thompson distribution
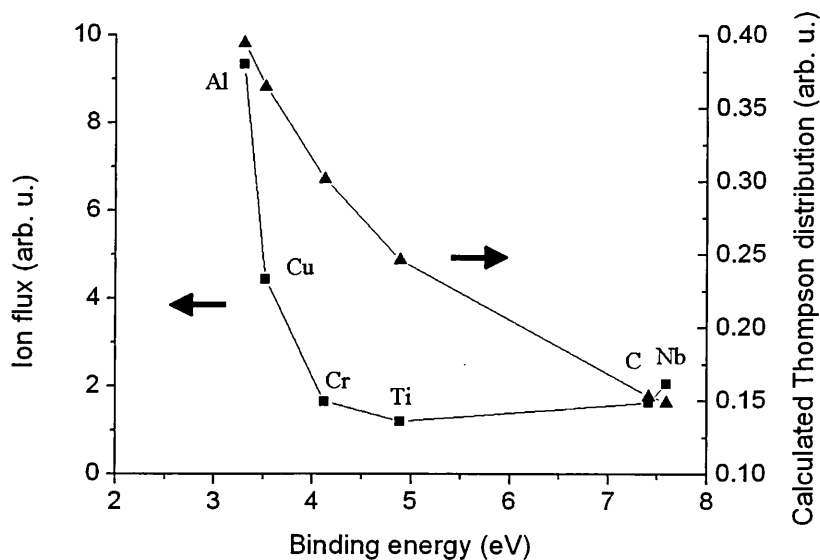
Figure 4.4.22 The ion flux of elements as a function of binding energy measured at high pressure of 3 Pa compared with calculated Thompson distribution

4.4.4 Summary

The ion energy and lifespan of ions were found to depend strongly on collisions of the sputtered flux with the surrounding gas and as such depended on the target material. Life-spans are longest for ions of the heavy mass elements due to rarefaction. Furthermore doubly charged ions are detected only for elements with mass heavier than Ar at both pressures.

At high pressure a second peak for singly charged metal ions around 1.2ms has been detected that could be the signal of bulk plasma slowly diffusing away from the target.

Metal to gas ion ratio increased for elements with higher sputter yield. The average energy measured in time resolved mode increased for elements that have significantly different mass than Argon indicating that energy losses are highest when masses are similar. At high pressure the average energy of singly charged ions reduced with heavier mass due to shorter mean free path that is reversely proportional to the size of the ions.

The metal ion flux showed dependence on binding energy of the element as predicted by Thompson distribution function.

4.5 Properties of CrAlSiN coatings in dependence on the power source and DC/HIPIMS power ratio

The CrAlSiN coating was deposited using AlSi target (89 at% of Al and 11 at% of Si) and pure Cr target in reactive Ar + N_2 atmosphere. AlSi target was running in DC mode only and Cr target was running in DC mode for deposition of one coating and in a HIPIMS mode for deposition of three coatings. The coatings were deposited with a different Cr to AlSi atomic ratio 40:60, 50:50 and 60:40 while Cr target was running in the HIPIMS mode and AlSi target was running in a DC mode. The Cr content was increased by increasing the peak HIPIMS power on the Cr target. A fourth coating was produced with 50:50 atomic ratio but for this coating both targets were running in a DC mode. After deposition the mass spectrometer was used to measure the ion energy distribution function of all relevant ions in the discharge. Atomic force microscopy (AFM) images of the coating surface were taken to investigate the grain column size of the coating. Scanning electron microscope (SEM) was used to study the surface topography of the coating and Energy dispersive X-ray spectroscopy (EDX) was used to gain information about the composition of the coating. At the end a relation between the compositions of the coating, thickness, mass spectrometer measurements and size of the columns was established.

CrAlSiN is a nanocomposite coating which comprises crystals of CrAlN wrapped in a SiN amorphous tissue-phase. Small crystallite size and high residual stresses are two very important microstructure features that contribute to the increase of the hardness in super-hard nanocomposites [90]. High internal residual stresses are needed to reduce the sliding at the grain boundaries and thus to prevent a reduction of the hardness at small crystallite size [91]. The high hardness in nanocomposites is usually explained by a high elastic recovery of the material and by a high resistance against crack formation or by prevention of the grain boundary sliding. The crystallite size and the morphology of the internal interfaces are the most important factors influencing the mechanical properties of CrAlN and CrAlSiN nanocomposites. The use of CrAlN and CrAlSiN coatings can be found in; use for punching of perforated sheets [92], as superelastic coatings for high end spindle bearings

166

or as thermal barriers redirecting the heat from the cutting tool into the chip [93]. In these applications, the microstructure and properties of the CrAlN and CrAlSiN coatings are altered by varying their chemical composition that influences primarily their phase composition.

Altered composition obtained using two deposition techniques DC magnetron sputtering and HIPIMS in order to investigate the properties of the deposited coating and to link the composition with the plasma parameters was the goal of here presented research.

Kurt J. Lesker CMS 18 deposition system was used to deposit coating on 304 austenitic stainless steel during deposition time of 5 hours, bias voltage was -75 V and the substrate was heated to temperature of 400 °C. The pressure in the chamber was 0.36 Pa with mixture 50% Ar gas and 50% N_2 gas. In the three deposition runs HIPIMS plasma discharge had a frequency of 304 Hz and pulse duration of 80 μs.

4.5.1 Composition of the deposited CrAlSiN coating

The composition of the coating is presented on Table 4.5.1. It comprises the information of the power applied to each target, the composition of the coating and the thickness. The label 'DC' stands for the deposition run with both targets running in DC mode with planned composition of 50at% Cr and 50at% Al and Si. The labels 4060, 5050, 6040 stand for deposition runs with AlSi target running in DC mode and Cr target in the HIPIMS mode with planned Cr to AlSi atomic ratio 40:60, 50:50 and 60:40, respectively. The samples should be stoichiometric and contain 50 at% of Nitrogen therefore the ratios presented in Table 4.5.1 are the ratio between Cr, Al and Si. The atomic percentage of Si in all runs was below 3 %. The composition of the coating in the DC run was 61 at% of Cr and 37 at% of Al. In the run 5050 the Cr and Al percentage was 50% and 47%, respectively and to obtain this composition which has a lower percentage of Cr compared to DC run the power on Cr target in 5050 was 50% higher than in the DC run. In mentioned two runs the power on AlSi target was the same. Furthermore the thickness of the DC coating was measured to be 4.7 ± 0.3 μm and for 5050 coating it was 4.2 ± 0.2 μm. This result confirms the lower deposition rate in HIPIMS plasma discharges compared to DC magnetron sputtering plasma discharges [94].

167

The thickness of 6040 coating, with 0.71 kW power on HIPIMS target and 0.28 kW on DC target is 3.4±0.1 μm. It shows that increasing the power on HIPIMS target and decreasing the power on the DC target the thickness of the coating reduces.

Label	P_{Cr} [kW]	P_{Al} [kW]	P(Cr)	Cr/all	Al/all	Si/all	$\frac{[Si]}{[Al]+[Si]}$	Thickness [μm]
DC	0.26	0.54	0.33	0.61	0.37	0.02	0.05	4.7±0.3
4060	0.2	0.6	0.25	0.44	0.53	0.03	0.05	3.7±0.3
5050	0.36	0.54	0.40	0.50	0.47	0.03	0.06	4.2±0.2
6040	0.71	0.28	0.72	0.80	0.19	0.01	0.05	3.4±0.1

Table 4.5.1: Power on the respective target, the P(Cr) ratio, the Cr, Al and Si contents, the [Si]/([Al]+[Si]) ratio and the coating thickness for the UBM and HIPIMS deposition runs. The chemical analysis was performed using EPMA/WDX. The thickness was measured using ball-cratering method. Comment: P(Cr) means $P_{Cr}/(P_{Cr}+P_{Al-Si})$, from [103]

4.5.2 Plasma composition

Using mass spectrometer the mass scan was performed to measure, according to mass, the ions that can be detected in the HIPIMS discharge with AlSi and Cr target in reactive atmosphere of Ar and N_2. The signal of Cr^{1+}, Cr^{2+}, Al^{1+}, Ar^{1+}, N^{1+} and N_2^{1+} was detected. On Figure 4.5.1 the composition of plasma detected in each deposition run is plotted. The ion percentage is calculated as an integral of the ion energy distribution function (IEDF) and presented as a percentage of total amount of ions detected in the plasma. The IEDF was measured in the time average mode over 30 pulses.

During a DC deposition run plasma is mostly comprised of gas ions of which 47% is singly charged nitrogen molecule, 45% is Ar gas and 6% is singly charged nitrogen atom. Only noticeable metal ion flux is of singly charged Al ions consisting 2% of total ion flux. Applying HIPIMS power supply on the Cr target in subsequent three deposition runs, contents of Cr ions, both singly and doubly charged, increases significantly. The percentage of Cr^{1+} ions increased from 1.4% to 4% by increasing the power from 0.2 to 0.71 kW, and the percentage of Cr^{2+} increased from 0.2 % to 2%. The power on AlSi target

in DC and 5050 deposition run was same nevertheless the percentage of Al^{1+} ions increased from 1% to 2.3%. The increase in the density of Al singly charged ions could be due to increased density of electrons produced using the HIPIMS power supply on the Cr target and since two targets were placed next to each other the increased number of Al atoms was ionised. In the deposition runs 4060, 5050 and 6040 the power on the AlSi target was reduced from 0.6 kW to 0.28 kW and the amount of material sputtered from the target was reduced. As a result the percentage of Al^{1+} ions decreased from 2.3% to 1%. The change of the power supply from DC to HIPIMS increased the percentage of singly charged nitrogen atoms from 5.7% to around 10.3%. It could be that due to high power pulses from the HIPIMS plasma discharge and increased density of high energy particles the frequency of nitrogen molecule dissociations increased. Furthermore the percentage of Ar ions decreased from 41.6% to 31.3% between deposition runs 4060 and 6040 that could be associated to faster increase in metal and atomic nitrogen density.
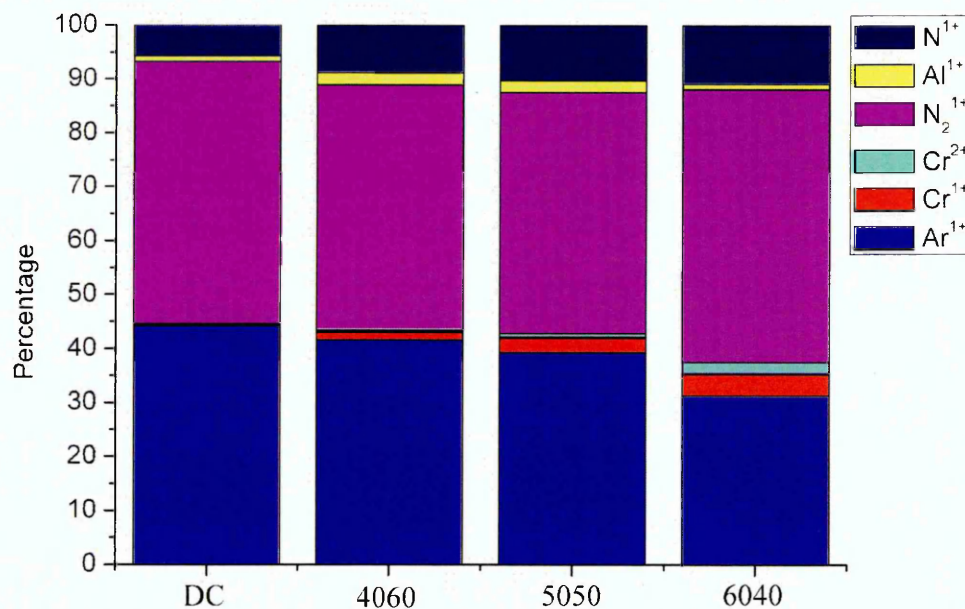
Figure 4.5.1 The composition of the plasma demonstrated as a percentage of the total ion flux for each deposition run

Ehiasarian et al. [95], Pintaske et al. [96] and Rossnagel et al. [97] used optical emission spectroscopy in order to investigated relation between the emission intensity and density of electrons; $I \propto n_e{}^m$. Electron density n_e is found to be proportional with the discharge current I_d and intensity of emission lines is proportional to the particle density. In a DC discharge the exponent m

is a number of electron collisions necessary to populate an energy level from which spontaneous emission is observed, and coefficient m was found to be around 1 for Argon atoms, below 2 for Ti atoms and below 3 for Cu ions. In HIPIMS plasma discharge it is shown [95] that electron density and intensity of Ar ions are proportional to the discharge current, where singly charged metal ions had a coefficient equal to 1.5. It means that increasing the power from deposition run 4060 to deposition run 6040, i.e. increasing power from 0.2 to 0.71 kW, the Ar ion density increase linearly with current whereas metal and atomic nitrogen increase with a coefficient equal to at least 1.5 which is much faster, so they gradually grow against Ar ions. Figure 4.5.2 shows the percentage of each ion species for different deposition runs and shows the increase and decrease in the percentage more clearly. The increase of the metal contents in the plasma compared to gas contents and increase of the metal contents compared to nitrogen contents with increasing power on the HIPIMS power supply is shown on Figure 4.5.3.
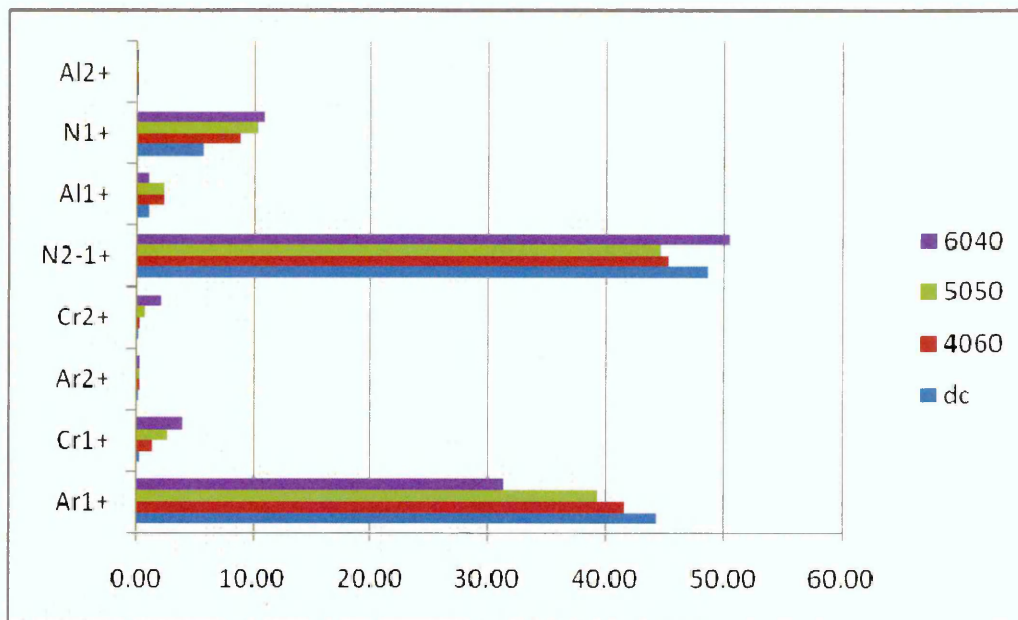
Figure 4.5.2 The percentage of each ion species for different deposition runs
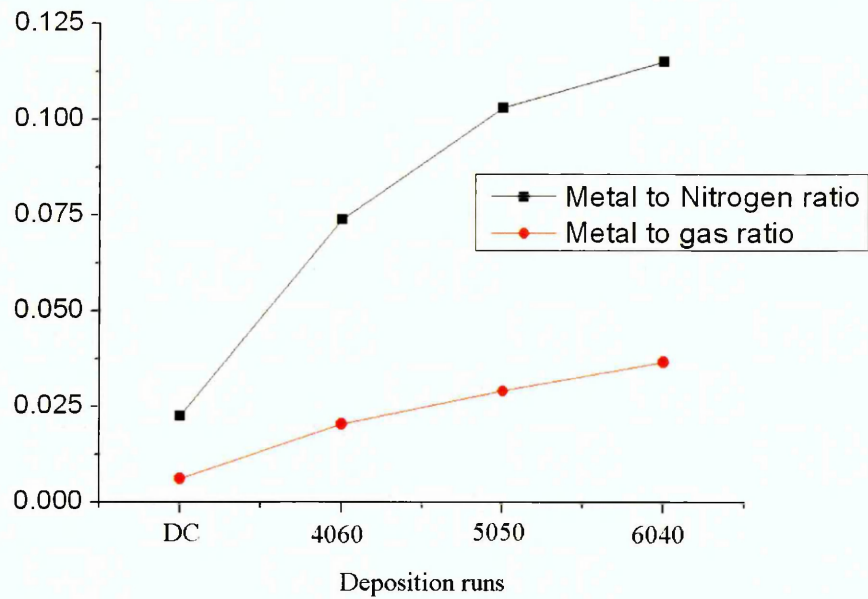
Figure 4.5.3 The dependence of the metal to gas ratio and metal to nitrogen ratio for four deposition runs

4.5.3 Surface analysis of the deposited CrAlSiN coating

SEM and AFM micrographs were recorded to investigate the surface of deposited coatings. SEM images are presented On Figure 4.5.4 and Figure 4.5.5. Figure 4.5.4 is the surface of the coating deposited when both targets were running in DC mode. Figure 4.5.5 is the coating surface deposited under 4060 conditions. The pictures were magnified 100 000 times. Comparing two pictures it can be seen that the surface of the coating deposited using HIPIMS on the Cr target, presented on Figure 4.5.5, produced smoother coating compared to coating produced using two targets running in DC mode. Furthermore on the first picture the surface is covered with pyramid structures that break-up the homogeneous surface of the coating. On the second picture the surface is continuous without disruptions.
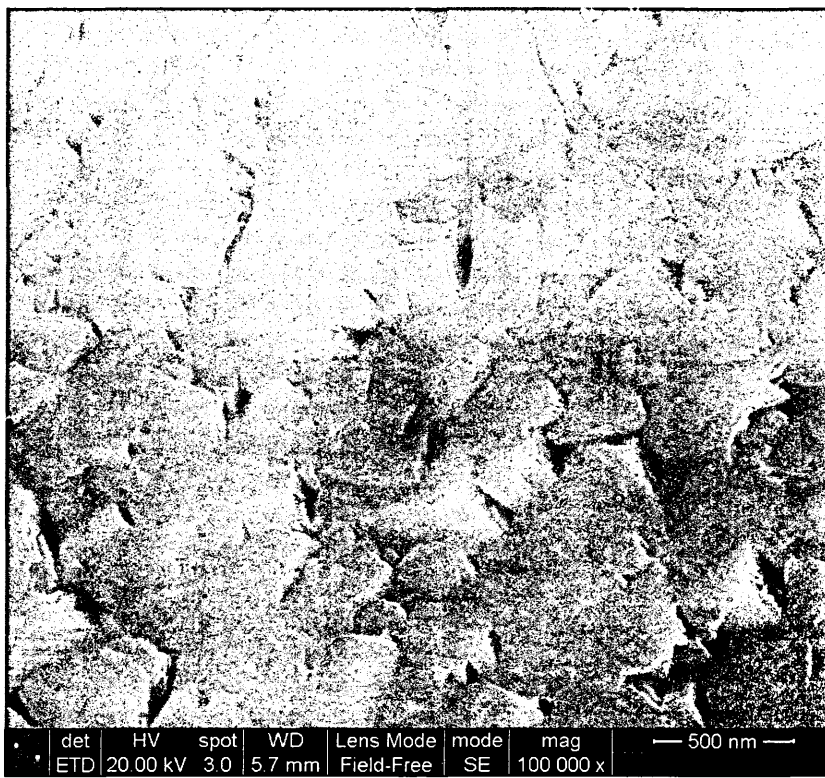
Figure 4.5.4 The SEM image of the CrAlSiN coating surface at DC deposition conditions
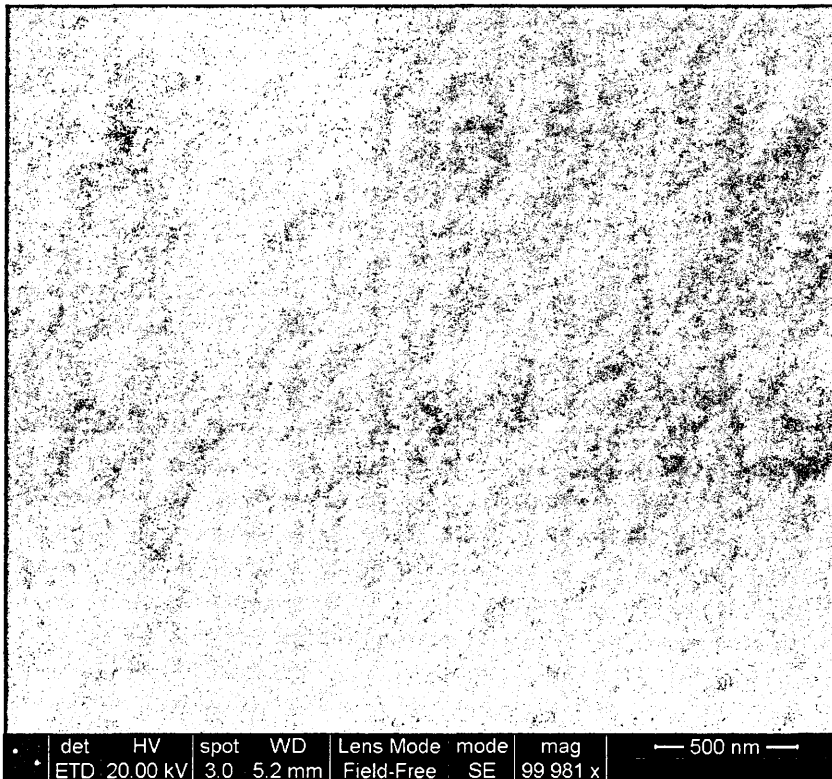
Figure 4.5.5 The SEM image of the CrAlSiN coating surface at 4060 deposition conditions

On Figure 4.5.6 to Figure 4.5.9 the AFM images of the coating surface for DC, 4060, 5050 and 6040 deposition conditions are presented, respectively.

The shapes visible on the AFM images correspond to the size of the columns. The surface of the shape appears to decrease when DC power supply is replaced by HIPIMS power supply and it reduces furthermore with increasing HIPIMS power. In order to compare the size of the column, on each figure the area of 10 shapes was measured and the average area is calculated. The results are presented in the Table 4.5.2. The size of the column is reduced from 0.25 μm^2 during DC deposition conditions to 0.16 μm^2 at 4060 deposition conditions. Increasing the power on HIPIMS power supply from 0.2 kW, during 4060 deposition, to 0.71 kW the surface of the column was further reduced to 0.11 μm^2.
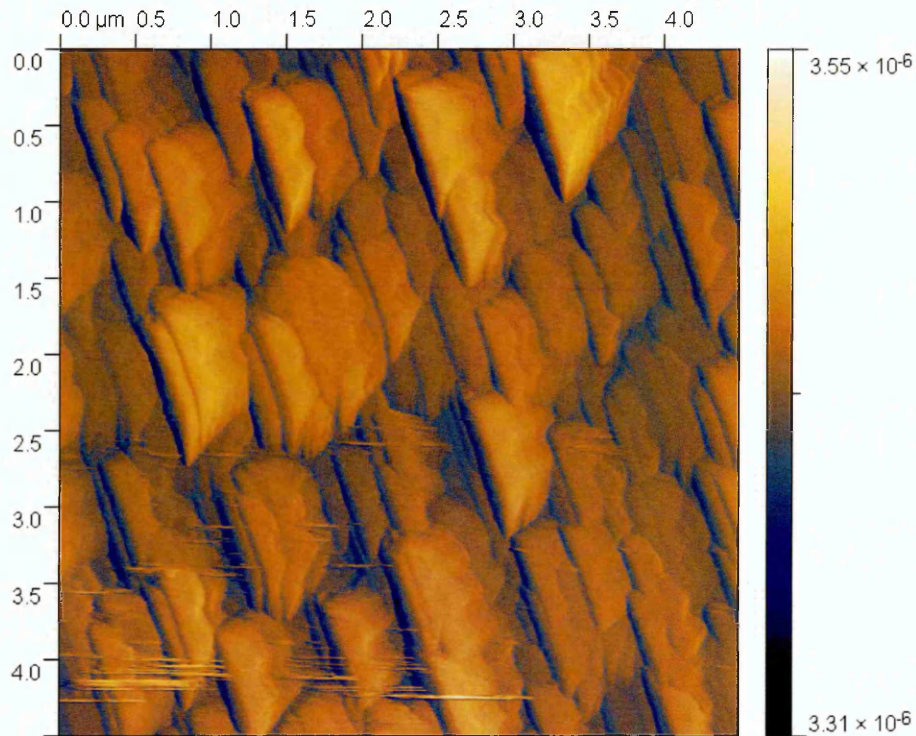
Figure 4.5.6 AFM image of surface of the CrAlSiN coating at DCDC deposition conditions
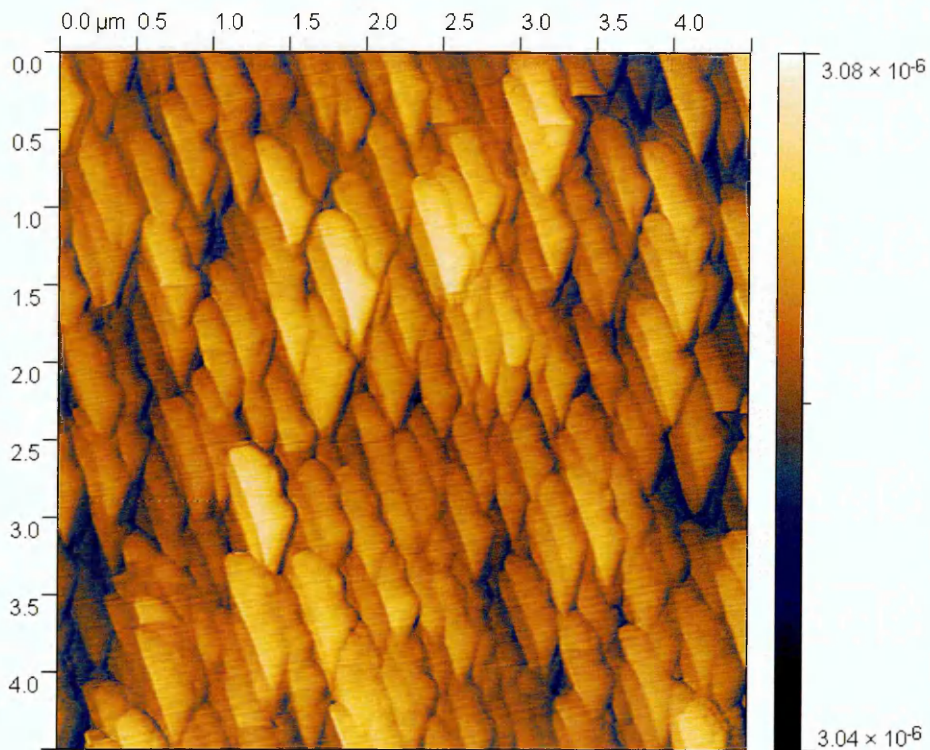
Figure 4.5.7 AFM image of surface of the CrAlSiN coating at 4060 deposition conditions
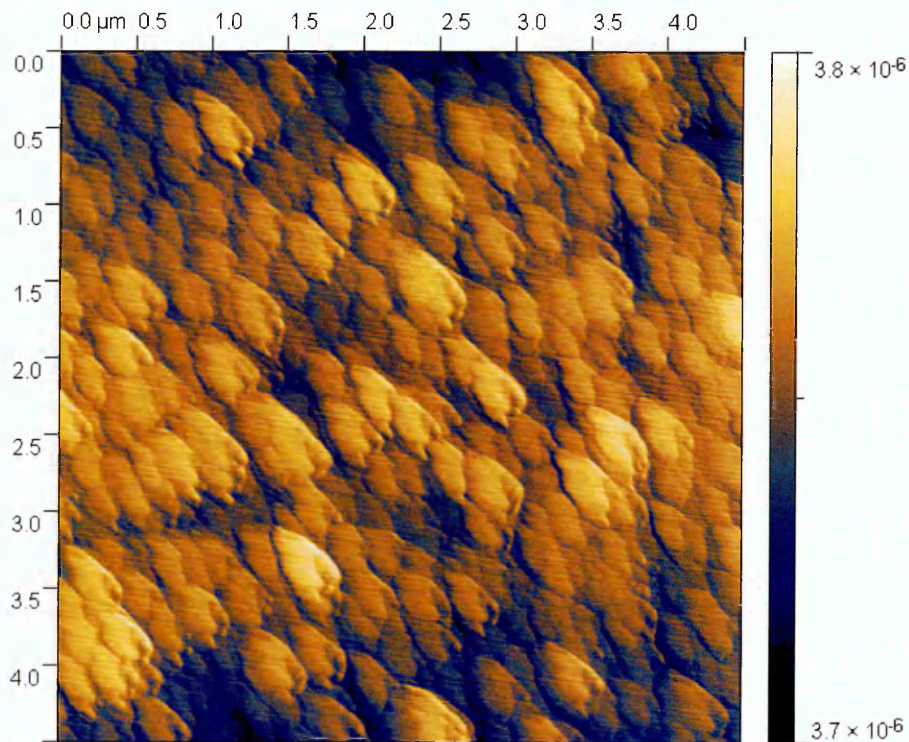
Figure 4.5.8 AFM image of surface of the CrAlSiN coating at 5050 deposition conditions
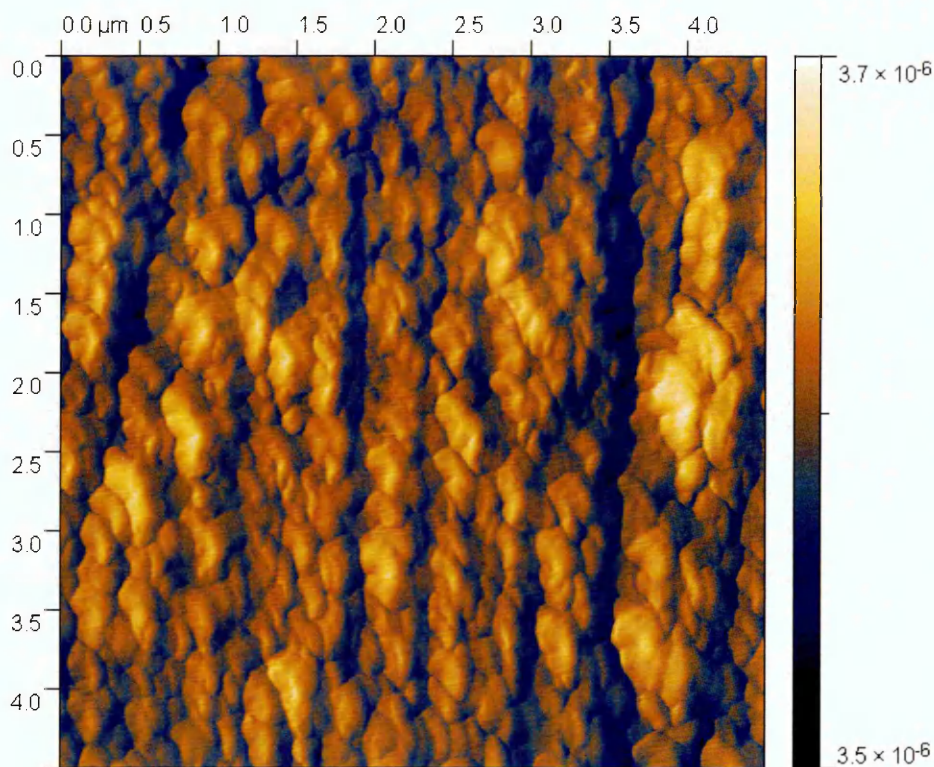
Figure 4.5.9 AFM image of surface of the CrAlSiN coating at 6040 deposition conditions

Deposition condition	Area (μm^2)	Standard deviation
DC	0.25	0.02
4060	0.16	0.01
5050	0.15	0.02
6040	0.11	0.02

Table 4.5.2 The area of the top of the columns visible on the AFM images for each deposition run

The size of the column, presented on table 4.5., was plotted on Figure 4.5.10 as a function of metal ion to gas ion ratio. The figure shows linear decrease in the column size with increase of the metal contents in the plasma. In chapter 2.5 detailed description of plasma surface interactions are given and it is mentioned that ion irradiation could directly enhance adatom diffusion during deposition through the initiation of shallow collision cascades and the excitation of surface phonons. On the other hand the excess energy of incident ions as well as the excess energy gained by adatoms involved in individual collisions cascades is lost to lattice i.e. the atoms become

175

thermalised with several vibration periods. The energetic particle bombardment can greatly affect 3D nucleation and growth kinetics of the polycrystalline film. In chapter 4.1.1 the metal ion to neutral ratio in the HIPIMS discharge was measured and it shows higher contents of metal ions compared to metal atoms up to 1 ms from the start of the pulse. Abundance of metal ions and increase in the metal to gas ion ratio with increase of the power on the HIPIMS target could lead to enhanced deposition. In particular it results in trapping and implanting of incident particles in the near surface region, the dislocation of small clusters during the early growth stage and enhancing adatom diffusion. Enhancing adatom diffusion enhances the chemical reactivity on the surface, which influences reactive deposition processes and eventually leads to creation of coatings with smoother surface and small column size.
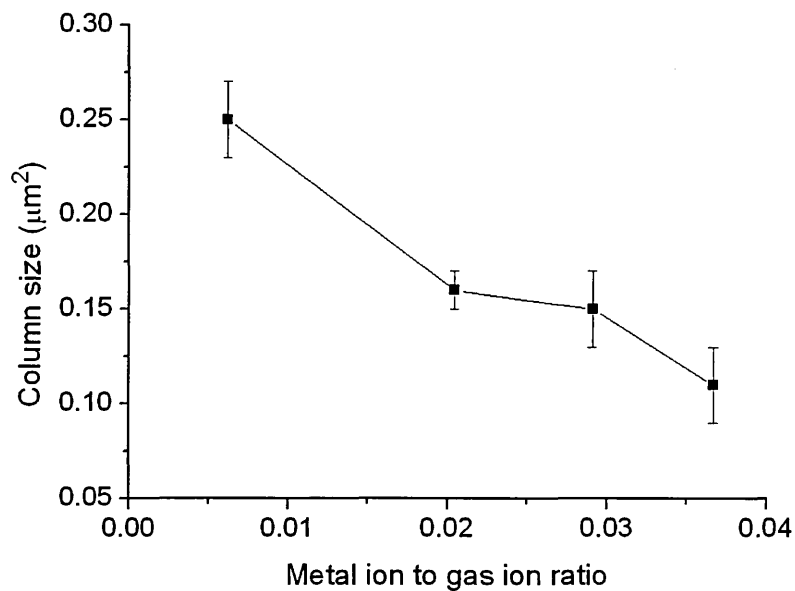
Figure 4.5.10 The size of the column as a function of the metal ion to gas ion ratio

176

4.5.4 Summary

Four CrAlSiN coating were produced using Cr and AlSi target in Ar and N_2 atmosphere. One coating was deposited with both targets applied to a DC magnetron sputtering power supply and three coatings were deposited with AlSi target running in DC mode and Cr target connected to the HIPIMS power supply. In addition to deposition the mass spectrometer measurements of the ion energy distribution function of metal and gas ions for every deposition run were performed. The mass spectrometer results show increase of metal contents, particularly Cr^{1+} and Cr^{2+} ions in the plasma with increasing power on the HIPIMS power supply, increase in the nitrogen ion contents and decrease in Ar ion contents. The metal ions arriving to the substrate transfer kinetic energy to adatoms and after loosing all energy it is incorporated in the coating. Gas ion arriving to the substrate bombards adatoms but unlike metal ions the gas ions recoil back to plasma. Therefore the energy delivered by metal ions is greater than energy delivered by gas ion.

The surface analysis of the deposited coatings using SEM showed the coating deposited with HIPIMS having surface without sharp structures compared to the coatings deposited in DC deposition run. In the images recorded by AFM the size of the columns is clearly visible. The size of the columns was calculated and it showed decrease in the column size with increasing power on the HIPIMS power supply. Understanding the process of ion implantation the link between size of the columns with metal to gas ion ratio was established. Increasing the metal contents in the plasma the size of the column was reduced possibly due to higher mobility of adatoms heated with metal ions impinging on the surface of the coating.

CHAPTER 5

Conclusions

Fundamental research of plasma parameters of the HIPIMS plasma discharge in dependence on applied power and working gas pressure has been performed and it has been presented in this thesis. The conclusions can be summarised as follows;

1.   It was observed that metal ion to neutral ratio in the HIPIMS increases with power. At all powers the highest ion to neutral ratio was observed after the end of the pulse after which the ratio reduced towards zero with time.

2.   The metal ion flux, measured in the HIPIMS plasma discharge with time-averaged plasma sampling mass spectrometer, comprised high- and low-energy particles whose combined IEDF could be described by a sum of two Maxwellian distributions. The main energy peak showed no dependence on target current as it originated from the post-discharge plasma. The high energy tail increased with increasing target current and could be attributed to the power applied in the pulse.

3.   The IEDFs of gas ions have significantly different shapes for different pressures. At low pressure, the IEDFs exhibited two Maxwellian distributions similar to the ones found for metal ions but had lower effective temperature. The high energy tail comprised gas ions heated up through collisions with sputtered atoms. At high pressure, the gas IEDF comprised only a single low-energy peak.

   The metal ion-to-gas ion ratio was higher for target materials with high sputter yield.

4.	Electrostatic probe measurements show higher ion saturation current at low pressure compared to high pressure measurements. At both pressures the ion saturation current increased linearly with power. The electron density calculated from Langmuir probe measurements at low pressure consists of one peak appearing shortly after the end of the pulse with its peak increasing with the power. At high pressure measurements the electron density comprises three peaks increasing with power and reaching the maximum at around 200 µs. The delay of the electron density peak at high pressure could be attributed to the short mean free path and suppressed diffusion of metal ions in the plasma.

5.	The ion energy distribution function of metal ions inside and shortly after the end of the pulse showed existence of highly energetic ions with energies of up to 70 eV and 40 eV for Cr^{1+} and Cr^{2+} ions, respectively. At the same time the gas ion energy distribution function comprising a main low energy peak and small high energy group of ions that is probably created through collisions with high energy metal ions. After the pulse, the high energy tail of the metal ion IEDF slowly diminished with time as a result of absorption by the substrate and surrounding walls, collisions with the surrounding low energy gas particles. The low energy part of the IEDF is thus preserved over longer times. The high energy tail of gas IEDF was found to disappear shortly after the end of the pulse and only the low energy peak was detected.

6.	The long lifespan of ions in the plasma, 1.2 ms for Cr^{2+} and Ar^{2+}, 2.5 ms for Cr^{1+} and 5 ms after the start of the pulse for Ar^{1+} showed that ion existence is not limited to only the period inside and shortly after the pulse but that both metal and gas ions exist long after the power supplied to the discharge is cut off. The long lifespan of ions impinging on the substrate could be beneficial to reduce residual stresses and inhibit the incorporation of contaminants in the coating.

7.	The time averaged measurements, measured at various distances from target (25 mm to 215 mm), show the dominance of the metal ions in the plasma at all distances both for low (0.3 Pa) and high (3 Pa) pressure. At low pressure both single and double charged metal and gas ions are detected

while at high pressure only single charged metal and gas ions are detected. The peak of the total ion flux has been detected in the region between 10 cm and 15 cm. The long lifespan of ions in that region, measured with the time resolved measurements, could lead to high ion fluxes in that region.

8.   The spatial distribution of Ar^{1+} ion flux has been found to be homogeneous at both pressures in the post discharge. In contrast, the spatial distribution of Ti^{1+} ion flux depends on pressure.   At low pressure it is homogeneous. At high pressure metal ions appear with high concentration at intermediate distances and decrease sharply near the chamber walls.

9.   The ion energy and lifespan of ions were found to depend strongly on collisions of the sputtered flux with the surrounding gas. Life-spans are longest for ions of the heavy mass elements due to rarefaction. Furthermore, only doubly charged ions of elements with mass heavier than Ar are detected at both pressures.

At high pressure a second peak for singly charged metal ions around 1.2ms has been detected that could be the signal of bulk plasma slowly diffusing away from the target.

Metal to gas ion ratio increased for elements with higher sputter yield. The average energy measured in time resolved mode increased for elements that have significantly different mass than Argon indicating that energy losses are highest when masses are similar. At high pressure the average energy of singly charged ions reduced with heavier mass due to shorter mean free path that is reversely proportional to the size of the ions. The metal ion flux showed dependence on binding energy as predicted by the Thompson distribution function.

10.   The mass spectrometer results, measured during deposition of CrAlSiN coatings, show increase of metal contents, particularly Cr^{1+} and Cr^{2+} ions in the plasma with increasing power on the HIPIMS power supply, increase in the nitrogen ion contents and decrease in Ar ion contents. The metal ions arriving to the substrate transfer kinetic energy to adatoms and after transferring all energy they is incorporated in the coating. Gas ion arriving at the substrate bombard adatoms but unlike metal ions gas ions recoil back to plasma.

180

Therefore the energy delivered by metal ions is greater than energy delivered by gas ion.

11.   The surface analysis of the deposited coatings using SEM showed smoother surface of the coating deposited with HIPIMS compared to coatings deposited in DC deposition run. In the images recorded by AFM the size of the columns is clearly visible. The size of the columns was calculated and it showed decrease in the column size with increasing power on the HIPIMS power supply. Increasing the metal contents in the plasma the size of the columns was reduced possibly due to higher mobility of adatoms heated with metal ions impinging on the surface of the coating.

References

[1] R. F. Bunshah, *Handbook of deposition technologies for films and coatings* (Noyes Publications, Westwood, 1994).

[2] W. D. Westwood, *Sputter Deposition* (AVS, New York, 2003).

[3] E. Kay, J. Appl. Phys. **34**, 760 (1963).

[4] R. K. Waits, in *Proceedings of the 24th National Symposium of the American Vacuum Society, 03*, USA, 1978), p. 179.

[5] J. Hopwood, Plasma Sources, Science and Technology **1**, 109 (1992).

[6] V. Kouznetsov, K. Macak, J. M. Schneider, U. Helmersson, and I. Petrov, Surface and Coatings Technology **122**, 290 (1999).

[7] A. P. Ehiasarian, W. -. Munz, L. Hultman, U. Helmersson, and I. Petrov, Surf Coat Technol **163-164**, 267 (2003).

[8] U. Helmersson, H. T. G. Hentzell, L. Hultman, M. K. Hibbs, and J. -. Sundgren, in *Physics and Chemistry of Protective Coatings, 12-14 April 1985*, Universal City, CA, USA, 1986), p. 79.

[9] A. Vetushka and A. P. Ehiasarian, Journal of Physics D: Applied Physics **41**, 015204 (2008).

[10] P. Kudlacek, J. Vlcek, K. Burcalova, and J. Luka, Plasma Sources Sci. Technol. **17**, 025010 (2008).

[11] M. B. Hopkins and W. G. Graham, J. Appl. Phys. **69**, 3461 (1991).

[12] J. T. Gudmundsson, J. Alami, and U. Helmersson, Appl. Phys. Lett. **78**, 3427 (2001).

[13] K. Macak, V. Kouznetsov, J. Schneider, U. Helmersson, and I. Petrov, Journal of Vacuum Science and Technology, Part A: Vacuum, Surfaces and Films **18**, 1533 (2000).

[14] S. Konstantinidis, J. P. Dauchot, M. Ganciu, and M. Hecq, Appl. Phys. Lett. **88**, 021501 (2006).

[15] J. Bohlmark, J. T. Gudmundsson, J. Alami, M. Latteman, and U. Helmersson, IEEE Trans. Plasma Sci. **33**, 346 (2005).

[16] A. P. Ehiasarian and R. Bugyi, in *SVC, Society of Vacuum Coaters - 47th Annual Technical Conference, Apr 24-29 2005* (Society of Vacuum Coaters,

Albuquerque, NM 87122-1914, United States, Denver, CO, United States, 2004), p. 486.

[17] P. Vasina, M. Mesko, J. C. Imbert, M. Ganciu, C. Boisse-Laporte, L. De Poucques, M. Touzeau, D. Pagnon, and J. Bretagne, Plasma Sources Sci. Technol. **16**, 501 (2007).

[18] A. P. Ehiasarian, R. New, W. -D. Munz, L. Hultman, U. Helmersson, and V. Kouznetsov, Vacuum **65**, 147 (2002).

[19] J. Alami, J. T. Gudmundsson, J. Bohlmark, J. Birch, and U. Helmersson, Plasma Sources Sci. Technol. **14**, 525 (2005).

[20] L. de Poucques, J. -C. Imbert, C. Boisse-Laporte, J. Bretagne, M. Ganciu, L. Teule-Gay, and M. Touzeau, Plasma Sources, Science and Technology **15**, 661 (2006).

[21] J. T. Gudmundsson, J. Alami, and U. Helmersson, Surf Coat Technol **161**, 249 (2002).

[22] P. 1. Vasina, M. 1. Mesko, M. 1. Ganciu, J. 1. Bretagne, C. 1. Boisse-Laporte, L. 1. de Poucques, and M. 1. Touzeau, Europhys. Lett. **72**, 390 (2005).

[23] R. E. Somekh, Journal of Vacuum Science & Technology A (Vacuum, Surfaces, and Films) **2**, 1285 (1984).

[24] W. Z. Park, T. Eguchi, C. Honda, K. Muraoka, Y. Yamagata, B. W. James, M. Maeda, and M. Akazaki, Appl. Phys. Lett. **58**, 2564 (1991).

[25] T. Nakano and S. Baba, Vacuum **51**, 485 (1998).

[26] S. Kadlec, Plasma Processes and Polymers **4**, S419 (2007).

[27] S. Kadlec, C. Quaeyhaegens, G. Knuyt, and L. M. Stals, Surf Coat Technol **89**, 177 (1997).

[28] A. Hecimovic, K. Burcalova, and A. P. Ehiasarian, J. Phys. D **41**, 095203 (2008).

[29] J. Bohlmark, M. Lattemann, J. T. Gudmundsson, A. P. Ehiasarian, Y. Aranda Gonzalvo, N. Brenning, and U. Helmersson, Thin Solid Films **515**, 1522 (2006).

[30] S. Kadlec, C. Quaeyhaegens, G. Knuyt, and L. M. Stals, Surf Coat Technol **97**, 633 (1997).

[31] J. Vlcek, P. Kudlacek, K. Burcalova, and J. Musil, Europhys. Lett. **77**, 5 (2007).

[32] J. Bohlmark, A. P. Ehiasarian, M. Lattemann, J. Alami, and U. Helmersson, in *SVC, Society of Vacuum Coaters - 48th Annual Technical Conference, Apr 23-28 2005* (Society of Vacuum Coaters, Albuquerque, NM 87122-1914, United States, Denver, CO, United States, 2005), p. 470.

[33] J. Vlcek, A. D. Pajdarova, and J. Musil, Contributions to Plasma Physics **44**, 426 (2004).

[34] M. V. V. Rao, R. J. Van Brunt, and J. K. Olthoff, Physical Review E (Statistical Physics, Plasmas, Fluids, and Related Interdisciplinary Topics) **54**, 5641 (1996).

[35] D. S. Rickerby and A. Matthews, *Advanced Surface Coatings* (Blackie & Son, 1991).

[36] B. Chapman, *Glow Discharge Processes* (Wiley, New York, 1980).

[37] M. A. Liberman and A. J. Lichtenberg, *Principles of Plasma Discharges and Materials Processing* (John Wiley and Sons, Inc., New York, 1994).

[38] I. P. Raizer, *Gas discharge physics* (Springer-Verlag, 1991).

[39] M. A. Hassouba, F. F. Elakshar, and A. A. Garamoon, Fizika A **11**, 81 (2002).

[40] J. D. Cobine, *Gaseous Conductors* (Dover, New York, 1958).

[41] S. M. Starikovskaia, Journal of Physics D (Applied Physics) **39**, 265 (2006).

[42] S. M. Starikovskaia, N. B. Anikin, S. V. Pancheshnyi, and A. Y. Starikovskii, Proceedings of the SPIE - The International Society for Optical Engineering **4460**, 63 (2002).

[43] S. M. Starikovskaia, N. B. Anikin, S. V. Pancheshnyi, D. V. Zatsepin, and A. Y. Starikovskii, in *15th ESCAMPIG - Europhysics Conference on Atomic and Molecular Physics of Ionized Gases, 05* (IOP Publishing, UK, 2001), p. 344.

[44] U. H. Kwon, S. H. Choi, Y. H. Park, and W. J. Lee, Thin Solid Films **475**, 17 (2005).

[45] T. Yagisawa and T. Makabe, Journal of Vacuum Science & Technology A (Vacuum, Surfaces, and Films) **24**, 908 (2006).

[46] M. Misina, L. R. Shaginyan, M. Macek, and P. Panjan, Surface and Coatings Technology **142-144**, 348 (2001).

[47] U. Helmersson, M. Lattemann, J. Bohlmark, A. P. Ehiasarian, and J. T. Gudmundsson, Thin Solid Films **513**, 1 (2006).

[48] M. F. Dony, A. Ricard, J. P. Dauchot, M. Hecq, and M. Wautelet, in *Fourth International Conference on Plasma Surface Engineering, 19-23 Sept. 1994*, Garmisch-Partenkirchen, Germany, 1995), p. 479.

[49] A. Ricard, C. Nouvellon, S. Konstantinidis, J. P. Dauchot, M. Wautelet, and M. Hecq, Journal of Vacuum Science & Technology A (Vacuum, Surfaces, and Films) **20**, 1488 (2002).

[50] C. Molle, A. Beauvois, M. Wautelet, J. P. Dauchot, and M. Hecq, in *10th International Conference on Quantitative Surface Analysis (QSA-10), 05* (Elsevier, Birmingham, UK, 1999), p. 17.

[51] K. Fukushima, E. Kusano, N. Kikuchi, T. Saito, S. Saiki, H. Nanto, and A. Kinbara, in *Fifth International Symposium on Sputtering and Plasma Processes (ISSP'99), 11* (Elsevier, Kanazawa, Japan, 2000), p. 586.

[52] A. P. Ehiasarian, P. E. Hovsepian, M. Lattemann, J. Bohlmark, and U. Helmersson, in *SVC, Society of Vacuum Coaters - 48th Annual Technical Conference, Apr 23-28 2005* (Society of Vacuum Coaters, Albuquerque, NM 87122-1914, United States, Denver, CO, United States, 2005), p. 480.

[53] S. Konstantinidis, A. Hemberg, J. P. Dauchot, and M. Hecq, Journal of Vacuum Science and Technology B: Microelectronics and Nanometer Structures **25**, 19 (2007).

[54] A. P. Ehiasarian, P. E. Hovsepian, L. Hultman, and U. Helmersson, Thin Solid Films **457**, 270 (2004).

[55] R. Wei, *Plasma surface engineering research and its practical applications* (Research Signpost, 2008).

[56] S. M. Rossnagel and H. R. Kaufman, Journal of Vacuum Science & Technology A (Vacuum, Surfaces, and Films) **6**, 223 (1988).

[57] E. Krikorian and R. J. Sneed, in *Proceedings of a Workshop on Thermodynamics and Kinetics of Dust Formation in the Space Medium, 6-8 Sept. 1978*, Houston, TX, USA, 1979), p. 129.

[58] D. M. Mattox and G. J. Kominiak, in *Proceedings of the 5th international vacuum congress part I, 01*, Boston, MA, USA, 1972), p. 528.

[59] G. Hakansson, J. -. Sundgren, D. McIntyre, J. E. Greene, and W. -. Munz, in *14th International Conference on Metallurgical Coatings, 10/26*, San Diego, CA, USA, 1987), p. 55.

[60] L. Hultman, U. Helmersson, S. A. Barnett, J. E. Sundgren, and J. E. Greene, J. Appl. Phys. **61**, 552 (1987).

[61] K. -H. Muller, J. Appl. Phys. **62**, 1796 (1987).

[62] B. A. Movchan and A. V. Demchishin, Fizika Metallov i Metallovedenie **28**, 653 (1969).

[63] J. A. Thornton, in *Conference on Structure/Property Relationships in Thick Films and Bulk Coatings, 07*, San Francisco, CA, USA, 1974), p. 666.

[64] Hüttinger Elektronik, *HMP 2/4 User's manual.*

[65] W. Lochte-Holtgreven, *Plasma diagnostics* (North-Holland Publishing company, Amsterdam, 1968).

[66] B. Vrsnak, *Temelji fizike plazme* (Skolska knjiga, Zagreb, 1996).

[67] V. A. Godyak, R. B. Piejak, and B. M. Alexandrovich, J. Appl. Phys. **73**, 3657 (1993).

[68] Y. Ralchenko, A. E. Kramida, and J. Reader, *NIST Atomic Spectra Database (version 3.1.5).*

[69] D. J. Griffiths, *Introduction to Quantum Mechanics* (Prentice-Hall, 1995).

[70] D. A. Skoog, F. J. Holler, and T. A. Nieman, **Principles of Instrumental Analysis** (Harcourt Brace College Publishers, 1992).

[71] *Optical spectrometers.*

[72] M. F. 1. Dony, J. P. 1. Dauchot, M. 1. Wautelet, M. 1. Hecq, and A. 1. Ricard, Journal of Vacuum Science & Technology A (Vacuum, Surfaces, and Films) **18**, 809 (2000).

[73] Hiden analytical, *PSM003 User's manual.*

[74] B. Henning and J. Holger, **Surface and Thin Film Analysis: A Compendium of Principles, Instrumentation, and Applications** (Wiley-VCH, 2003).

[75] *Quadrupole Mass Spectrometry.*

[76] N. Takahashi, T. Hayashi, H. Akimichi, and Y. Tuzi, in *47th International Symposium of the American Vacuum Society, 07* (AIP for American Vacuum Soc, Boston, MA, USA, 2001), p. 1688.

[77] *Isotopes of Chromium.*

[78] J. W. Hearle, J. T. Sparrow, and P. M. Cross, **The Use of the Scanning Electron Microscope** (Pergamon Press, 1974).

[79] P. J. Grundy and G. A. Jones, *Electron Microscopy in the Study of Materials* (Edward Arnold, 1976).

[80] J. Klesel, *Scanning Electron Microscopy.*

[81] R. J. Ross, C. Boit, and D. Staab, *Microelectronic Failure Analysis* (ASM International, 1999).

[82] S. A. Hussain, *Introduction to Recent Topics of Material Science.*

[83] M. W. Thompson, Phillos. Mag. **18**, 377 (1968).

[84] D. Wanless, Journal of Physics B (Atomic and Molecular Physics) **4**, 522 (1971).

[85] A. Anders, *A Formulary for Plasma Physics* (Akademie-Verlag, Berlin, 1990), p. 275.

[86] K. Nakajima, K. -. Onisawa, K. -. Chahara, T. Minemura, M. Kamei, and E. Setoyama, Vacuum **51**, 761 (1998).

[87] I. Petrov, P. B. Barna, L. Hultman, and J. E. Greene, Journal of Vacuum Science and Technology A: Vacuum, Surfaces and Films **21**, S117 (2003).

[88] J. Alami, K. Sarakinos, G. Mark, and M. Wuttig, Appl. Phys. Lett. **89**, 154104 (2006).

[89] A. Hecimovic and A. P. Ehiasarian, Journal of Physics D: Applied Physics **42**, 135209 (2009).

[90] S. Veprek and S. Reiprich, Thin Solid Films **268**, 64 (1995).

[91] S. Veprek and A. S. Argon, Journal of Vacuum Science and Technology B: Microelectronics and Nanometer Structures **20**, 650 (2002).

[92] E. Spain, J. Avelar-Batista, M. Letch, J. Housden, and B. Lerga, Surface and Coatings Technology **200**, 1507 (2005).

[93] H. Scheerer, H. Hoche, E. Broszeit, B. Schramm, E. Abele, and C. Berger, Surface and Coatings Technology **200**, 203 (2005).

[94] J. A. Davis, W. D. Sproul, D. J. Christie, and M. Geisler, in *SVC, Society of Vacuum Coaters - 47th annual technical conference*, Apr 24-29 2004 (Society of Vacuum Coaters, Albuquerque, NM 87122, United States, Denver, CO, United States, 2004), p. 215.

[95] A. P. Ehiasarian, A. Vetushka, A. Hecimovic, and S. Konstantinidis, J. Appl. Phys. **104**, 083305 (2008).

[96] R. Pintaske, T. Welzel, M. Schaller, N. Kahl, J. Hahn, and F. Richter, Surface and Coatings Technology **99**, 266 (1998).

[97] S. M. Rossnagel and K. L. Saenger, in *35th National Symposium of the American Vacuum Society, 2-7 Oct. 1988, 05/,* Atlanta, GA, USA, 1989), p. 968.

[98] Guimaraes F, Almeida J, Bretagne J, J. Vac. Sci. Technol. A. 1991 Jan 0;9(1):133-140.

[99] Guimaraes F, Bretagne J, Plasma Sources Sci. Technol. 1993 Aug;2(3):127-137.

[100] Paschen F., Annalen der Physik. 1889;273(5):69-96.

[101] Vašina P, Meško M, de Poucques L, Bretagne J, Boisse-Laporte C, Touzeau M, Plasma Sources Sci. Technol. 2008 8;17(3):035007.

[102] Guimaraes F, Almeida JB, Bretagne J,. Plasma Sources Sci. Technol. 1993 Aug;2(3):138-144.

[103] Ch. Wüstefeld, D. Rafaja, A.P. Ehiasarian, A. Hecimovic, V. Klemm, J. Kutzner, J. Kortus, D. Heger, Thin Solid Films submitted (2010)